Unravelling the Structure–Property Relationship in Eumelanin: From Natural Photoprotection to Tailored Photophysics

A thesis submitted for the degree of

Doctor of Philosophy

in

Chemistry

by

Kavya Vinod

PHD201023

Indian Institute of Science Education and Research
Thiruvananthapuram (IISER TVM),
Thiruvananthapuram – 695551
Kerala, India

April 2026

Declaration

I hereby declare that the Ph.D. thesis entitled **"Unravelling the Structure–Property Relationship in Eumelanin: From Natural Photoprotection to Tailored Photophysics"** is an independent work carried out by me at the School of Chemistry, Indian Institute of Science Education and Research Thiruvananthapuram (IISER TVM), under the supervision of **Prof. Mahesh Hariharan** and it has not been submitted anywhere else for any other degree, diploma or title. In keeping with the general practice of reporting the scientific observations, due acknowledgements have been made wherever the work described is based on the findings of other investigators.

Place: IISER Thiruvananthapuram **Kavya Vinod**

Date: 27.03.2026

Certificate

This is to certify that the work embodied in the thesis entitled **"Unravelling the Structure–Property Relationship in Eumelanin: From Natural Photoprotection to Tailored Photophysics"** has been carried out by **Kavya Vinod (PHD201023)** under my supervision at the School of Chemistry, Indian Institute of Science Education and Research Thiruvananthapuram (IISER TVM) and the same has not been submitted elsewhere for a degree.

Place: IISER Thiruvananthapuram
Date: 27.03.2026

Prof. Mahesh Hariharan
(Thesis Supervisor)

Dedicated to

my loving family

"Watch and pray, dear, never get tired of trying, and never think it is impossible to conquer your fault."

— Louisa May Alcott, Little Women

Acknowledgements

My thesis carries within it the contributions, kindness, and belief of many people, without whom this journey would not have been possible.

My sincere thanks go to my supervisor Prof. Mahesh Hariharan, who introduced me to the world of melanin and encouraged me to explore it with curiosity and independence. Having the space to think freely, try ideas, and learn from my own experiments shaped not only this thesis but also the way I approach science. His guidance, encouragement, and emphasis on growing both as a researcher and as a person have played an important role in my journey, and I remain deeply grateful for that.

I sincerely thank Prof. J. N. Moorthy, Director of IISER Thiruvananthapuram, for ensuring that we had access to the excellent research environment at IISER Thiruvananthapuram. I also thank the current and former Heads of the School of Chemistry for consistently supporting my research through the CIL and other facilities in the department. My heartfelt thanks to my doctoral committee members, Prof. K. George Thomas and Prof. Vinesh Vijayan, for their insightful comments and constant support throughout my work.

I extend my sincere thanks to the faculty of the School of Chemistry. I am especially grateful to Dr. Adithya Lakshmanna for his guidance during troubleshooting phases in the laser lab, and to Prof. Reji Varghese for his consistent support during the course of this work. I am immensely grateful to Dr. Brijith Thomas (New York University Abu Dhabi), not only for the collaboration in solid-state NMR but also for being a constant source of motivation and clarity throughout my PhD. My sincere thanks also go to Prof. Yasuhiro Kobori (Kobe University) for the collaboration on transient EPR and for the warmth and generosity extended during my research stay in Kobe. I am thankful to Prof. Frank Würthner, Prof. Henrik Ottosson and Prof. David Casanova whose collaborations widened my scientific horizon and took me beyond the boundaries of my thesis.

To all past and present members of the Hariharan Lab—Dr. Nanditha G. N., Dr. Bappa G., Dr. Swati D., Dr. Aasif K., Dr. Indrajit G., Dr. Souvik R., Dr. Remya R., Dr. Ebin S., Dr. Devika S., Dr. Athira T. J., Ms. Amalu M., Dr. Lijina M. P., Dr. Swathi Krishna P. E., Dr. Niyas M. A., Mr. Vishnu V., Ms. Meera M., Mr. Alfy B., Mr. Deepu G., Mr. Krishnaprasad., Mr. Dilip P. S., Dr. Aniruddha M., Mr. Jibin S., Mr. Philip D. M., Ms. Anjana V. M., Ms. Suvarna S. C., Ms. Fathima T., Mr. Sharath D., Mr. Amalnadh T., Mr. Tamizharasan T., Mr. Abhijith M., Ms.

Sona S., Mr. Gokul G., Mr. Ariharasudhan R., Ms. Adheena P., Ms. Tessy P., Ms. Raniya P., Mr. Jeswin S., Ms. Akshaya N., Ms. Keerthy P. S., Mr. Vivek V. D., Mr. Akhilesh K. U., Mr. Sohan D. J., Ms. Diana T., Ms. Pallavi P. D., Ms. Hruidya C. B., Ms. Medha G., Ms. Meby J., Ms. Meera J., Mr. Lukhmanul H. K., Mr. Hanock B., Ms. Anitta B., Ms. Nitha M., Mr. Aivin T., Mr. Avinash H., Mr. Binil V., Ms. Anjana S. K., Ms. Agaja K., Ms. Najuma N., Ms. Megha S., Ms. Aswathy H., Ms. Greeshma G., Ms. Dhanushya P., Mr. Jagannathan V., Ms. Aarjoo J., Ms. Sujitha S., Mr. Devanath M. B., Mr. Avanindhra B., Mr. Anjelo J., Mr. Anzil B. M., Ms. Gayathri P. R., Mr. Harish K., Ms. Gouri R., and Ms. Meenakshy B.—each interaction, shared challenge, moment of laughter, and everyday exchange contributed to a sense of community that made the lab feel like a second home.

My warmest thanks go to Dr. Devika Sasikumar, whose guidance and friendship were anchors during the early and uncertain days of my PhD; Dr. Ebin Sebastian, who taught me the intricacies of transient absorption spectroscopy with patience; and Dr. Nanditha Nair, who guided me through the maze of synthesis when everything was new and overwhelming. I am grateful to the BS-MS, I-PhD, PhD, and project students—Mr. Amalnadh T., Ms. Najuma Noushad, Mr. Lukhmanul Hakeem K., Ms. Diana Thomas, Mr. Sohan D. Jadhav, Ms. Pallavi P. Das, Ms. Nitha Mohan, Ms. Medha Gangopadhyay, Ms. Meby Johnson, and Ms. Adheena P.—who worked with me on various projects. Their energy and curiosity to explore new ideas made the work lighter and far more enjoyable. I would also like to thank Dr. Gowtham Raj, Ms. Jemshiya K., Dr. Reshma Mathew, Dr. Anook Nazar E. A., Dr. Livin Paul, and Mr. Muhammed Raees for their experimental assistance and for the many constructive discussions that helped shape different parts of my doctoral work.

My sincere thanks extend to the administrative staff, and to all the teaching and non-teaching staff of IISER Thiruvananthapuram, whose silent support helped my course. I am particularly grateful to Mr. Adarsh B. for assistance with NMR experiments; Mr. Nibith K. for GC-MS, elemental analysis, and FT-IR measurements; Mr. Alex P. A. for XPS and SC-XRD analysis; Ms. Athira S., and Ms. Ansumol for MALDI-TOF measurements; Mr. Aneesh for SEM imaging; and Mr. Pradeep K. G. for HRMS support. I also wish to acknowledge the staff of the library, IT, purchase, finance, and mess departments for their timely help throughout my PhD. I gratefully acknowledge CSIR for the financial support that made this research possible.

I am fortunate to have had friends who made this long journey feel lighter and fuller. Merin and Dhanusree have been solid pillars in my life—their presence, shared worries, small celebrations, and everyday conversations added joy and balance to the most intense periods of

this work. I am also grateful to Mr. Philip D. M., Mr. Jibin S., Mr. Aniruddha M., Ms. Preetika V., Ms. Megha R., Ms. Ann T. B., Mr. Mehul T., Mr. Prajoy M., and Mr. Abhishek S., offering comfort and humour exactly when it was needed most. A special thanks to Philip for listening to my countless rants and thoughts along the way. I am very thankful to my PhD batchmates for creating a sense of belonging at IISER TVM, right when we joined the institute. I am deeply grateful to Prof. Kuruvilla Joseph, Dr. Meegle S. Mathew, Prof. C. Sivasankar, and Dr. Kuzhalmozhi Madarasi, whose mentorship during my undergraduate years offered my first real exposure to chemistry research. Those early experiences strengthened my confidence, and played an important role in guiding me toward pursuing science.

Finally, my deepest love and gratitude belong to my family. My mother, Dr. Sudha K., and father, Vinod Kumar K. P., nurtured both curiosity and courage from childhood, creating the foundation that has shaped every stage of my personal and academic growth. My sister, Arya, has been a constant source of steadiness and reassurance through every high and low. I am also deeply grateful to my partner, Akash, whose unwavering care and encouragement carried me forward through my PhD journey. And to my grandmother, Madhavi, whose strength and resilience continue to be a guiding light. I am also grateful to my extended family—father, Pradeepkumar C. M. and mother, Rajasree T.—for welcoming me so warmly into their family and encouraging me to pursue my work with patience. A heartfelt thanks to my brother, Akshay, for his enthusiasm whenever we discussed my research, and to my grandmother, Lakshmi, for her warmth and genuine interest in my work. My family has always understood the demands and sacrifices that my work required, meeting them with patience and motivation that have kept me focused throughout.

Above all, I owe my deepest gratitude to God. Through every high and low, there was a quiet strength to lean on, and a grace that carried me forward in this journey.

Preface

Eumelanin is a brown-black pigment present throughout the biological realm. Eumelanin is crucial for photoprotection due to its ability to efficiently absorb light across a broad spectrum of wavelengths and promptly dissipate the absorbed energy safely. Eumelanin is chemically heterogeneous and architecturally chaotic, comprising several indole-derived constituents that exist in various oxidation states and are interconnected in multiple arrangements. Conventional chromophores possess clearly delineated molecular structures, which is not applicable in case of eumelanin. The dynamic supramolecular structure complicates the relationship between structure and properties, rendering it difficult to ascertain their correlation. The unique photophysical characteristics of eumelanin, such as broadband electronic absorption, ultrafast excited-state deactivation, and exceptional photostability, arise from the intricate interplay between molecular disorder and supramolecular structure. These characteristics not only facilitate eumelanin's role in photoprotection in organisms but also render it an effective paradigm for enhancing functional organic photonic materials.

While beginning my work on eumelanin, the trials were simple but surprisingly interesting. There was a lot of literature on its spontaneous polymerization, but seeing it happen in person was a whole new experience. Solutions of the monomeric building blocks of eumelanin were prepared and left on the workbench overnight. The solution that was transparent the night before had turned into a deep, inky black by the next morning. How could something so simple change into a pigment that serves its purpose so efficiently? Nature never picks its chemistry by chance, and as I investigated more about it, I began to appreciate how carefully this molecular design is put together to do its job.

This thesis explores how molecular structure, aggregation, and excitonic interactions govern the excited-state dynamics of eumelanin and related organic systems, providing a unified perspective from monomeric building blocks to functional multimeric assemblies and designed emitters. The work is motivated by the fundamental question of how structural disorder and supramolecular organization influence photophysical processes, with implications for both biological photoprotection and the rational design of organic photonic materials. *Chapter 1* introduces eumelanin, the ubiquitous brown-black pigment, and its extraordinary photoprotective properties. Here, the relationship between chemical heterogeneity, supramolecular organization, and ultrafast excited-state deactivation is dissected, showing how structural disorder underpins both broadband absorption and efficient energy dissipation. This

chapter lays the conceptual foundation for understanding eumelanin's photophysics and establishes strategies for investigating its structure–property relationships. *Chapter 2* focuses on DHICA, a key eumelanin monomer, and elucidates its crystal structure and assembly-specific behaviour. Using three-dimensional electron diffraction, solid-state NMR, and density functional theory, how exciton delocalization operates within the π–π stacked and hydrogen-bonded network, is uncovered. Extending these insights to ^{13}C-labelled DHICA-based polymer provides a window into the molecular heterogeneity that defines eumelanin's functional properties.

Molecular size and aggregation profoundly influence how eumelanin dissipates electronic energy. *Chapter 3* examines model eumelanin multimers, *i.e.*, DMICE, DMICE-D, and DMICE-T, to understand the effect of aggregation on electronic absorption and ultrafast energy relaxation. By combining solution- and thin-film photophysics, it is demonstrated that increasing multimer length and aggregation amplifies excitonic interactions, enhances non-radiative decay pathways, and recapitulates eumelanin's characteristic photoprotective energy dissipation. The interplay of Coulombic and charge-transfer couplings is shown to control these photophysical outcomes. *Chapter 4* explores aggregation-induced modulation of excited-state energy landscapes in eumelanin-inspired hybrid charge-transfer emitters, HD and BrD. The chapter reveals how J- versus H-type aggregation selectively governs delayed fluorescence and room-temperature phosphorescence, highlighting the role of supramolecular arrangement in tuning singlet–triplet energy gaps and reverse intersystem crossing. This chapter connects the fundamental insights from natural eumelanin to the rational design of functional bio-organic luminescent materials. Taken together, this thesis establishes a comprehensive framework for linking molecular structure, aggregation, and excitonic interactions to photophysical outcomes in eumelanin-based molecules. By progressing from monomers to multimers and functional derivatives, the thesis provides a roadmap for understanding and harnessing the excited-state dynamics of eumelanin-inspired systems for both fundamental and applied research in photophysics and materials science.

Table of Contents

List of Figures

List of Tables

List of Schemes

Abstract

Eumelanin, an abundant biological pigment, exhibits remarkable photoprotection through broadband electronic absorption and ultrafast excited-state deactivation. Despite extensive research, the relationship between its chemical heterogeneity, supramolecular organization, and photophysical behaviour remains incompletely understood. This thesis explores the structure–property relationships of eumelanin and related indole-based systems, from monomeric units to multimers and engineered emitters, to uncover the molecular and supramolecular factors governing energy dissipation. *Chapter 1* establishes the conceptual framework of eumelanin, showing how intrinsic chemical disorder and supramolecular interactions enable eumelanin's photoprotective properties. *Chapter 2* elucidates the crystal structure and assembly of DHICA, a key monomer of eumelanin, using three-dimensional electron diffraction, solid-state NMR, and density functional theory, revealing that charge-transfer exciton delocalization within the π-stacked, hydrogen-bonded network dominates energy transfer. *Chapter 3* examines model multimers (DMICE, DMICE-D, DMICE-T) in solution and thin films, demonstrating that increasing multimer size and aggregation enhances excitonic interactions, broadens electronic absorption, and accelerates ultrafast energy dissipation, with both intermolecular and intramolecular electronic couplings modulating photophysical outcomes. *Chapter 4* extends these principles to synthetic eumelanin-based emitters (HD and BrD), showing that J- versus H-type aggregation selectively tunes singlet–triplet gaps, reverse intersystem crossing, and influence the balance between delayed fluorescence and room-temperature phosphorescence. Collectively, this work offers a comprehensive framework for understanding how molecular structure, aggregation, and excitonic interactions shape excited-state dynamics in eumelanin. By elucidating the structure–property relationships in eumelanin, this work lays the foundation for the rational design of bio-inspired materials with precisely tunable optical properties.

Chapter 1

Introduction to Eumelanin: Structural and Photophysical Complexity

1.1. Melanin in Nature

Melanin is one of the most ubiquitous pigments in nature.[1] Its name, derived from the Greek *melanos* ("black" or "dark"), reflects the colour of many melanized structures. Beyond its characteristic appearance, melanin plays an important role in biological protection and survival, enabling organisms to regulate temperature, shield themselves from radiation, and neutralize reactive species.[2] Its presence is well recognised in humans, animals, plants, fungi, and microorganisms alike, underscoring its evolution as a multifunctional biomaterial. Unlike most biological macromolecules, melanin does not arise from a template-driven or sequence-controlled process. Instead, it emerges through oxidative reactions involving a variety of indole-based precursor molecules, which then undergo enzymatic transformations by tyrosinase and assemble into complex, heterogeneous structures ranging from nanoscale oligomers to micron-sized aggregates. These structures are stabilized by an interplay of covalent bonds, hydrogen bonds, aromatic stacking, and other noncovalent forces.[3] This chemical and structural diversity, coupled with poor solubility and high molecular weight, has made it particularly challenging to define a clear molecular architecture for melanin or to establish simple structure–function relationships.

The scientific exploration of melanin stretches back centuries.[1] Early investigations described its dark pigmentary nature, but only later was its biosynthetic origin traced to the oxidation of tyrosine.[1] The isolation of key intermediates, such as 5,6-dihydroxyindole (DHI) and its carboxylated analogue DHICA, laid the groundwork for the polymer model of melanin (later categorised as eumelanin).[4-6] Over time, distinct classes of melanin were recognized: eumelanin, pheomelanin, neuromelanin, pyomelanin, and allomelanin, each associated with

specific biological systems and functions (Figure 1.1).[6] Among these, eumelanin has emerged as the most extensively explored due to its prominent role in human pigmentation and photoprotection.

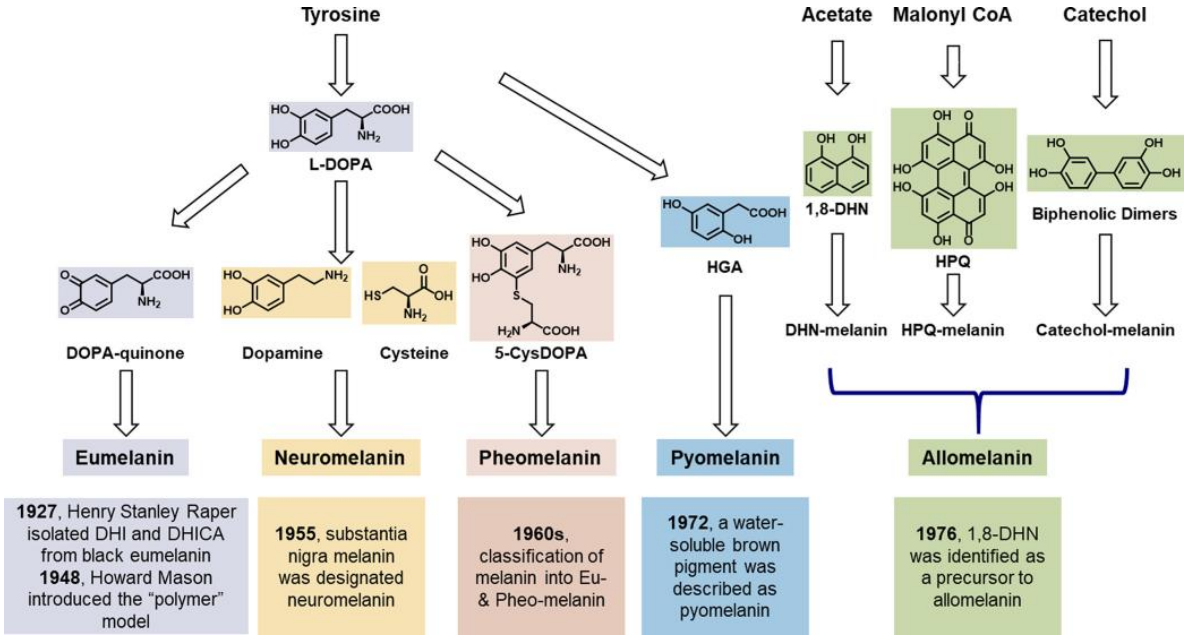

Figure 1.1: Overview of the biosynthetic pathways for the five main classes of melanin: eumelanin, pheomelanin, neuromelanin, and the nitrogen-free melanins, allomelanin and pyomelanin (Reproduced from Ref. 6; Copyright © 2021 American Chemical Society).

In animals, eumelanin, pheomelanin, and neuromelanin dominate pigmentation processes, while pyomelanin and allomelanin are more common in plants and microbes.[6] Their optical signature is defined by broadband electronic absorption across the UV–visible–NIR range, giving rise to low photoluminescence. In humans, eumelanin is responsible for brown to black skin and hair pigmentation, while pheomelanin contributes to lighter tones and red hair.[1] Both pigments are produced within specialized organelles called melanosomes.[7] Functionally, eumelanin is renowned for its exceptional ability to absorb and dissipate light energy harmlessly, acting as a natural photoprotective barrier. In contrast, pheomelanin tends to promote photochemical damage through reactive pathways, although it may also serve structural or biosynthetic roles in pigment formation.[8] Small variations in molecular structure

and polymerization chemistry can therefore lead to strikingly different biological outcomes. Melanin's remarkable chemistry and multifunctionality reinforce essential biological roles, such as photoprotection, radical scavenging, and adaptive pigmentation and provide an inspiration for innovation in materials science.[9] By combining chemical diversity with supramolecular organization, melanin achieves robust energy dissipation, structural resilience, and optical versatility. Understanding these natural design principles not only highlights the biological significance of melanin but also inspires the development of synthetic, eumelanin-inspired materials with tunable optical and photoprotective properties, bridging the gap between nature and functional technology.

1.2. Eumelanin as a Natural Pigment

Eumelanin, derived from the Greek prefix *"eu,"* meaning "good" or "well," is the most extensively studied member of the melanin family.[9] It is widely distributed in nature, occurring in human skin and hair, bird feathers, squid ink, lichens, and even fossilized dinosaur remains.[7] Its biosynthetic pathway originates from the amino acid tyrosine, which undergoes enzymatic oxidation by tyrosinase to produce levodopa (L-DOPA) and subsequently dopaquinone. Through a series of intramolecular transformations, dopaquinone yields the two principal monomeric building blocks of eumelanin: 5,6-dihydroxyindole (DHI) and 5,6-dihydroxyindole-2-carboxylic acid (DHICA). These monomers undergo further oxidation, coupling, and aggregation to generate the highly complex, heterogeneous macromolecular pigment that defines eumelanin's structure and function (Figure 1.2).[10]

Computational studies and structural modelling suggest that these monomers assemble into planar oligomers, which stack further into higher-order, amorphous structures, providing the hierarchical architecture characteristic of eumelanin.[2] Among its monomeric components, DHICA plays a particularly important role in natural eumelanin, often constituting more than half of the subunits in some samples.[11] The carboxyl group in DHICA introduces atropisomerism due to restricted rotation between adjacent units, while the zwitterionic nature of these subunits contributes to the pigment's photoprotective capabilities.[12]

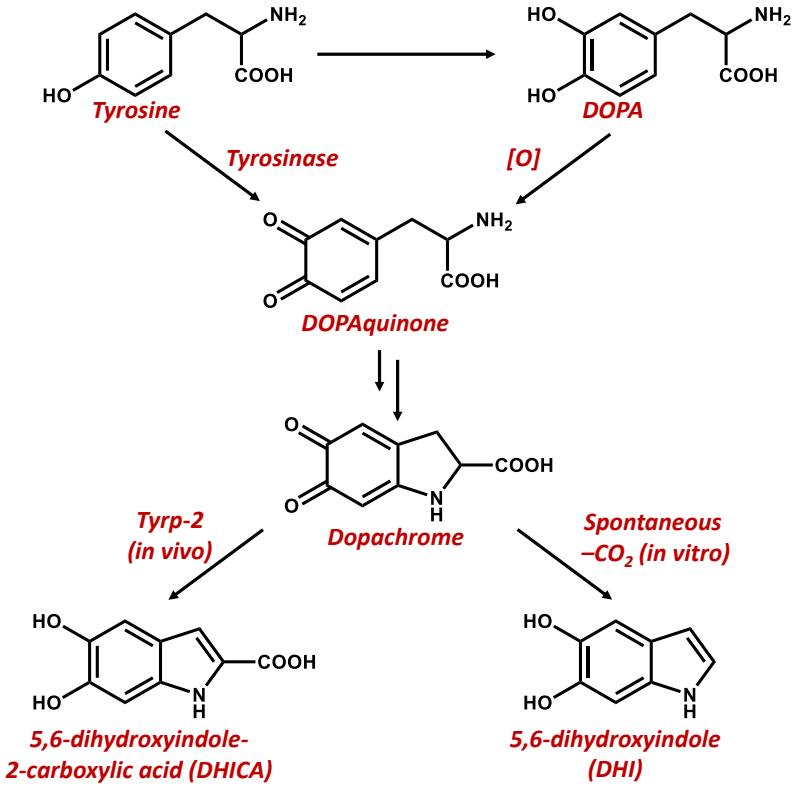

Figure 1.2: Biosynthetic and synthetic pathways for natural eumelanin, showing the two monomers – DHI and DHICA.

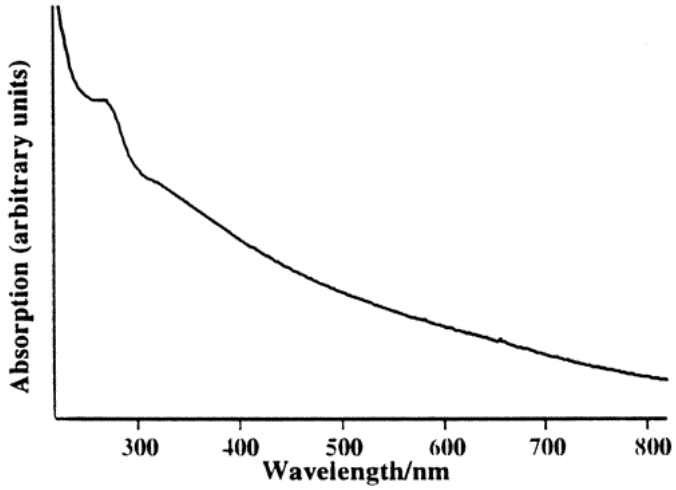

Figure 1.3: Optical spectrum of an aqueous solution of eumelanin from Sepia officinalis at room temperature (Adapted from ref. 13; Copyright © 1999 American Chemical Society).

Eumelanin serves two primary roles: coloration and photoprotection. Its broad, featureless absorption across the UV and visible regions is uncommon for organic chromophores, resembling the optical behaviour of inorganic semiconductors (Figure 1.3).[14-16] This broad absorption, combined with extremely low fluorescence quantum yields, ensures that more than 99.9% of absorbed photons are dissipated non-radiatively as harmless heat, a key attribute for photoprotection. The pigment's optical behaviour also reveals complex excitonic interactions and the influence of molecular aggregation, explaining why eumelanin continues to challenge conventional characterization techniques. Collectively, these properties illustrate how eumelanin's chemical composition, supramolecular assembly, and excited-state dynamics converge to support its biological function.

1.3. Eumelanin Compared to Well-Characterized Biomolecules

Some of the most celebrated breakthroughs in molecular biology have come from solving the structures of well-defined biomolecules. The discovery of the DNA double helix revealed the physical basis of genetic inheritance.[17] The triple-helical structure of collagen explained the remarkable tensile strength of connective tissues.[18] High-resolution structures of myoglobin and hemoglobin illuminated, atom by atom, how proteins bind and transport oxygen.[19, 20] These landmark achievements were possible because these molecules are chemically uniform, sequence-defined, and structurally ordered. Their regularity made them ideal candidates for structural elucidation by X-ray diffraction, NMR spectroscopy, and other high-resolution techniques, enabling a direct link between molecular structure and biological function. Eumelanin stands in sharp contrast to these molecular archetypes. It is not encoded by a fixed genetic sequence, nor does it adopt a single well-defined structure.[21] Instead, eumelanin is produced through spontaneous oxidative polymerization of heterogeneous monomers, primarily DHI and DHICA, generating a complex mixture of oligomers and supramolecular aggregates.[22] This inherent chemical and structural heterogeneity have long hindered efforts to obtain a molecular-level structural model comparable to those available for DNA, proteins, or collagen.

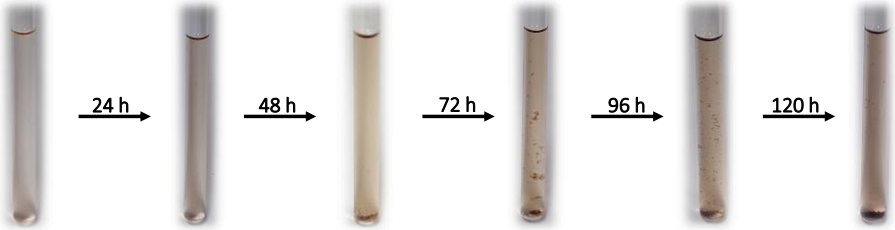

Figure 1.4: DHICA in acetone-d_6 showing the spontaneous autoxidative polymerization, turning to insoluble black material.

The challenge is compounded by the labile nature of its monomeric building blocks. DHI and DHICA remain stable when stored under an inert atmosphere and in the absence of oxygen, but they undergo rapid oxidation and polymerization upon exposure to air, even at low temperatures such as −20 °C. Within days, the pale starting material converts into black eumelanin pigment, and at room temperature this process occurs within a week. In solution, polymerization is even faster, producing an insoluble black solid within hours (Figure 1.4).[23] This insolubility, combined with the absence of long-range molecular order, renders conventional characterization methods such as X-ray crystallography and solution NMR ineffective. Unlike DNA or proteins, eumelanin cannot be represented by a single molecular structure. It exists as a dynamic, disordered ensemble whose properties arise from the interplay between chemical diversity, polymerization pathways, and supramolecular aggregation. This structural complexity is precisely why, despite its ubiquity and importance, the molecular architecture of eumelanin remains unresolved. Yet, this very complexity is intimately tied to its biological function. Eumelanin's ability to dissipate energy efficiently, scavenge radicals, and provide broad-spectrum photoprotection emerges from its disordered, heterogeneous nature. While molecules like DNA and collagen reveal how order enables function, eumelanin exemplifies how functional disorder can also be a powerful design principle in nature.

1.4. Structural Complexity in Eumelanin

Eumelanin polymers exhibit a remarkable degree of structural heterogeneity that arises at multiple organizational levels, beginning with the chemical nature of their building blocks (Figure 1.5).[9] One major source of this heterogeneity is the diversity of monomeric and intermediate species incorporated during melanin formation. This chemical variability often

emerges from competing pathways at critical branching points in the synthetic or biosynthetic sequence, for example, dopachrome rearrangement, which results in the inclusion of multiple intermediates due to inherently slow oxidation kinetics.[24] Additional factors, such as the deliberate co-polymerization of different monomers, the presence of reactive additives, post-synthetic transformations like o-quinone fission, and the physical adsorption of residual monomer or oligomer species onto the growing polymer matrix, further contribute to this complexity. Evidence for such chemical heterogeneity has come from degradation studies, model pathway investigations, solid-state NMR, and, most prominently, MALDI-MS.[24] These studies have consistently shown broad structural diversity in DHI- and DHICA-based melanins formed under both chemical and biomimetic enzymatic conditions.[25]

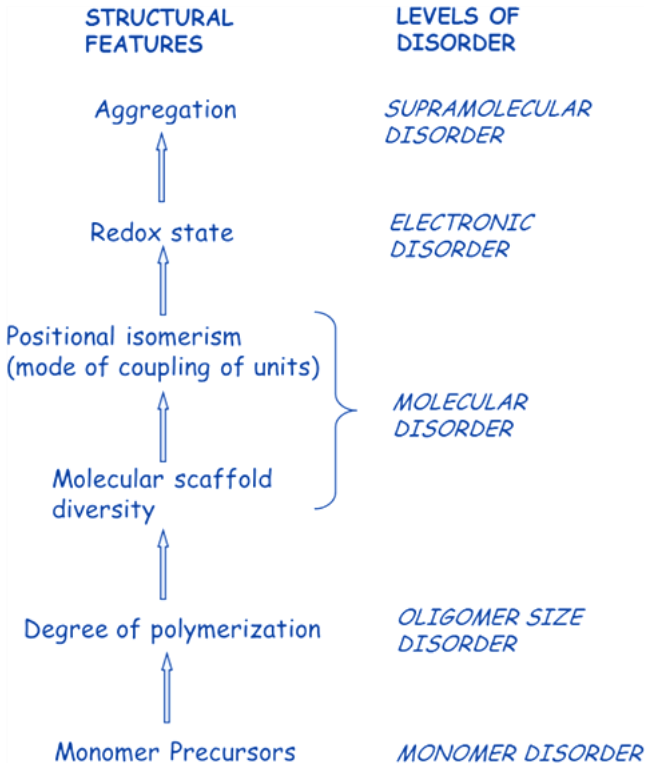

Figure 1.5: Simplified representation of chemical disorder in eumelanin across multiple structural hierarchies and length scales (Adapted from ref. 10; Copyright © 2014 American Chemical Society).

Another layer of disorder is introduced through variations in molecular size, which reflect differences in the degree and mode of polymerization (Figure 1.6). Slow oxidation

kinetics and the adsorption of growing chains onto precipitating particles can result in broad distributions of oligomer lengths, giving rise to molecular weight dispersion. Mass spectrometry has revealed oligomers containing up to 30 units in DHI melanin, although this likely represents a lower bound due to technical limitations.[26-28] Direct evidence for the polymeric nature of polydopamine has also been obtained through single-molecule force spectroscopy, which allows the mechanical properties of individual chains to be probed.[28] At the molecular level, heterogeneity is further amplified by differences in coupling positions and bonding modes, which generate multiple isomeric structures within each oligomer size class. This arises from the intrinsic regioselectivity of monomer coupling as well as the influence of oxidation conditions on preferred linkage patterns. The successful isolation of isomeric oligomers underscores how the specific mode of polymerization directly shapes the chemical diversity of eumelanin structures.[29]

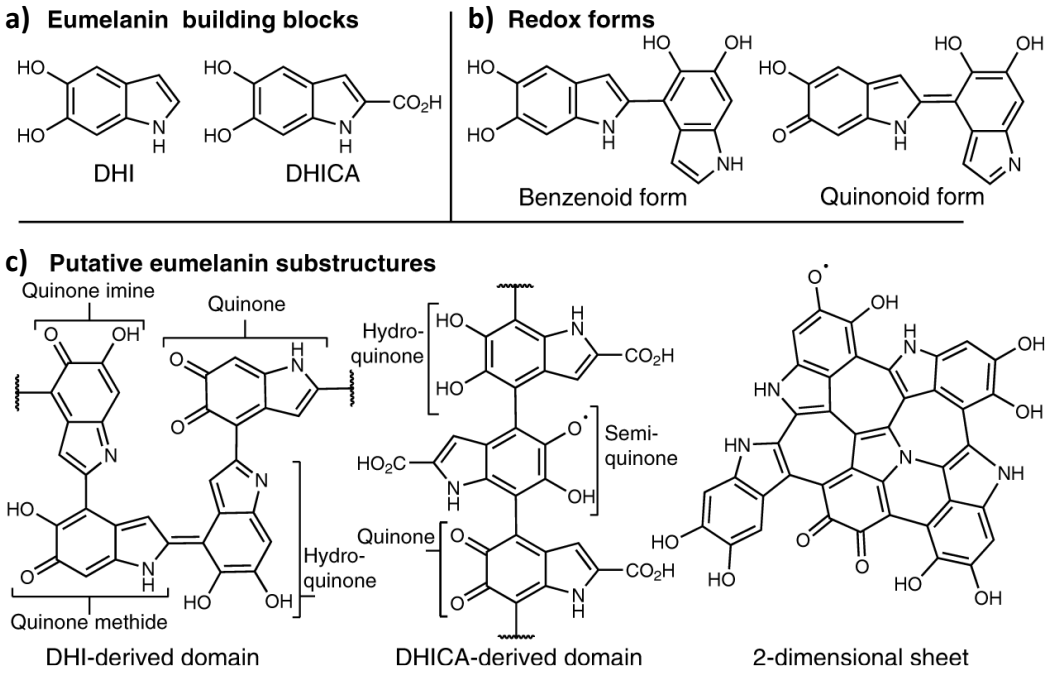

Figure 1.6: Proposed structural motifs representing different subunits of eumelanin (Adapted from ref. 30; Copyright © 2020 Springer Nature).

Redox heterogeneity represents another defining feature of eumelanin. The polymer's oligomeric components can exist in various oxidation states, including catechol, semiquinone,

and quinone forms.[25] The distribution of these states is governed by factors such as the oxidizing nature of individual components, the pH and type of oxidizing agent, the degree of π-electron delocalization, and sample aging. EPR spectroscopy provides direct insight into this electronic disorder, with the signal width reflecting the range of accessible redox states.[31] Complementary electrochemical measurements, including cyclic voltammetry, reveal the ability of the polymer to buffer both oxidizing and reducing agents.[32, 33] Organic electrochemical transistor studies further indicate slow equilibration between redox states, with hysteresis in current response pointing to a gradual relaxation from kinetically trapped states to more stable electronic configurations.[34] This molecular and electronic complexity ultimately extends to the supramolecular level, where oligomers assemble through a variety of noncovalent interactions. The resulting architectures are influenced by the relative proportion of planar and twisted segments, the efficiency of π–π stacking and cation–π interactions, and the capacity for hydrogen bonding.[35] Depending on these factors, the resulting assemblies can exhibit varying degrees of order, ranging from amorphous networks to partially organized domains. Techniques such as AFM, SEM, TEM, and X-ray scattering have provided clear evidence of this supramolecular disorder, revealing its critical role in defining the structural and functional properties of eumelanin materials.[36, 37]

1.5. Excitonic Coupling in Molecular Aggregates

Deciphering melanin's inherent photoprotective role and directing the development of next-generation organic photovoltaic and light-harvesting materials require an understanding of how molecular structure influences the photophysical characteristics of eumelanin and related molecular assemblies. The investigation of structure–property correlations have profound historical origins in the context of molecular aggregation. In the 1930s, Scheibe and Jelley independently noted a significant red shift in the absorption spectra of concentrated solutions of 1,1′-diethyl-2,2′-cyanine chloride (pseudoisocyanine or PIC), demonstrating that dense molecular packing can significantly modify optical characteristics.[38, 39] These pioneering results established the foundation for comprehending the emergence of electronic effects in molecular assemblies.[40]

To elucidate these phenomena in molecular crystals, Davydov created the concept of excitons, which are quasiparticles that characterize the delocalization of electronic excitation among interacting molecules.[41] Kasha expanded on these discoveries to develop the molecular exciton theory, which established how the spatial arrangement of chromophores affects the photophysical properties.[42] This approach was very helpful in understanding natural light-harvesting complexes, where the efficiency of energy transmission is controlled by the precise structure of pigments. When multiple chromophores absorb light, their transition dipole moments (TDMs) interact, leading to excitonic coupling, a fundamental process that mediates the exchange and delocalization of electronic excitation energy among neighbouring molecules. Such coupling may arise within a single molecule (intramolecular) or between distinct molecules (intermolecular), depending on the system's geometry and electronic environment.

Kasha's exciton model, formulated in the 1960s, described these interactions using the point dipole approximation, where each chromophore's transition density is simplified as a dipole vector.[42] The coupling between these dipoles gives rise to characteristic spectroscopic features that define the excited-state dynamics of multichromophoric assemblies. Despite its simplicity, this model provided a powerful framework for quantifying long-range Coulombic interactions (J_{Coul}) between chromophores and remains foundational for interpreting excitonic effects in molecular aggregates and optoelectronic materials. The ideal dipole approximation is employed to estimate the J_{Coul} interactions and can be represented as:[43, 44]

$$J_{Coul} = \frac{\mu^2(\cos\alpha - 3\cos^2\theta)}{4\pi\varepsilon_0 R^3} \qquad \text{(Eq. 1.1)}$$

Here, R is the intermolecular distance, θ is the angle between the polarization direction of the dipole and the vector linking the centres of the two molecules, α corresponds to the dihedral angle between their molecular planes, and ε_0 represents the permittivity of free space. The term ($\cos\alpha - 3\cos^2\theta$) defines the orientation factor (κ).

Kasha's exciton model classifies molecular aggregates into H- and J-types according to the spatial orientation of their TDM vectors. Chromophores stack face-to-face resulting in H-aggregates (H stands for hypsochromic) (Figure 1.7). The excitonic energy levels separate as a result of Coulombic interactions in the face-to-face arrangement. Energy level splitting causes

a net dipole moment cancellation that optically forbids transitions to the lower energy excitonic state, while permitting transitions to the higher energy state. A blue-shifted absorption maximum and either weak or nonexistent fluorescence emission in the H-aggregate in comparison to the monomer are the photophysical manifestations of the excitonic energy level splitting.[45]

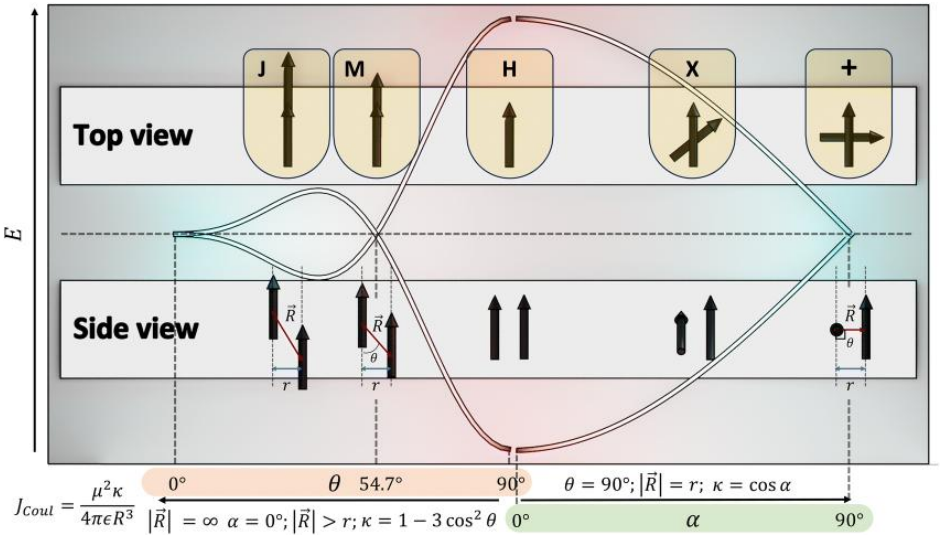

Figure 1.7: Scheme demonstrating the correlation between slip angle (θ), rotational angle (α) and the orientation factor (κ) (Adapted from ref. 46; Copyright © 2023 Royal Society of Chemistry).

Conversely, the chromophores of J-aggregates, named for Jelley, are arranged from head to tail (Figure 1.7).[47] Transitions to the lower excitonic state with a net dipole moment become accessible by the splitting of the excitonic energy level. Red-shifted absorption and red-shifted enhanced emission bands in comparison to the monomer are characteristics of the lower energy state transitions. Apart from the well-known H- and J-type aggregates, Kasha also suggested that there is a unique class of aggregates that result from insignificant Coulombic interactions and are distinguished by electronically degenerate states and cross-oriented transition dipoles (Figure 1.7).[48] Another type of aggregates referred to as magic angle-stacked aggregates, which have been shown to exhibit monomer-like characteristics. These are parallelly ordered slip-stacked molecular aggregates with a slip angle of 54.7º (magic angle) between the transition dipoles (Figure 1.7).[49] However, the orbital interactions between the

chromophoric units in densely packed chromophoric arrangements (d ≈ 3.5 Å) are not taken into account by Kasha's salient dipole-dipole excitonic model, necessitating the use of sophisticated electronic coupling models to describe the aggregate's overall photophysics.

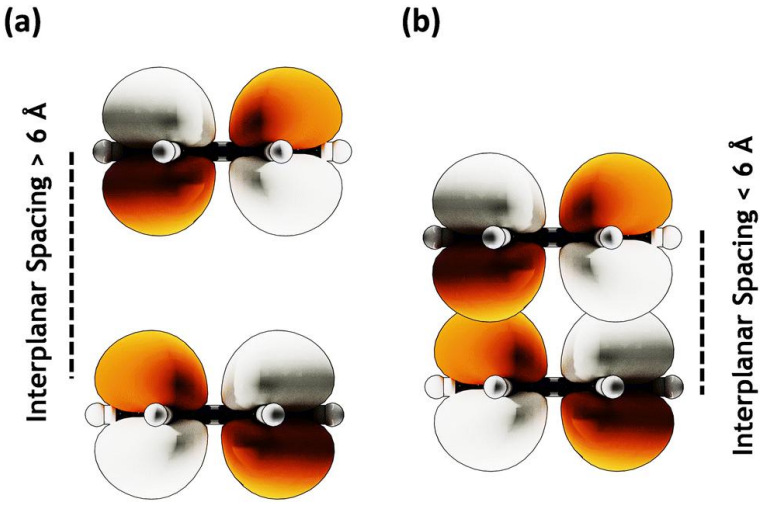

Figure 1.8: Molecular orbitals with (a) larger interplanar separations (≥ 6 Å), where orbital overlap is negligible, and (b) smaller separations (≤ 6 Å), where significant orbital overlap occurs (Adapted from ref. 46; Copyright © 2023 Royal Society of Chemistry).

Intramolecular excitonic coupling plays a crucial role in governing the excited-state dynamics of covalently linked multichromophoric systems. Previous studies have shown that both through-bond and through-space interactions contribute to charge separation and energy transfer processes in such systems. However, in molecular assemblies where the chromophores are separated by only a few angstroms, through-space interactions typically dominate, as the proximity of the monomeric units enables strong electronic communication.[46] When the interchromophoric distance becomes sufficiently small, significant orbital overlap between neighbouring units can occur, leading to short-range excitonic coupling (Figure 1.8).[50] Building on Kasha's molecular exciton theory, Spano and co-workers introduced the concept of charge-transfer (CT)-mediated coupling (J_{CT}), which extends the classical model to account for short-range interactions in π–π stacked molecular architectures (d ≤ 6 Å).[51] In such systems, both long-range Coulombic and short-range charge-transfer interactions shape the optical response. The CT-mediated coupling can be approximated as:

$$J_{CT} = \frac{-2t_e t_h}{E_{CT} - E_{S_1}} \qquad \text{(Equation 1.2)}$$

where t_e and t_h represent the electron and hole transfer integrals, and E_{CT} and E_{S_1} correspond to the energies of the charge-transfer state of the dimer and lowest singlet excited state of the monomer, respectively.

The magnitude of CT coupling is highly sensitive to the molecular geometry, particularly the slip angle (θ) and rotational displacement (α) between adjacent chromophores, as these parameters determine the relative phase alignment and spatial overlap of the interacting molecular orbitals. Predicting the strength of CT interactions remains challenging due to the variable distribution of frontier molecular orbitals (FMOs), which depend on the molecular symmetry and geometry of the system.[52-54] Electron and hole couplings arise from the spatial overlap between the LUMOs and HOMOs of neighbouring chromophores, respectively. The overall excitonic coupling in a molecular aggregate is the sum of long-range Coulombic (J_{Coul}) and short-range charge-transfer (J_{CT}) contributions, expressed as:

$$J_{Total} = J_{Coul} + J_{CT} \qquad \text{(Equation 1.3)}$$

In closely packed chromophoric assemblies (d ≤ 6 Å), the interplay between Coulombic and charge-transfer couplings determines the extent and character of exciton delocalization, exerting a defining influence on the observed photophysical behaviour of the system.

1.6. Photophysical Properties of Eumelanin

Two of eumelanin's key functions are coloration and photoprotection. As such, optical properties of the melanin pigment are essential to its function. It is therefore somewhat ironic that in general, eumelanin has defied optical characterization. This has led to the unfortunate state of affairs that we do not have a clear understanding of how UV and visible radiation interacts with the macromolecule to generate properties such as the monotonic broadband absorbance. Once again, explaining these most fundamental of issues requires a detailed and appropriate structural model at the molecular and aggregate level. Only then can one hope to construct a consistent mesoscopic understanding.

1.6.1. Broadband Electronic Absorption

Eumelanin exhibits a broad, featureless absorption extending from the ultraviolet to the near-infrared, in both solution and the condensed phase. This behaviour stands in stark contrast to typical organic chromophores, which display well-defined electronic and vibronic transitions. Instead, the spectral profile of eumelanin resembles that of amorphous inorganic semiconductors, prompting models that describe it as an organic material with a continuum of electronic states rather than discrete molecular bands.[55] The monotonic absorption emerges during the oxidative polymerization of precursors such as DHI and DHICA, and further spectral changes appear during degradation or when low–molecular weight fractions are isolated.[55] These observations reflect the intrinsic chemical diversity of the pigment. Although early hypotheses suggested that the smooth spectrum might arise predominantly from scattering (Rayleigh scattering from nanoscale domains or Mie scattering from larger aggregates), quantitative measurements have shown that scattering contributes only modestly in well-solubilized samples. The dominant contribution to eumelanin's optical profile therefore originates from electronic transitions intrinsic to the material.[16, 56-58]

Efforts to define a fundamental bandgap have yielded values between 1.2 and 3.4 eV depending on methodology, while photopyroelectric spectroscopy has revealed a discontinuity near 1.7 eV.[14] This value aligns with the computed HOMO–LUMO gap of indolequinone, a major oxidation product of eumelanin precursors, suggesting that overlapping transitions from multiple chemically distinct species shape the overall absorption.[55] Two principal models have been advanced to explain this broadband behaviour. The first model, "chemical disorder" model, proposes that eumelanin's heterogeneous mixture of redox states, coupling motifs, and oligomeric structures produces a dense manifold of overlapping electronic transitions that merge into the observed monotonic spectrum.[59] The second model which is the (geometric disorder) focuses on supramolecular architecture: planar protomolecular units stack at 3–4 Å separations, generating regions of geometric order that enable strong excitonic coupling, while rotational disorder and lateral slips between layers broaden the exciton band and redistribute oscillator strength. Both models will be discussed in detail in the following sub-sections.

1.6.1.1. Chemical Disorder Model

The chemical disorder model primarily acknowledges that eumelanin comprises a heterogeneous collection of structurally distinct species rather than a singular chemical entity.[59] Under controlled synthetic conditions, the pigment is observed as a mixture of monomers, dimers, and higher oligomers, each exhibiting various redox states. Typical molecular units comprise DHI, DHICA, and their oxidized derivatives, including indolequinone and quinone-imine.[60, 61] The polymerization and reactivity of these building blocks result in a diverse array of molecular architectures, each characterized by distinct electronic structures. An important consequence of this heterogeneity is that each species possesses a different HOMO–LUMO energy gap. As a result, the overall absorption spectrum of eumelanin can be understood as the superposition of many individual electronic transitions. Instead of sharp, well-resolved bands, the overlapping contributions from a large number of chemically distinct chromophores merge into the smooth, exponentially increasing absorption profile that characterizes all melanins.

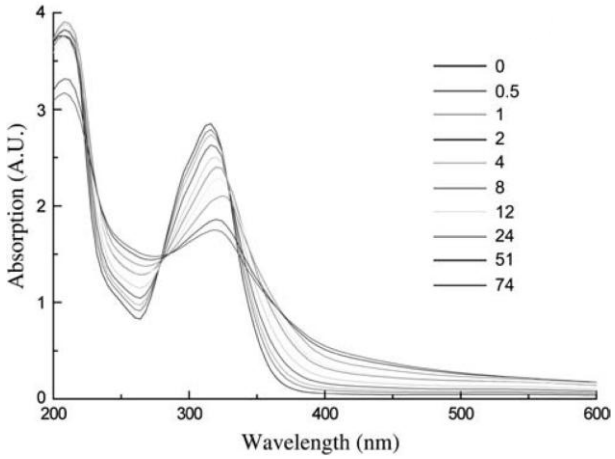

Figure 1.9: UV-visible absorption spectra DHICA in NaOH solution at various times (legend represents hours) (Adapted from ref. 59; Copyright © 2006 Elsevier).

Computational investigations support this framework. Density functional theory has shown that even simple DHICA oligomers exhibit significant red-shifts in their electronic gaps relative to the monomer. Moreover, small structural variations, such as different bonding modes in dimers, introduce measurable changes in the HOMO–LUMO gap, often differing by several tenths of an electron volt.[62] These findings imply that even a limited set of oligomers is

sufficient to begin reproducing the broad spectral envelope observed experimentally. Experimental observations mirror these predictions.[59] During oxidative polymerization of DHICA, the initially well-defined absorption features progressively red-shift and broaden, eventually transforming into the characteristic monotonic spectrum of eumelanin (Figure 1.9). This spectral evolution reflects the formation of increasingly diverse reaction products with lower-energy transitions. By framing eumelanin's optical properties as an emergent consequence of chemical heterogeneity, the chemical disorder model challenges the long-standing view that melanins require an amorphous semiconductor-like band structure to explain their behaviour. Instead, it suggests that eumelanin's functional robustness arises precisely from its complexity.

1.6.1.2. Geometric Disorder Model

The broadband absorption of eumelanin can be further understood by considering its supramolecular architecture alongside its chemical heterogeneity. The geometric disorder model is centred on the observation that eumelanin aggregates comprise planar oligomeric units arranged in close proximity (Figure 1.10).[63] This geometric arrangement is characterized by interlayer separations of approximately 3–4 Å, aligning with findings from diffraction studies.[35, 64-66] This dense arrangement facilitates substantial excitonic coupling among adjacent chromophores, permitting the delocalization of electronic excitations across several units. Calculations utilizing the Frenkel exciton framework indicate that these couplings significantly affect the spectral response of aggregated eumelanin.[63] In contrast to crystalline organic materials, eumelanin lacks a regular, periodic arrangement. Molecular dynamics simulations and experimental observations consistently demonstrate significant geometric disorder within the stacks.[63, 67] Adjacent protomolecules demonstrate no favoured rotational alignment, allowing for unrestricted lateral slipping along molecular planes. This disorder interrupts coherent excitonic structures and expands the distribution of exciton energies. Consequently, oscillator strength, which denotes the intensity linked to specific transitions, is distributed across a broad energy spectrum instead of being confined to distinct spectral features.

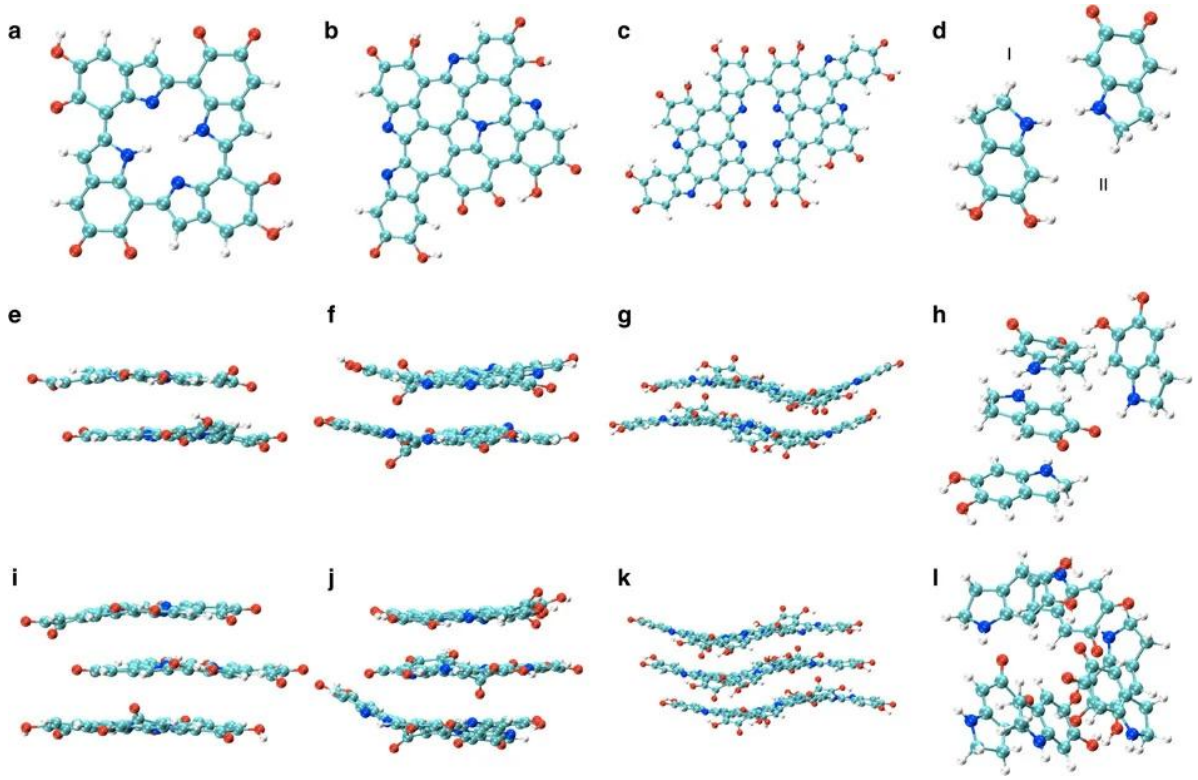

Figure 1.10: Geometric order-disorder in various proposed eumelanin sub-structures. (a) Tetrameric model (b) Pentameric model and (c) octameric models (d) Monomeric model. Two-layer stacked structure of the (e) tetrameric model, (f) pentameric model and (g) octameric model, respectively. (h) Two-set stacked structure of the monomeric model. Three-layer stacked structure of the (i) tetrameric model, (j) pentameric model and (k) octameric model, respectively. (l) Three-set stacked structure of the monomeric model (Adapted from ref. 63; Copyright © 2014 Springer Nature).

The interplay of tight stacking (order) and random orientation (disorder) results in two key optical properties of eumelanin. Excitonic interactions broaden absorption throughout the UV–visible spectrum, whereas geometric disorder blurs distinct peaks, resulting in the smooth, featureless envelope characteristic of the pigment. The model effectively accounts for the monotonically increasing absorption at higher energies, a characteristic that chemical disorder models find challenging to replicate.[63] The spectra from disordered excitonic systems exhibit compressed transitions at elevated energies, resulting in increased intensity at shorter wavelengths. Chemical disorder contributes to the variety of electronic transitions from

different molecular species, while geometric disorder elucidates how chemically identical oligomers can collectively produce a broadband absorption spectrum in disordered stacks. These models demonstrate that the optical properties of eumelanin arise not from molecular precision, but from a strategic combination of heterogeneity, packing, and supramolecular disorder, which are characteristics that nature seems to have optimized for the development of a resilient and effective photoprotective pigment.

1.6.2. Ultrafast Energy Dissipation

Eumelanin dissipates absorbed photons through several ultrafast and interconnected pathways that collectively govern its excited-state behaviour and photoprotective function (Figure 1.11). These include proton-transfer reactions[68-73], internal conversion driven by excitonic relaxation[74-76], charge and energy transfer between chromophoric units[30, 77], photoionization and radical formation[78-81], intersystem crossing to triplet states[82, 83], and vibrational energy transfer to the surrounding medium.[30] The balance among these pathways depends on molecular composition, aggregation, and local environment, ultimately determining whether eumelanin acts predominantly as an efficient energy sink or, under certain conditions, a source of photochemical reactivity.

Excited-state proton transfer (ESPT) is one of the most rapid and effective nonradiative decay routes in eumelanin precursors containing ortho-hydroxy groups. Following photoexcitation, intramolecular proton migration coupled with electronic rearrangement redirects energy out of the excited state on femtosecond timescales.[68] In DHICA, this mechanism dominates singlet-state relaxation and is highly sensitive to solvent and pH[71], whereas DHI undergoes alternative hydrogen-transfer pathways that lead to characteristic picosecond decay kinetics.[82] Even in oligomeric and aggregated forms, proton-transfer–mediated relaxation remains efficient, contributing to eumelanin's exceptionally low fluorescence yields.[68, 84] Eumelanin can also generate transient radicals through direct photoionization or via ultrafast charge separation processes that often involve proton-coupled electron transfer.[78-81] Both UV and UVA excitation can produce solvated electrons and radical cations almost instantaneously, while ground-state radicals increase under irradiation. Although these species form readily, they typically recombine on ultrafast timescales, converting

electronic excitation into heat and limiting photochemical damage under physiological conditions. Persistent radicals and longer-lived intermediates, however, can emerge under high-energy excitation and may contribute to phototoxic outcomes.

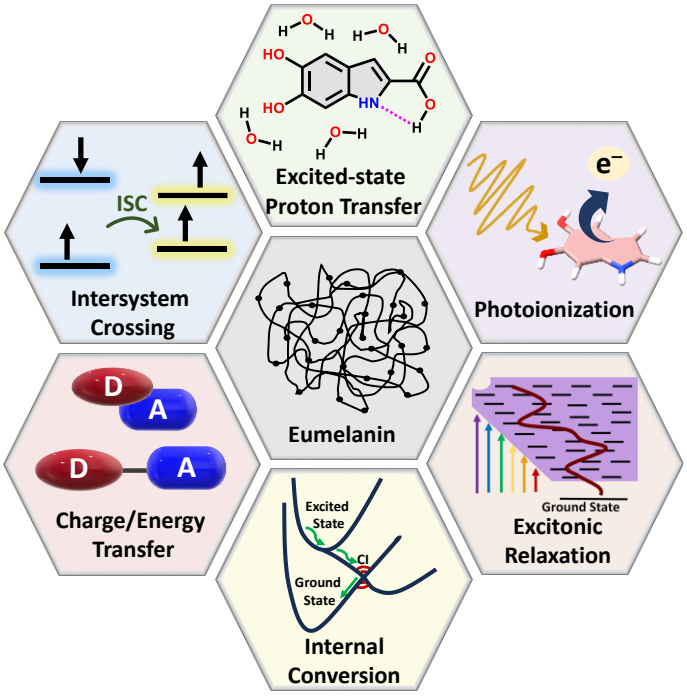

Figure 1.11. Possible photo-deactivation pathways in natural eumelanin.

Excitonic interactions within eumelanin aggregates provide a further rapid relaxation channel. Strong coupling between chromophores funnels high-energy UV excitations into lower-energy states within a few hundred femtoseconds, after which internal conversion returns the system to the ground state on picosecond timescales.[74-76] Despite strong interchromophore interactions, excitons tend to localize within a few nanometres due to energetic disorder, limiting long-range migration and promoting efficient local relaxation. This behaviour is a defining hallmark of eumelanin-like materials and contributes to their characteristic broadband photostability. Charge-transfer dynamics also play a central role.[74] Ultrafast formation of CT states occurs within tens of femtoseconds, with recombination usually completing within a few picoseconds under visible excitation. UV excitation, however, can produce longer-lived CT species, reflecting the higher photochemical reactivity at short wavelengths.[77] Spectroscopic signatures of polarons and polaron pairs further connect eumelanin's behaviour with that of

disordered organic semiconductors, where geminate recombination and localized relaxation dominate the excited-state landscape.[30] Triplet formation through intersystem crossing (ISC) generally represents a minor pathway in eumelanin due to rapid singlet-state relaxation, but it does occur under certain structural and excitation conditions. DHI can populate triplet states on picosecond timescales, while DHICA largely suppresses ISC through efficient ESPT.[82, 85] In engineered eumelanin analogues, triplet yields can increase with multimer length, making ISC relevant to both energy dissipation and potential phototoxicity.[86, 87]

1.7. Open Questions in Eumelanin Chemistry: Challenges and Prospects

Although eumelanin has been studied for more than a century, several fundamental questions about its structure and photophysics remain open. Its importance in biology is well established, yet the pigment resists many of the standard tools used to characterize biomolecular architecture. Two challenges continue to shape the field: defining eumelanin's structure across different length scales and fully understanding the pathways through which it dissipates absorbed energy. The structural problem is longstanding. Eumelanin is not a single molecule but an ensemble of chemically diverse species derived from DHI, DHICA, and their oxidized forms.[88] These units polymerize spontaneously, giving rise to mixtures of oligomers and aggregates that evolve over time. Their insolubility and tendency to undergo further oxidation complicate any attempt at isolation or crystallization. Techniques such as solid-state NMR, 3D electron diffraction, and DFT calculations have helped clarify local bonding patterns and some aspects of π–π stacking, but we still lack a complete description of how monomers link, how oligomers assemble, and how these assemblies relate to the functional nanostructures observed in biological eumelanin.[89] A unified structural model that connects molecular composition with mesoscale organization remains an open goal.

The second challenge concerns eumelanin's excited-state dynamics. The pigment dissipates energy extremely efficiently, but the specific relaxation channels such as proton transfer[68, 69, 71], internal conversion[90, 91], charge or energy transfer[75, 77], radical formation[78, 79], and intersystem crossing[82], operate on overlapping timescales and are sensitive to subtle

structural variations. As a result, it is difficult to assign distinct photophysical behaviour to any single molecular species within the heterogeneous ensemble. Ultrafast transient absorption, 2D spectroscopy, and pulsed EPR have provided important insights, yet correlating these measurements with defined structural motifs remains difficult. Establishing such correlations is essential for understanding when eumelanin behaves purely as a photoprotective material and when it may generate photochemically active species.

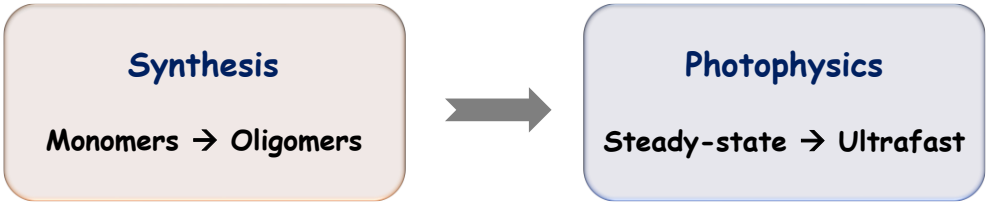

Figure 1.12: Overview of the thesis framework linking molecular synthesis, from monomers to defined oligomers to photophysical characterization spanning steady-state and ultrafast timescales.

A coherent way forward in addressing the open questions surrounding eumelanin is to adopt a top-to-bottom framework that systematically links structure to function (Figure 1.12). This begins with well-defined monomers and extends through dimers, higher-order oligomers, and finally the supramolecular aggregates that constitute the functional pigment. At each stage, structural characterization must be paired with both steady-state and time-resolved spectroscopic measurements to follow how electronic interactions evolve with increasing molecular complexity. Such an approach allows individual contributions such as, chemical composition, coupling motifs, aggregate geometry, and energetic disorder, to be disentangled in a controlled manner. By progressively building complexity rather than starting from the fully heterogeneous natural material, this strategy offers the best opportunity to resolve how eumelanin's molecular architecture governs its ultrafast excited-state behaviour. Ultimately, a top-to-bottom model provides a realistic path toward understanding the pigment as a whole while simultaneously enabling the rational design of eumelanin-inspired materials with predictable photophysical properties.

1.8. Aim and Objectives of the Thesis

The aim of this thesis is to clarify how molecular structure, aggregation, and excitonic interactions shape the photophysical behaviour of eumelanin and related organic systems. Although eumelanin plays a central role in biological photoprotection, its properties remain poorly understood due to its chemical heterogeneity and complex supramolecular organization. This work combines structural analysis, spectroscopy, and computation to connect molecular architecture with optical function.

The specific objectives are:

1. To define the structural characteristics of key eumelanin building blocks: This includes elucidating the molecular and packing structures of DHI, DHICA, and protected indole derivatives, which form the basis of higher-order assemblies.
2. To examine how oligomerisation and aggregation influence excited-state dynamics: Model multimers (monomer, dimer, trimer) are used to determine how increasing molecular size and proximity affect absorption profiles, excitonic coupling, and ultrafast energy dissipation.
3. To identify the major pathways of excited-state relaxation: The work investigates how internal conversion, proton transfer, charge transfer, and intersystem crossing operate across different structural regimes and contribute to efficient energy dissipation.
4. To extend these insights to designed eumelanin-inspired emitters: By studying HD and BrD, the thesis explores how controlled aggregation (J- versus H-type) modulates singlet–triplet energetics and the balance between delayed fluorescence and room-temperature phosphorescence.
5. To establish a framework for designing functional organic materials inspired by eumelanin: The goal is to translate structure–property relationships into strategies for creating materials with tunable photophysical properties.

These objectives support a top-to-bottom understanding of eumelanin, linking its molecular origin to its emergent photoprotective behaviour and technological potential.

Chapter 2

Structural Elucidation and Exciton Coupling in a Key Eumelanin Precursor

Abstract

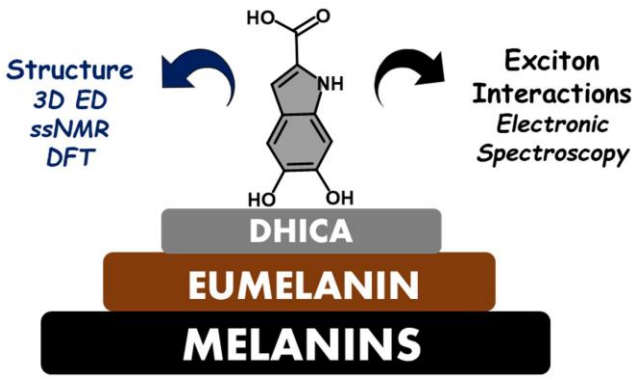

Eumelanin, a versatile biomaterial found throughout the animal kingdom, performs essential functions like photoprotection and radical scavenging. The diverse properties of eumelanin are attributed to its elusive and heterogenous structure with DHI (5,6-dihydroxyindole) and DHICA (5,6-dihydroxyindole-2-carboxylic acid) precursors as the main constituents. Despite DHICA being recognized as the key eumelanin precursor, its crystal structure and functional role in the assembled state remain unknown. Herein, we employ a synthesis-driven, bottom-up approach to elucidate the structure and assembly-specifics of DHICA, a critical building block of eumelanin. We introduce an interdisciplinary methodology to analyse the nanocrystalline assembly of DHICA, employing three-dimensional electron diffraction (3D ED), solid-state NMR and density functional theory (DFT), while correlating the structural aspects with the electronic spectroscopic features. The results underscore charge-transfer exciton delocalization as the predominant energy transfer mechanism within the π–π stacked and hydrogen-bonded crystal network of DHICA. Additionally, extending the investigation to the ^{13}C-labelled DHICA-based polymer improves our understanding of the chemical heterogeneity across the eumelanin pigment, providing crucial insights into the structure of eumelanin.

2.1. Introduction

Eumelanin, a natural biomaterial, is instrumental in protecting the skin from harmful radiation and environmental toxins.[92, 93] Eumelanin is recognized for its broadband UV-visible absorption and efficiency in dissipating excitation energy, thereby preventing cellular damage.[15] The structure of eumelanin is highly heterogeneous and ambiguous.[10] It is believed to consist of a three-dimensional network of interconnected aromatic units, derived from the oxidative polymerization of 5,6-dihydroxyindole-2-carboxylic acid (DHICA) and 5,6-dihydroxyindole (DHI). Chemical and spectral evidence from eumelanin identified so far points to different levels of chemical, structural and supramolecular disorder within eumelanin.[9, 94, 95] Characterizing eumelanin proves challenging due to its disordered, amorphous nature and insolubility in most common solvents, rendering conventional characterization techniques impractical (Table A2.1).[6] The challenges associated with the structure elucidation of eumelanin have evaded the exact mechanism of energy dissipation and photoprotection in the biomaterial. Considering the complexities associated with understanding eumelanin chemistry, a bottom-up approach by elucidating the structure and supramolecular assembly of the monomeric units is crucial (Scheme 2.1).[30, 69-71, 73, 84]

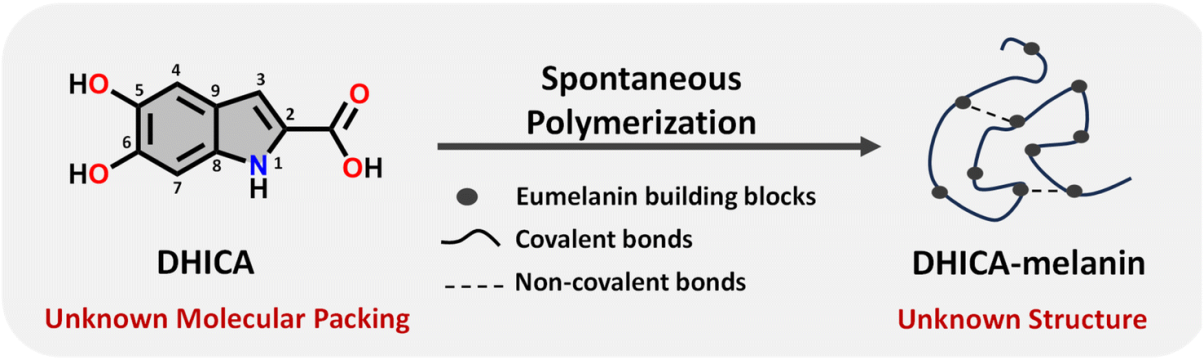

Scheme 2.1: Schematic diagram representing the spontaneous polymerization of DHICA, the monomeric unit of eumelanin into the black polymeric DHICA-melanin.

Detailed knowledge of the interchromophoric interactions between monomers and their higher-order assemblies can reveal how non-covalent interactions influence the macroscopic properties, providing critical insights into the foundational elements of the bio-pigment.[96] Structure elucidation is also a key factor for determining the electronic coupling within the

interacting units, allowing further insights into the exciton dynamics of the eumelanin constituents.[12] Understanding the inter/intramolecular non-covalent interactions in eumelanin monomers could also reveal hints about the oxidative polymerization mechanism, especially given their susceptibility to excited state reactions.[69, 73] Among the two eumelanin precursors, previous experimental and theoretical research has focused mostly on DHI while DHICA remains less explored.[67, 70, 82, 83, 97-101] Using single-crystal XRD (SC-XRD), the assembly pattern of DHI was previously established where DHI forms hydrogen-bonded enantiomeric helical stacks with Frenkel exciton delocalisation within the helix.[98] However, the requirement of suitably large and well-diffracting single crystals is a substantial drawback of structure elucidation with SC-XRD. Unlike DHI, obtaining larger diffracting crystals for DHICA is difficult owing to the superior polymerization tendency of the eumelanin precursor due to which DHICA can only be crystallized as crystals of nanometre size with limited diffraction ability.[102] Furthermore, conventional crystallographic techniques encounter challenges in the case of DHICA due to the inherent disorder, warranting the employment of 3D ED and solid-state NMR.

In our prior research, we employed 3D ED and NMR crystallography[103, 104] to elucidate the structure of a disordered microcrystalline nitroperylenediimide system.[105] Our continued interest in inspecting the structure–property relationship in eumelanin counterparts motivated us to implement 3D ED[105, 106], magnetic resonance and electronic spectroscopy along with DFT calculations to understand the intricate structure and photophysical properties of DHICA.[86, 98, 107] By utilizing the extensive capabilities of solid-state NMR[108, 109], we further extend our investigations to the synthesised ^{13}C-labelled polymer of DHICA, *i.e.*, DHICA-melanin. The applied multi-level approach attempts to unravel the complexities inherent in a disordered material such as eumelanin, opening avenues for advancements in eumelanin chemistry.

2.2. Results and Discussion

2.2.1. Synthesis and Optical Properties

DHICA was synthesized non-enzymatically using l-3,4-dihydroxyphenylalanine (L-DOPA) as the starting material, following previous literature with minor modifications to improve the

yield (yield = 76%; Scheme A2.1 and Figures A2.1–A2.5).[110] ^{13}C-labelled DHICA was synthesized with selectively ^{13}C-labelled L-DOPA (yield = 71%; Scheme A2.2). The off-white powder of DHICA upon solubilizing in milliQ water, resulted in a brown-black solution over time. The black powder was collected and centrifuged to obtain DHICA-melanin (Scheme A2.3 and Figure A2.5). The UV-visible absorption spectrum of DHICA in the solution state ranges in the near UV region peaking at λ_{S1}^{abs} = 315 nm and λ_{S2}^{abs} = 200 nm pertaining to the $S_0 \rightarrow S_1$ and $S_0 \rightarrow S_2$ electronic absorption bands respectively (Figure A2.6a).[68] The solid-state Kubelka–Munk diffuse reflectance transformed absorption spectra of DHICA and DHICA-melanin are presented in Figure 2.1.

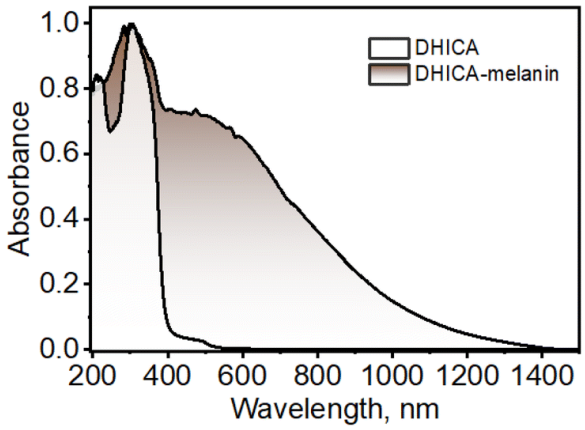

Figure 2.1: UV-visible-NIR diffuse-reflectance transformed absorption spectra of DHICA and DHICA-melanin in the solid state.

The absorption spectrum of DHICA in the solid state is broader with respect to that of the monomer and ranges from λ_{solid}^{abs1} = 200–400 nm, while revealing an additional shoulder band at λ_{solid}^{abs2} = 400–550 nm which was absent in the monomeric solution. In extended systems such as molecular crystals, aggregates or polymers, exciton interactions may occur between molecular sites depending on the strength of the electronic coupling, causing differences in the photophysics of the aggregate with respect to the isolated molecule.[111] The substantial differences in the solid-state UV-visible spectra of DHICA compared to the monomeric state are suggestive of the intermolecular interactions between the DHICA units in a tightly packed molecular environment. The electronic coupling between the DHICA molecules is intrinsic to

the spatial orientation of the chromophores, and to examine the nature of exciton interactions in DHICA, the aggregate architecture has to be considered.

The concentration-dependent UV-visible absorption of DHICA in milliQ water shows visible differences at high (aggregate) concentrations of DHICA compared to low (monomer) concentrations. The emergence of a broad UV-visible absorption band from 400–600 nm is observed with the increase in concentration from 0.01–1.0 mM (Figure A2.6b). The broad red-shifted absorption band for higher concentrated solutions of DHICA resembles the shoulder band in the absorption spectrum in the solid state, pointing to aggregate formation in the high concentrated solutions. The effect of aggregation is also evident in the fluorescence emission where the emission red-shifts from λ_{max}^{emi} = 385 nm in the monomer to λ_{max}^{emi} = 397 nm in the aggregate ($\Delta\lambda$ = 12 nm; Figures A2.6c and A2.6d). Temperature-dependent fluorescence measurements show a breakdown of the aggregates at higher temperatures as demonstrated by the blue-shift in the fluorescence emission as temperature increases from 10–90 °C (Figure A2.7). The formation of larger-sized aggregates was also evident from TEM and DLS measurements in higher concentrations of DHICA (Figures A2.8 and A2.9).

The electronic absorption spectrum of the synthesized polymer of DHICA (DHICA-melanin) exhibits differences from previously established synthetic melanins.[68, 112] The UV-visible-NIR absorption band of DHICA-melanin shows a peak maximum at λ_{max}^{abs} = 310 nm and a broad absorption band covering the entire visible region and tailing towards the NIR region (Figure 2.1). The monotonic increase in absorption towards higher energy in DHICA-melanin is reminiscent of the excitonic model proposed for the broadband absorption of natural eumelanin.[63] The synthesized DHICA-melanin is distinguished by the absorption in the 1000–1400 nm range while the previously reported DHICA-melanins have an absorption maximum at 320 nm, tailing towards 700 nm. The differences in the absorption spectra between the synthesized DHICA-melanins could be due to the formation of higher-order oligomers that co-exist with the monomer-like units. There could also be extensive π-delocalization within the DHICA substructures, leading to stabilization of energy levels in the synthesized DHICA-melanin, compared to other synthesized eumelanins.[25, 59, 113] Similar to the non-emissive nature

of naturally derived eumelanin, DHICA-melanin did not display an attributable fluorescence emission (Figure A2.10).

2.2.2. Structure Elucidation using 3D ED and Solid-State NMR

To comprehend the distinct solid-state UV-visible absorption of DHICA, realization of the molecular structure and packing of DHICA is essential. As the polymerization tendency of 5,6-DHICA prohibits traditional crystallization methods based on slowly oversaturating a solution, crystal structure determination needed to be performed with a powder sample. This precluded SC-XRD, but the nanocrystalline powder was still suitable for 3D ED (Figures 2.2 and A2.11, Table A2.2). Data were recorded on an ELDICO ED-1 electron diffractometer and analysed as further detailed in the supporting data. DHICA crystallizes in the triclinic space group $P\bar{1}$ (a = 7.49 Å, b = 10.23 Å, c = 10.81 Å, α = 82.27°, β = 87.80°, and γ = 70.10°) with two molecules in the asymmetric unit (Table 2.1). Each of the independent molecules are interconnected as in chains through extensive hydrogen bonding. Depending on the arrangement of the molecules, two types of H-bonded chains, head-to-tail and head-to-head, are identified (Figure A2.12). For DHICA, based on the electron diffraction data alone, the position of the nitrogen atom is ambiguous due to the low sensitivity of the scattering factors for neighbouring elements.

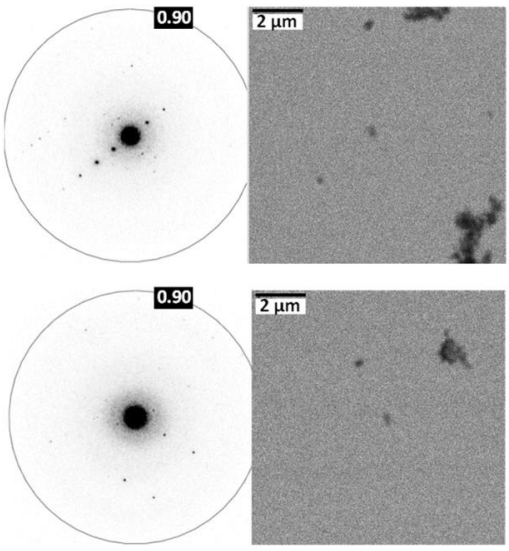

Figure 2.2: Selected TEM images and electron diffraction patterns obtained for DHICA.

Table 2.1: The crystallographic details of 3D ED kinematic refinement against merged data from three crystals.

Parameters	**DHICA**
a, *b*, *c* (Å)	7.49(7), 10.23(9), 10.81(10)
α, *β*, *γ* (°)	82.27(3), 87.79(13), 70.09(13)
Space group	$P\bar{1}$
Formula	$C_9H_7NO_4$
Independent reflections	2729
Parameters	264
Restraints (non-H)	0
Constraints (non-H)	0
Resolution (Å)	0.83
Completeness (%)	96.9
R_{int} (%)	14.88
R_1 [$I > 2\sigma(I)$] (%)	13.65
wR_2 [all data] (%)	36.04
Goodness of fit	1.09

To address this challenge in the 3D ED measurements, we employed solid-state NMR in conjunction with DFT calculations. Three sets of information are obtained from the solid-state NMR: (i) chemical shift information related to the electron distribution around the nuclei, which is sensitive to molecular packing, (ii) orientation related to the spin–spin coupling interactions and (iii) quadrupolar interaction, which is related to the coordination environment around the quadrupolar nuclei ^{14}N. ^{1}H NMR, ^{13}C Cross Polarization (^{13}C CP), 2D CP Heteronuclear Correlation (2D $^{13}C\{^{1}H\}$ CP HETCOR), ^{1}H–^{1}H Double Quantum-Single Quantum (DQ-SQ), 2D CP Incredible Natural Abundance Double Quantum Transfer Experiment (INADEQUATE), $^{1}H\{^{14}N\}$ Dipolar Heteronuclear Multiple-Quantum Coherence ($^{1}H\{^{14}N\}$ DHMQC) and $^{1}H\{^{14}N\}$ Resonance-Echo Saturation-Pulse Double-Resonance (RESPDOR) along with CASTEP calculations were performed to comprehend the spatial arrangement of molecules with respect to each other.

The 2D $^{13}C\{^{1}H\}$ CP HETCOR spectra provide information about the proton–carbon correlations, relying on the through-space dipolar couplings. To identify the ^{1}H–^{1}H spin pairs in close proximity to each other in DHICA, two dimensional ^{1}H–^{1}H DQ-SQ correlation magic

angle spinning (DQ-SQ MAS) NMR experiments were performed (Figure 2.3). The 2D CP INADEQUATE spectra rely on J-coupling between adjacent carbon atoms, enabling the mapping of through-bond correlations. The presence of the –NH proton in DHICA enables the utilization of ^{14}N solid-state NMR, offering insights into the coordination environment of the nitrogen species of the molecule.[114] The ^{1}H{^{14}N} DHMQC[115] and ^{1}H{^{14}N RESPDOR[116] experiments provide information about the nitrogen environment using proton detection. The assignment of ^{1}H and ^{13}C chemical shifts were done using 2D ^{13}C{^{1}H} CP HETCOR and 2D CP INADEQUATE spectra obtained on labelled and unlabelled samples of DHICA. Additionally, the assignment of solid-state NMR chemical shifts was facilitated by solution state NMR and simulation of chemical shifts using the software package CASTEP.[117]

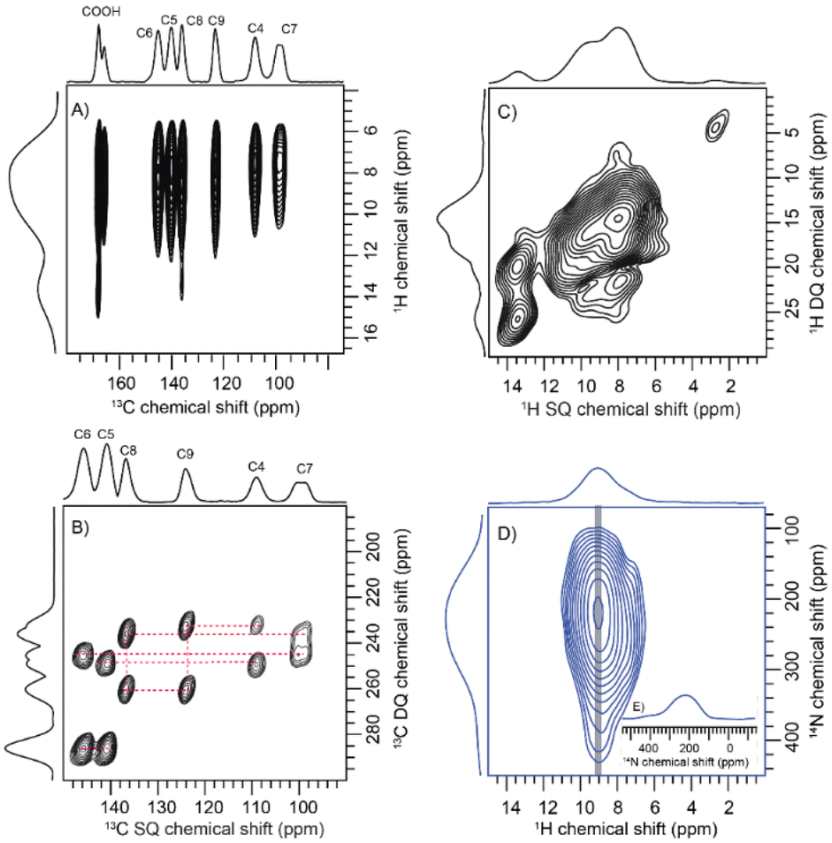

Figure 2.3: (a) The 2D ^{13}C{^{1}H} cross-polarization heteronuclear correlation (CP HETCOR) NMR spectrum of ^{13}C labelled DHICA obtained at a spinning rate of 60 kHz and a magnetic field of B_o = 14.1 T, utilizing natural isotopic abundance with a contact time of 5 ms; (b) the 2D CP INADEQUATE spectrum of ^{13}C labelled DHICA obtained at 60 kHz spinning speed;

(c) the ^{1}H–^{1}H DQ-SQ spectrum of the sample collected at 60 kHz with a recoupling time corresponding to two rotor cycles; (d) the $^{1}H\{^{14}N\}$ DHMQC spectrum of the DHICA monomer acquired at a spinning speed of 50 kHz; (E) the one-dimensional slice extracted from the ^{14}N dimension of the $^{1}H\{^{14}N\}$ DHMQC spectrum.

The solid-state NMR measurements were performed on two sets of DHICA samples; (i) the unlabelled DHICA and (ii) selectively ^{13}C-labelled DHICA (C2 and C3 carbons are unlabelled). To gather information about the various carbons in DHICA, solid-state ^{13}C NMR is performed (Figure A2.13, Tables A2.3–A2.10). The $^{13}C\{^{1}H\}$ CP HETCOR spectrum (Figure 2.3A) of the ^{13}C labelled DHICA monomer at short contact time has mainly two peaks corresponding to C7 and C4 carbons, which appear at 99.25 ppm and 107.70 ppm respectively. Among the aromatic carbons, C3 is challenging to observe in the $^{13}C\{^{1}H\}$ CP HETCOR spectrum of the ^{13}C labelled sample (Figure A2.14). Three types of aromatic C–H cross peaks are observed in the 2D $^{1}H\{^{13}C\}$ CP HETCOR correlation spectrum at a short contact time of 0.5 ms on the unlabelled sample. The C–H groups of C3, C4 and C7 appear at 115.39 ppm, 107.70 ppm and 99.25 ppm respectively. In the CP INADEQUATE spectrum, a correlation of C4 carbon with 139.68 ppm and 122.79 ppm is observed. For C7 carbon, a correlation with 144.50 ppm and 135.61 ppm is observed in the CP INADEQUATE spectrum (Figure 2.3B). Five sets of new correlation peaks are observed in the $^{1}H\{^{13}C\}$ CP HETCOR spectrum collected at a long contact time of 5 ms for the unlabelled DHICA sample.

The observed ^{13}C chemical shifts at 122.79 ppm, 135.61 ppm, 139.65 ppm and 144.51 ppm in the long contact times correspond to carbon atoms without directly attached protons. The peak corresponding to 135.61 ppm shows a correlation with C7 carbon and a peak at 122.79 ppm. Similarly, 122.79 ppm shows correlation with C4 carbon and a peak at 135.61 ppm. In the 2D CP INADEQUATE spectrum (Figure 2.3B), the peak at 139.65 ppm shows a correlation with both C4 carbon and a peak at 144.51 ppm. Similarly, the peak at 144.51 ppm exhibits a correlation with both C7 carbon and a peak at 139.65 ppm. Thus, it can be concluded that 139.65 ppm corresponds to the C5 carbon and 144.51 ppm corresponds to the C6 carbon. The carbon on the –COOH group appears at 167.28 ppm and 165.32 ppm and correlation with any nearby carbon is not observed in the CP INADEQUATE spectrum due to the absence of nearby

labelled carbons. In the proposed packing the –COOH moiety exists in two different environments, in one asymmetric unit it exists as a dimer whereas in the other the –COOH is in proximity to the –OH group. The carboxylic acid group which is closer to the protons will give an intense peak in the CP spectrum relative to the other (Figure A2.14 and A2.15). To investigate the –NH group, the $^{1}H\{^{14}N\}$ DHMQC and $^{1}H\{^{14}N\}$ RESPDOR spectra were acquired. The quadrupolar coupling constant (Cq) of the –NH in DHICA is around 4 MHz. The $^{1}H\{^{14}N\}$ DHMQC spectrum of the precursor L-DOPA and related compounds are also shown in the ESI for reference.[118] The computed ^{14}N NMR chemical shifts of the NH protons using DFT in CASTEP, are slightly different in the two independent DHICA molecules in the crystal structure. The RESPDOR $^{1}H\{^{14}N\}$ curve of DHICA corresponds to the direct N–H bond (Figure 2.3B and 2.3C), in line with the observations made in a standard sample of histidine hydrochloride monohydrate (Figure A2.16).[119]

In addition to ^{13}C solid-state NMR, ^{1}H solid-state NMR chemical shifts are utilized to gain insights into the chemical environments surrounding proton atoms (Figure A2.17). Chemical shift data obtained from proton NMR are categorized into four main categories based on the functional groups, –OH, –NH, –CH and –COOH. The ^{1}H NMR peaks observed at 9.2, 7.3, 9.8 and 9.5 ppm are arising from the hydroxyl protons of DHICA. Additionally, the protons in the NH group are observed at 8.7 and 8.9 ppm. In the ^{1}H–^{1}H DQ-SQ spectrum (Figure 2.3C), a broad autocorrelation peak appears at around 8.7 ppm and 8.9 ppm corresponding to the NH protons. Due to peak overlap, distinguishing the various protons in the ^{1}H–^{1}H DQ-SQ spectrum is challenging. The aromatic protons appear at around 7.0 ppm in the ^{1}H spectrum and corresponding autocorrelation peaks are observed in the ^{1}H–^{1}H DQ-SQ spectrum. The $^{1}H\{^{13}C\}$ CP HETCOR spectrum at short contact time facilitates the assignment of aromatic protons (Table A2.3). The protons on carbon C3 were assigned using the $^{13}C\{^{1}H\}$ CP HETCOR spectrum of the unlabelled sample, which corresponds to 7.1 ppm. The protons on C4 and C7 correspond to 7.4 and 7.3 ppm respectively.

The ^{1}H NMR peak appearing at 14.5 ppm in the $^{13}C\{^{1}H\}$ CP HETCOR spectrum at a short contact time aligns with the DFT calculated chemical shift of the carboxylic acid proton (Figure A2.14). In $^{13}C\{^{1}H\}$ CP HETCOR at a long contact time of 5 ms (Figure 2.3A), a proton

chemical shift is observed at 13.4 ppm, correlating with a carbon chemical shift of 167.28 ppm. The root mean square deviation (RMSD) between the ^{1}H chemical shifts observed in solution-state and solid-state NMR is calculated to be 1.4 ppm. The observed longitudinal relaxation time (T_1) for carboxylic acid protons is 5 s and that of aromatic protons is 7 s (Figure A2.18). The peak appearing at around 1.0 ppm is possibly due to the trace amounts of hexane residue retained in the sample during purification.

Table 2.2: Comparison of the relative energies and ^{13}C RMSD values derived from four different possible structures obtained through 3D ED.

Label	Relative energy (kcal mol^{-1})	^{13}C RMSD (ppm)
Case A	0.00	1.58
Case B	6.02	4.92
Case C	4.39	5.40
Case D	7.74	7.18

The ^{13}C{^{1}H} CP HETCOR spectrum obtained with long contact time provide details regarding both intermolecular and intramolecular correlations, pointing towards the distance constraints (Figures 2.3A and A2.19). Though the chemical shifts are distinguishable, it is difficult to differentiate between inter and intramolecular correlations in the case of DHICA. But the chemical shift is sensitive to the packing, and it is a valuable tool to understand the spatial arrangement of the molecules. Four distinct model cases (A, B, C and D) were devised to account for the uncertainties identified in the 3D ED measurements (Figure A2.20 and Tables 2.2, A2.3–A2.10). These cases account for the possible orientations related to the flipping around of the long axis of the two independent DHICA molecules. Subsequently, DFT calculations, along with NMR chemical shift predictions using CASTEP, were performed for each model.

Among the four cases, case A demonstrated the lowest root mean square deviation (RMSD) of 1.58 ppm in the ^{13}C chemical shift (Tables A2.3–A2.11). Similar to the ^{13}C chemical shift, the ^{1}H chemical shift is also sensitive to packing and can be compared with the simulated chemical shift. The obtained ^{1}H RMSD for case A is 0.34 ppm. The calculated energies show a minimum for case A in line with the RMSD of the ^{13}C chemical shift (Table 2.2). Inspection of the structure reveals that this orientation has the closest interchain N–H···O

contacts for both the DHICA units (Figure A2.21). Case A was thus used for the final structure refinement which is presented further.

2.2.3. Insights into the Molecular Packing

DHICA crystallized in the $P\bar{1}$ space group (Table 2.1). Hydrogen bonding and π–π stacking are identified as the dominant interactions in the DHICA crystal architecture (Figure 2.4). Among hydrogen bonding, both conventional and unconventional hydrogen bonds are recognized in the crystal packing. Each of the DHICA stacks are linked by C···C contacts along the *a*-axis while inter-stacks are connected by O···H and C···H contacts. The crystalline assembly is propagated through co-linear stacks (θ = 0.00°) directed by O···H contacts as well as near-orthogonal stacks (θ = 83.91°) led by C···H contacts (Figure 2.4 and A2.22). Six dimers (D1–D6, Figure A2.23) are identified within the crystal packing where D1, D2, and D3 are π–π stacked while D4, D5, and D6 are H-bonded. Hirshfeld surface analysis[120] enumerates the H···H (29.3%), O···H (19.5%), C···C (10.1%) and C···H (7.3%) contacts which majorly contribute to the crystal packing in DHICA (Figure A2.24). The crystal assembly of DHICA exhibits extensive π–π stacking, which is not found in the packing of the other eumelanin monomer, DHI.[98] DHI exhibited extended hydrogen bonding between its hydroxyl substituents resulting in a helical assembly. A herringbone packing motif was observed in DHI whereas the π–π stacking influences DHICA to pack in the beta motif.

Efficient molecular self-assembly relies on the recognition among intermolecular functionalities, typically resulting in the creation of smaller repeating units or supramolecular synthons. The supramolecular synthons in the DHICA crystals were analysed by using Bader's quantum theory of atoms in molecules (QTAIM) analysis.[121] The (3 + 1) ring critical points were identified in each of the hydrogen bonded dimers (Figure A2.25 and A2.26). The synthons in D1–D3 dimers are facilitated by C···C–H, C···N–H, C···O–H and O···C–C contacts while in D4–D6 dimers, synthon formation is orchestrated by the hydrogen bonds between the –COOH and –OH groups. Notably, the D6 dimer demonstrated resonance assisted hydrogen bonding (RAHB) with greater energetic stability (Figure A2.27). Resonance assisted hydrogen bonds (RAHBs) are particularly strong hydrogen bonds present in uncharged molecules, where the conjugated bonds display an equalization of lengths through a pseudo-ring.[122] Along with

RAHB, bifurcated hydrogen bonding, previously discovered in DHI crystals are also observed in the D6 dimer of DHICA (Figure A2.27).

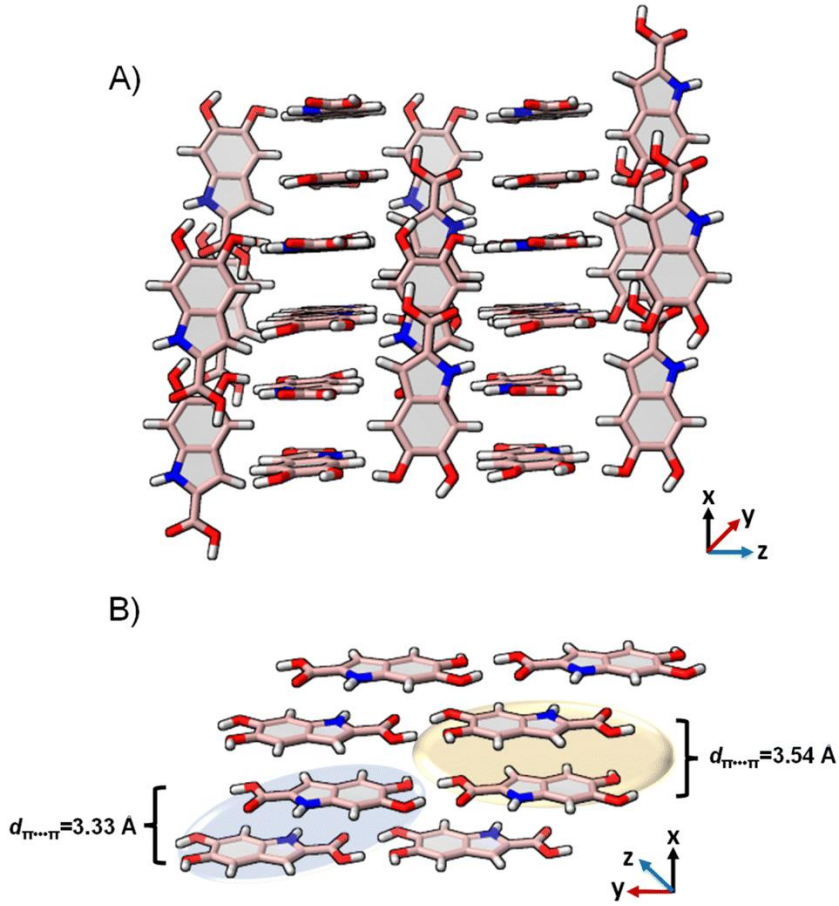

Figure 2.4: (a) The crystal packing of DHICA showing the near-perpendicular orientation of the π–π stacks; (b) π–π stacked dimers connected to the adjacent stack through hydrogen bonding.

Truncated symmetry adapted perturbation theory (SAPT(0)) analysis[123] of DHICA dimers reveals a notable increase in stabilization for the D6 dimer ($E^{\mathrm{SAPT(0)}}_{\mathrm{int}}$ = –25.75 kcal mol^{-1}, Table A2.12). This enhancement may be attributed to the presence of an eight-membered supramolecular synthon within the dimer, as outlined in Figure A2.26. The overall stabilization of the D6 orientation results from a more substantial contribution of electrostatic ($E_{\mathrm{elc}}^{\mathrm{SAPT(0)}}$ = –36.46 kcal mol^{-1}) and induction ($E_{\mathrm{ind}}^{\mathrm{SAPT(0)}}$ = –17.83 kcal mol^{-1}) energies to the total SAPT energy. The prominent role of RAHB and bifurcated hydrogen bonding in forming the D6

synthon clarifies the energy stability observed for the D6 dimer in the SAPT(0) analysis with respect to other dimer orientations. The conventionally hydrogen bonded dimers D1 and D2 are mostly stabilized by electrostatic energies while dispersion energies contribute the most to the total stabilization energies of the π–π stacked dimers (D1–D3).

2.2.4. Exciton Interactions within the Molecular Assembly

The molecular architecture of the eumelanin precursor herein presents a valuable framework for understanding the underlying mechanisms of energy dissipation responsible for the characteristic photo-functionality of eumelanin. Previous experimental and theoretical studies have implied the presence of excitation energy transfer phenomena within eumelanin.[74, 77, 124] The efficiency of energy transfer between assembled chromophores is dictated by the intrinsic electronic coupling over both short and long distances.[54] The long-range coulombic coupling stems from the relative orientation of transition dipoles of individual monomers (Equation A2.2).[51, 125, 126] At lower interchromophoric separations, additional contributions due to charge transfer coupling (J_{CT}) are also instrumental to the overall electronic coupling (Equation A2.3).[51, 125] The calculated coulombic and charge transfer coupling constants are given in Table 2.3. While coulombic coupling is prominent in all of the dimers (D1–D6), charge transfer coupling contributes the most in the case of the stacked dimers D1, D2 and D3. Among the π–π stacked dimers, the D1 dimer with an intermolecular distance of $d_{\pi-\pi}$ = 3.33 Å exhibits the highest values of electron (t_e = 0.146 eV) and hole transfer integrals (t_h = −0.164 eV), facilitating a higher quotient of CT coupling (J_{CT} = 0.157 eV). Fragment-based excited-state analysis by Plasser was employed to investigate the exciton delocalization within DHICA units in the crystalline structure using the TheoDORE package (Tables A2.13–A2.18).[127]

The degree of exciton delocalization among the fragment units is assessed through the participation ratio (PR). The level of involvement of fragments in exciton delocalization is represented by the mean position, denoted as the POS value, which signifies the extent of participation of one or more units. The classification of excited states into charge transfer or Frenkel is determined by the CT number, which tends towards one for pure charge transfer states and towards zero for pure Frenkel states. In dimers D1, D2, and D3, exhibiting significant orbital overlap, the higher excited states show high CT character (CT_{D1} = 0.86, PR_{D1} = 2.00;

CT_{D2} = 0.91, PR_{D2} = 2.00; CT_{D3} = 0.88, PR_{D3} = 1.99) suggesting the excitation energy transfer of the charge transfer excitons within the π–π stacked units in the crystalline assembly.

Table 2.3: Calculated coulombic (J_{Coul}) and charge transfer coupling (J_{CT}), along with the hole (t_h) and electron (t_e) transfer integrals for the π–π stacked (D1–D3) and the hydrogen-bonded (D4–D6) dimers of DHICA.

Dimer	t_e (eV)	t_h (eV)	J_{CT} (eV)	J_{Coul} (eV)
D1	0.146	−0.164	0.157	−0.123
D2	0.181	−0.096	0.081	−0.488
D3	0.043	0.149	−0.017	−0.009
D4	0.025	−0.022	0.000	−0.097
D5	0.024	0.010	0.000	0.066
D6	0.017	0.081	−0.002	0.115

Conversely, hydrogen-bonded dimers D3, D5, and D6 display minimal CT character in the excited states, indicating their limited contribution to CT exciton generation and subsequent delocalization within the crystalline structure. The strong exciton coupling in the π–π stacks promotes the delocalization of excitons, ultimately leading to efficient charge transfer by channelling the excitation energy within the stack. The charge-density difference plots for the excited states also depict the delocalised excitons within the D1-D3 dimers (Figure A2.28). The remarkable topology and significant charge transfer characteristics of DHICA signify the uniquely efficient energy transfer mechanism adopted by the DHICA monomer architecture compared to that of DHI, reminiscent of the diverse energy funnelling mechanisms in eumelanin/eumelanin-like materials.[30, 77, 128]

2.2.5. Probing DHICA-melanin with Solid-state NMR

Having established the molecular assembly and spectroscopic features of the key eumelanin monomer, DHICA, we analyse the structure of the polymer of DHICA, that is, DHICA-melanin. DHICA-melanin exhibits an amorphous nature, and is insoluble in most common solvents, posing challenges for conventional characterization techniques. The amorphous nature of DHICA-melanin is evident from the broad peak observed in the PXRD pattern (Figure A2.29) as well as the absence of diffraction patterns in 3D ED experiments. However, by

extending the solid-state NMR experiments previously discussed for DHICA, we can gain insights into the molecular structure of DHICA-melanin (Tables A2.19 and A2.20). The $^{13}C\{^{1}H\}$ CP HETCOR experiments along with CP INADEQUATE (Figure 2.5A) experiments were performed on ^{13}C labelled samples to fully assign the chemical shifts in DHICA-melanin (Figures A2.30–A2.33).

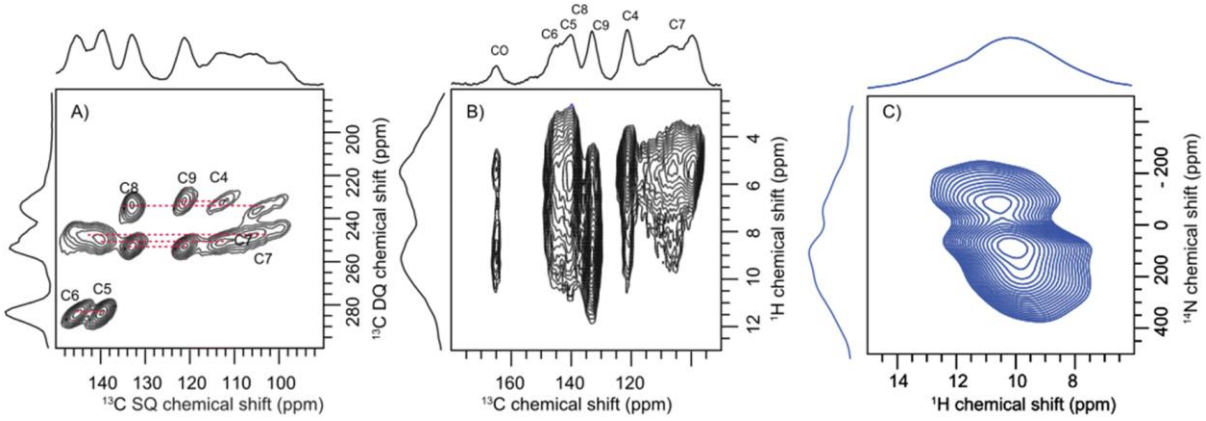

Figure 2.5 (a) The 2D CP INADEQUATE spectrum of ^{13}C selectively labelled DHICA-melanin showing the correlation between the adjacent carbon atoms. (b) The 2D $^{13}C\{^{1}H\}$ CP HETCOR NMR spectrum of DHICA-melanin at a spinning speed of 60 kHz and a magnetic field strength of B_o = 14.1 T; (c) the $^{1}H\{^{14}N\}$ DHMQC spectrum of DHICA-melanin collected at 50 kHz spinning speed.

A comparison of the solid-state ^{1}H NMR spectra of DHICA and DHICA-melanin is shown in Figure A2.17. The two-dimensional $^{13}C\{^{1}H\}$ CP HETCOR spectrum of DHICA-melanin at short contact time shows the CH carbons (Figure 2.5). As expected, the $^{13}C\{^{1}H\}$ CP HETCOR spectrum of DHICA-melanin exhibits broader features relative to the monomer, reflecting the amorphous nature of DHICA-melanin. The $^{13}C\{^{1}H\}$ CP HETCOR spectrum acquired with long contact time, assists in identifying all the individual carbon atoms within DHICA-melanin. To resolve the individual carbon peaks, CP INADEQUATE spectrum was collected for ^{13}C labelled DHICA-melanin. While most correlations observed in DHICA are also present in DHICA-melanin, there is a noticeable distribution of chemical shifts for C7 in DHICA-melanin. The localized broadening observed at around C7 may reflect variations in the packing of melanin units or the presence of multiple conformational states. A similar

broadening is seen for C4, which could also be attributed to disorder. To further elucidate the potential heterogeneities in the structure and packing of DHICA-melanin, advanced theoretical calculations are necessary.

The carboxylic acid proton which appeared at around 13.4 ppm in DHICA is not present in DHICA-melanin. The $^{13}C\{^{1}H\}$ CP HETCOR correlation peak at 160 ppm indicates that the carbonyl group is in proximity to protons on the hydroxyl group. The peak observed at 145.2 ppm in the HETCOR correlation spectrum of DHICA-melanin is in line with the observation of a peak at 145.60 ppm in DHICA, which belongs to C6 carbon. In the case of C8 and C9 carbons in the monomer, peaks appear at 135.61 ppm and 122.79 ppm, respectively, whereas in DHICA-melanin, these peaks shift to 132.92 ppm and 121.65 ppm. To understand about the nitrogen environments, $^{1}H\{^{14}N\}$ DHMQC spectrum were acquired at various recoupling times. The broad $^{1}H\{^{14}N\}$ DHMQC spectrum suggests the presence of more than one nitrogen species in the system, primarily attached to protons, as indicated by the experiments conducted with a short recoupling time of 80 μs (Figure 2.5C). The NH peaks shift from 9.0 ppm to 10.0 ppm and 10.7 ppm clearly showing the formation of new nitrogen species in DHICA-melanin. Compared to the $^{1}H\{^{14}N\}$ DHMQC spectrum of histidine hydrochloride monohydrate and L-DOPA, the broad peak is possibly a combination of different nitrogen environments (Figure A2.34).

The FT-IR spectrum of DHICA has a prominent N–H stretching band at 3435 cm^{-1}, a broad O–H and COO–H stretching band at 3265 cm^{-1} and aromatic sp^2-hybridized C–H stretching peaks.[129] In the case of DHICA-melanin, in addition to the N–H and O–H stretching bands, a sp^3-hybridized C–H stretching peak is observed at 2980 cm^{-1}. The sp^3-hybridized C–H bending, which is not found in DHICA is another prominent vibrational mode in the FT-IR spectrum of DHICA-melanin (Figure 2.5), corroborating the presence of saturated indoline products along with indole moieties.[130, 131] Additionally, the scanning electron microscope (SEM) images of DHICA-melanin exhibited a lamellar morphology with superficial attachment of globular particles on the surface (Figure A2.35). Comprehensive insights into the structure of DHICA-melanin will necessitate the application of advanced NMR and theoretical methods, which could be a potential direction for future research.

2.3. Conclusion

To conclude, the detailed structure and excitonic properties of DHICA, a critical yet underexplored constituent of eumelanin is elucidated in this work. DHICA crystallizes in an antiparallel stacking arrangement within a hydrogen-bonded network and exhibits the $P\bar{1}$ space group with unit cell parameters of a = 7.49 Å, b = 10.23 Å, c = 10.81 Å, α = 82.27°, β = 87.80°, and γ = 70.10 Å. One of the challenges in correlating the photophysics of DHICA with its structure lies in the difficulty in crystallizing DHICA, which is hindered by its inherent disorder and nanocrystalline nature. Hence, we employed an interdisciplinary approach integrating 3D ED, solid-state NMR and DFT calculations to solve the crystal structure of DHICA. The ambiguity in the orientation of the N–H group of DHICA in 3D ED experiments was addressed by generating a library of structures with solid-state NMR and DFT calculations. The broad absorption spectrum of DHICA in the solid state is due to the significant charge transfer and coulombic coupling within the crystal architecture of DHICA.

Charge transfer exciton delocalization within the π–π stacks of DHICA serves as the major energy dissipation channel within the crystalline assembly of the eumelanin precursor, as suggested by fragment based excited state analysis. A series of solid-state NMR experiments was performed to get an insight into the structure of the insoluble polymer of ^{13}C labelled DHICA, *i.e.*, DHICA-melanin. Distribution of chemical shifts at the C7 carbon and multiple nitrogen species has been recognized from the solid-state NMR spectra of ^{13}C-labelled DHICA-melanin. Advanced solid-state NMR experiments, coupled with theoretical modelling, will be required to enhance our understanding of the intricate structure of eumelanin. Extending our methodology to other members of the melanin family could be intriguing and holds promise for advancing melanin-centred biomedical research.

2.4. Experimental Section

2.4.1. Syntheses and Characterization

2.4.1.1. Synthesis and characterization of DHICA

L-DOPA (1 g, 5 mmol) in water (500 mL) was stirred under argon while a degassed solution of

$K_3[Fe(CN)_6]$ (6.6 g, 20 mmol) and $NaHCO_3$ (2.5 g, 30 mmol) in water (60 mL) was added slowly. After 2 min, 1 M NaOH (70 mL) was added, and the mixture was stirred for 15 min to promote oxidative cyclization. $Na_2S_2O_5$ (5 g, 26 mmol) was added, and the product was extracted with ethyl acetate, washed with saturated NaCl, dried over Na_2SO_4, and concentrated. Addition of hexane yielded DHICA (76%).

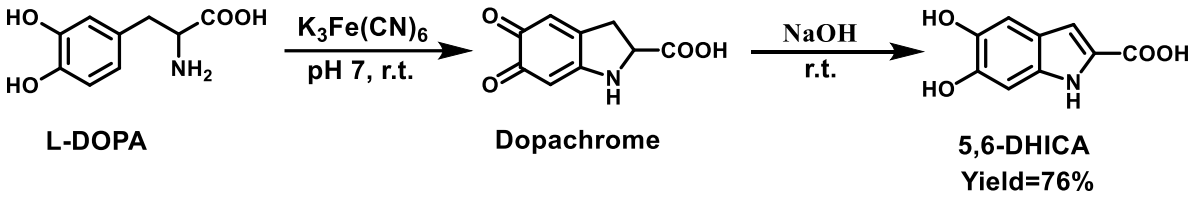

Scheme A2.1: Reaction scheme for the synthesis of DHICA from L-DOPA.

^{1}H NMR (500 MHz, CH_3COCH_3, ppm) δ = 10.83 (s, 1H), 10.36 (s, 1H), 7.97 (s, 1H), 7.79 (s, 1H), 7.03 (s, 1H), 6.98 (s, 1H), 6.96 (s, 1H).

^{13}C NMR (125 MHz, $CDCl_3$, ppm) δ = 163.9, 146.2, 141.7, 133.2, 125.7, 120.7, 107.9, 104.6, 96.2.

HRMS (APCI) m/z calculated for $[(M–H)^–]$; 192.0302; found 192.0292.

^{13}C-labelled DHICA was prepared analogously from ^{13}C-L-DOPA (0.2 g, 1 mmol) (Yield = 71%).

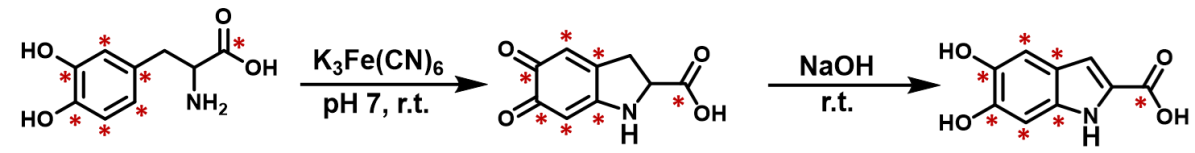

Scheme A2.2: Reaction scheme for the synthesis of ^{13}C-labelled DHICA from ^{13}C-labelled L-DOPA.

2.4.1.2. Synthesis of DHICA-melanin

DHICA (500 mg) was dissolved in 200 mL Milli-Q water and stirred at ambient conditions for 7 days, during which the solution turned black. The mixture was centrifuged (8000 rpm), and the brown supernatant was discarded. The precipitate was washed repeatedly with Milli-Q water until the supernatant was clear, followed by multiple acetone washes. The black solid

was air-dried to yield 100–150 mg of DHICA-melanin.

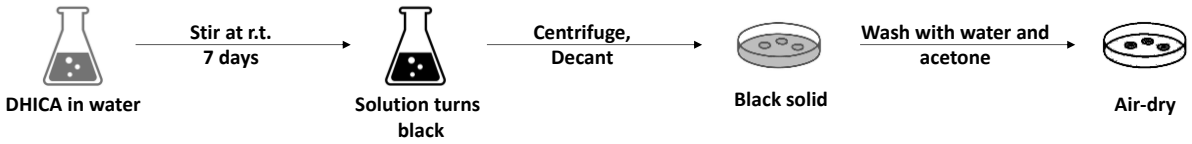

Scheme A2.3: Reaction scheme for the synthesis of unlabelled and ^{13}C labelled DHICA-melanin.

2.5. Additional Figures

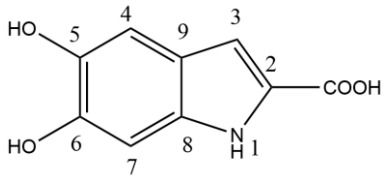

Figure A2.1: The chemical structure of 5,6-dihydroxyindole-2-carboxylic acid (DHICA) along with numbering scheme used in the manuscript.

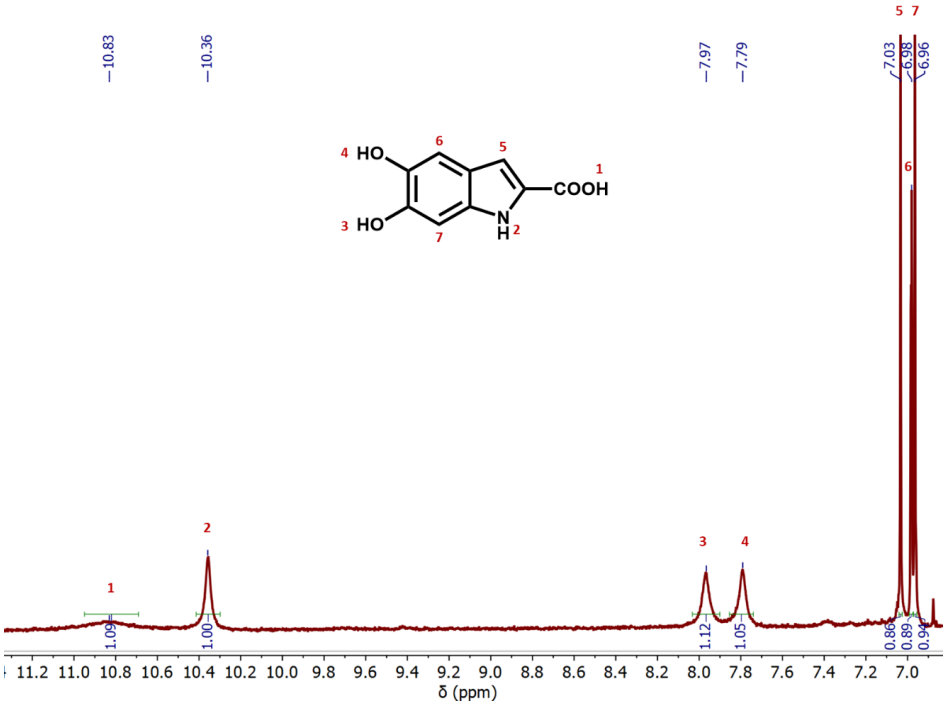

Figure A2.2: Solution-state ^{1}H-NMR spectra of DHICA.

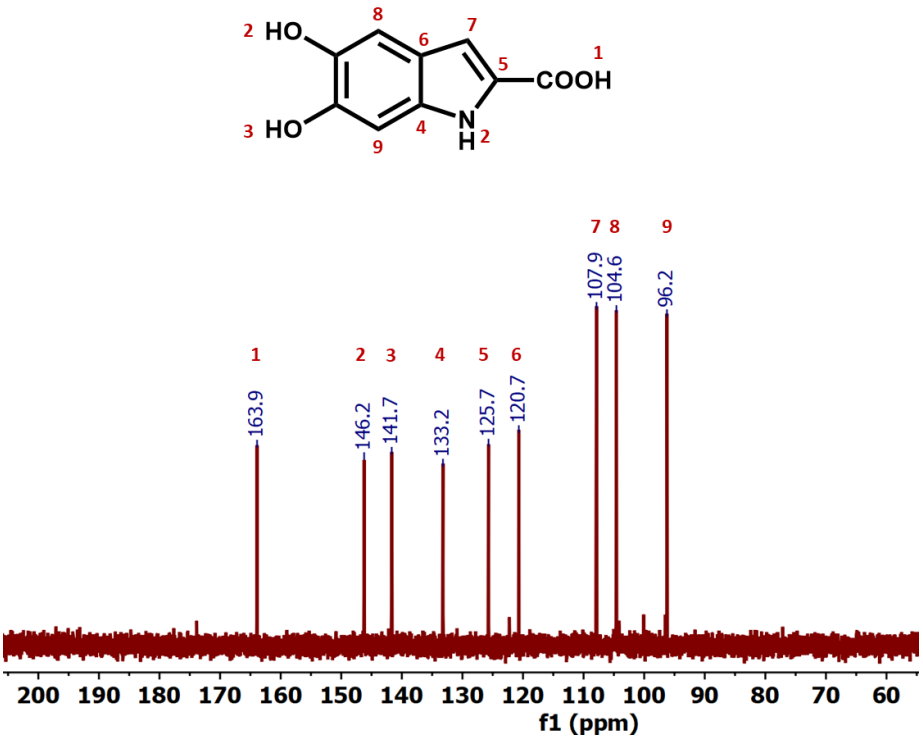

Figure A2.3: Solution-state ^{13}C-NMR of DHICA.

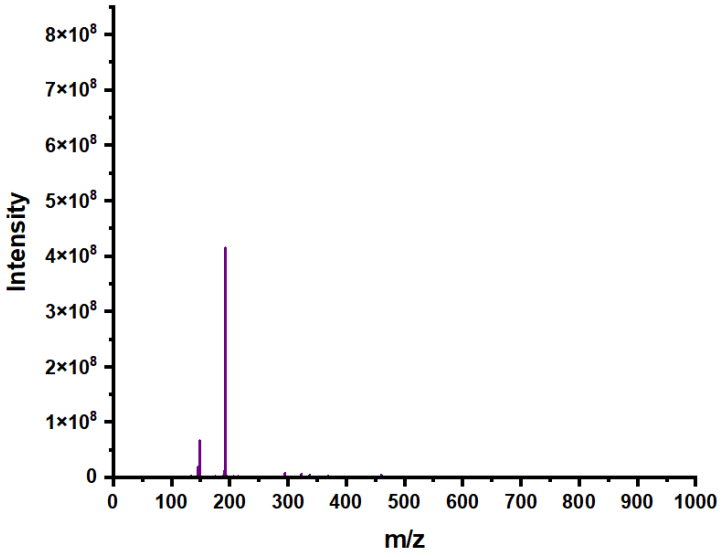

Figure A2.4: The HRMS spectrum of DHICA.

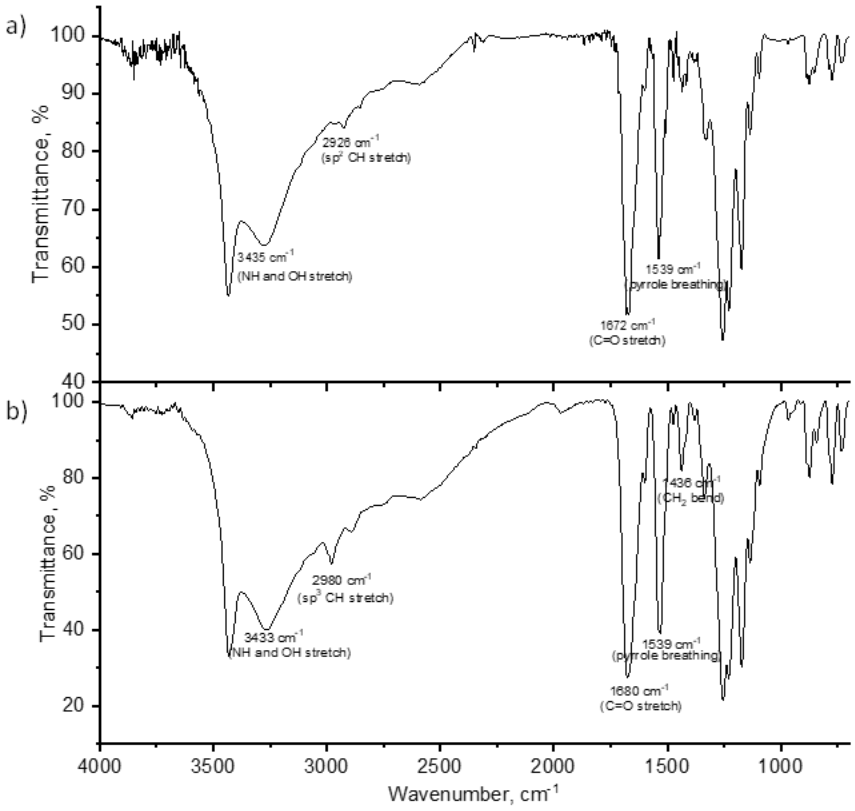

Figure A2.5: FT-IR spectra of a) DHICA and b) DHICA-melanin in KBr pellets.

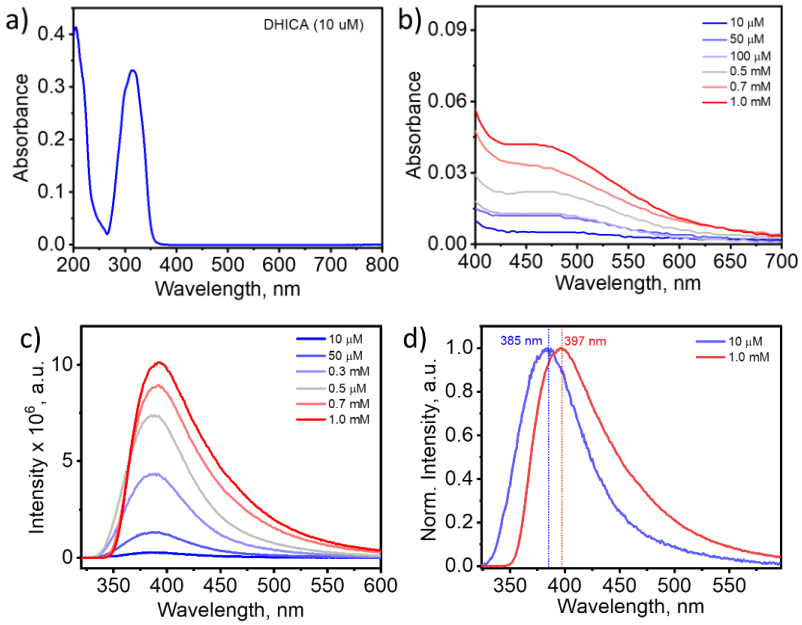

Figure A2.6: a) UV-Vis absorption spectrum of DHICA in milliQ water (10 µM); b) Concentration dependent absorption spectra of DHICA in water (10 µM-1 mM), showing the

emergence of the aggregate band as concentration increases; c) Concentration dependent fluorescence spectra of DHICA in water (10 µM-1 mM); d) Normalized fluorescence spectra of DHICA in water at 10 µM and 1 mM, showing the red-shift in the fluorescence maxima with increase in concentration.

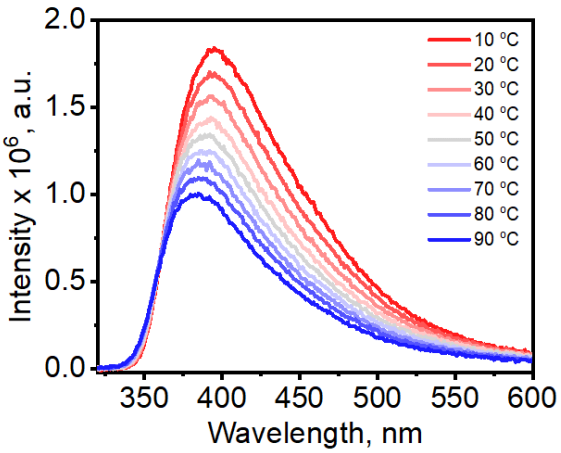

Figure A2.7: Temperature dependent fluorescence emission of DHICA in water at 1 mM concentration.

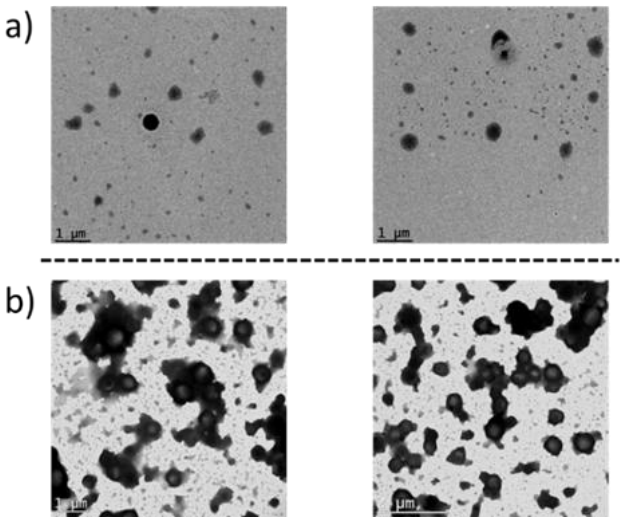

Figure A2.8: TEM images of a) 100 µM DHICA and b) 1 mM DHICA in water, showing the aggregate formation at higher concentrations.

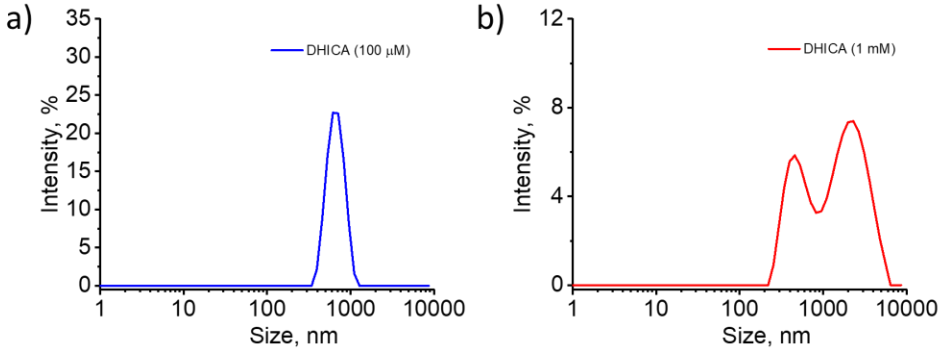

Figure A2.9: DLS size profiles of a) 100 μM DHICA and b) 1 mM DHICA in water, showing the aggregate formation with increase in particle size at higher concentrations.

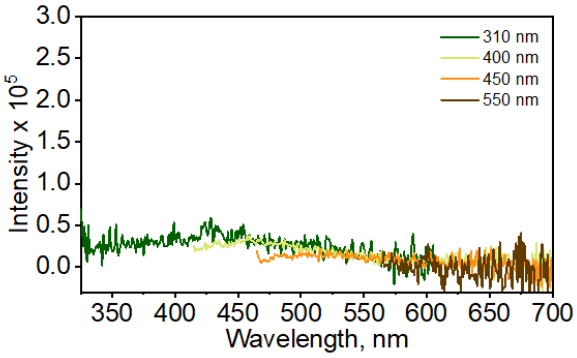

Figure A2.10. Fluorescence emission spectrum of DHICA-melanin in the solid state at different excitation wavelengths.

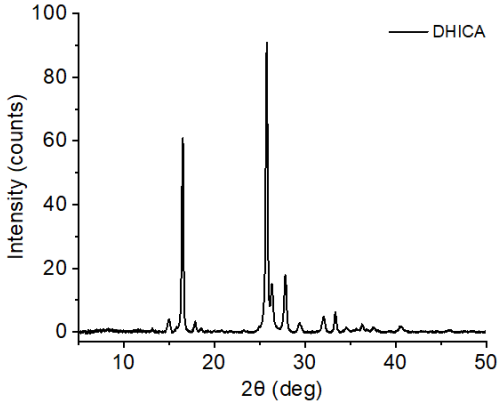

Figure A2.11: The powder X-ray diffraction pattern of DHICA collected at room temperature.

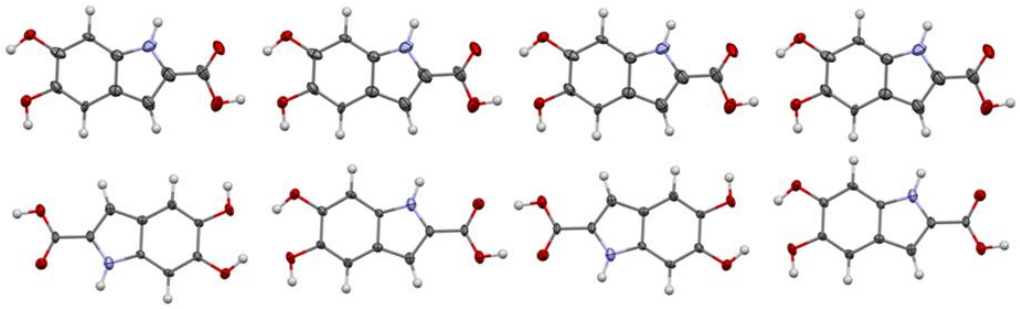

Figure A2.12: Two different chain motifs in the crystalline assembly of DHICA: head-to-tail (top), head-to-head (bottom). Motifs correspond to the two independent molecules and are uniform within each layer.

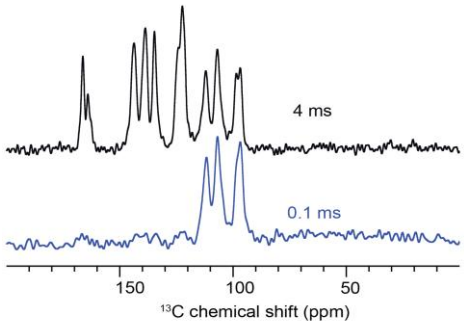

Figure A2.13: Comparative ^{13}C Cross-Polarization solid-state NMR spectra of unlabelled DHICA monomer at -30°C and a spinning rate of 24 kHz, recorded at contact times of 0.1 ms (bottom) and 1 ms (top). Two clearly distinguishable sets of peaks are observable for the carboxylic acid group, suggesting that molecules are present in two asymmetrical locations.

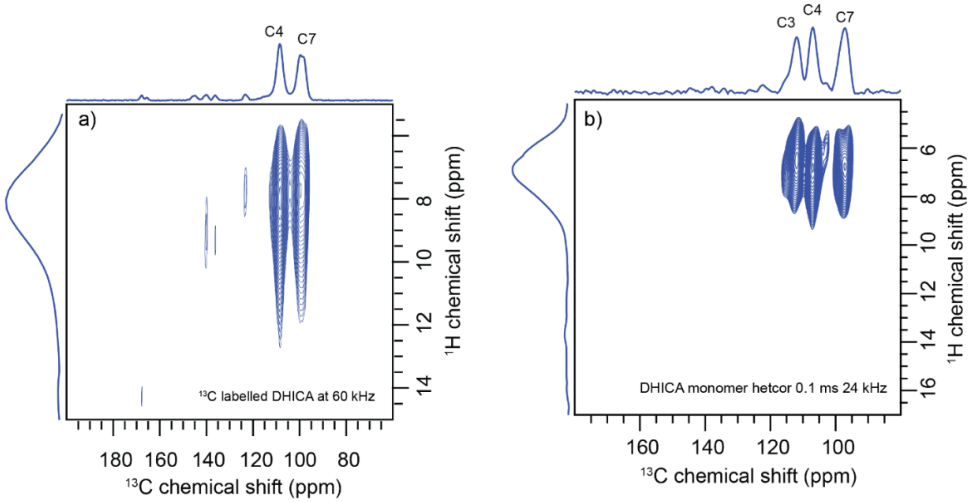

Figure A2.14: The two dimensional ^{1}H-^{13}C HETCOR spectra of a) ^{13}C labelled DHICA and b) unlabelled DHICA collected at a contact time of 0.1 ms.

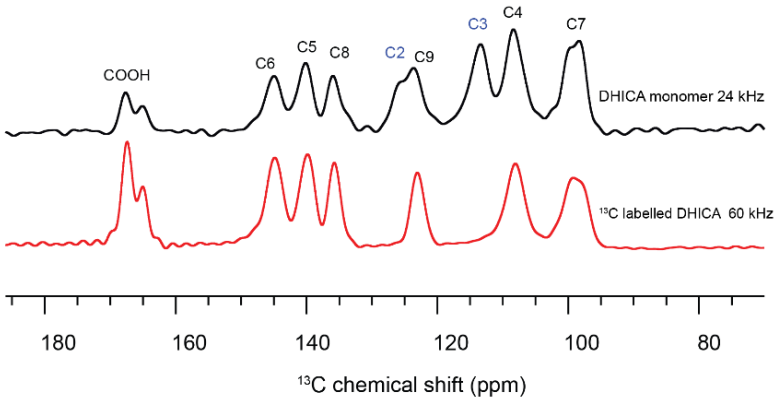

Figure A2.15: Comparative ^{13}C Cross-Polarization solid-state NMR spectra of unlabelled and ^{13}C labelled DHICA monomer at -30°C and a spinning rate of 24 kHz and 60 kHz respectively.

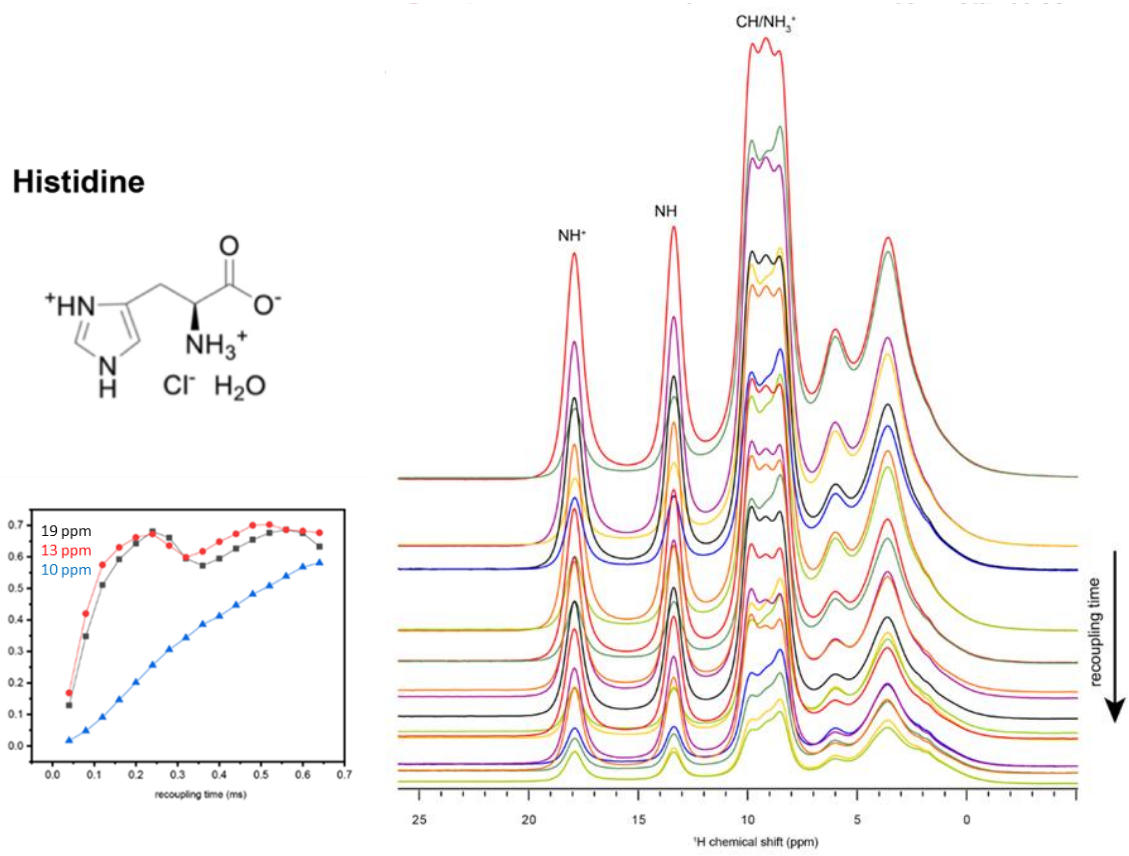

Figure A2.16: The ^{1}H{^{14}N} RESPDOR curve of histidine hydrate monochloride obtained at a spinning speed of 60 kHz.

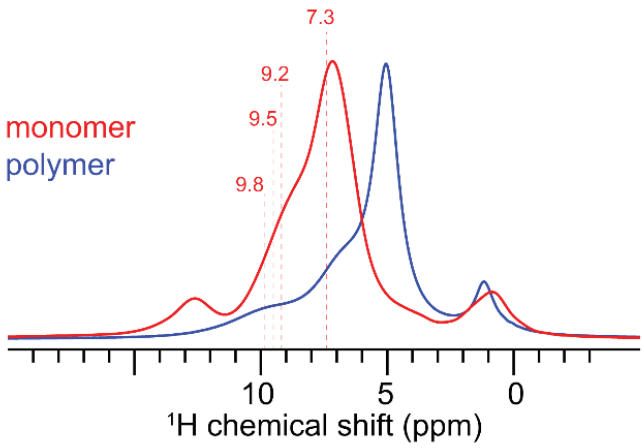

Figure A2.17: The solid-state ^{1}H NMR spectra of DHICA and DHICA-melanin. The marked positions (dotted vertical lines), correspond to chemical shift assignments of the hydroxyl protons of DHICA, based on DFT calculations. A shift towards higher field in the chemical shift is observed for the main aromatic peak. An aliphatic peak is also seen at around 1 ppm. DHICA is precipitated out using hexane and washed with hexane to give the off-white powder. The aliphatic peaks at 1.29 and 0.88 ppm are probably due to the trace amounts of hexane. The absence of these same proton signals in the ^{1}H-^{13}C HETCOR spectra may be attributed to the mobility of hexane.

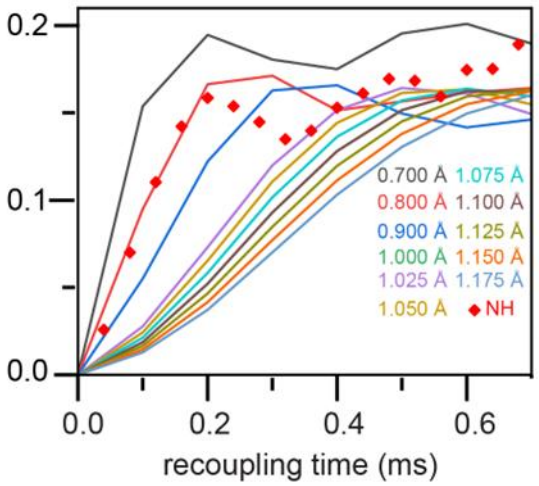

Figure A2.18: The $^{1}H\{^{14}N\}$ RESPDOR curve of DHICA along with the simulation using simpson. Relative low dephasing compared to histidine might be due to the overlap of proton peaks.

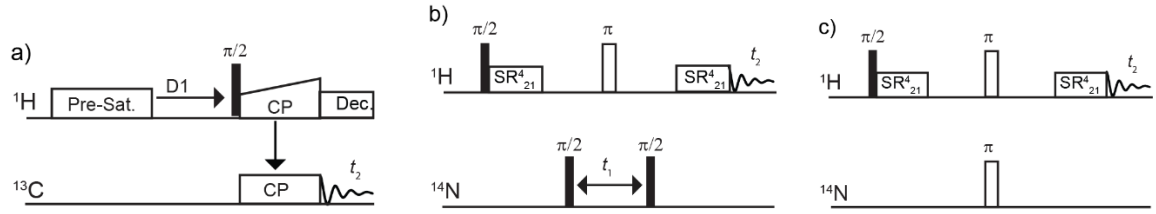

Figure A2.19: Pulse sequence used for the solid-state NMR measurements a) ^{1}H{^{13}C} CP HETCOR b) ^{1}H{^{14}N} DHMQC and c) ^{1}H{^{14}N} RESPDOR.

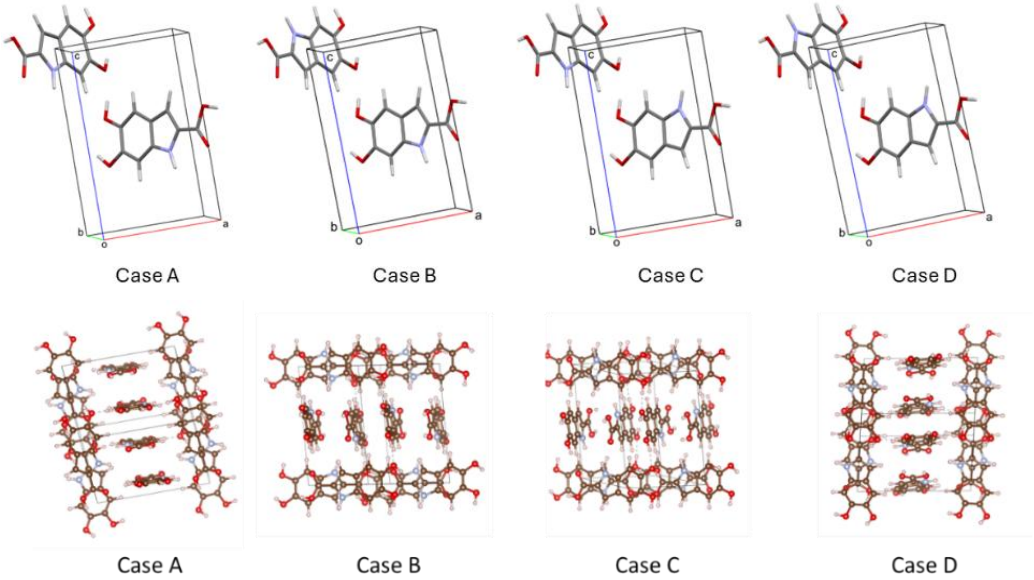

Figure A2.20: The four different cases used for the DFT calculation and NMR chemical shift prediction of DHICA (top: asymmetric unit, bottom: packing).

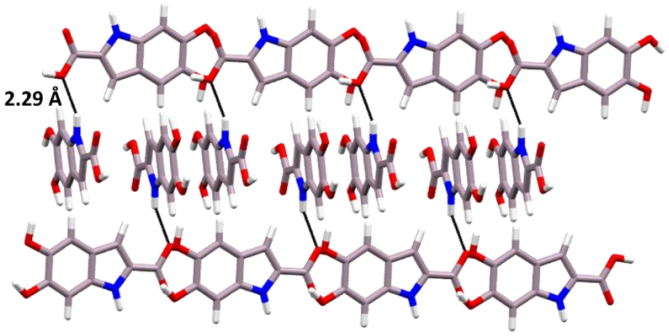

Figure A2.21: Interchain N-H•••O contacts for the DHICA units.

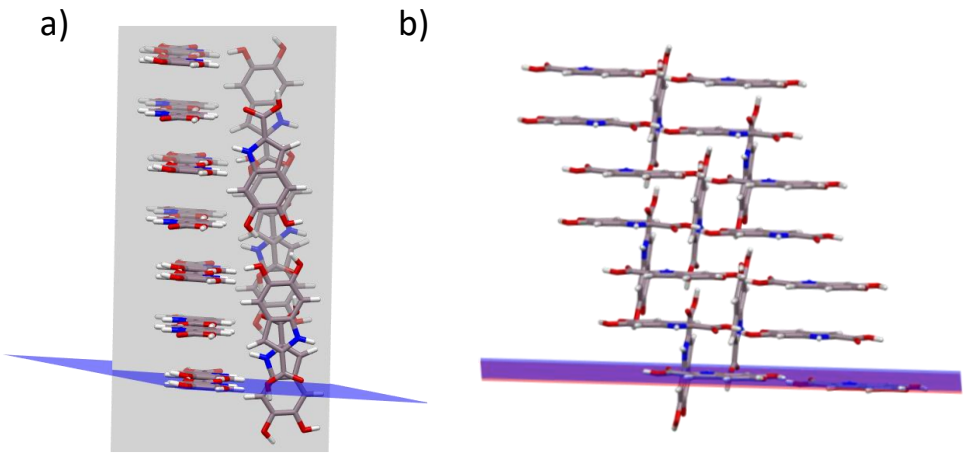

Figure A2.22: a) The near-orthogonal and b) co-linear stacks in the crystal assembly of DHICA.

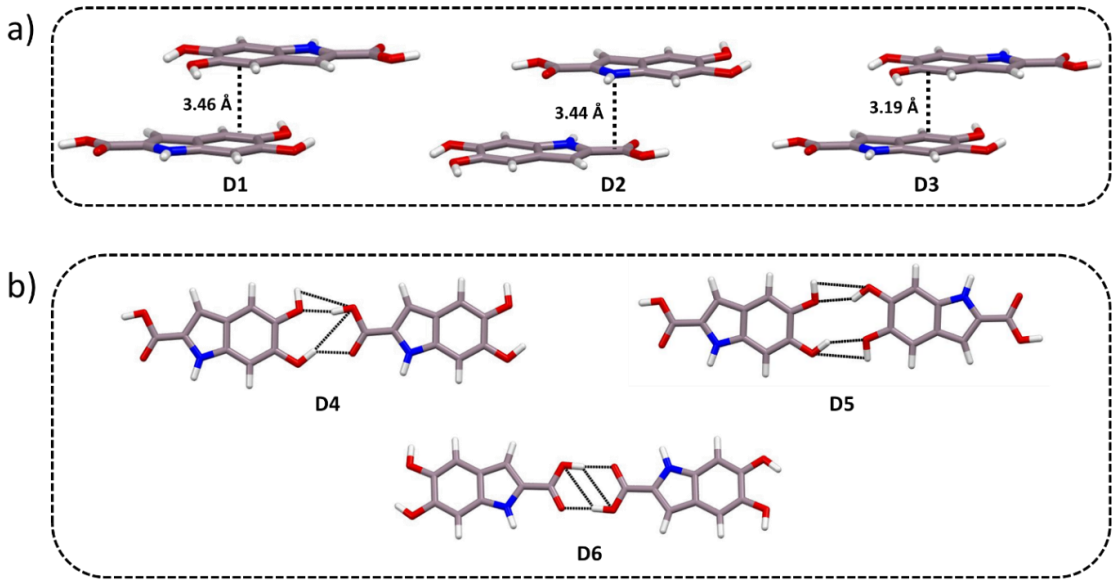

Figure A2.23: Different orientations of DHICA motifs in the crystal. a) π-π stacked dimers (D1–D3) and b) the hydrogen-bond directed dimers (D4-D6) observed in the crystal.

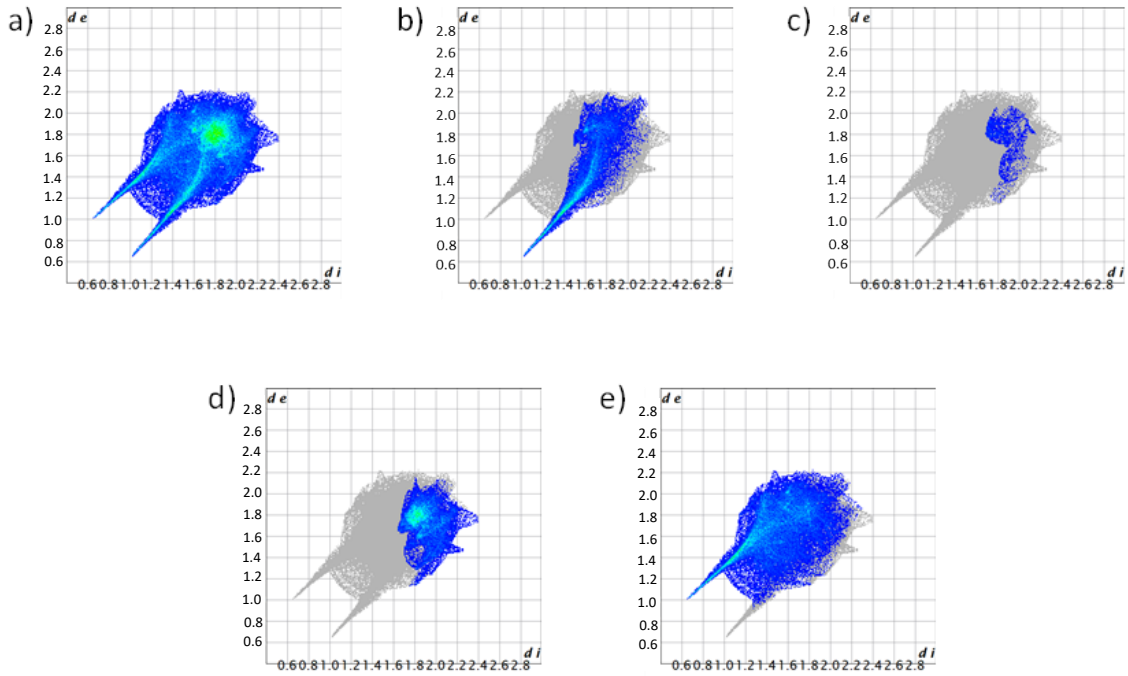

Figure A2.24: Hirshfeld surface plot for a) contacts from all elements, b) contacts from O, c) contacts from N, d) contacts from C and e) contacts from H.

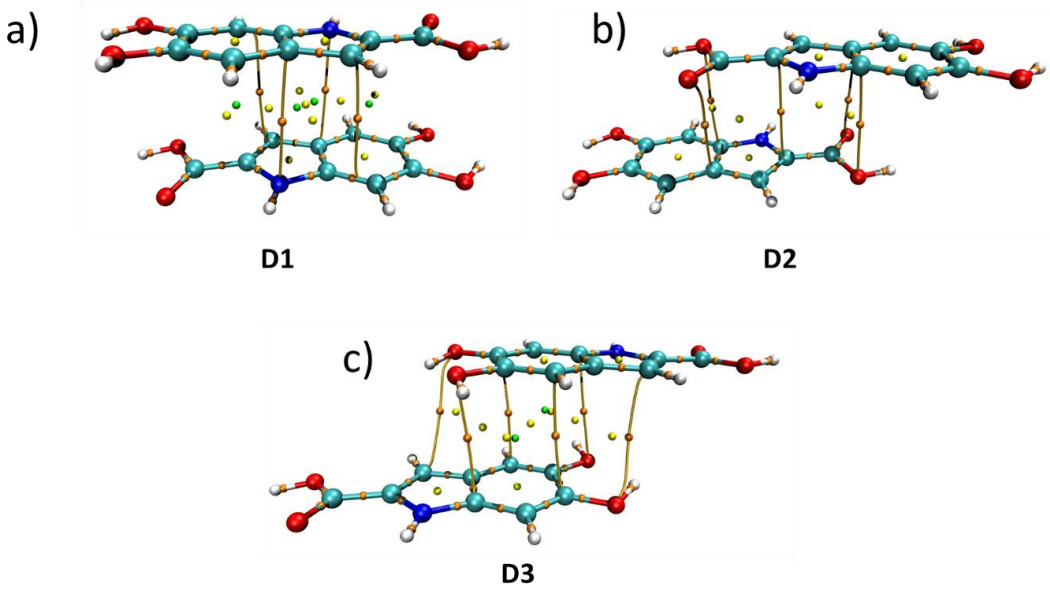

Figure A2.25: QTAIM electron density maps showing the synthon formation from π-π stacking in DHICA dimers a) D1, b) D2 and c) D3.

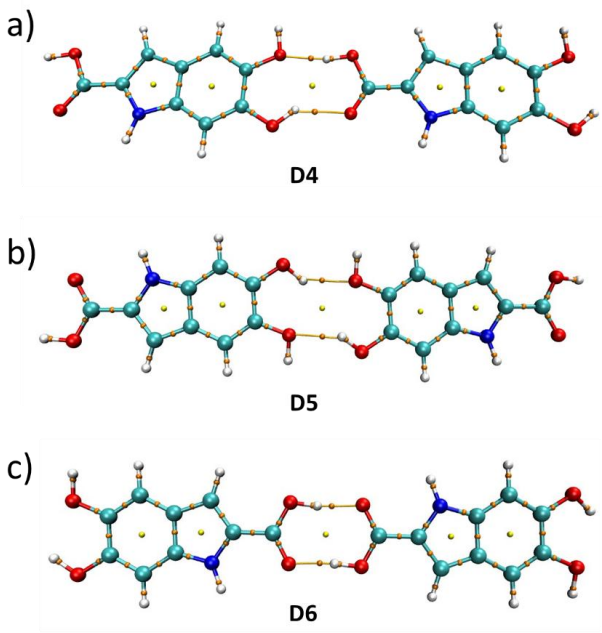

Figure A2.26: QTAIM electron density maps showing the synthon formation from hydrogen bonding interactions in DHICA dimers a) D4, b) D5 and c) D6.

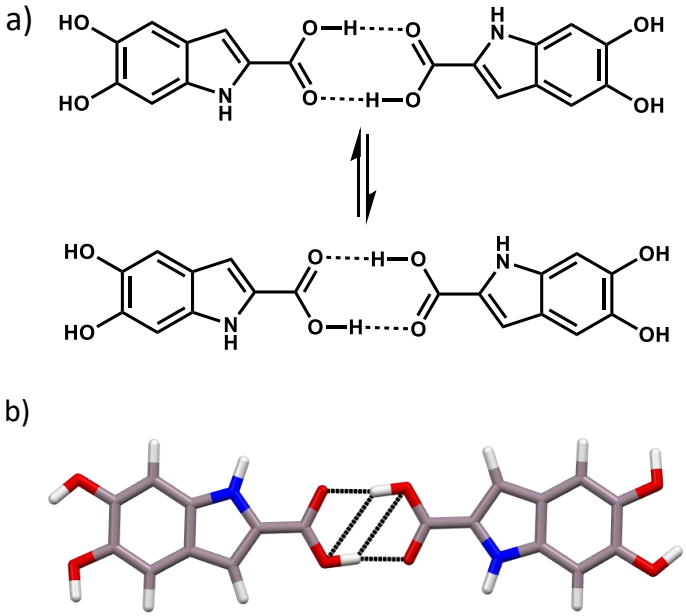

Figure A2.27: The D6 dimer in DHICA showing a) resonance assisted hydrogen bond (RAHB); b) bifurcated hydrogen bonding.

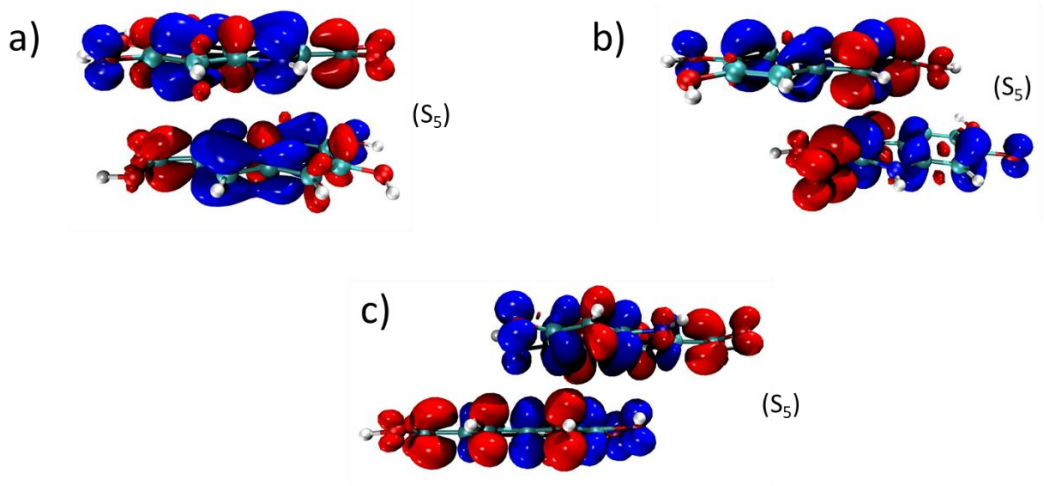

Figure A2.28: The charge-density difference plots (iso-value=0.0008 e-bohr^{-3}) for a) D1 dimer, b) D2 dimer and c) D3 dimer. The red represents the positive and blue represents negative values respectively.

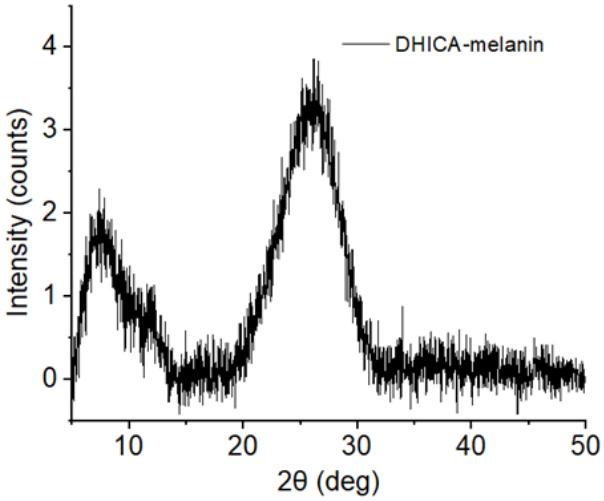

Figure A2.29: The powder X-ray diffraction pattern of DHICA-melanin collected at room temperature.

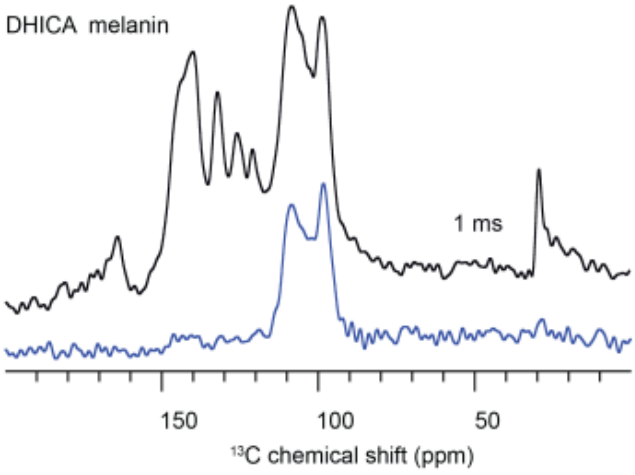

Figure A2.30: The ^{13}C Cross-Polarization solid-state NMR spectra of unlabelled DHICA-melanin at -30°C with a spinning rate of 24 kHz. Spectra were collected at two different contact times: 0.1 ms (bottom) and 4 ms (top). With longer contact times, new correlation peaks begin to appear, mostly from the quaternary carbons in the 120–160 ppm range.

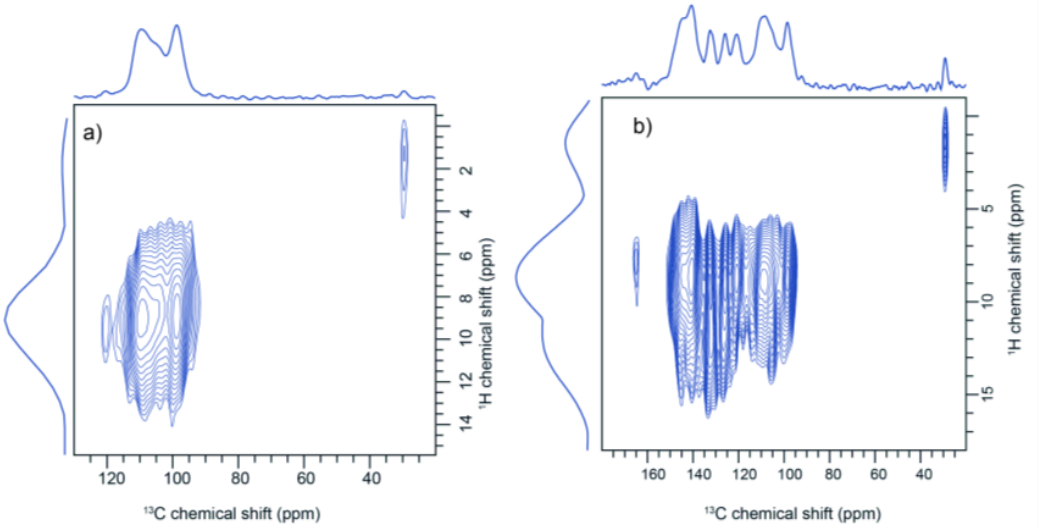

Figure A2.31: The ^{1}H-^{13}C HETCOR spectra of the unlabelled DHICA-melanin collected at a contact time of a) 0.1 ms b) 2 ms at 24 kHz spinning speed. At long contact time new correlation with quaternary carbons and carbonyl group is observed. Aliphatic peaks are observed in the ^{1}H-^{13}C HETCOR spectra, which could be from the unlabelled carbons in the polymer suggesting the presence of saturated indoline(s).

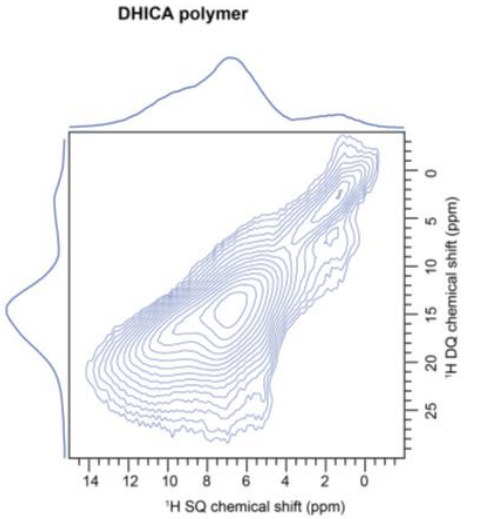

Figure A2.32: The 2D ^{1}H dipolar double-quantum – single-quantum (DQ-SQ) spectrum of DHICA-melanin collected at 60 kHz spinning speed. A correlation is observed between the aliphatic peak and the aromatic peak indicating the spatial proximity.

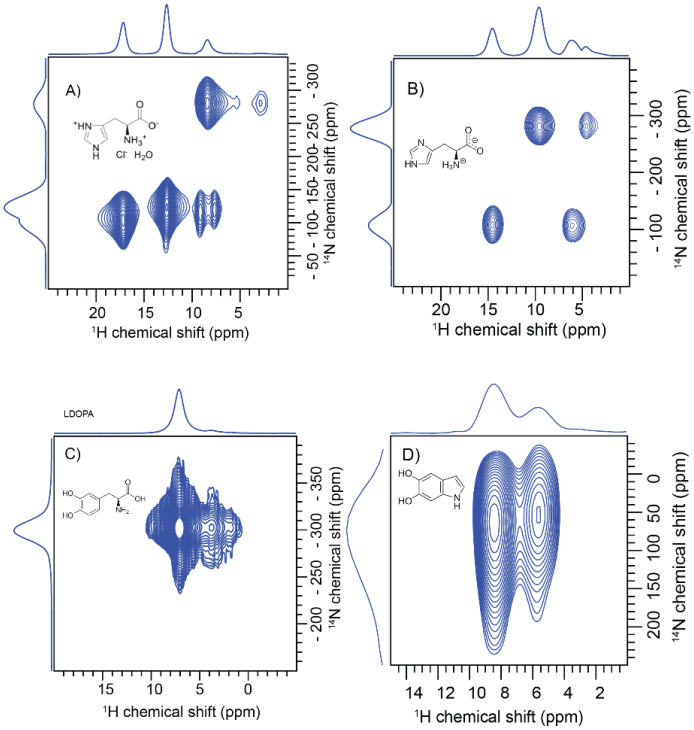

Figure A2.33: The ^{1}H{^{14}N} DHMQC spectra of A) Histidine hydrate monochloride B) Histidine C) L-DOPA[1] and D) DHI. The quadrupolar coupling constant Cq for the histidine and L-DOPA is around 1 MHz.

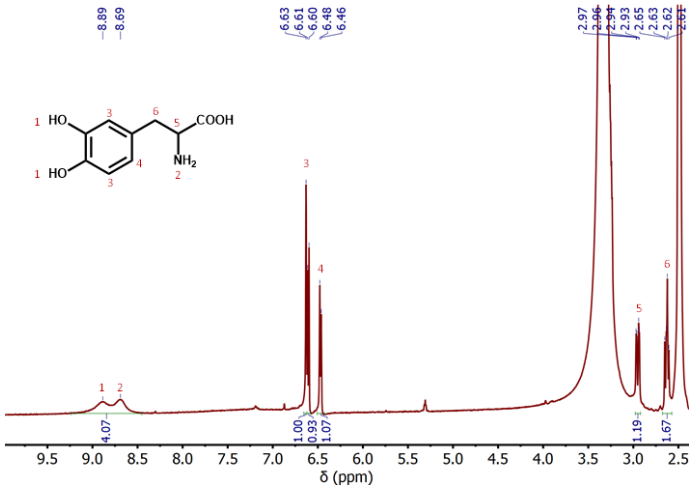

Figure A2.34: The ^{1}H-NMR spectra of L-DOPA in DMSO-d6 solvent.

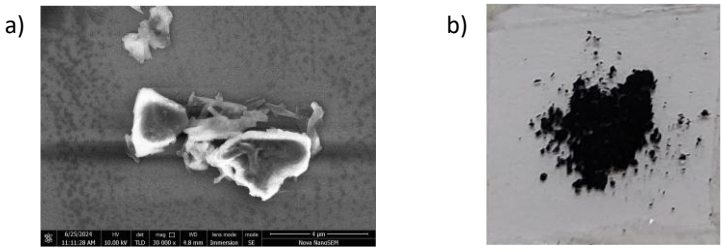

Figure A2.35: a) The SEM image and b) optical image of DHICA-melanin.

2.6. Additional Tables

Table A2.1: Previous attempts to elucidate the structure of eumelanin and its precursors.

Contributed by	**Journal**	**Methods employed to identify the aggregate structure**
Meredith and coworkers	Soft Matter, 2009, 5, 3754-3760	Low voltage–high resolution transmission electron microscopy
Bielawski, Paul, Freeman and coworkers	Langmuir, 2012, 28, 6428–6435	Solid state ^{15}N and ^{13}C-NMR, PXRD
Buehler and coworkers	Nat. Commun., 2014, 5, 3859	First-principles computational investigation
Warren and coworkers	ACS Nano, 2018, 12, 12050–12061	Transmission electron microscopy and pump-probe spectroscopy

Kohler and coworkers	Chem. Sci., 2020, 11, 1248-1259	Transmission electron microscopy and pump-probe spectroscopy
Hariharan and coworkers	Chem. Sci., 2022, 13, 2331-2338	Single-crystal X-ray diffraction
Hariharan, Thomas and coworkers	Chem. Sci., 2024, 15, 16015-16024	3D ED, solid-state NMR, DFT calculations

Table A2.2: 3D ED data collection details for the DHICA crystals used in refinement.

No.	Approximate size [µm]	Angular range [°]	Rotation per frame [°]	Exposure time [s]	Total exposure [s]	Frames measured
1	0.4 x 0.3 x 0.2	−30 to +70	1	1	100	100
2	0.4 x 0.4 x 0.3	−60 to +50	1	1	110	110
3	0.5 x 0.3 x 0.2	−60 to +60	1	1	120	120

Table A2.3: The predicted ^{13}C NMR chemical shift and root mean square deviation for the case A.

Numbering scheme	Solution state NMR $\delta_{iso,sol}$ (ppm)	Solid state NMR $\delta_{iso,expt}$ (ppm)	Chemical shielding σ (ppm)	Predicted chemical shift $\delta_{iso,cal}$ (ppm)
C2	125.7	125.05	47.84	123.89
C3	107.9	115.39	60.49	111.24
C4	104.6	107.70	63.9	107.83
C5	146.2	139.68	32.11	139.62
C6	141.7	144.51	25.96	145.77
C7	96.2	99.25	76.38	95.35
C8	133.2	135.61	37.34	134.39
C9	125.7	122.79	48.02	123.71
C10	163.9	167.28	4.80	166.93
C2'	125.7	123.09	49.04	122.69
C3'	107.9	115.39	57.33	114.40
C4'	104.6	107.70	65.12	106.61
C5'	146.2	139.68	31.02	140.71
C6'	141.7	144.51	27.24	144.49
C7'	96.2	97.59	73.71	98.02
C8'	133.2	135.61	37.51	134.22

C9'	125.7	122.79	49.47	122.26
C10'	163.9	165.32	7.70	164.03
			RMSD	1.58

Table A2.4: The predicted ^{13}C NMR chemical shift and root mean square deviation for the case B.

Numbering scheme	Solution state NMR $\delta_{iso,sol}$ (ppm)	Solid state NMR $\delta_{iso,expt}$ (ppm)	Chemical shielding σ (ppm)	Predicted chemical shift $\delta_{iso,cal}$ (ppm)
C2	125.7	125.05	46.72	124.74
C3	107.9	115.39	55.75	115.71
C4	104.6	107.70	73.96	97.50
C5	146.2	139.68	27.69	143.77
C6	141.7	144.51	30.21	141.25
C7	96.2	99.25	66.43	105.03
C8	133.2	135.61	47.38	124.08
C9	125.7	122.79	37.81	133.65
C10	163.9	167.28	5.30	166.16
C2'	125.7	123.09	48.57	122.89
C3'	107.9	115.39	58.53	112.93
C4'	104.6	107.7	64.46	107.00
C5'	146.2	139.68	30.63	140.83
C6'	141.7	144.51	26.67	144.79
C7'	96.2	97.59	74.89	96.57
C8'	133.2	135.61	37.62	133.84
C9'	125.7	122.79	49.00	122.46
C10'	163.9	165.32	8.49	162.97
				4.92

Table A2.5: The predicted ^{13}C NMR chemical shift and root mean square deviation for the case C.

Numbering scheme	Solution state NMR $\delta_{iso,sol}$ (ppm))	Solid state NMR $\delta_{iso,expt}$ (ppm)	Chemical shielding (ppm)	Predicted chemical shift $\delta_{iso,cal}$ (ppm)
C2	125.7	125.05	47.12	124.52
C3	107.9	115.39	59.78	111.86

C4	104.6	107.70	64.65	106.99
C5	146.2	139.68	31.73	139.91
C6	141.7	144.51	26.58	145.06
C7	96.2	99.25	76.45	95.19
C8	133.2	135.61	37.74	133.90
C9	125.7	122.79	47.99	123.65
C10	163.9	167.28	4.47	167.17
C2'	125.7	123.09	49.51	122.13
C3'	107.9	115.39	56.23	115.41
C4'	104.6	107.70	73.7	97.94
C5'	146.2	139.68	26.18	145.46
C6'	141.7	144.51	30.44	141.20
C7'	96.2	97.59	64.68	106.96
C8'	133.2	135.61	48.48	123.16
C9'	125.7	122.79	38.72	132.92
C10'	163.9	165.32	8.75	162.89
			RMSD	5.40

Table A2.6: The predicted ^{13}C NMR chemical shift and root mean square deviation for the case D.

Numbering scheme	**Solution state NMR $\delta_{iso,sol}$ (ppm)**	**Solid state NMR $\delta_{iso,expt}$ (ppm)**	**Chemical shielding (ppm)**	**Predicted chemical shift $\delta_{iso,cal}$ (ppm)**
C2	125.7	125.05	46.3	125.32
C3	107.9	115.39	58.08	113.54
C4	104.6	107.70	75.08	96.54
C5	146.2	139.68	27.26	144.36
C6	141.7	144.51	30.84	140.78
C7	96.2	99.25	66.10	105.52
C8	133.2	135.61	47.55	124.07
C9	125.7	122.79	37.93	133.69
C10	163.9	167.28	4.87	166.75
C2'	125.7	123.09	49.68	121.94
C3'	107.9	115.39	56.93	114.69
C4'	104.6	107.7	73.43	98.19
C5'	146.2	139.68	25.70	145.92
C6'	141.7	144.51	29.60	142.02
C7'	96.2	97.59	66.41	105.21

C8'	133.2	135.61	48.77	122.85
C9'	125.7	122.79	38.66	132.96
C10'	163.9	165.32	9.74	161.88
			RMSD	7.18

Table A2.7: The predicted ^{1}H NMR chemical shift and root mean square deviation for the case A.

Numbering scheme	Solution state NMR $\delta_{iso,sol}$ (ppm)	Solid state NMR $\delta_{iso,expt}$ (ppm)	Chemical shielding (ppm)	Predicted chemical shift $\delta_{iso,cal}$ (ppm)
1NH	10.36	8.9	21.09	8.84
3	7.05	7.1	23.05	6.88
4	7.00	7.4	23.11	6.82
5 OH	7.78	9.2	20.68	9.25
6 OH	7.97	7.3	22.91	7.02
7	6.98	7.3	23.05	6.88
COOH	10.71	14.5*	14.94	14.99
1'NH	10.36	8.7	21.23	8.70
3'	7.05	6.5	23.77	6.16
4'	7.00	6.8	22.81	7.12
5' OH	7.78	9.8	19.90	10.03
6' OH	7.97	9.5	20.09	9.84
7'	6.98	6.8	23.21	6.72
COOH'	10.71	10.2	19.13	10.80
RMSD				0.34

**The COOH peak assigned to 13.4 ppm based on the $^{1}H\{^{13}C\}$ HETCOR spectrum with a long contact time of 5 ms, results in an RMSD of 0.52.*

Table A2.8: The predicted ^{1}H NMR chemical shift and root mean square deviation for the case B.

Numbering scheme	Solution state NMR $\delta_{iso,sol}$ (ppm)	Solid state NMR $\delta_{iso,expt}$ (ppm)	Chemical shielding σ (ppm)	Predicted chemical shift $\delta_{iso,cal}$ (ppm)
1	10.36	8.9	21.87	8.03
3	7.05	7.1	22.65	7.25
4	7.00	7.4	23.06	6.84

5 OH	7.78	9.2	20.44	9.46
6 OH	7.97	7.3	23.4	6.50
7	6.98	7.3	22.74	7.16
COOH	10.71	14.5*	14.15	15.75
1'	10.36	8.7	21.88	8.02
3'	7.05	6.5	23.67	6.23
4'	7.00	6.8	22.74	7.16
5' OH	7.78	9.8	19.72	10.18
6' OH	7.97	9.5	19.96	9.94
7'	6.98	6.8	23.24	6.66
COOH'	10.71	10.2	19.12	10.78
RMSD				0.58

**The COOH peak assigned to 13.4 ppm based on the $^{1}H\{^{13}C\}$ HETCOR spectrum with a long contact time of 5 ms, results in an RMSD of 0.78.*

Table A2.9: The predicted ^{1}H NMR chemical shift and root mean square deviation for the case C.

Numbering scheme	**Solution state NMR $\delta_{iso,sol}$ (ppm)**	**Solid state NMR $\delta_{iso,expt}$ (ppm)**	**Chemical shielding σ (ppm)**	**predicted chemical shift $\delta_{iso,cal}$ (ppm)**
1	10.36	8.9	21.28	8.66
3	7.05	7.1	22.94	7.00
4	7.00	7.4	23.07	6.87
5 OH	7.78	9.2	20.78	9.16
6 OH	7.97	7.3	22.69	7.25
7	6.98	7.3	23.04	6.90
COOH	10.71	14.5*	15.16	14.78
1'	10.36	8.7	22.76	7.18
3'	7.05	6.5	22.91	7.03
4'	7.00	6.8	22.95	6.99
5' OH	7.78	9.8	19.43	10.51
6' OH	7.97	9.5	19.56	10.38
7'	6.98	6.8	22.93	7.01
COOH'	10.71	10.2	19.65	10.29
RMSD				0.57

**The COOH peak assigned to 13.4 ppm based on the $^{1}H\{^{13}C\}$ HETCOR spectrum with a long contact time of 5 ms, results in an RMSD of 0.67.*

Table A2.10: The predicted ^{1}H NMR chemical shift and root mean square deviation for the case D.

Numbering scheme	Solution state NMR $\delta_{iso,sol}$ (ppm)	Solid state NMR $\delta_{iso,expt}$ (ppm)	Chemical shielding σ (ppm)	Predicted chemical shift $\delta_{iso,cal}$ (ppm)
1	10.36	8.9	21.82	8.17
3	7.05	7.1	22.86	7.13
4	7.00	7.4	23.11	6.88
5 OH	7.78	9.2	20.64	9.35
6 OH	7.97	7.3	23.33	6.66
7	6.98	7.3	22.77	7.22
COOH	10.71	14.5*	14.33	15.66
1'	10.36	8.7	22.65	7.34
3'	7.05	6.5	23.28	6.71
4'	7.00	6.8	23.04	6.95
5'OH	7.78	9.8	19.51	10.48
6'OH	7.97	9.5	19.6	10.39
7'	6.98	6.8	23.08	6.91
COOH'	10.71	10.2	19.89	10.10
RMSD				0.64

**The COOH peak assigned to 13.4 ppm based on the $^{1}H\{^{13}C\}$ HETCOR spectrum with a long contact time of 5 ms, results in an RMSD of 0.82.*

Table A2.11: Comparison of energy for cases A, B, C and D along with the RMSD of ^{1}H chemical shift.

Label	Final Energy (eV)	^{1}H RMSD (ppm)
Case A	-14234.94	0.34
Case B	-14234.68	0.58
Case C	-14234.75	0.57
Case D	-14234.61	0.64

Table A2.12: Interaction energies[a] of DHICA dimers evaluated using symmetry-adapted perturbation theory (SAPT(0)) aug-cc-pVDZ calculations.

Dimer	E_{int}^{SAPT}	Electrostatic Energy (E_{elc})	Dispersion Energy (E_{dis})	Induction Energy (E_{ind})	Exchange Energy (E_{ex})
D1	-12.09	-3.42	-18.91	-0.86	11.09
D2	-11.65	-5.64	-15.42	-0.99	10.41
D3	-13.22	-6.93	-18.88	-1.65	14.24
D4	-7.66	-15.29	-6.61	-6.65	20.89
D5	-7.36	-10.09	-5.26	-2.41	10.40
D6	-25.75	-36.46	-8.57	-17.83	37.11

**All energy values are given in kcal/mol.*

Table A2.13: Fragment based excited state analysis for dimer D1 in the crystalline assembly of DHICA.

State	dE(eV)	f	POS	PR	CT
S1	3.874	0.000	1.500	2.000	0.214
S2	4.143	0.000	1.500	2.000	0.139
S3	4.269	0.470	1.500	2.000	0.055
S4	4.323	0.414	1.500	2.000	0.106
S5	4.512	0.023	1.500	2.000	0.864
S6	4.630	0.000	1.500	2.000	0.789
S7	4.883	0.020	1.500	2.000	0.959
S8	4.985	0.000	1.500	2.000	0.836
S9	5.254	0.094	1.500	2.000	0.216
S10	5.322	0.001	1.469	1.992	0.019

Table A2.14: Fragment based excited state analysis for dimer D2 in the crystalline assembly of DHICA.

State	dE(eV)	f	POS	PR	CT
S1	3.944	0.000	1.500	2.000	0.172
S2	4.253	0.095	1.500	2.000	0.084
S3	4.274	0.930	1.500	2.000	0.044
S4	4.301	0.046	1.500	2.000	0.029
S5	4.635	0.000	1.500	2.000	0.918

S6	4.755	0.000	1.500	2.000	0.809
S7	5.173	0.000	1.500	2.000	0.906
S8	5.222	0.018	1.500	2.000	0.799
S9	5.314	0.000	1.437	1.968	0.056
S10	5.317	0.004	1.564	1.968	0.118

Table A2.15: Fragment based excited state analysis for dimer D3 in the crystalline assembly of DHICA.

State	dE(eV)	f	POS	PR	CT
S1	4.235	0.000	1.499	2.000	0.033
S2	4.246	1.036	1.501	2.000	0.062
S3	4.398	0.000	1.494	2.000	0.074
S4	4.419	0.072	1.506	2.000	0.055
S5	4.955	0.000	1.500	1.998	0.881
S6	4.966	0.010	1.500	1.998	0.890
S7	5.082	0.000	1.144	1.327	0.007
S8	5.083	0.000	1.856	1.327	0.008
S9	5.213	0.000	1.500	2.000	0.615
S10	5.333	0.031	1.500	2.000	0.867

Table A2.16: Fragment based excited state analysis for dimer D4 in the crystalline assembly of DHICA.

State	dE(eV)	f	POS	PR	CT
S1	4.106	1.234	1.568	1.964	0.005
S2	4.211	0.007	1.431	1.963	0.003
S3	4.303	0.120	1.026	1.053	0.002
S4	4.400	0.066	1.976	1.049	0.003
S5	5.319	0.000	2.000	1.001	0.001
S6	5.461	0.130	1.972	1.058	0.042
S7	5.481	0.048	1.044	1.096	0.084
S8	5.508	0.001	1.069	1.153	0.120
S9	5.526	0.060	1.190	1.447	0.353
S10	5.540	0.023	1.244	1.524	0.429

Table A2.17: Fragment based excited state analysis for dimer D5 in the crystalline assembly of DHICA.

State	dE(eV)	f	POS	PR	CT
S1	4.258	1.290	1.500	1.500	0.003
S2	4.346	0.000	1.500	1.500	0.002
S3	4.485	0.001	1.566	1.566	0.002
S4	4.487	0.102	1.434	1.434	0.002
S5	5.070	0.000	2.000	1.001	0.000
S6	5.070	0.000	1.000	1.001	0.000
S7	5.520	0.001	1.545	1.984	0.009
S8	5.521	0.279	1.455	1.984	0.005
S9	5.611	0.000	1.498	2.000	0.136
S10	5.664	0.011	1.503	2.000	0.102

Table A2.18: Fragment based excited state analysis for dimer D6 in the crystalline assembly of DHICA.

State	dE(eV)	f	POS	PR	CT
S1	4.186	1.393	1.500	2.000	0.009
S2	4.348	0.000	1.500	2.000	0.005
S3	4.421	0.006	1.252	1.605	0.005
S4	4.421	0.088	1.748	1.604	0.004
S5	5.482	0.155	1.496	2.000	0.011
S6	5.499	0.000	1.504	2.000	0.004
S7	5.530	0.124	1.500	2.000	0.008
S8	5.556	0.000	1.500	2.000	0.029
S9	5.572	0.000	1.500	2.000	0.061
S10	5.599	0.007	1.500	2.000	0.062

Table A2.19: T_1 measurement of the samples.

SI No.	Compound	T_1
1	DHI	100 s
2	DHICA	4 s
3	DHICA melanin	0.7 s

Table A2.20: Summary of the observed similarities and differences between monomer and polymer.

Technique	DHICA	DHICA-melanin
SEM	Globular	Layered/sheet arrangements
FT-IR	NH stretching band at 3435 cm^{-1}; OH and COOH stretching bands at 3265 cm^{-1}	NH stretching band at 3435 cm^{-1}; OH and COOH stretching bands at 3265 cm^{-1}; sp^3 -CH stretching peak at 2980 cm^{-1}
UV-Visible absorption	Absorption spectrum is broad and ranges from 200-570 nm in crystalline state compared to monomeric solution	Broad absorption ranges from 200-1400 nm
Solubility	Soluble but difficult to crystalize	Insoluble
3D ED	Triclinic space group $P\bar{1}$ with a=7.49 Å, b=10.23 Å, c=10.81 Å, α=82.27°, β=87.80°, γ=70.10°	Broad diffraction pattern
Solid-state NMR	No aliphatic moiety	Observation of aliphatic peaks
	Only one nitrogen species with a broad NMR spectrum	Multiple nitrogen species
	-	Distribution of chemical shift in the case of C7
	N-H peaks are observed around 9 ppm	N-H peaks are observed around 11 ppm
	Observation of carbonyl group	Observation of carbonyl group
	Presence of carboxylic acid proton	Absence of carboxylic acid proton

2.7. Appendix

2.7.1. Materials and Methods

All chemicals used for the synthesis were obtained from commercial suppliers and used as received without further purification. All reactions were carried out in oven-dried glassware before use and wherever necessary, were performed under dry nitrogen using standard gastight syringes, cannula, and septa. Solvents used for the spectroscopic measurements were dried and distilled by standard laboratory purification techniques. Yields refer to chromatographically and spectroscopically homogenous substances. IR spectra were recorded on a Shimadzu

IRPrestige-21 FT-IR spectrometer as neat KBr pellets for all the derivatives. High resolution mass spectra (HRMS) were recorded on Thermo Scientific Q Exactive mass spectrometer using electrospray ionization (ESI, positive mode) technique. Photophysical measurements of the derivatives were carried out in a cuvette of 1 cm path length and concentration dependent measurements were performed in a cuvette of 1 mm path length. Electronic absorption and emission spectra were recorded on UV-Vis-NIR Perkin Elmer Lambda 950 and Horiba Jobin Yvon Nanolog spectrometers respectively. The UV-Vis absorption spectra in the solution state were measured using the transmission mode and the Kubelka-Munk transformed reflectance spectra in the crystalline state were measured in the diffuse reflectance mode. The diffuse reflectance spectra allow no separation of the reflection, refraction and diffraction occurring from the crystalline samples. ^{1}H and ^{13}C NMR in solution were measured on a 500 MHz Bruker Advance DPX spectrometer using 1,1,1,1-tetramethyl silane (TMS) as the internal standard. Data was processed using Mestrenova software. PXRD patterns were recorded on a Rigaku SmartLab diffractometer with Cu Kα radiation at room temperature.

2.7.2. 3D Electron Diffraction

Samples were deposited as dry powder on standard TEM grids (amorphous carbon on Cu) after gentle grinding and measured at room temperature in continuous rotation mode on an ELDICO ED-1 diffractometer (LaB_6 source, 160 kV, $\lambda = 0.02851$ Å; Dectris QUADRO detector) using ELDIX. Suitable crystals were selected in STEM mode, and diffraction data were collected with a pseudo-parallel beam (~750 nm). Regions affected by beam damage or shadowing were excluded.

Data were processed with APEX4; frames were integrated per crystal, then merged, scaled, and corrected using SAINT and SADABS. Space groups were assigned from systematic absences, E statistics, and successful refinement. Structures were solved with ShelXT and refined using ShelXL/ShelXle under kinematic approximation with neutral scattering factors. Non-H atoms were refined anisotropically without restraints; H atoms were placed in calculated positions, refined with a riding model, and assigned U_{iso} values relative to parent atoms (hydroxy: 1.5 U_{eq}(O); other groups: 1.2 U_{eq}(C/N)). Carboxylic acid protons were restrained to expected

neutron O–H distances. Crystallographic data (Deposition No. 2347665) are available from the CCDC (www.ccdc.cam.ac.uk/structures).

2.7.3. Solid-state NMR

All solid-state NMR spectra were acquired on a Bruker Avance HD 600 WB spectrometer operating at 14.1 T ($\nu_0(^1H)$ = 600.5 MHz).

2.7.3.1. Experiments at 24 kHz MAS:

Samples (fine powder) were packed in 3.2 mm ZrO_2 rotors and spun at 24 kHz. ^1H–^{13}C ramp-CP experiments were performed with a ^{13}C nutation frequency of 60 kHz and a ^1H frequency of ~84 kHz (+1 Hartmann–Hahn). Recycle delays were 2–3 s. $^1H\{^{13}C\}$ CP-HETCOR spectra were acquired with contact times of 50 µs and 1.0 ms, using 32–128 t_1 increments with 256–512 scans each. SPINAL64 decoupling (~83 kHz) was applied during acquisition, and DUMBO homonuclear decoupling (~100 kHz) during t_1. Scaling factors were calibrated with alanine (^1H) and adamantane (^{13}C). All measurements were performed at −30 °C to minimize autoxidative polymerization of DHICA.

2.7.3.2. Experiments at 60 kHz MAS:

Single-pulse ^1H spectra were recorded with $\nu_H \approx 185$ kHz, 16 transients, and 2 s delays. ^{13}C spectra were obtained via ramped $^1H \rightarrow ^{13}C$ CP at the double-quantum Hartmann–Hahn condition ($\nu_H = 20 \pm 5$ kHz; $\nu_C = 40$ kHz), with SPINAL64 decoupling at 150 kHz. $^{13}C\{^1H\}$ 2D HETCOR spectra were recorded with $\tau_{CP} = 1.0$ ms, $\tau_{relax} = 6.0$ s, and 32 (t_1) × 2048 (t_2) points. Data were zero-filled to 64 × 4096 and apodized ($\cos^2$ along t_1; exponential 50 Hz FWHM along t_2). ^2Q–^1Q ^1H correlation spectra were acquired using the BaBa recoupling scheme over two rotor periods ($\tau_{exc} = \tau_{rec} = 33.3$ µs), $\nu_H \approx 185$ kHz, $\tau_{relax} = 2.0$ s, 48 × 512 points, and 32 transients per t_1. Data were zero-filled to 256 × 2048 and Lorentzian-apodized (50 Hz). CP-INADEQUATE experiments were performed at 60 kHz MAS with $\nu_H = 160$ kHz and $\nu_C = 130$ kHz, $\tau_{relax} = 6$ s, and evolution delays of 1 ms. 256 t_1 increments with 64 transients were collected; SPINAL64 decoupling (150 kHz) was applied during t_1 and t_2.

2.7.3.3. Experiments at 50 kHz MAS (^1H–^{14}N):

^{14}N chemical shifts were indirectly referenced using IUPAC frequency ratios and nitromethane scale. DHMQC and RESPDOR spectra were acquired at 50 kHz MAS with ^{1}H referencing to TMS (adamantane secondary). Symmetry-based SR421 recoupling was applied at the 2nd-order rotary resonance condition. Optimal dipolar recoupling times were 160 µs (DHICA) and 240 µs (DHICA-melanin). ^{14}N excitation/reconversion pulses (1 rotor period) used RF ≈ 37 kHz. RESPDOR used a 1.5-cycle saturation pulse (30 µs) at 64 kHz. Dipolar dephasing curves ($1-S/S_0$) were obtained from ^{1}H signals with and without ^{14}N dephasing. Simulations were performed with SIMPSON v4.1.1.

2.7.2. Morphological Characterization

2.7.2.1. Transmission Electron Microscopy (TEM)

TEM measurements were performed on FEI Tecnai 30 G2 and JEOL 2010 microscopes operated at 100 kV. Samples were prepared by drop-casting DHICA solutions (100 µM and 1 mM) in Milli-Q water onto 400-mesh carbon-coated Cu grids and allowing the solvent to evaporate under dust-free conditions. Images were obtained without staining.

2.7.2.2. Scanning Electron Microscopy (SEM)

SEM measurements were carried out on an FEI Nova NanoSEM 450. Samples were drop-cast onto 400-mesh carbon-coated Cu grids, dried under ambient conditions, and sputter-coated with a thin layer of chromium using a JEOL JFC-1100 coater. Images were collected using a JEOL JSM-5600 LV microscope.

2.7.2.3. Dynamic Light Scattering (DLS)

DLS measurements were performed on a Malvern Zetasizer Nano ZS (655 nm laser) using 3 mL glass cuvettes at 25 °C and a 173° backscattering angle. At 100 µM, DHICA showed a monomodal particle size distribution (D_H = 628 nm), while at 1 mM, a bimodal distribution (D_H = 487 nm and 2300 nm) was observed, indicating aggregation at higher concentrations.

2.7.3. Computational Analysis

2.7.3.1. DFT Calculations for Structure Prediction

Initial structure relaxation was performed using the FORCITE module in Materials Studio with the Universal force field. Geometry optimization employed the Smart algorithm with convergence tolerances of 0.0001 kcal mol^{-1} (energy) and 0.005 kcal $Å^{-1}$ (force), with a maximum of 500 iterations. Plane-wave DFT calculations were carried out using the GIPAW method implemented in CASTEP 2017. Geometry optimization and NMR property calculations used the GGA–PBESOL exchange–correlation functional with on-the-fly ultrasoft pseudopotentials. Dispersion interactions were treated using the Tkatchenko–Scheffler scheme. An energy cutoff of 900 eV and a Monkhorst–Pack grid with a k-point spacing of 0.05 $Å^{-1}$ were used to ensure accuracy and computational efficiency.

2.7.3.2. Hirshfeld Analysis

Important intermolecular interactions within the structure of DMICE, BDMICE and IDMICE were identified through Hirshfeld surface analysis using CrystalExplorer. The Hirshfeld surface is defined as a set of points in 3D space where the ratio of promolecule and procrystal electron densities is equal to 0.5. The exploration of intermolecular contacts is provided by mapping normalized contact distances (d_{norm}), which is a function of a closest distance from the point to the nuclei interior (d_i) and exterior (d_e) to the surface as well as on the van der Waals radii (r_{vdw}). 2D fingerprint plots derived from the Hirshfeld surface analyses, by plotting the fraction of points on the surface as the function of di and de, provides a visual summary of intermolecular contacts within the crystal.

2.7.3.3. Quantum Theory of Atoms in Molecules (QTAIM)

The wave function generation for the molecules was carried out at wb97xd/def2-svp using Gaussian 16 and the subsequent location of the critical points and the topology analysis were carried out using Multiwfn 3.7. Quantum theory of atoms in molecules (QTAIM) analyses helps to understand the description of interatomic interaction in the single crystal X-ray structure. A bond is defined along the bond line between two nuclei, called a bond path, along which electron density is concentrated. The (3, -1) bond critical point (BCP) is a point along the bond path at the interatomic surface, where the shared electron density reaches a minimum. (3, +1) ring critical point (RCP) and (3, +3) cage critical point (CCP) represents critical points in the ring and cage respectively where the electron density is minimum.

2.7.3.4. Symmetry Adapted Perturbation Theory (SAPT)

SAPT(0) analysis was employed to determine the non-covalent interaction energies of different non-covalent dimers of DMICE, BDMICE and IDMICE. The SAPT module of the psi4 code was employed, with def2-svp basis set. SAPT(0) calculations provide the contributing components of interaction energy. The results obtained from SAPT(0) analysis is a second order perturbation expansion constituting first order electrostatic and exchange energy parts and second order dispersion, induction and their exchange counterparts as the perturbation terms.

$$E_{int}^{SAPT(0)} = E_{elc}^{(1)} + E_{ex}^{(1)} + E_{ind}^{(2)} + E_{ind-ex}^{(2)} + E_{dis}^{(2)} + E_{dis-ex}^{(2)} \qquad \text{(Equation A2.1)}$$

2.7.3.5. TheoDORE Analysis

The excitations of the different dimers obtained from the crystal structure were analysed using TheoDORE. We study dimer systems, where each of the monomers is considered as a fragment. The parameters used to investigate the excited state characteristics are participation ratio (PR), mean position (POS) of initial orbital (hole) and final orbital (electron), and charge transfer character (CT). The magnitude of PR relates to the number of fragments participating in the excitation; hence, in our investigation, the PR ranges from 1 to 2. POS provides the mean position of hole and electron for a particular excitation. Charge transfer states and delocalized Frenkel states show POS = 1.5. If the Frenkel state is localized on monomer A, then POS = 1, and if localized on monomer B, POS = 2, for a dimer AB. Finally, CT is related to the total weight of configurations where initial and final orbitals are situated on different fragments. A CT value of 1 denotes the presence of a charge-separated state, and CT = 0 refers to Frenkel states.

2.7.3.6. Electronic Coupling Calculations

All the calculations are carried out in Gaussian 16 employing the ωB97XD functional and 6-311G+(d,p) basis set at DFT level of theory unless stated otherwise. In order to compute long range Coulombic coupling, electronic energy transfer (EET) module available in gaussian 16 program is utilized. Electronic energy transfer (EET) or resonance energy transfer (RET) refers to the process of energy transfer from a photoexcited donor molecule to a nearby ground-state acceptor molecule. In Gaussian 16, the EET analysis employs a quantum mechanical model

based on a DFT description of the wavefunction, incorporating a time-dependent variational approach. This involves performing an excited-state calculation on each fragment and subsequently computing all the couplings among the resulting states. J_{Coul} is the Coulombic coupling between electronic transitions where,

$$J_{Coul} = \iint dr_1\, dr_2\, \frac{\rho_D^{tr*}(r_1)\rho_A^{tr}(r_2)}{|r_1 - r_2|} \qquad \text{(Equation A2.2)}$$

Where, $\rho_D^{tr}(r_1)$ and $\rho_A^{tr}(r_2)$ are the transition densities (the diagonal element of the density matrix) respectively of donor and acceptor. TD-DFT calculation was performed on each of the dimers after defining each monomer as a fragment for the S_0 to S_1 transition and Coulombic coupling between the states was procured.

Electron and hole transfer coupling values were calculated by employing the CATNIP Tool version 1.9. CATNIP uses post-processed Gaussian 16 output files for the respective analyses. The short-range exciton coupling stemming from the degree of overlap of wave functions on proximal molecules has a crucial role in defining the excitonic interaction and is determined as,

$$J_{CT} = \frac{-2t_e t_h}{E_{CT} - E_{S_1}} \qquad \text{(Equation A2.3)}$$

where t_e and t_h are the electron and hole-transfer coupling which depend on the LUMO–LUMO and HOMO–HOMO orbital overlap of the monomers, respectively, E_{CT} is the energy of the charge-transfer state, and E_{S1} is the energy of first Frenkel exciton state calculated from TD-DFT. The total coupling between neighbouring molecules can be represented as,

$$J_{Total} = J_{Coul} + J_{CT} \qquad \text{(Equation A2.4)}$$

Chapter 3

Exciton Coupling and Structural Disorder Governing Photoprotection in Eumelanin Multimers

Abstract

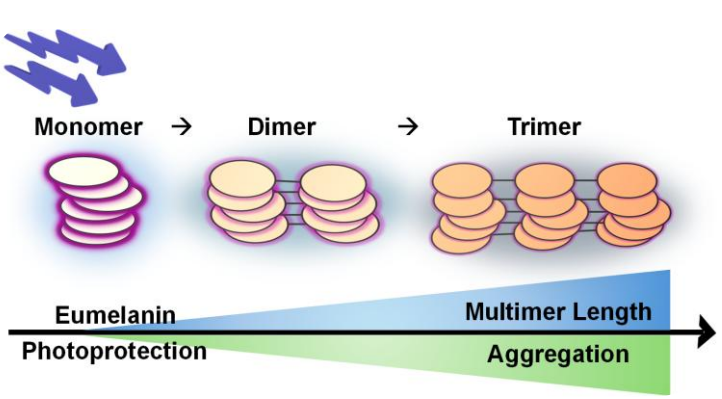

Eumelanin, a ubiquitous pigment in animals, is known for its ability to protect against UV-induced damage by efficiently dissipating energy as heat. Despite its importance, the mechanisms underlying eumelanin's broadband absorption and ultrafast energy relaxation remain unclear, primarily due to the inherent structural complexity of the pigment. To address this, we employed model eumelanin multimers, including a monomer (DMICE), dimer (DMICE-D), and trimer (DMICE-T), and investigated their optical properties in both solution and aggregated thin films. Our results reveal that increasing multimer size and aggregation significantly broaden the absorption spectrum, a phenomenon attributed to amplified excitonic interactions. The non-radiative decay processes, governed by internal conversion and intersystem crossing, become increasingly efficient as the multimer lengthens. In thin films, the dimer and trimer exhibit ultrafast excited state relaxation (<30 picoseconds), driven predominantly by internal conversion, which closely parallels eumelanin's characteristic ultrafast energy dissipation. By quantifying the exciton interactions within the multimers, we uncover the interplay of coulombic and charge-transfer couplings in modulating the observed optical behaviour. This work provides insights into how structural organization and excitonic interactions contribute to eumelanin's unique photophysical properties and its photoprotective role, thereby advancing development of eumelanin-inspired biomimetic materials.

3.1. Introduction

Eumelanin, the most abundant type of melanin in nature, serves as a vital photoprotective pigment in animals.[94] It absorbs throughout the UV-visible range of light and dissipates the absorbed energy non-radiatively to protect tissues from harmful UV-induced damage. Despite its critical biological function, the underlying structural factors that govern eumelanin's broadband UV-visible absorption and ultrafast energy dissipation remain poorly understood.[6, 75] The inherent instability and rapid polymerization of eumelanin monomers to form the insoluble black pigment hinder detailed characterization of its molecular and aggregated structures.[6, 75] An intricate understanding of the broadened absorption and energy dissipation mechanism in eumelanin is essential for designing synthetic materials that replicate eumelanin's unique photoprotective properties.[75] Two prominent models have been proposed to explain eumelanin's broadband absorption and unique optical properties. The chemical disorder model attributes the absorption broadening to a superposition of absorption bands from a diverse pool of oligomers with varying lengths, structures, and oxidation states.[59] In contrast, the geometric disorder model highlights the role of excitonic coupling between stacked molecular units in aggregates, suggesting that these interactions contribute significantly to the pigment's spectral properties.[63]

Recent advances in mass spectrometry,[132] X-ray diffraction,[133] atomic force microscopy,[89, 96] and computational calculations[2, 95, 134] have increasingly supported that shorter multimers dominate eumelanin's composition.[74, 100, 135-137] A careful bottom-up approach through the synthesis of stable eumelanin multimers and ordered aggregates of multimers is crucial to disentangle the contributions of chemical and geometric disorder to eumelanin's optical behaviour (Table A3.1).[10, 90, 91, 93, 138] In this context, chemical disorder encompasses variations in multimer length, functionalization, and connectivity among indole-based oligomers, while geometric disorder refers to differences in their spatial arrangement and intermolecular interactions within the aggregated state.[1, 59] Herein, we designed and synthesized chemically stable eumelanin model systems using a blocked derivative of 5,6-dihydroxyindole carboxylic acid (DHICA), namely 5,6-dimethoxyindole carboxylic acid ethyl

ester (DMICE). DMICE serves as a simplified and chemically well-defined analogue of the precursor of eumelanin.

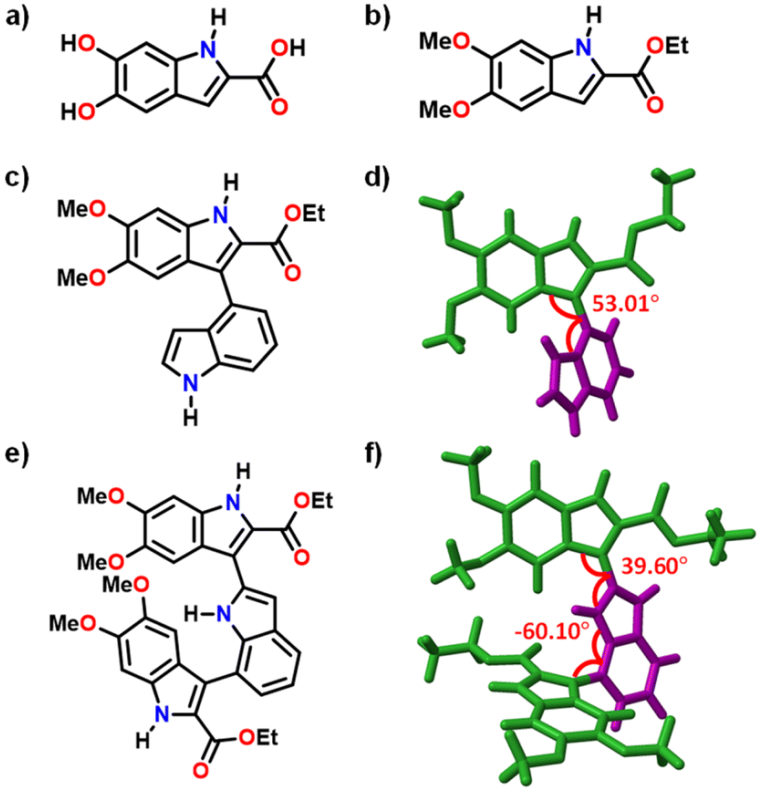

Figure 3.1: Molecular structures of a) DHICA, b) DMICE and c) DMICE-D; d) crystal structure of DMICE-D; e) molecular structure of DMICE-T and f) optimized structure of DMICE-T.

Blocking the hydroxyl and carboxylic acid groups prevent the fast polymerization of the monomer resulting in a benchtop stable molecule aiding further syntheses and experiments.[107] Alkyl protection suppresses excited-state proton transfer (ESPT) and complex photochemistry in these molecules, enabling access to slower alternative relaxation pathways and offering versatile models for disentangling the excited-state dynamics of eumelanin.[69, 70, 73, 75] As the most probable polymerization sites on the indole ring are the second, third and seventh carbons,[112] we consider a heterodimer (DMICE-D) linked at C3 and C4 and a heterotrimer (DMICE-T) with two DMICE subunits connected at the C2 and C7 positions (Figures 3.1 and A3.1). These stable model multimers represent the key intermediates in

eumelanin biosynthesis and allow us to systematically explore their photophysical properties in monomeric and aggregated states (Figure A3.2). The steady-state and time-resolved spectroscopic features of DMICE, DMICE-D, and DMICE-T are explored to understand how multimer length and aggregation modulates the absorption spectrum as well as the efficiency of non-radiative decay, thereby enhancing photoprotection.

3.2. Results and Discussion

3.2.1 Synthesis and Structural Elucidation

Novel DMICE-T was synthesized through Suzuki coupling of iodinated DMICE with indole-2,7-boronic acid pinacol ester, using XPhos Pd G2 as the catalyst and 1,4-dioxane as the solvent at 75 °C, resulting in moderate yields of the product. Similarly, DMICE-D was synthesized by coupling with indole-2-boronic acid, producing good yields (Figures 3.3-3.9).[139] Upon slow evaporation of a chloroform solution of DMICE-D layered with *n*-hexane, high-quality colourless single crystals suitable for X-ray crystallography were obtained. The crystal structure of DMICE-D, determined *via* single-crystal X-ray diffraction, confirmed its molecular structure (Figure 3.1). DMICE-D crystallized in a monoclinic crystal system with a space group of $P2_1/c$ and exhibited a dihedral angle of ∼53° (Figure 3.1 and Table A3.2). Geometry optimizations at multiple DFT levels showed comparable results with the crystal structure, with ωB97X-D/6-311G+(d,p) giving the closest agreement (Table A3.3). The optimized geometry of DMICE-D revealed a dihedral angle of ∼54°, consistent with the angle determined by single-crystal X-ray diffraction (Figure A3.10). For DMICE-T, the optimized structure indicated a dihedral angle of 39.60° between the first DMICE subunit and the indole ring, and −60.10° between the second DMICE subunit and the indole ring (Figure 3.1 and Table A3.4).

3.2.2 Optical Properties

The electronic properties of DMICE, DMICE-D, and DMICE-T in toluene were explored through UV-visible absorption spectroscopy, fluorescence emission spectroscopy, and time-correlated single photon counting measurements (TCSPC), as illustrated in Figure 3.2. The

electronic absorption spectrum of DMICE in toluene revealed an absorption maximum at 325 nm, which exhibited good similarity to the absorption characteristics of the unsubstituted DHICA, as previously reported.[107] This ascertains that DMICE serves as an excellent model for eumelanin monomer, offering the added advantage of benchtop stability, which is a crucial factor considering the fast oxidative polymerisation into eumelanin. Interestingly, the dimer DMICE-D displayed only slight differences in its absorption spectrum when compared to that of the monomer DMICE, suggesting that the dimer retains many of the electronic characteristics of the monomer. In contrast, DMICE-T demonstrated a more complex absorption profile, displaying a prominent absorption band with a maximum at 331 nm alongside a tail band observed till 420 nm. The observed broadening in the absorption spectra of the trimer, when compared to the dimer and monomer, demonstrates that an increase in the number of connected units leads to a decrease in the excitation energy of the molecule.

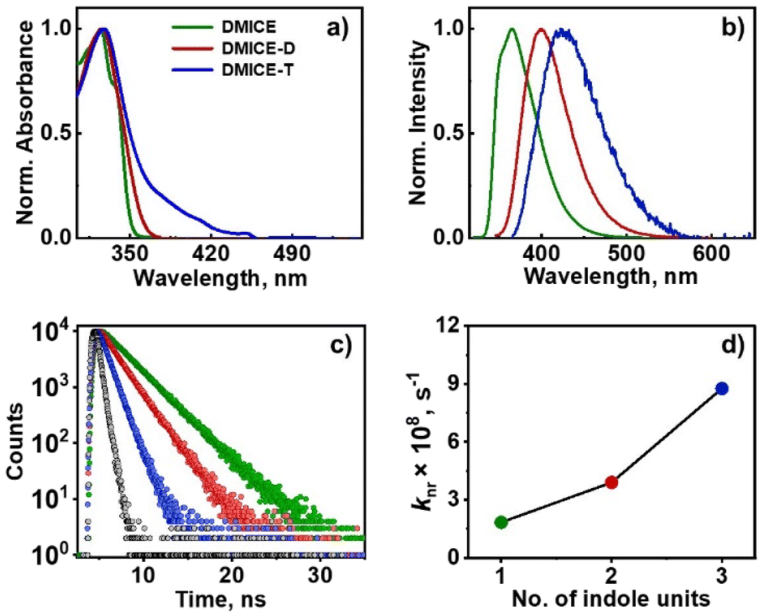

Figure 3.2: a) Normalized UV-vis absorption spectra; b) normalized emission spectra; c) time-resolved fluorescence decay profile of DMICE29 (green line), DMICE-D (red line) and DMICE-T (blue line) in toluene at room temperature; d) knr plotted against the number of indole units from n = 1, 2 and 3.

Table 3.1: Spectral and photophysical parameters of DMICE, DMICE-D and DMICE-T in toluene.

Compound	λ_{abs}[a] (nm)	λ_{emi}[b] (nm)	ϕ_f[c] (%)	τ_{fl}[d] (ns)	k_r[e] × 10^8 (s^{-1})	k_{nr}[f] ×10^8 (s^{-1})	λ[g] (eV)
DMICE	325	365	49.7±0.5	2.72±0.08	1.82±0.01	1.84±0.01	0.227
DMICE-D	326	400	27.5±0.9	1.86±0.11	1.48±0.01	3.90±0.03	0.350
DMICE-T	331	425	13.6±2.0	1.02±0.16	1.33±0.03	8.76±0.03	0.404

[a] UV-visible absorption band maximum. [b] Fluorescence maximum. [c] Fluorescence quantum yield. [d] Fluorescence lifetime measured using TCSPC. [e] Radiative rate constant. [f] Non-radiative rate constant. [g] Reorganization energy.

Computed vertical excitation energies of DMICE, DMICE-D as well as DMICE-T also support the incremental lowering of the S_1–S_0 energy gap with increase in multimer length (Figure A3.11 and Table A3.5). This result underscores the significant influence of varying lengths of eumelanin oligomers and the consequent degree of chemical disorder on the overall electronic absorption spectrum of eumelanin.[140] Furthermore, the orientations of transition dipoles within individual units, along with the extent of conjugation, could play a crucial role in the observed bathochromic shift of the trimer relative to both the dimer and the monomer (explained *vide infra*). Upon photoexcitation, DMICE-D exhibited a fluorescence emission maximum centred at 400 nm, while DMICE-T showed a fluorescence emission maximum at 425 nm (Figures 3.2b and A3.12). This results in a significant bathochromic shift of ~3868 cm^{-1} for DMICE-T and ~2397 cm^{-1} for DMICE-D, compared to the monomeric DMICE (Table 3.1). The fluorescence quantum yields, determined using a relative method, revealed a marked decrease as the molecular complexity increases from DMICE to DMICE-D and further to DMICE-T. Specifically, DMICE displayed a fluorescence quantum yield (ϕ_f) of 49.3%, which declined to 27.5% for DMICE-D and further to 13.6% for DMICE-T, demonstrating the impact of multimer length on fluorescence efficiency. The fluorescence quantum yield (ϕ_f) is defined as the ratio of the radiative rate k_r to the sum of both radiative and non-radiative rates, $k_r + k_{nr}$.[141] On examining the time-resolved fluorescence decay profiles of DMICE in toluene, a mono-exponential decay pattern with a lifetime of 2.72 ns was observed. In comparison, DMICE-D showed a reduced fluorescence lifetime of 1.86 ns, while DMICE-T

exhibited a shorter fluorescence lifetime of 1.02 ns, indicating a substantial decrease in fluorescence lifetimes as we move from the monomer to the dimer and trimer.

Given that the radiative rates remain almost constant across the series, the observed variations in fluorescence rates are primarily linked to changes in non-radiative rates, as shown in Table 3.1. The non-radiative rate constant, k_{nr}, shows an increase as the number of indole units increases (Figure 3.2d). As the number of indole units increases from monomer to dimer to trimer, the non-radiative decay channels for dissipating excitation energy become more efficient in the eumelanin counterparts.[142] The observed increase in k_{nr} with the addition of indole units is also driven by elevated reorganization energy suggesting that structural relaxation plays a dominant role in driving the observed k_{nr} trend (Table 3.1).[143] This trend is reflected in both the fluorescence quantum yields and fluorescence lifetimes across these molecular species (Table 3.1). Eumelanin precursors undergo multiple excited state decay pathways, including ESPT,[69, 70, 75] electron injection,[69, 78] intersystem crossing,[82] and charge transfer.[30, 77] Previous literature on DHICA and its oligomers reveal ultrafast sub-picosecond decay in acidic buffers driven by ESPT, with fluorescence decay rates independent of subunit coupling.[68] On the other hand, in protected derivatives like DMICE, where ESPT is blocked,[107] there is a dependence of the fluorescence lifetimes on oligomer length, allowing the deconvolution of non-radiative decay pathways beyond ESPT.

Further, the influence of the local dielectric environment on the excited state optical properties of eumelanin multimers were investigated through solvent-dependent UV-visible absorption and fluorescence measurements (Table A3.6). The UV-visible absorption spectra of DMICE-D and DMICE-T remained largely similar in toluene (TOL, $\varepsilon = 2.38$) and acetonitrile (ACN, $\varepsilon = 37.5$), exhibiting minimal shifts in λ_{abs}. In contrast, the fluorescence spectra showed significant solvent-dependent differences with respect to fluorescence maxima as well as fluorescence quantum yields (Figures 3.3f and A3.13). A notable red shift in the emission wavelength (λ_{emi}) was observed when changing the solvent from TOL to ACN, with shifts of ~1852 cm^{-1} for DMICE-D and ~1503 cm^{-1} for DMICE-T. Additionally, the fluorescence quantum yield (ϕ_f) decreased substantially in ACN compared to TOL, with values of 17.5% for DMICE-D and 4.6% for DMICE-T, both drastically lower than the ϕ_f of DMICE.[107] The

solvent-dependent variations in fluorescence quantum yields and red shifts in emission wavelengths strongly suggest the role of charge-transfer states in the excited state dynamics of DMICE-D and DMICE-T.[144, 145]

In the oligomeric scaffolds investigated, individual indole units are connected through single C–C bonds, positioning them in close proximity to enable electronic interactions and excited state delocalization across multiple subunits.[30, 68] The structural proximity within indole units provides a foundation for investigating how excitonic interactions within each unit contribute to the electronic properties observed in the dimer and trimer. To examine this, the long-range electronic coupling between the indole units was quantified (Figures A3.14 and Tables A3.7 and A3.8), providing insight into the spectral characteristics of these oligomers. In the case of DMICE-D, the long-range electronic coupling was calculated to be $-3.2\ cm^{-1}$, which is small enough to indicate a minimal impact on the electronic spectrum of the dimer. This minimal coupling supports the similarity of the dimer's absorption spectrum with respect to that of the monomer, without significant shifts in wavelength or spectral broadening. However, for the trimer DMICE-T, the calculated long-range electronic coupling was $-138.7\ cm^{-1}$, a considerably higher value indicative of the relatively larger red-shifted absorption in the UV-visible absorption spectrum. This increased coupling in the trimer correlates with a modest red shift in the absorption spectrum, leading to slight extension into the visible region—unlike the dimer, whose absorption remains largely confined to the UV.

While DMICE-D as well as DMICE-T exhibits limited absorption in the visible range, higher-order and more conjugated oligomers are expected to display red-shifted features that better approximate eumelanin's broadband spectrum. The transition dipole moments for the $S_0 \rightarrow S_1$ transitions for DMICE, DMICE-D and DMICE-T are also shown as Figures A3.15–A3.17. The dihedral angle between the two units, and consequently their transition dipoles, significantly influences the minimal red-shifts observed for DMICE-D. The simulated electronic absorption spectrum shows an incremental red-shift with changes in the orientation between the units in DMICE-D (Figures A3.18 and A3.19). Additional examples of geometrically optimized homo-dimer and linear trimer of DMICE exhibit minimal red-shifts, underscoring the combined effect of multimer length, connectivity, functional groups and

transition dipole orientations in determining the absorption spectra for the eumelanin-based systems (Figures A3.20 and A3.21). These observations reinforce that both transition dipole alignment and conjugative interactions contribute significantly to the broadening and shifting of the electronic absorption spectrum, particularly as molecular complexity increases.[140] Additionally, excited-state calculations on a geometry-optimized homodimer of DMICE reveal similar charge-transfer character, indicating that such behaviour is not exclusive to the heterodimer architecture (Figure A3.22).

3.2.3. Eumelanin Multimer Aggregates

After confirming the distinct spectroscopic differences between DMICE, DMICE-D and DMICE-T at monomeric concentrations (~5 μM), we extended our investigation to the molecular systems in aggregated conditions. To gain insights into the optical properties in aggregated conditions, 1 mM solutions of DMICE, DMICE-D and DMICE-T were drop-casted on cleaned quartz substrates, following which the UV-visible absorption spectra and fluorescence were monitored.[145] Figure 3.3 displays the absorption and emission spectra of DMICE-D and DMICE-T in non-aggregated state (5 μM solution in TOL) as well as in aggregated state (thin film). A significant change in the absorption and fluorescence spectra with respect to solution and film indicates aggregate formation. In solution, DMICE-D exhibited an absorption spectrum spanning till 375 nm with absorption peak maximum at 325 nm. In contrast, the thin film of DMICE-D displayed a broadened band with significant absorption till 406 nm and tailing towards 480 nm, reflecting the intermolecular interactions resulting in aggregate formation. Similarly, for DMICE-T, the absorption spectra in TOL showed a maximum at 331 nm, while the absorption spectrum for the thin film demonstrated a broadened, red-shifted absorption band featuring till 500 nm. The distinct differences in both DMICE-D and DMICE-T at low concentrated solutions *versus* thin films suggest the excitonic coupling within the aggregates, leading to new, close-lying electronic energy states.

To determine if aggregation was unique to DMICE-D and DMICE-T, we also examined the thin film of DMICE. In solution (5 μM in TOL), DMICE showed an absorption maximum at 325 nm, while in thin film, a broadened band emerged in the absorption spectrum featuring

till 390 nm (Figure A3.23).[107] This broadening and red-shift in spectral characteristics in film indicates that exciton interactions may be occurring in DMICE, DMICE-D, and DMICE-T in aggregated forms. Significant decrease in the fluorescence yields and fluorescence lifetimes is also observed in the thin films. The absolute fluorescence quantum yields for the thin-film samples are estimated to be 8.9%, 3.8%, and 2.3% for DMICE, DMICE-D, and DMICE-T, respectively. Such spectral changes, characterized by new excitonic states and aggregation-caused quenching, are commonly observed in molecular aggregates and photosynthetic pigments, where aggregation introduces new electronic interactions depending on molecular arrangement and interaction strength, impacting their optical properties.[51, 146]

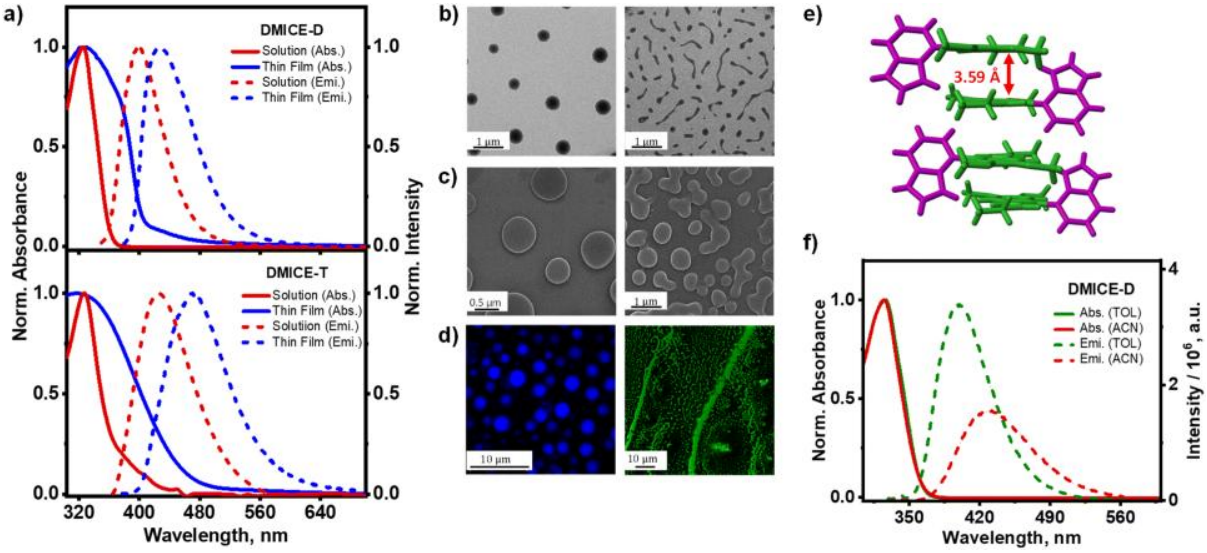

Figure 3.3: a) Normalized absorption and emission spectra of solution and thin film aggregates of DMICE-D (top) and DMICE-T (bottom) at room temperature; b) TEM, c) SEM, d) confocal fluorescence images of DMICE-D (left) and DMICE-T (right); e) crystal packing of DMICE-D exhibiting alternate distichous assembly; f) normalized absorption and emission spectra of DMICE-D in TOL (green line) and ACN (red line). Note: the solution-phase data in TOL from figure 3.2 are included here for ease of comparison.

To investigate the morphology of aggregates formed by DMICE, DMICE-D, and DMICE-T, transmission electron microscopy (TEM), scanning electron microscopy (SEM), and confocal microscopy imaging were performed (Figure 3.3).[147, 148] The TEM and SEM

images revealed that DMICE-D forms aggregates with a distinct disk-like morphology with diameters ranging from 0.4 to 0.6 μm (Figure A3.24). In contrast, DMICE-T aggregates displayed an elongated, fibre-like morphology, arising from the assembly of smaller, disk-like substructures (Figure A3.25). Confocal microscopy further confirmed the fluorescent nature of these aggregates, corroborating the disk-like structure of DMICE-D and the extended fibre formation observed in DMICE-T. For comparison, DMICE aggregates were also examined. Unlike DMICE-D and DMICE-T, DMICE showed a lamellar morphology, characterized by structures with an average length of 15–20 μm, as observed in both SEM and confocal fluorescence microscopy (Figures A3.26 and A3.27). Recent studies on allomelanin (fungal melanin) dimers underscore the value of morphology in understanding molecular assemblies and show that hydrogen bonding and π–π stacking drive aggregate formation and guide microstructure formation.[149, 150] This structural diversity aligns with previously reported observations of morphological heterogeneity in eumelanin pigments, which exhibit a range of aggregate forms, including spherical, rod-like, hollow-rod, and hollow-platelet structures.[22, 151-153]

3.2.4. Excited State Energy Dissipation of Monomer versus Aggregates

To investigate the excited state relaxation mechanisms responsible for non-radiative decay in the eumelanin multimers, femtosecond transient absorption (fsTA) measurements were performed (experimental details in Appendix). Figure 3.4 presents the fsTA spectra and corresponding deconvoluted time constants for DMICE-D in TOL (Figure 3.4a) and ACN (Figure A3.29). Upon photoexcitation of DMICE-D in TOL at λ_{exc} = 320 nm using a 100 fs pump pulse, a distinct positive absorption feature emerges between 450 and 700 nm, resembling the singlet absorption previously reported for DHICA and DMICE (Figure 3.4a).[75, 87, 107] Evolution-associated spectra (EAS) for DMICE-D in TOL were derived through global fitting of the fsTA data in a time-wavelength framework, modelled as a sequential A → B → C → GS (ground state) process. The spectral deconvolution reveals three components: the first component (A), attributed to internal conversion from the excited singlet state, decays with a time constant of τ_1 = 6.7 ps. The second component (B), red-shifted by 5 nm relative to component A, decays with a time constant of τ_2 = 2.43 ns. The decay time constant of

component B matches closely to the fluorescence lifetime, ascertaining it to be the S_1 excited state decay. With the decay of the S_1 state, a non-decaying species at 440–490 nm persists, with a decay time constant of $\tau_3 > 4$ ns. The overlay of fitted traces *versus* experimental traces along with the deconvoluted species for DMICE-D in TOL are presented in Figure A3.30. The fsTA spectra of DMICE-D in polar solvent ACN also demonstrates similar spectral traces but different decay constants. In ACN, DMICE-D initially exhibits a well-defined absorption feature across 450–700 nm (Figure A3.29). This evolves within few picoseconds to populate a second species in the same wavelength range, followed by a persistent band at ~440 nm. Spectral deconvolution reveals that the first component (internal conversion) decays within τ_1 = 3.7 ps, subsequently populating the second component (S_1 decay), which decays with a time constant of τ_2 = 2.18 ns. As observed similar for DMICE-D in TOL, DMICE-D in ACN also revealed a consequent, long-lived species (>4 ns).

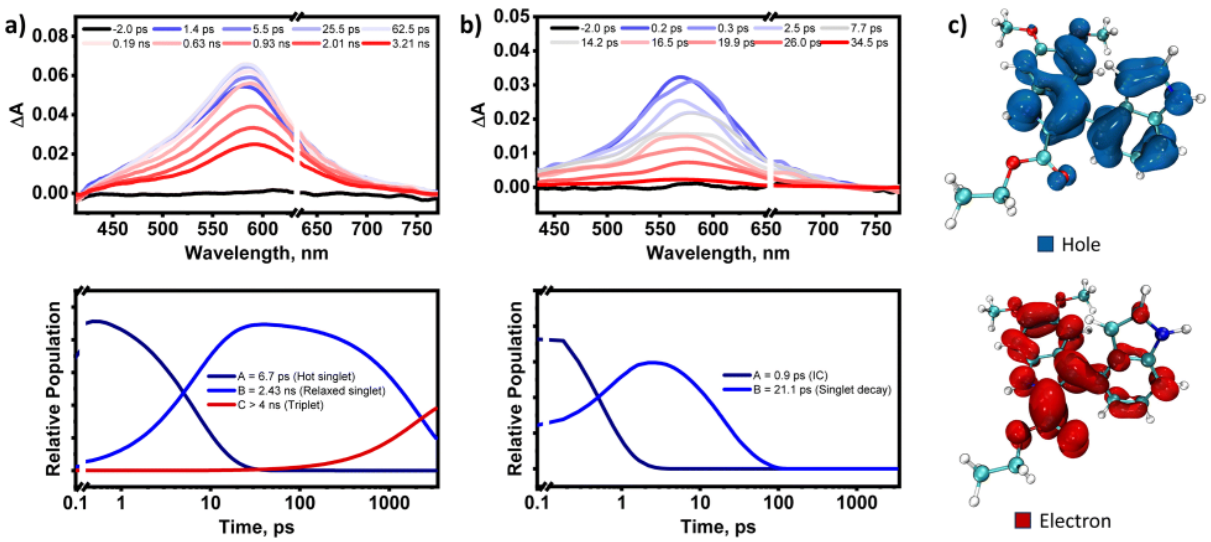

Figure 3.4: a) (Top) Femtosecond transient absorption (fsTA) spectra of DMICE-D in TOL; (bottom) relative population of the two components extracted from sequential global fitting; b) (top) fsTA spectra of neat film of DMICE-D; (bottom) relative population of the two components extracted from sequential global fitting; c) hole and electron iso-surface plots of DMICE-D at the S_1 state.

The solvent-dependent kinetics of the excited state species as observed from fsTA, along with steady-state fluorescence, reveals a partial charge-transfer (CT) character of the S_1 state. The hole–electron iso-surfaces of the S_1 state for the dimer also corroborate the experimentally observed partial charge-transfer nature, with the hole delocalized across both units and the electron localized within the DMICE unit of DMICE-D (Figure 3.4c). In contrast, the S_2 state exhibits Frenkel exciton character, with both the hole and electron confined to the DMICE unit of the dimer (Figure A3.31). This aligns with recent findings emphasizing the role of CT states in the excited state deactivation pathways of eumelanin and related systems.[30, 77, 128] The CT character of S_1 likely facilitates the formation of triplet states *via* intersystem crossing (ISC) as observed in several examples of organic chromophores like aromatic aldehydes.[154-156] Nanosecond transient absorption (nsTA) measurements corroborate the presence of a long-lived species at 420–470 nm with a lifetime of 1.2 μs in TOL and 0.8 μs in ACN, further confirming ISC *via* the S_1 state (Figures A3.32 and A3.33). Analysis of the natural transition orbitals (NTOs) for the S_1 state and the near-degenerate T_5 state shows a change of orbital character from $n\pi^*$ character to $\pi\pi^*$ character involving the non-bonding orbitals from the carbonyl group (Figure A3.34 and Table A3.10), following El-Sayed's rule.

Prior investigations on unprotected DHI and DHICA oligomers have predominantly utilized fluorescence-based approaches, wherein excited-state proton transfer (ESPT) emerged as a principal relaxation pathway.[68, 71, 84] However, the presence of free hydroxyl groups in the molecules facilitated rapid polymerization and the *in situ* generation of photoactivated species, complicating a comprehensive interpretation of the excited-state landscape. Consequently, phenomena such as charge transfer and intersystem crossing remained largely unexplored, likely obscured by the predominance of ESPT-mediated processes. The fsTA spectra of DMICE-T in TOL closely resemble those of DMICE-D, with notable differences in decay constants. Upon photoexcitation at 320 nm, a distinct positive absorption feature between 450 and 700 nm, characteristic of singlet absorption, is observed (Figure A3.35). Spectral deconvolution identifies two components in the initial timescales followed by a consequent non-decaying component: the first component is attributed to internal conversion to the S_1 state and decays with a time constant of τ_1 = 7.4 ps. The second component, that is, S_1 decay occurs with a longer time constant of τ_2 = 0.98 ns. The similarity in excited state spectra and multi-

component decay dynamics between DMICE-D and DMICE-T highlights their comparable deactivation pathways. In ACN, the fsTA spectra of DMICE-T exhibit similar features to those in TOL, with spectral deconvolution revealing an initial relaxation time constant of τ_1 = 3.3 ps. The relaxed singlet state decays faster in ACN, with a time constant of τ_2 = 0.34 ns (Figure A3.36). These differences in decay kinetics across solvents may be influenced by the chromophore size and the extent of electronic coupling between individual indole units in the multimers.[30]

Like observed in the dimer, the iso-surface analysis of the S_1 state of the trimer also reveals prominent CT exciton characteristics, with the hole distributed across the indole and DMICE fragment and the electron confined to the same DMICE unit. The S_2 state also exhibits CT exciton behaviour (Figure A3.37), while the higher excited state S_3 demonstrates Frenkel exciton character (Figure A3.38). Consistent with the observations for DMICE-D, nsTA measurements confirm the presence of triplet excited states at 420–470 nm for DMICE-T, with a lifetime of 1.3 μs and 0.7 μs, in TOL and ACN respectively (Figures A3.39 and A3.40). The NTO analysis further supports the orbital character change from ππ* to nπ* in the S_1 state and near-degenerate T_6 state, facilitating ISC (Figure A3.41 and Table A3.10). A summary of the evaluated decay rate constants for the eumelanin multimers in TOL and ACN are presented in Tables A3.11 and A3.12.

Having established the excited state decay channels of the multimers in monomeric state, we explore the excited state dynamics of the multimers in the aggregate state. Femtosecond transient absorption (fsTA) measurements were conducted on thin films of DMICE, DMICE-D, and DMICE-T following photoexcitation at 320 nm to investigate the excited state dynamics of excitonically coupled multimers in the solid state. Thin films were prepared by coating $CHCl_3$ solutions of the samples onto cleaned quartz substrates (see Appendix for details). The fsTA spectra of the DMICE-D thin film exhibited an excited state absorption (ESA) feature spanning 440–700 nm, closely resembling the singlet absorption signature of the molecule in solution (Figure 3.4b). Spectral deconvolution was modelled using a sequential kinetic scheme (A → B → GS, where GS represents the ground state; Figure A3.42). The initial decay component, characterized by a time constant of τ_1 = 0.9 ps, is

attributed to internal conversion between excitonically coupled singlet states. This rapid decay is followed by a slower relaxation process, with a time constant of τ_2 = 21.1 ps, representing internal conversion to the ground state. In contrast to the monomeric state of DMICE-D, which exhibits singlet decay within ~2 ns, the aggregate state demonstrates significantly faster singlet decay, occurring within <30 ps. Although excimer formation or defect-state trapping could potentially account for the observed picosecond decay in the thin films, these pathways are deemed unlikely given the absence of broad, featureless excited state absorption and red-shifted emission characteristic of excimer states.[157-159]

The involvement of higher-order processes such as singlet–singlet annihilation or non-radiative Förster energy transfer, were ruled out based on fluence-dependent measurements, which showed no significant changes in spectral features or kinetic decay profiles in the thin films with increasing pump fluence (Figure A3.43).[75, 160, 161] This behaviour parallels observations in eumelanin material, where ultrafast internal conversion occurs *via* localized excitonic coupling without evidence of exciton migration or annihilation.[75] The absence of long-lived triplet excited states in the thin films is notable, hinting at similarities with eumelanin's ultrafast relaxation dynamics (Figure A3.44). Triplet states in biomolecules like eumelanin are undesirable because they can generate reactive oxygen species (ROS), causing oxidative damage and phototoxicity.[162] These findings highlight the pronounced influence of excitonic coupling on the excited state dynamics of eumelanin-like systems in the solid state, offering critical insights into their photophysical behaviour under aggregated conditions.

In the thin film, fsTA spectra of DMICE-T also initially exhibited a well-defined absorption feature across 450–700 nm. This excited state species evolved within hundreds of femtoseconds to populate a broader species in the same wavelength range (Figures A3.45 and A3.46). Spectral deconvolution reveals that the first component (singlet species) decays within τ_1 = 0.5 ps, subsequently populating the second component, which decays with a time constant of τ_2 = 19.3 ps. The ultrafast internal conversion from the S_1 state (within ps) in the thin films of both DMICE-D and DMICE-T dominate over the slower intersystem crossing observed for the eumelanin analogues in solution, thereby enhancing the potential photoprotective role of the aggregates. Excited state energy calculations also indicate a denser

manifold of closely spaced singlet excited states in DMICE-D and DMICE-T, which may facilitate faster internal conversion in the solid state, consistent with the observed rapid deactivation to the ground state (Table A3.5). For comparison, the fsTA of DMICE thin films was also measured. In the thin film, the fsTA spectra of DMICE display a distinct absorption feature spanning 450–700 nm, which evolves within a few picoseconds, transitioning into a broader spectral species within the same wavelength range (Figure A3.47). Spectral deconvolution reveals that the first component (singlet species) decays within τ_1 = 4.4 ps, subsequently populating the second component, which decays with a time constant of τ_2 = 122.5 ps. The biexponential excited state absorption (ESA) signals observed in the eumelanin multimer aggregates indicate ultrafast internal conversion (IC) between electronically coupled singlet states, followed by slower IC dynamics to the ground state (S_0).

Such ultrafast non-radiative decay, similar to the mechanisms observed in photoprotective compounds like DNA and RNA nucleobases, serves to minimize the potential for energy transfer or photochemical reactions. Time-resolved studies on nucleosides and single-stranded DNA have shown that their lowest singlet excited state decays within picoseconds *via* internal conversion to the ground state, driven by efficient non-radiative pathways.[163, 164] This behaviour, effectively replicated by the monomer, dimer as well as trimer aggregates, aligns with eumelanin's intrinsic photoprotective properties. Future studies employing advanced spectroscopic techniques may further elucidate excitonic coupling pathways in the aggregated films. The observed behaviour of DMICE-D and DMICE-T in monomeric and aggregate states highlight the interplay of intramolecular exciton interactions within the eumelanin multimers, along with intermolecular electronic coupling between states of varying energies in the solid-state aggregates. This duality aligns with eumelanin's complex excited state dynamics, where both intra- and inter-molecular effects contribute to its optical properties and photoprotective functions. By capturing these interactions in simplified model systems, our findings provide valuable insights into the fundamental processes at play in eumelanin.

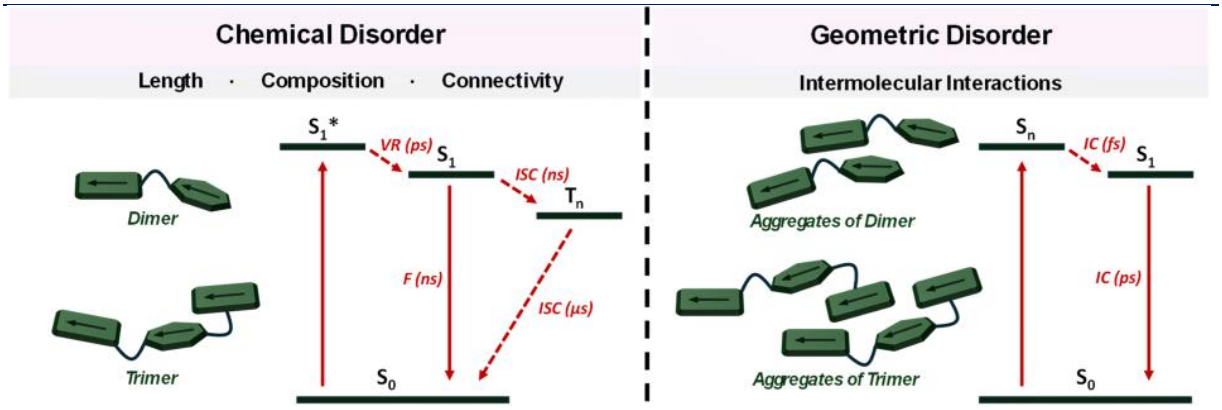

Figure 3.5: Energy deactivation profile of (left) monomeric forms of DMICE-D and DMICE-T; (right) aggregates of DMICE-D and DMICE-T (F = fluorescence, ISC = intersystem crossing, VR = vibronic relaxation, IC = internal conversion).

Figure 3.5 illustrates a schematic representation of the energy dissipation mechanisms within the chemically and geometrically disordered eumelanin multimers. The distinctive optical properties of eumelanin arise from its structural features, which combine elements of both chemical and geometric order and disorder. Chemical order–disorder refers to the defined molecular structure and resulting interactions within the moiety.[59] In contrast, geometric order–disorder enables strong excitonic coupling (J_{Coul} and J_{CT}) among eumelanin multimers through stacking, which disperses the electronic absorption across the exciton energy levels.[63] Heterogeneous stacking and diverse chromophore orientations are manifestations of structural disorder, which enhance excitonic coupling and facilitate non-radiative decay *via* internal conversion.[63] A comparison of the structural and photophysical features of DMICE-based multimers with respect to natural eumelanin is provided in Table A3.13. Table A3.14 highlights how chemical protection in DMICE-based systems enables identification of excited-state processes compared to unprotected DHI/DHICA oligomers. A comprehensive understanding of the involved interactions reveals the complexity and richness of eumelanin's optical properties, opening up new avenues for research into its potential applications in areas such as photonics and biomimetic materials.

3.3. Conclusion

In summary, we have synthesized and examined model eumelanin multimers in their monomeric, crystalline and aggregated films to decipher the origin of the unique photophysical properties of eumelanin. A significant decrease in the fluorescence quantum yield and fluorescence lifetime is observed in DMICE-T compared to DMICE-D and DMICE indicating that the non-radiative decay pathways are much faster and more efficient in the trimer than the dimer and monomer. Our spectroscopic investigations of eumelanin multimer aggregates reveal that chemical as well as geometric disorders are both crucial factors contributing to the broadened absorption and ultrafast energy dissipation of eumelanin. In solution, the multimers exhibit nanosecond-scale excited state lifetimes, driven by internal conversion and intersystem crossing. In contrast, excitonically coupled molecules in thin films demonstrate ultrafast excited state deactivation (<30 ps), dominated by internal conversion, mimicking eumelanin's ultrafast energy dissipation. These findings highlight the importance of structural order–disorder and excitonic interactions in modulating eumelanin's optical behaviour and photoprotection mechanisms, paving way for future innovations in sustainable energy, bioelectronics, and photoprotective coatings.

3.4. Experimental Section

3.4.1. Syntheses and Characterization

3.4.1.1. Synthesis and characterization of DMICE-D:

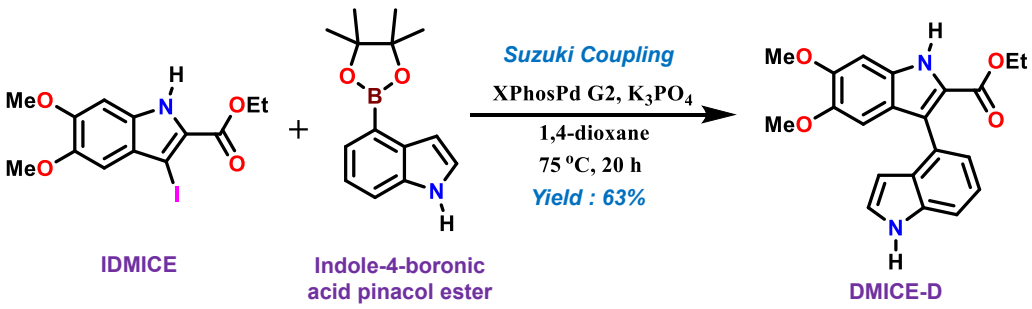

Scheme A3.1: The reaction scheme for the synthesis of DMICE-D.

The synthesis procedure follows the reported literature with minor modifications. To a Schlenk

tube added XPhosPd G2 (4 mol%, 0.0024 mmol), IDMICE (1 equiv, 0.06 mmol) and indole-4-boronic acid pinacol ester (1.25 equiv, 0.075 mmol), evacuated with vacuum and purged with N_2. 1,4-dioxane (0.66 mL) and 0.5 M K_3PO_4 (3 equiv, 0.18 mmol) were then added to the Schlenk tube. The reaction mixture was heated at 75° C for 20 h and quenched with the addition of H_2O. The crude mixture was extracted with EtOAc, dried with $MgSO_4$, filtered, and concentrated in vacuo. The product was purified via column chromatography (silica, hexanes: EtOAc: 3:2 to 2:1) to yield off-white powders of DMICE-D (63% yield; off-white solid).

^{1}H NMR (500 MHz, $CDCl_3$, ppm): δ = 8.92 (s, 1H), 8.23 (s, 1H), 7.44 (d, J = 7.8 Hz, 1H), 7.30 (m, 2H), 7.18 (s, 1H), 6.89 (d, J = 14.7 Hz, 2H), 6.31 (s, 1H), 4.14 (m, 2H), 3.97 (s, 3H), 3.75 (s, 3H), 1.00 (t, J = 7.1 Hz, 3H).

^{13}C NMR (125 MHz, $CDCl_3$, ppm): δ = 162.27, 150.41, 146.11, 136.00, 131.01, 128.08, 126.59, 123.90, 123.23, 122.22, 122.19, 121.73, 121.35, 110.28, 103.30, 102.66, 93.63, 60.52, 56.27, 56.24, 13.94.

HRMS (APCI) (m/z): Calculated for $C_{21}H_{21}N_2O_4$ $[M+H]^+$: 365.1496, found: 365.1486 $[M+H]^+$

Melting Point (°C): 129.6 °C

3.4.1.2. Synthesis and characterization of DMICE-T:

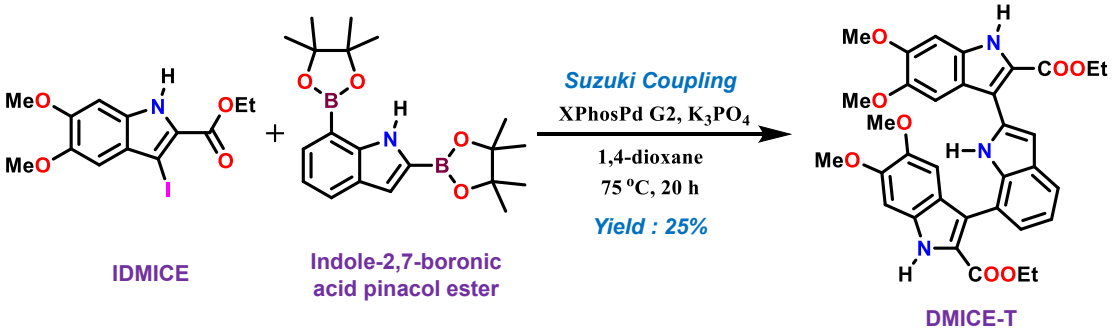

Scheme A3.2: The reaction scheme for the synthesis of DMICE-T.

To a Schlenk tube that is evacuated and purged with N_2, added XPhosPd G2 (4 mol%, 0.01084 mmol, 0.04 equiv), IDMICE (2.1 equiv, 0.569 mmol) and indole-2,7-boronic acid pinacol ester (1 equiv, 0.271 mmol), evacuated with vacuum and purged with N_2. 1,4-dioxane (6.26 mL) and

0.5 M K_3PO_4 (3 equiv, 0.813 mmol) were then added to the Schlenk tube. The reaction mixture was heated at 75 °C for 20 h and quenched with the addition of H_2O. The crude mixture was extracted with EtOAc, dried with $MgSO_4$, filtered, and concentrated in vacuo. The product was purified via column chromatography (silica, DCM:EtOAc : 100:1) to yield wheatish powders of DMICE-T (25% yield; wheatish solid).

^{1}H NMR (500 MHz, $CDCl_3$, ppm): δ = 11.25 (s, 1H), 9.13 (s, 1H), 8.78 (s, 1H), 7.74 (d, J = 7.8 Hz, 1H), 7.61 (s, 1H), 7.33 (d, J = 7.1 Hz, 1H), 7.24 (s, 1H), 7.16 (s, 1H), 6.98 (s, 1H), 6.92 (s, 1H), 6.83 (s, 1H), 4.26 (q, J = 7.1 Hz, 2H), 4.10 (m, 1H), 4.04 (s, 3H), 3.99 (dd, J = 10.5, 7.2 Hz, 1H), 3.95 (d, J = 3.1 Hz, 6H), 3.77 (s, 3H), 1.25 (t, J = 6.5 Hz, 3H), 0.76 (t, J = 7.1 Hz, 3H).

^{1}H NMR (500 MHz, $(CD_3)_2SO$, ppm): δ = 11.75 (s, 1H), 11.67 (s, 1H), 11.46 (s, 1H), 7.63 (m, 1H), 7.43 (s, 1H), 7.13 (m, 3H), 6.98 (d, J = 15.3 Hz, 2H), 6.77 (s, 1H), 4.20 (q, J = 6.9 Hz, 2H), 4.03 (dq, J = 14.2, 6.9 Hz, 1H), 3.90 (m, 1H), 3.87 (s, 3H), 3.83 (s, 6H), 3.62 (s, 3H), 1.18 (t, J = 7.0 Hz, 3H), 0.74 (t, J = 7.0 Hz, 3H).

^{13}C NMR (125 MHz, $CDCl_3$, ppm): δ = 162.31, 161.87, 151.05, 150.57, 146.90, 146.43, 135.46, 131.48, 131.35, 131.30, 128.77, 123.96, 122.85, 121.46, 120.16, 120.03, 119.66, 119.51, 119.49, 118.04, 116.69, 103.26, 102.32, 102.06, 93.76, 93.62, 61.55, 60.58, 56.57, 56.31, 56.25, 56.21, 14.36, 13.49.

HRMS (APCI) (m/z): Calculated for $C_{34}H_{32}N_3O_8$ $[M-H]^-$: 610.2195, found: 610.2187 $[M-H]^-$

Melting Point (°C): 239.1 °C

3.5. Additional Figures

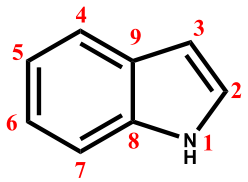

Figure A3.1: Structure of indole with the numbering of atoms.

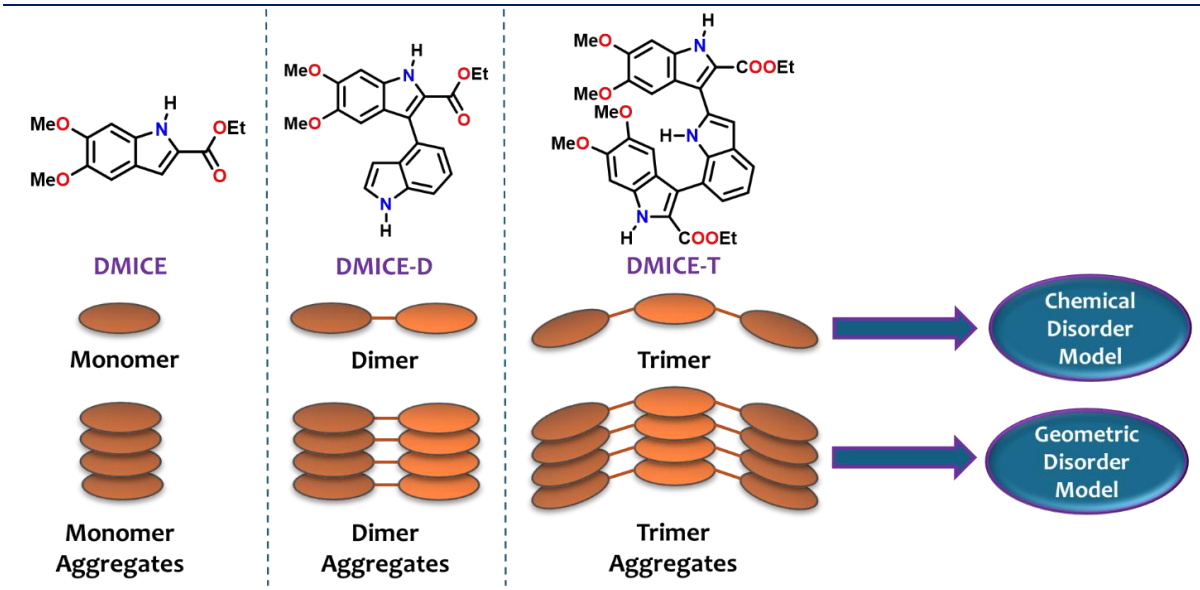

Figure A3.2: Schematic representation of our approach in understanding the influence of chemical and geometric disorder model through photophysical investigation of model eumelanin oligomers in solution, aggregate and crystalline states.

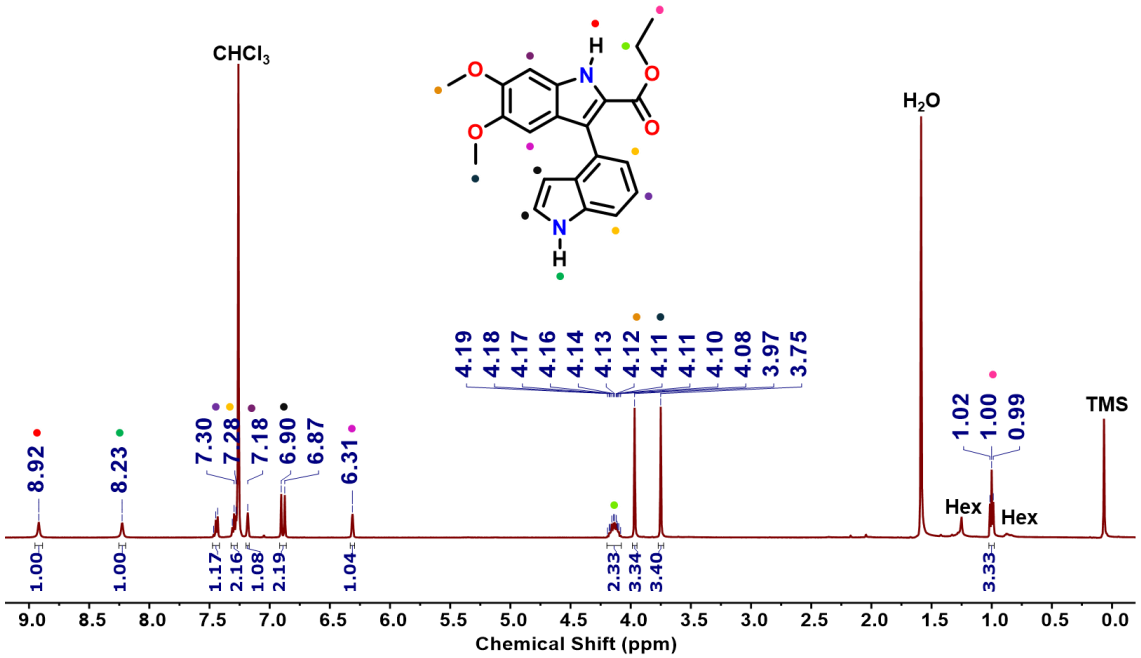

Figure A3.3: ^{1}H-NMR of DMICE-D in $CDCl_3$.

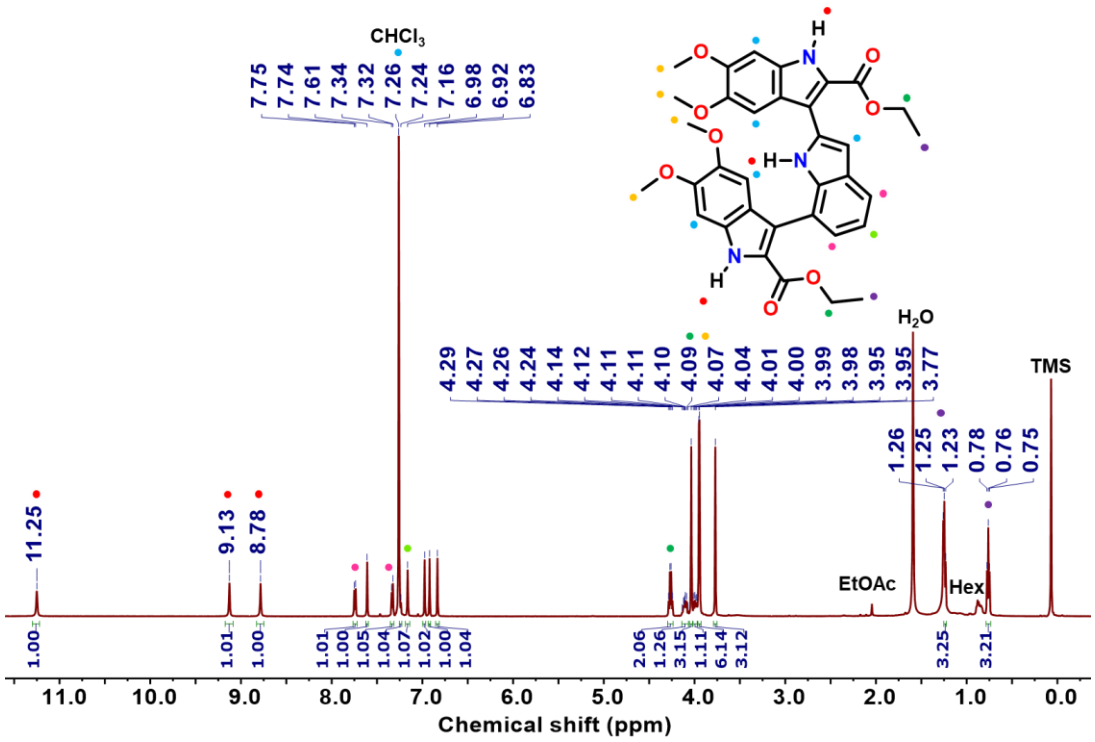

Figure A3.4: ^{1}H-NMR of DMICE-T in $CDCl_3$.

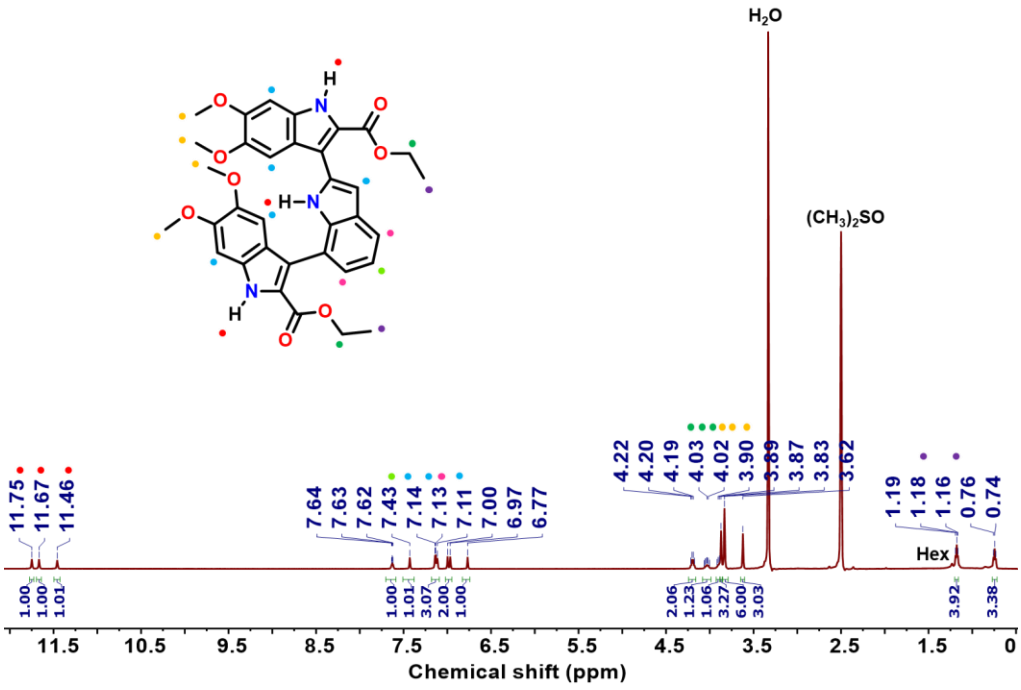

Figure A3.5: ^{1}H-NMR of DMICE-T in DMSO-d_6.

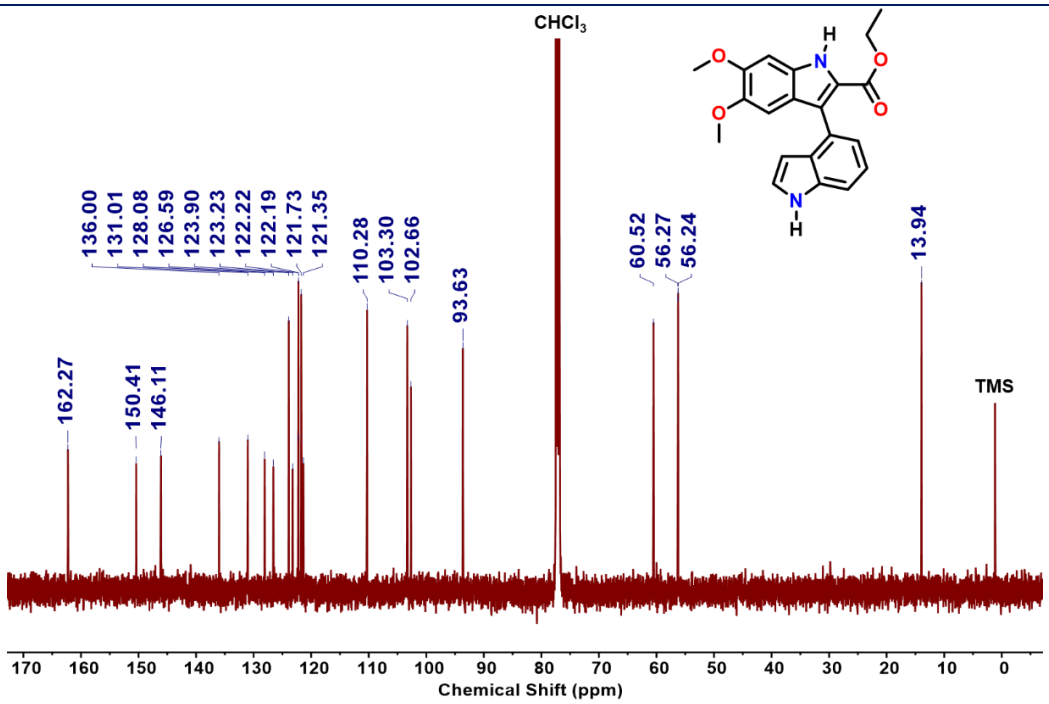

Figure A3.6: ^{13}C-NMR of DMICE-D in $CDCl_3$.

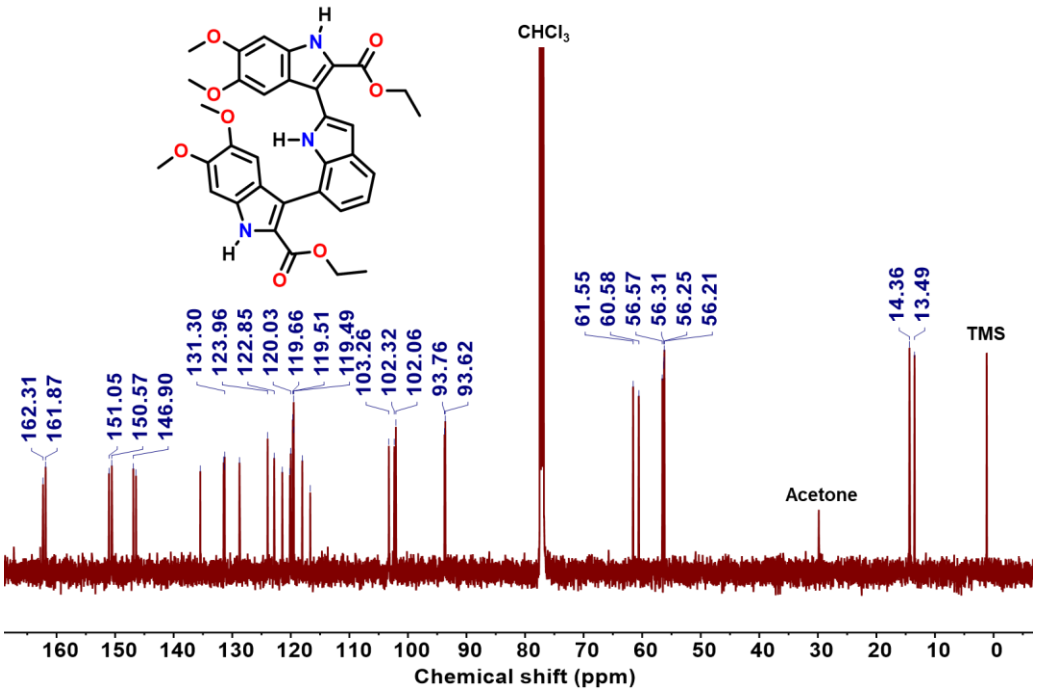

Figure A3.7: ^{13}C-NMR of DMICE-T in $CDCl_3$.

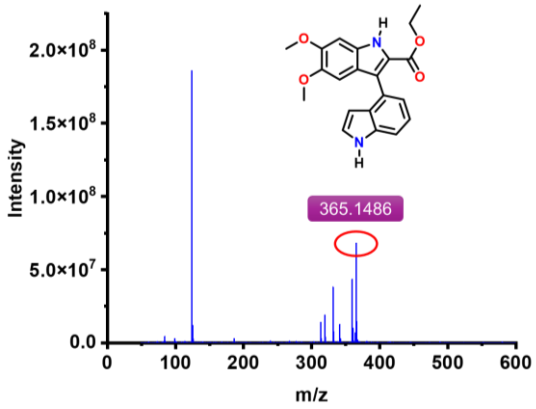

Figure A3.8: HRMS spectrum of DMICE-D.

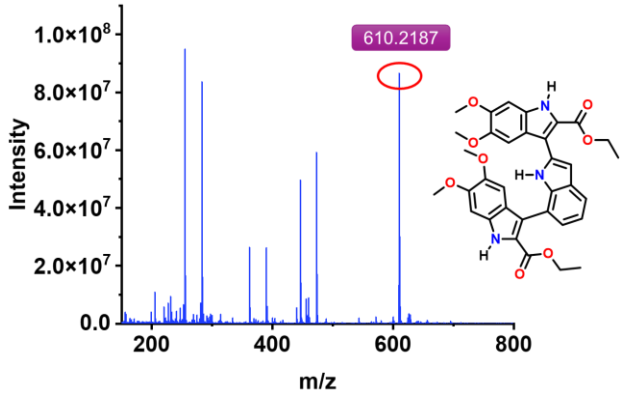

Figure A3.9: HRMS spectrum of DMICE-T.

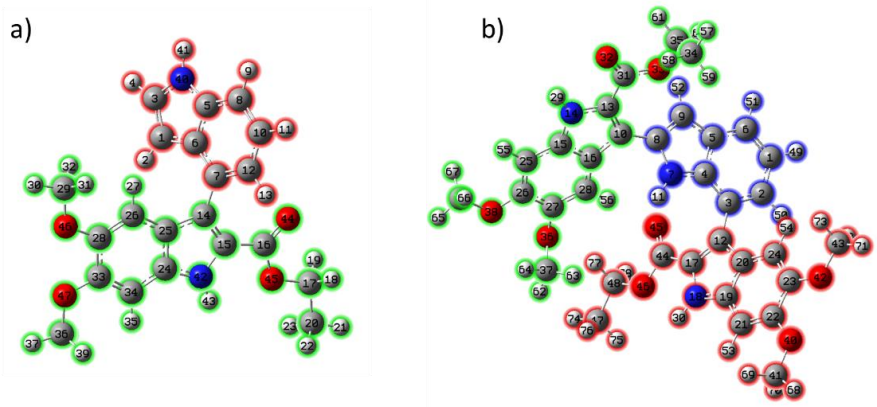

Figure A3.10: Optimized structure of a) DMICE-D and b) DMICE-T, at the ωb97xd/6-311G+(d,p) level of theory.

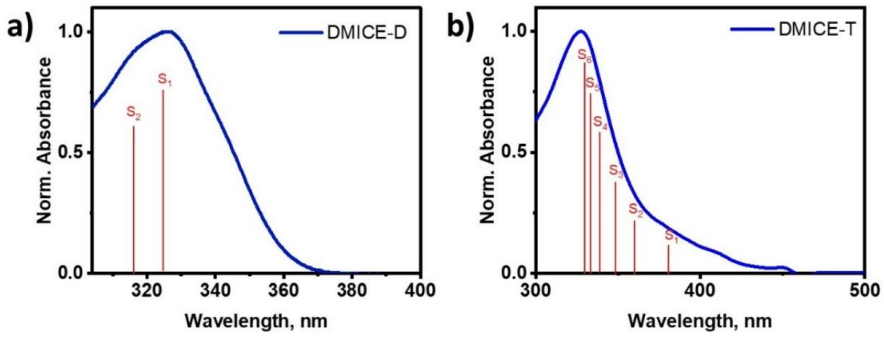

Figure A3.11: Comparison of experimental UV-vis absorption spectrum of a) DMICE-D and b) DMICE-T with the computed vertical excitation energies (red lines). Note: The vertical excitation energies are computed at the ωb97xd/6-311G+(d,p) level of theory and corrected with respect to the λ_{max} of the experimental absorption.

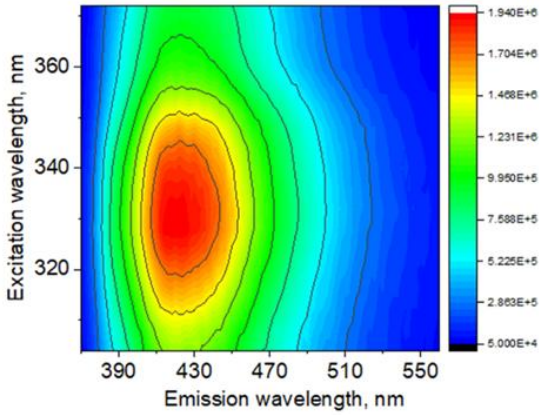

Figure A3.12: Excitation dependent fluorescence spectra of DMICE-T.

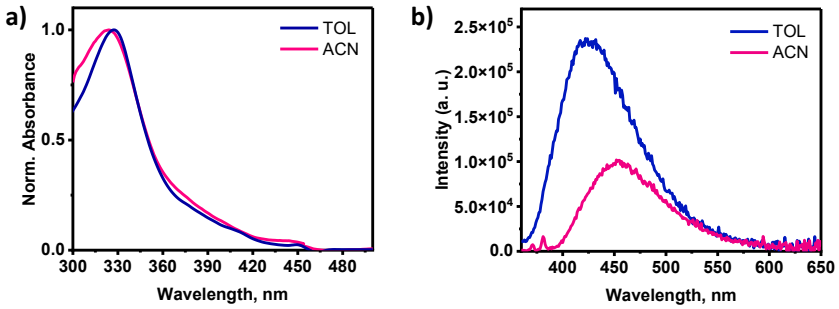

Figure A3.13: a) UV-vis absorption and b) fluorescence emission spectra of DMICE-T in TOL and ACN.

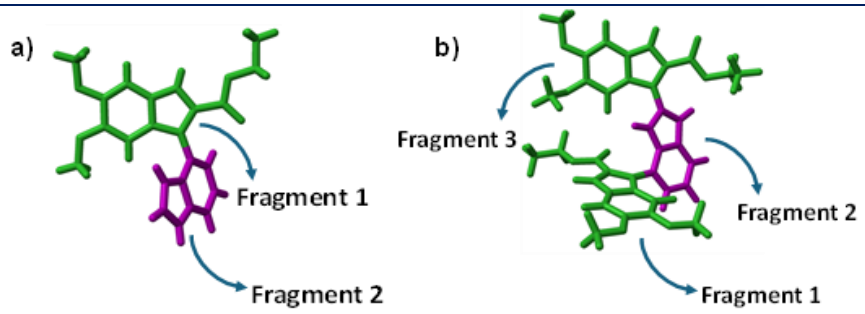

Figure A3.14: Fragmentation used for computing long-range Coulombic coupling via Electronic Excitation Transfer (EET) method in a) DMICE-D and b) DMICE-T.

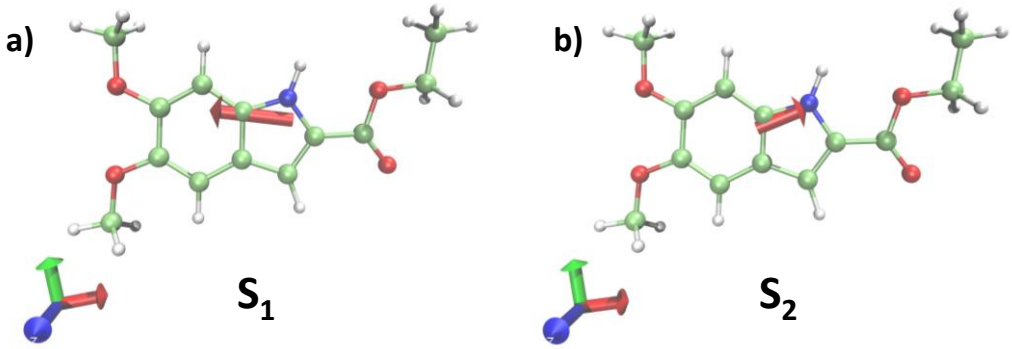

Figure A3.15: Transition dipole moments for DMICE in a) S_1 state and b) S_2 state.

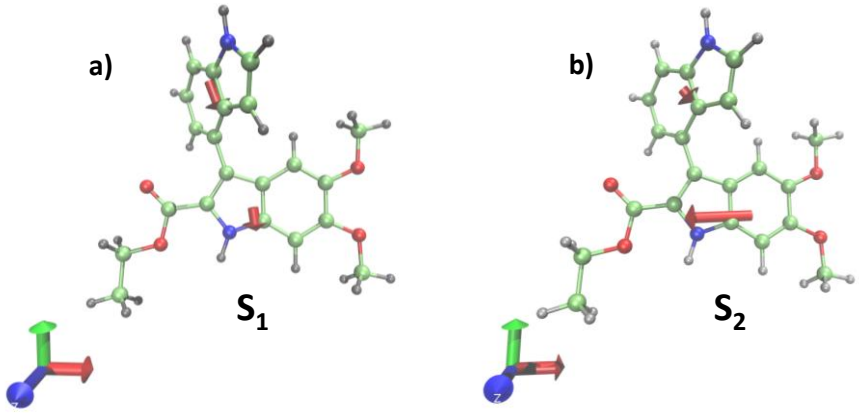

Figure A3.16: Transition dipole moments for DMICE-D in a) S_1 state and b) S_2 state.

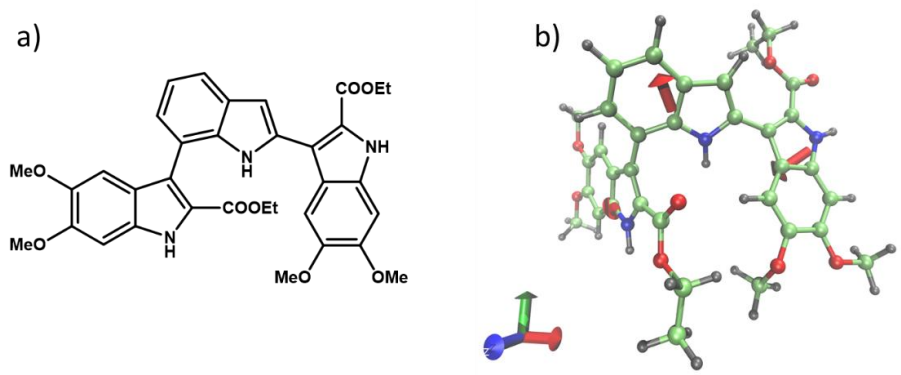

Figure A3.17: a) Molecular structure and b) transition dipole moments for DMICE-T in S_1 state.

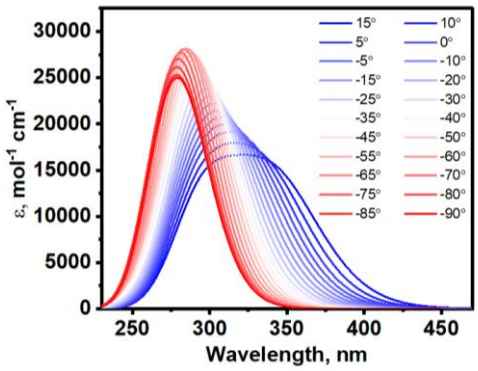

Figure A3.18: Simulated electronic absorption spectra of DMICE-D upon changing the dihedral angle between the indole units, computed at the ωb97xd/6-311+g(d,p) level of theory.

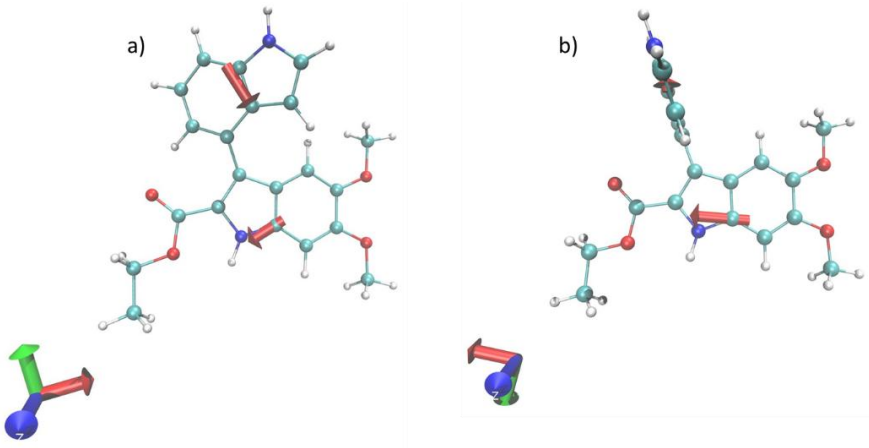

Figure A3.19: Transition dipole moments for DMICE-D in S_1 state for geometries with inter-fragment torsional angle a) 0° and b) 90°.

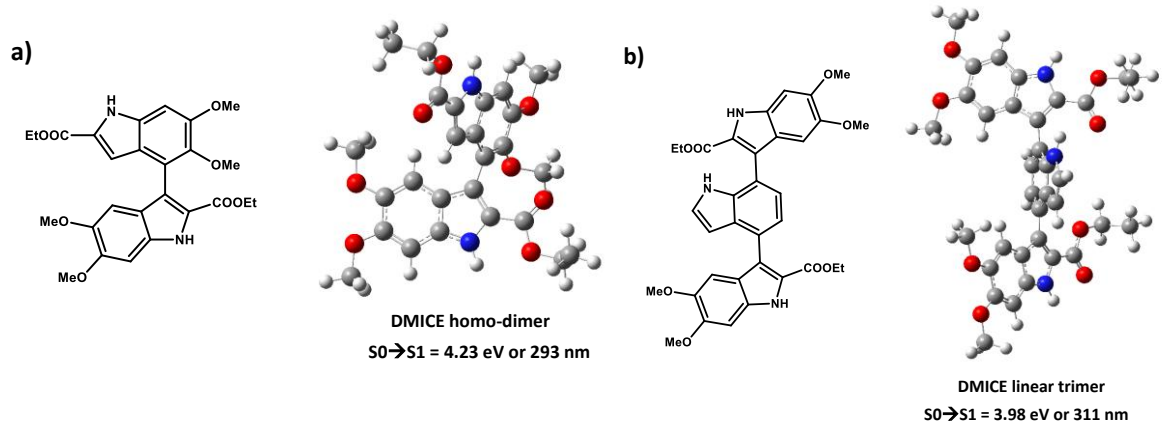

Figure A3.20: Optimized geometries and vertical excitation energies of the S_1 state for a) DMICE homo-dimer and b) DMICE linear trimer, computed at the computed at the ωb97xd/6-311+g(d,p) level of theory.

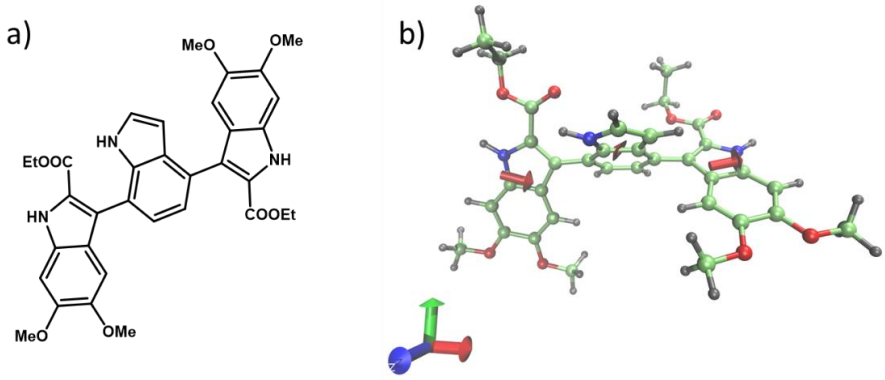

Figure A3.21: a) Structure and b) transition dipole moment in S_1 state for linear DMICE-T.

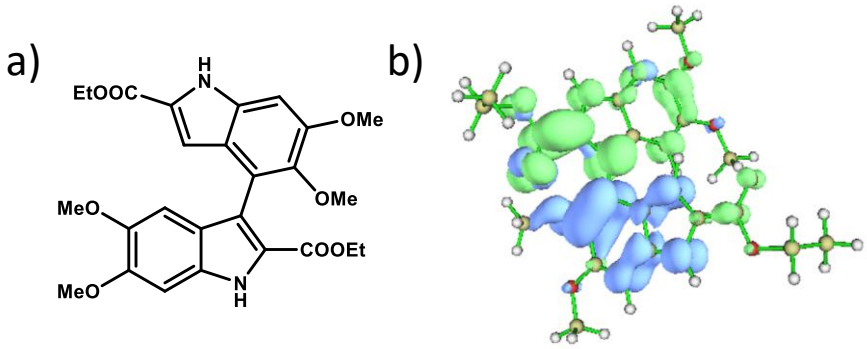

Figure A3.22: a) Structure and b) overlapped hole (blue) and electron (green) isosurface at the S_5 state of homodimer of DMICE.

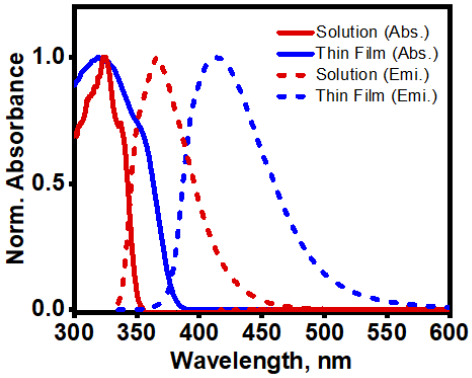

Figure A3.23: Normalized absorption and emission spectra of solution (blue lines) and thin film aggregates (red lines) of DMICE.

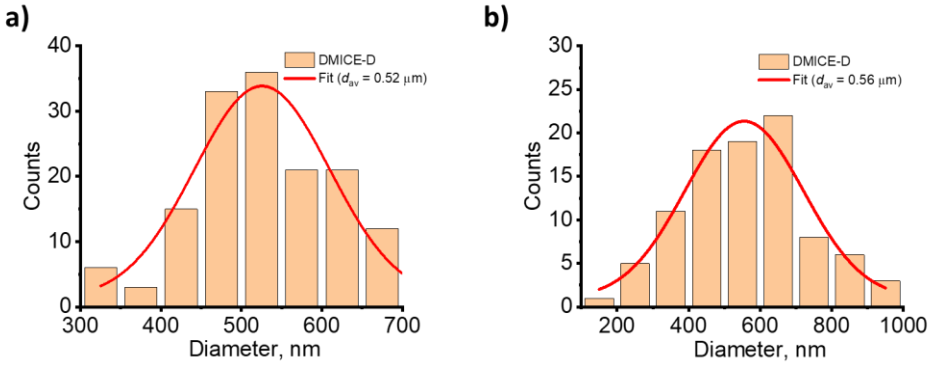

Figure A3.24: Histogram showing average size of DMICE-D aggregates in a) TEM and b) SEM.

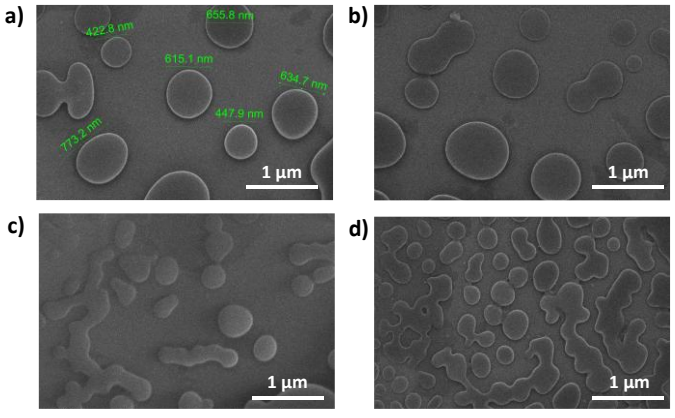

Figure A3.25: SEM images of DMICE-T showing distinct globular particles and elongated structures resulting from their assembly.

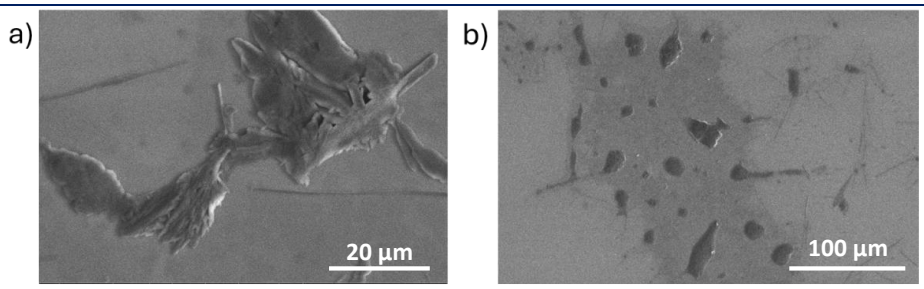

Figure A3.26: SEM images of DMICE aggregates showing lamellar morphology.

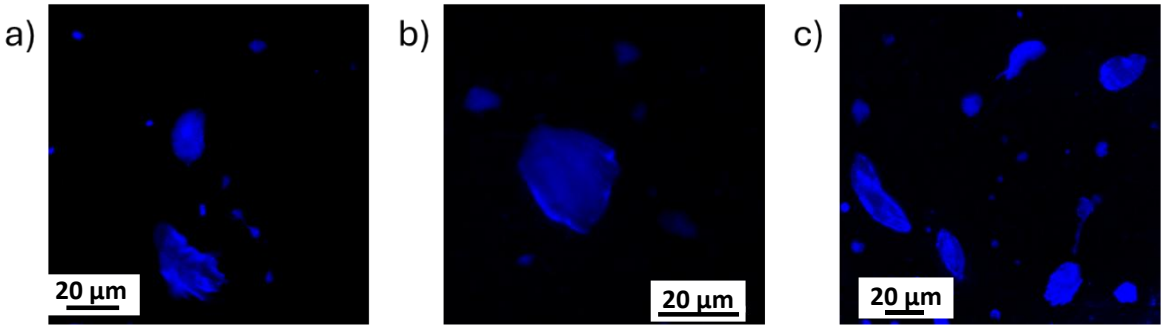

Figure A3.27: Confocal laser fluorescence microscopic images of DMICE aggregates showing lamellar morphology.

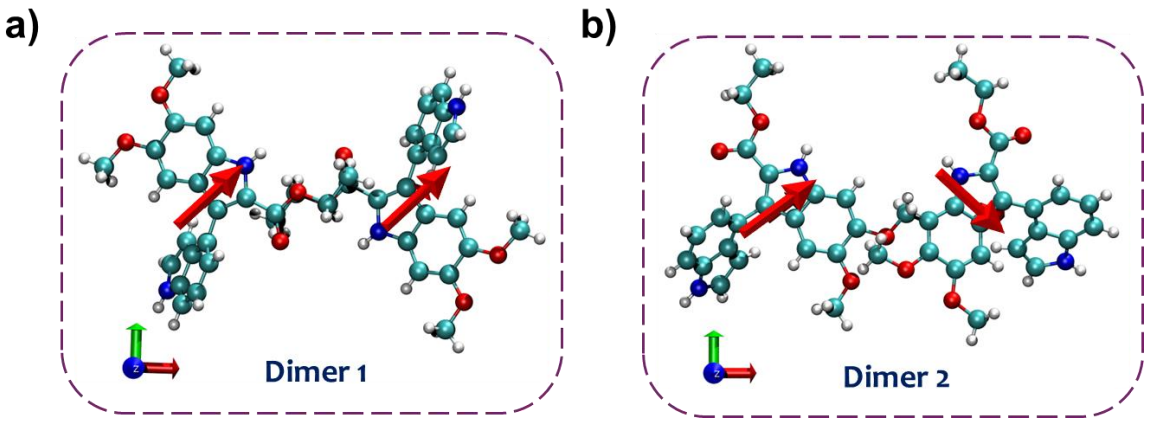

Figure A3.28: Two types of dimers within the crystal assembly of DMICE-D, named as a) DMICE-D1 and b) DMICE-D2, showing different transient dipole orientations.

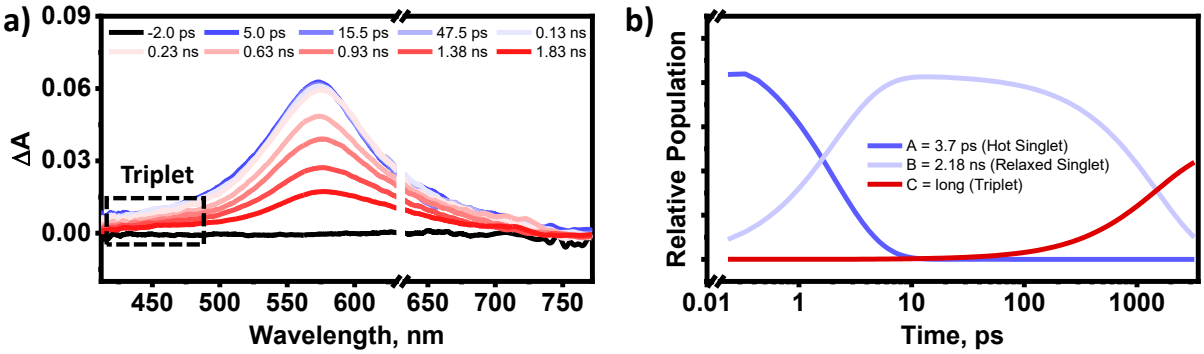

Figure A3.29: The fsTA spectra and corresponding deconvoluted time constants for DMICE-D in ACN.

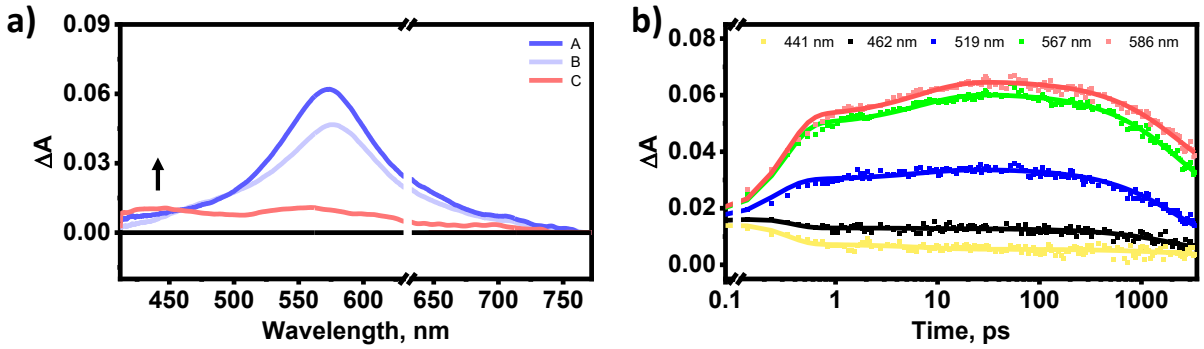

Figure A3.30: a) The evolution associated spectra (EAS) and b) the overlaid experimental versus fitted traces at different wavelengths for DMICE-D in TOL.

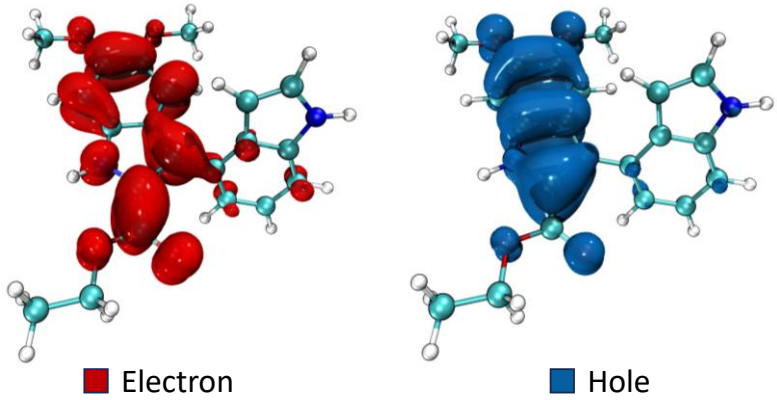

Figure A3.31: Electron and hole iso-surface plots of DMICE-D at the S_2 state.

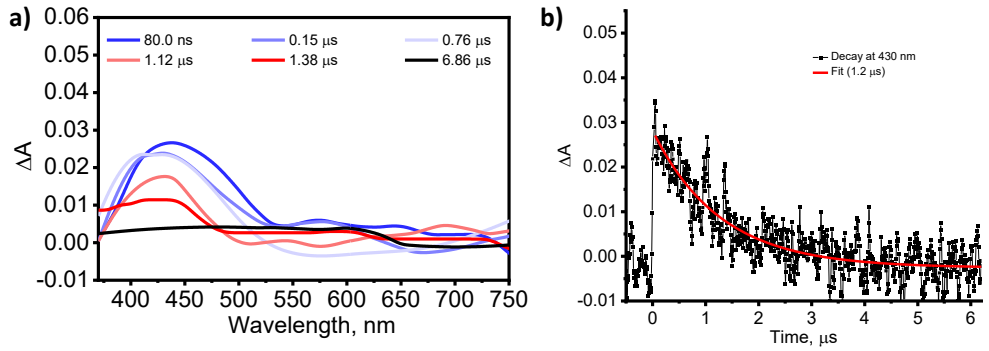

Figure A3.32: a) The nsTA spectra and b) decay trace at 440 nm for DMICE-D in TOL.

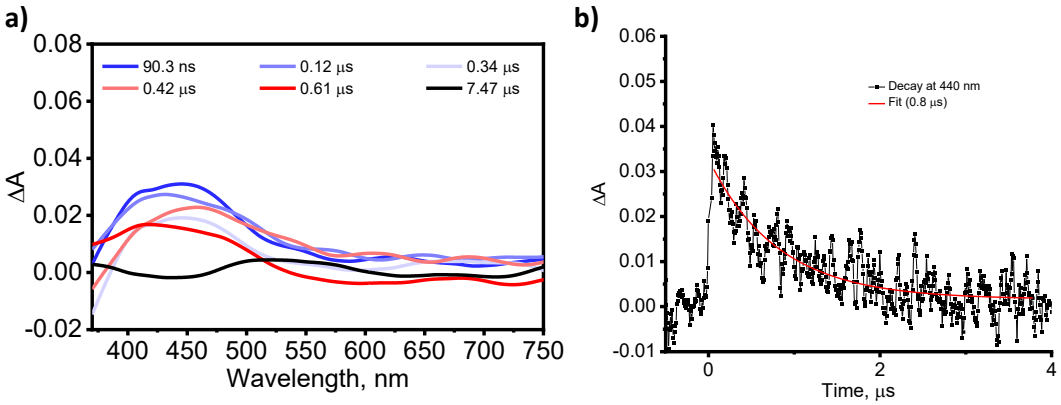

Figure A3.33: a) The nsTA spectra and b) decay trace at 440 nm for DMICE-D in ACN.

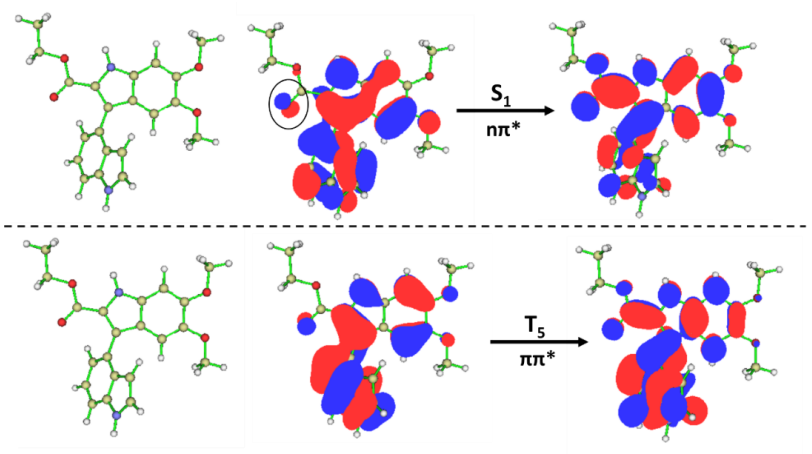

Figure A3.34: Natural transition orbitals (NTOs) of DMICE-D at the S_1 and T_5 states, showing the participation of non-bonding orbitals of the carbonyl group of the DMICE units for the S_1 state. Respective molecular orientation is shown on the left.

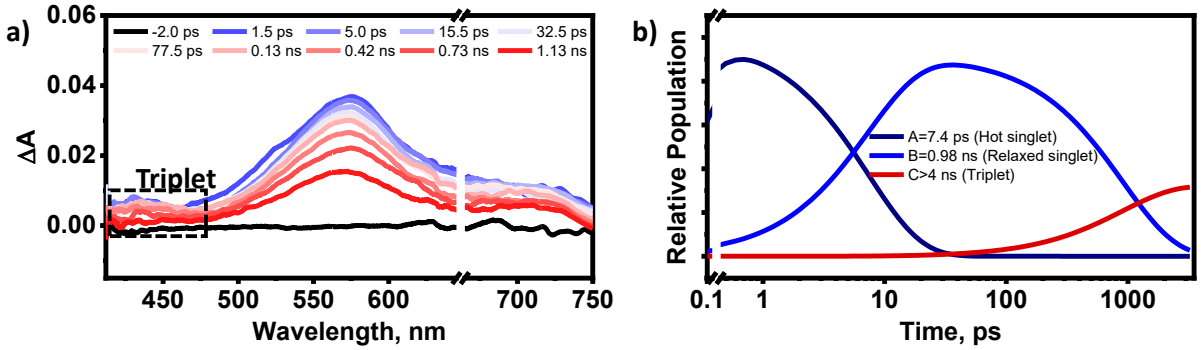

Figure A3.35: The fsTA spectra and corresponding deconvoluted time constants for DMICE-T in TOL.

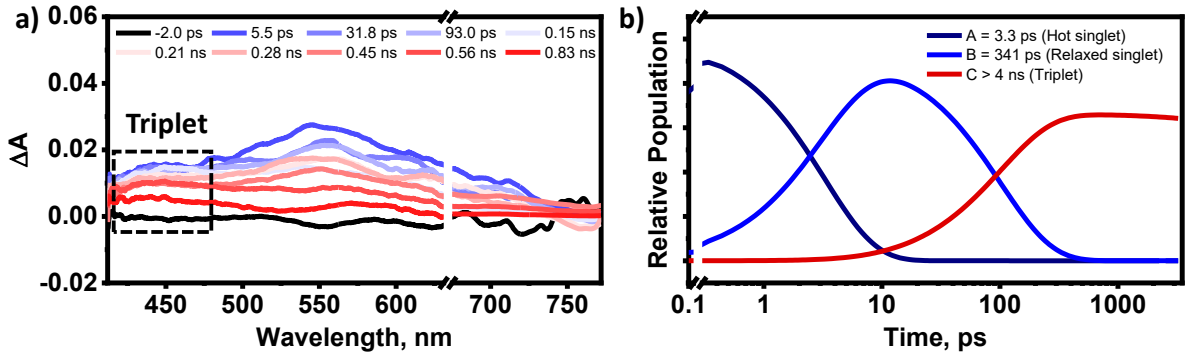

Figure A3.36: The fsTA spectra and corresponding deconvoluted time constants for DMICE-T in ACN.

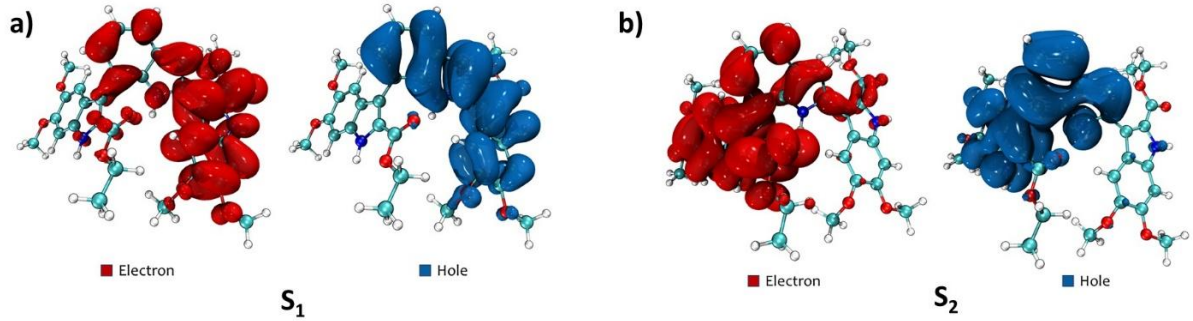

Figure A3.37: Electron and hole iso-surface plots of DMICE-T at the S_1 and S_2 states, showing CT character.

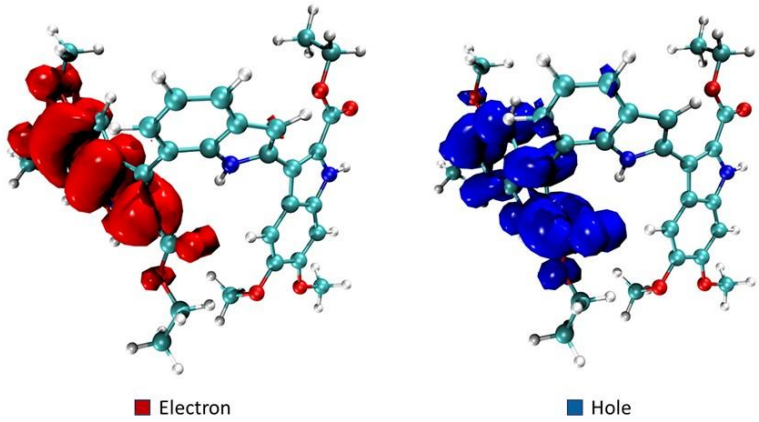

Figure A3.38: Electron and hole iso-surface plots of DMICE-T at the S_3 state, showing Frenkel exciton nature.

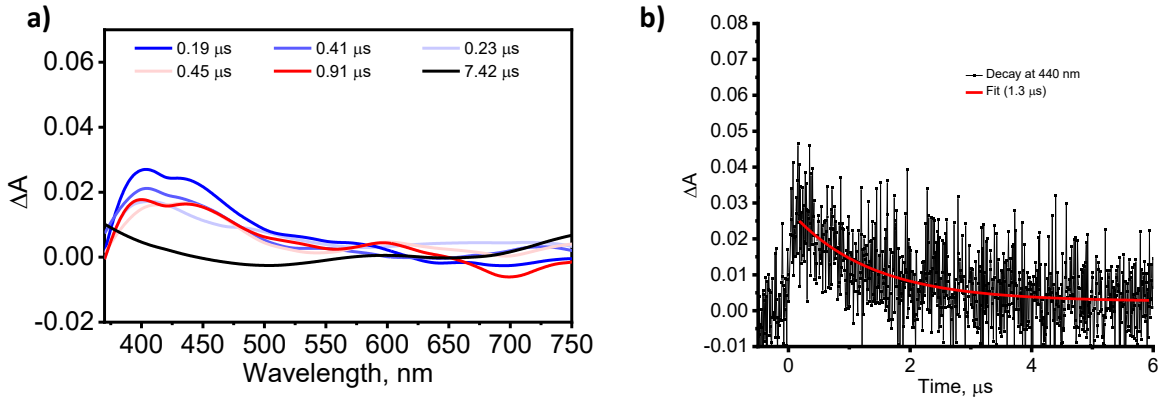

Figure A3.39: a) The nsTA spectra and b) decay trace at 440 nm for DMICE-T in TOL.

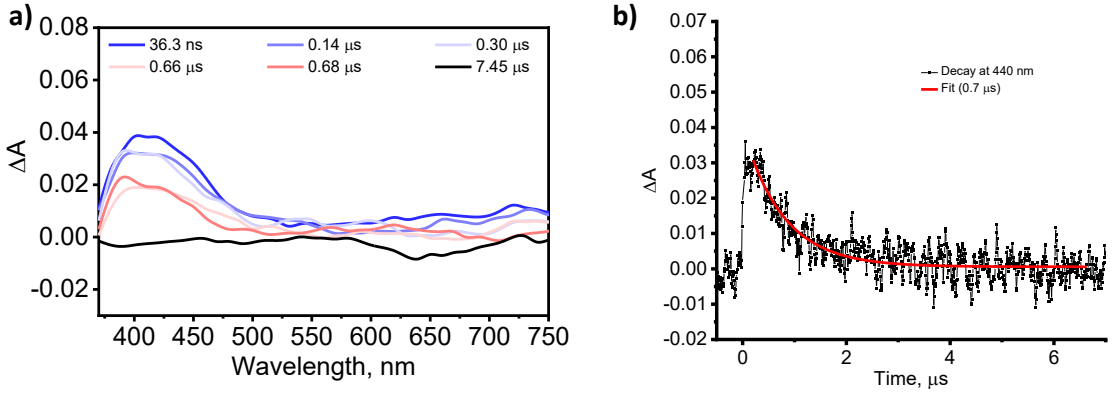

Figure A3.40: a) The nsTA spectra and b) decay trace at 440 nm for DMICE-T in ACN.

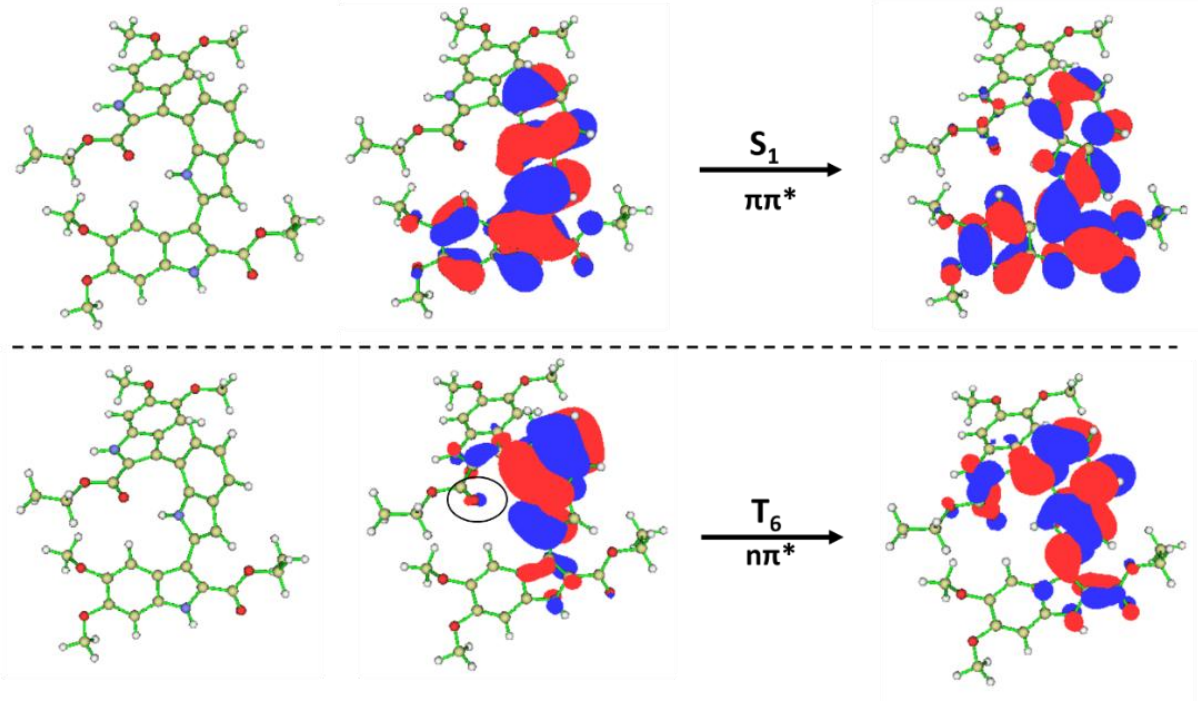

Figure A3.41: Natural transition orbitals (NTOs) of DMICE-T at the S_1 and T_6 states, showing the participation of non-bonding orbitals of the carbonyl group of the DMICE units for the T_6 state. Respective molecular orientation is shown on the left.

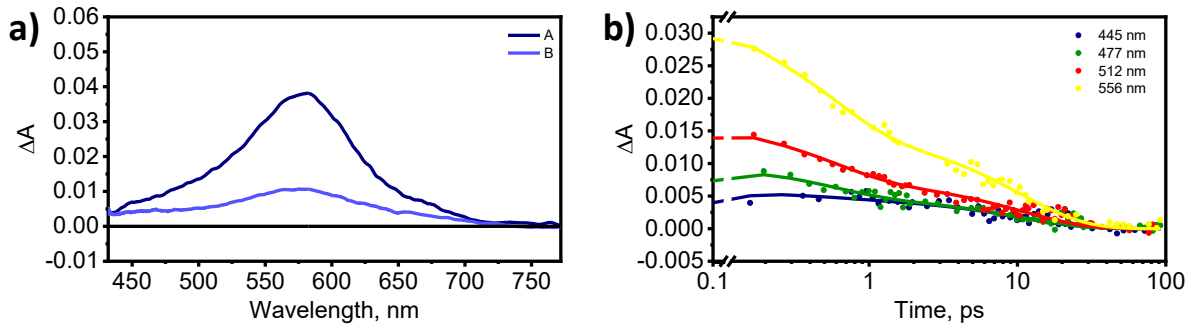

Figure A3.42: a) The evolution associated spectra (EAS) and b) the overlaid experimental versus fitted traces at different wavelengths for DMICE-D thin film.

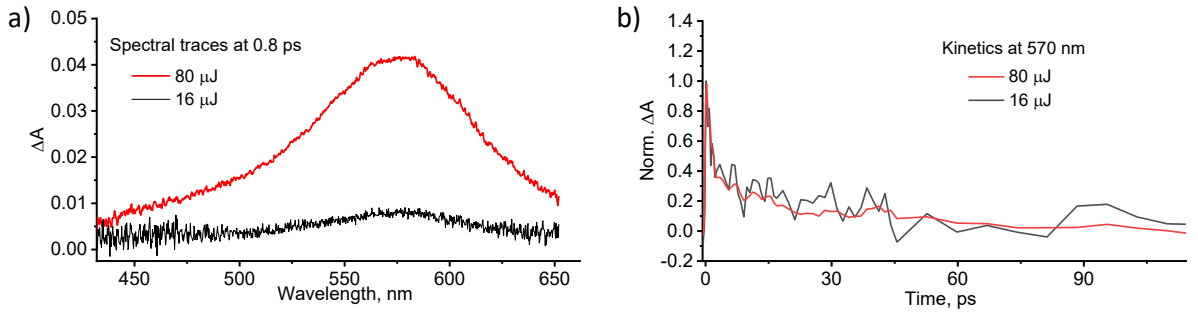

Figure A3.43: a) Spectral traces of DMICE-D thin film at 0.8 ps for different pump fluences; b) Normalized kinetic traces of DMICE-D thin film at 570 nm for different pump fluences.

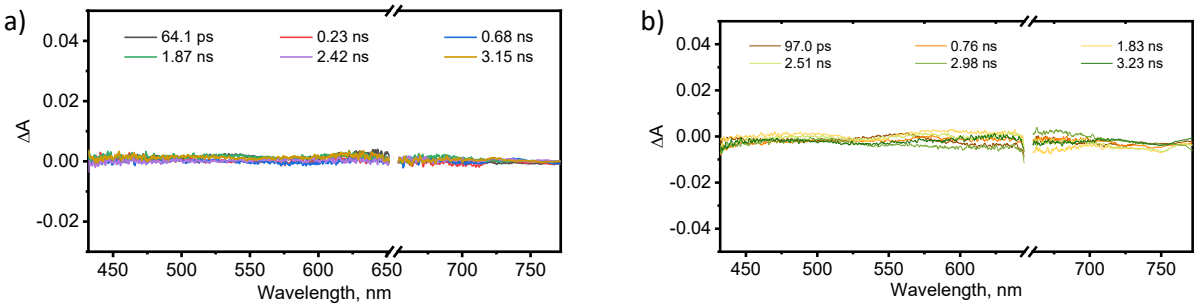

Figure A3.44: Transient absorption spectral traces of a) DMICE-D film and b) DMICE-T film beyond 50 ps.

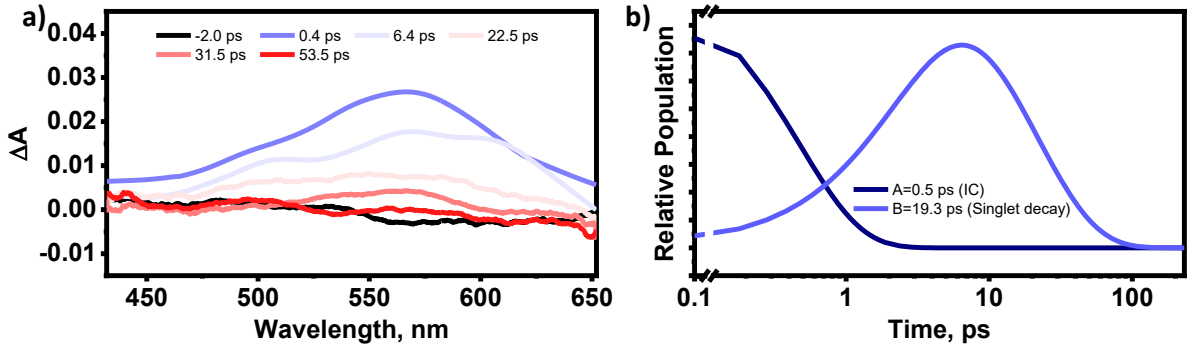

Figure A3.45: The fsTA spectra and corresponding deconvoluted time constants for DMICE-T thin film.

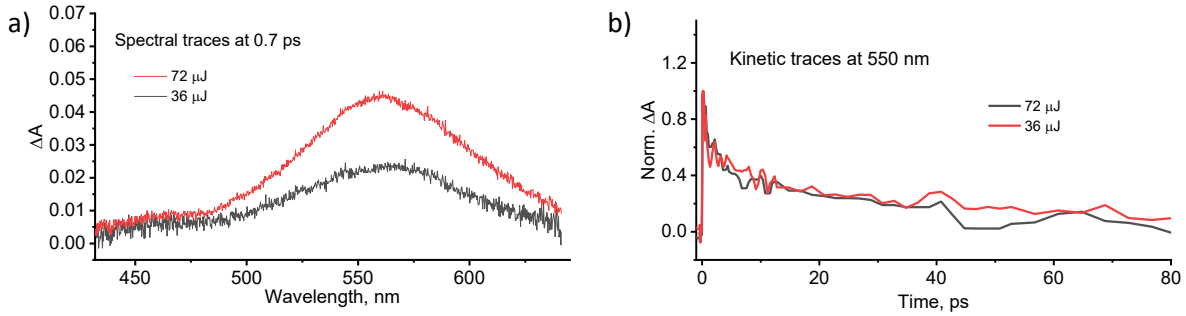

Figure A3.46: a) Spectral traces of DMICE-T thin film at 0.7 ps for different pump fluences; b) Normalized kinetic traces of DMICE-T thin film at 570 nm for different pump fluences.

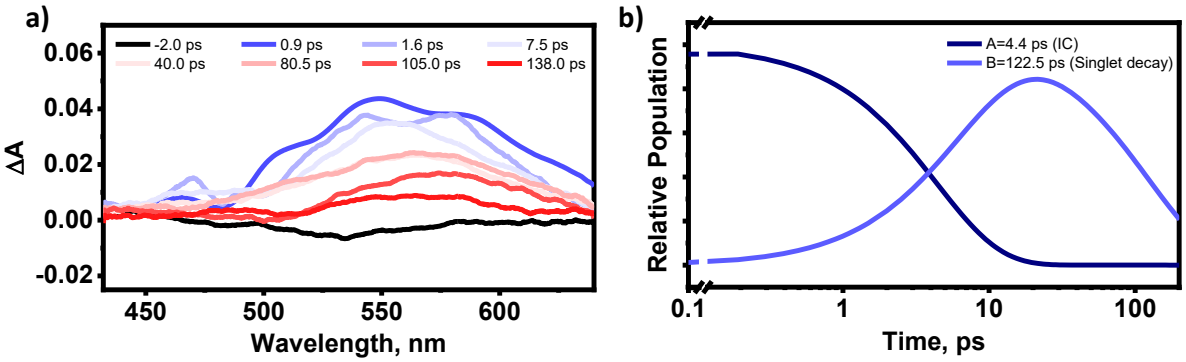

Figure A3.47: The fsTA spectra and corresponding deconvoluted time constants for DMICE thin film.

3.6. Additional Tables

Table A3.1: Previous works on elucidating the structure-property relationship in eumelanin and eumelanin substructures.

Contributed by	Journal	Methods employed
Buehler and coworkers	***Nat. Commun.***, 2014, *5*, 3859	Molecular dynamics (MD) simulations, DFT
Blancafort and coworker	***Angew. Chem. Int. Ed.,*** 2021, 60, 18800	Density functional theory (DFT)
Hodgkiss and co-worker	***Proc. Natl. Acad. Sci.***, 2022, 119, e2212343119	Time-resolved spectroscopy

Buehler and coworkers	***Chem. Sci.***, 2017, 8, 1631-1641	Molecular dynamics (MD) simulations, DFT
Sundström and coworkers	***J. Am. Chem. Soc.*** 2014, *136*, 11626–11635	Fluorescence spectroscopy
Hariharan, Thomas and coworkers	***Chem. Sci.***, 2024, D4SC05453A	3D-ED, solid state NMR
Hariharan and coworkers	***Current work*****,** 2024	Single crystal XRD, Time-resolved spectroscopy, Electron Microscopy

Table A3.2: Crystallographic data and refinement parameters for DMICE-D.

Parameters	**DMICE-D**
Formula	$C_{21}H_{20}N_2O_5$
Formula weight	380.39
Colour	Colourless
Crystal system	Monoclinic
Space group, z	P 21/c, 4
A (å)	14.018(3)
B (å)	17.554(3)
C (å)	7.8113(15)
A (deg)	90
B (deg)	104.941(5)
Γ (deg)	90
Volume, a^3	1857.1(6)
R-factor	6.64
Temp (K)	296
$Density_{calc}(mg/m^3)$	1.360
No. of reflections collected	31352
Independent reflections	4644
$2\theta_{max}$ (deg)	28.471
R indices, wr2, (i>2s(i))	0.0664, 0.1446
R indices, wr2 (all data)	0.1613, 0.1789
Goodness of fit	1.025
CCDC number	2389911

Table A3.3: DFT optimized geometry parameters of DMICE-D computed at different functionals/basis sets.

Functional/basis set	Dihedral angle, ϕ (°) (C6–C7–C14–C25)	Bond angle, θ (°) (O44–C16–O45)	Bond length, x (Å) (C15–C16)
ωb97xd/6-311g+(d,p)	54.49	123.03	1.47
cam-b3lyp/6-311g+(d,p)	57.71	122.76	1.47
b3lyp/6-311g+(d,p)	58.66	122.75	1.48
hseh1pbe/6-311g+(d,p)	54.31	122.79	1.47

Table A3.4: DFT optimized geometry parameters of DMICE-T computed at different functionals/basis sets.

Functional/ basis set	Dihedral angle (°) (C16–C10–C8–N7)	Dihedral angle (°) (C4–C3–C12–C17)	Bond angle (°) (O32–C31–O33)	Bond length (Å) (C13–C31)
ωb97xd/ 6-311g+(d,p)	39.59	60.11	124.44	1.47
cam-b3lyp/ 6-311g+(d,p)	38.81	61.76	124.04	1.47
b3lyp/ 6-311g+(d,p)	38.81	61.76	124.04	1.46
hseh1pbe/ 6-311g+(d,p)	36.13	60.07	124.12	1.46

Table A3.5: Vertical excitation energies of DMICE, DMICE-D and DMICE-T computed at the ωb97xd/6-311+g(d,p) level of theory.

DMICE			DMICE-D			DMICE-T		
State	**dE(eV)**	**f**	**State**	**dE(eV)**	**f**	**State**	**dE(eV)**	**f**
S_1	4.205	0.484	S_1	4.225	0.221	S_1	3.880	0.342
S_2	4.320	0.114	S_2	4.339	0.461	S_2	4.141	0.145
S_3	5.319	0.000	S_3	4.767	0.070	S_3	4.317	0.410
S_4	5.486	0.020	S_4	4.858	0.039	S_4	4.449	0.469
S_5	5.536	0.087	S_5	5.117	0.073	S_5	4.503	0.028
S_6	5.737	0.002	S_6	5.388	0.000	S_6	4.603	0.047

S_7	5.859	0.003	S_7	5.460	0.015	S_7	4.868	0.080
S_8	5.966	0.002	S_8	5.503	0.012	S_8	5.023	0.047
S_9	6.270	0.003	S_9	5.536	0.009	S_9	5.140	0.047
S_{10}	6.311	0.000	S_{10}	5.563	0.006	S_{10}	5.330	0.006

Table A3.6: Solvent-dependent steady-state optical properties of DMICE-D and DMICE-T.

Compound	Solvent	λ_{abs} (nm)	λ_{emi} (nm)	φ_{fl} (%)
DMICE-D	TOL	326	400	27.5
	ACN	325	432	17.5
DMICE-T	TOL	331	425	13.6
	ACN	331	454	4.6

Table A3.7: Electronic coupling calculated via the excitation energy transfer (EET) method at the cam-b3lyp/6-311g+(d,p) for DMICE-D.

Fragment	Coulomb (meV)	Exact exchange (meV)	Exchange correlation (meV)
1 & 2	0.40	3.36	0.49

Table A3.8: Electronic coupling calculated via the excitation energy transfer (EET) method at the cam-b3lyp/6-311g+(d,p) for DMICE-T.

Fragment	Coulomb (meV)	Exact exchange (meV)	Exchange correlation (meV)
1 & 2	0.00	1.14	1.67
2 & 3	0.00	-1.34	-0.12
1 & 3	-17.19	0.17	0.00

Table A3.9: Coulombic and charge transfer coupling values calculated at the cam-b3lyp/6-311g+(d,p) for the identified DMICE-D dimers within the crystal packing.

J	Dimer 1	Dimer 2
J_{CT} (cm^{-1})	-12.74	9.41
J_{Coul} (cm^{-1})	47.85	54.34
J_{Total} (cm^{-1})	34.71	63.75

Table A3.10: Vertical excitation energies of nearest triplet states to the S_1 state for DMICE-D and DMICE-T at the ωb97xd/6-311+g(d,p) level of theory.

Compound (S_1 energy)	Triplet State	Energy (eV)
DMICE-D (S_1 = 4.19 eV)	T_1	2.74
	T_2	3.13
	T_3	3.38
	T_4	4.94
	T_5	4.14
	T_6	4.53
DMICE-T (S_1 = 3.88 eV)	T_1	2.58
	T_2	2.79
	T_3	3.13
	T_4	3.36
	T_5	3.55
	T_6	3.74
	T_7	3.88

Table A3.11: Summary of decay rate constants of different species (obtained from fsTA and nsTA) for DMICE-D in TOL and ACN.

Solvent	Component A	Component B	Component C
TOL	6.7 ps	2.43 ns	1.2 µs
ACN	3.7 ps	2.18 ns	0.80 µs

Table A3.12: Summary of decay rate constants of different species (obtained from fsTA and nsTA) for DMICE-T in TOL and ACN.

Solvent	Component A	Component B	Component C
TOL	7.4 ps	0.98 ns	1.3 µs
ACN	3.3 ps	0.34 ns	0.77 µs

Table A3.13: Comparison of structural and photophysical features of DMICE-based multimers and natural eumelanin.

Property	**DMICE-D / DMICE-T**	**Natural Eumelanin**	**Remarks**
Monomeric Unit	Substituted indole (DMICE)	DHI, DHICA, indolequinones	DMICE retains the indole scaffold with blocking groups to prevent polymerization
Polymerization Tendency	Bench-stable, controlled oligomers	Spontaneous polymerization into heterogeneous polymers	Structural modification stabilizes the molecules
UV-vis Absorption	In UV regime (DMICE-D), till ~420 nm (DMICE-T)	Broad UV-vis-NIR profile	DMICE-T shows modest visible absorption; longer oligomers may extend further
Absorption Profile	Structured, molecule-specific	Broad, featureless	Aggregation and heterogeneity in eumelanin lead to featureless spectra; hard to dissect
Excited-State Lifetime	Ns-µs (monomers), sub–ns (aggregates)	Ps timescale (*Proc. Natl. Acad. Sci. U.S.A.*, 2022, 119, *43*, e2212343119)	Ultrafast internal conversion among neighbouring coupled chromophores
Triplet State Formation	Observed (µs lifetime)	Less likely in polymer though suspected in monomers (*J. Phys. Chem. B* 2009, *37*, 12575–12580)	Heavy-atom-free ISC possible in monomers
Excited state charge-transfer	Sub-ns timescale excited CT states	Sub-ps timescale excited CT states (J. Phys. Chem. Lett. 2024, 15, 13, 3639–3645)	Excited CT states are predominant

Table A3.14: Comparison of protected (DMICE-based) and unprotected (DHI/DHICA) eumelanin multimers.

Property	**Unprotected DHI/DHICA oligomers** (*J. Phys. Chem. B*, 2012, 116, *44*, 13151; *J. Am. Chem. Soc.*, 2014, 136, *33*, 11626)	**Protected DMICE-based oligomers** (This work)
Chemical stability	Low (prone to oxidative polymerization and in situ photochemical reactions)	High (methyl protection blocks uncontrolled polymerization)
Excited-State Proton Transfer (ESPT)	Observed; contributes to ultrafast fluorescence	Suppressed due to methyl protection
Fluorescence lifetimes (in solution)	Multiexponential: short-lived (ps) + long-lived (ns) components	Predominantly ns components in solution
Fluorescence lifetimes (in aggregates/films)	Unexplored due to fast polymerisation	Multiexponential with emerging ps components (indicative of exciton effects)
Triplet-state formation/ISC	Unexplored due to fast polymerisation	Directly observed and quantified using transient absorption
Exciton effects	Unexplored due to fast polymerisation	Isolated and studied systematically across oligomer length
Interpretability of photophysics	Complicated by overlapping decay pathways and chemical heterogeneity	Mechanistic contributions (e.g., ISC, exciton coupling) isolated and resolved
Experimental tools	Time-resolved fluorescence spectroscopy	Transient absorption (fsTA and nsTA), time-resolved fluorescence spectroscopy, microscopy

3.7. Appendix

3.7.1. Materials and Methods

Detailed information regarding the materials and methods used is provided in Section 2.7.1. For thin-film measurements, cleaned square quartz substrates were used, and 1 mM sample solutions in chloroform were uniformly drop cast, followed by vacuum drying and storage under nitrogen. Diffuse-reflectance spectra were recorded, and Kubelka–Munk transformed absorption spectra were obtained using UVProbe (Shimadzu). Quantum yields were measured using an integrating sphere on a Horiba Jobin Yvon Fluorolog spectrometer (λ_{exc} = 340 nm for DMICE, 370 nm for DMICE-D, and 380 nm for DMICE-T). Fluorescence lifetimes were recorded using an IBH TCSPC system with a 310 nm excitation source (pulse width < 1 ns), and the decay profiles were deconvoluted and fitted with exponential functions using DAS 6.3 to minimize χ^2 values. Confocal imaging was performed using a Nikon Eclipse Ti microscope.

3.7.2. X-ray Diffraction

The single crystal was mounted using oil (Infineum V8512) on a glass fiber. All measurements were made on a CCD area detector with graphite monochromated Mo Kα radiation. The data was collected using Bruker APEXII detector and processed using APEX2 from Bruker. The structure was solved by direct method and expanded using Fourier technique. The non-hydrogen atoms were refined anisotropically. Hydrogen atoms were included in idealized positions, but not refined. Their positions were constrained relative to their parent atom using the appropriate HFIX command in SHELX-97.[1] All programs used during the crystal structure analysis are incorporated in the WINGX software.[2] The full validation of CIF and structure factor of the crystal structure was performed using the checkCIF utility and found to be free of major alert levels. Three-dimensional structure visualization and the exploration of the crystal packing of crystals under study were carried out using Mercury 2021.2.0.[3]

3.7.3. Estimation of radiative (k_r) and non-radiative (k_{nr}) rate constants

The radiative and non-radiative rate constants were calculated as follows.

$$\phi_F = \frac{k_r}{k_r + k_{nr}} \qquad \text{(Equation A3.1)}$$

$$\tau_F = \frac{1}{k_r + k_{nr}} \qquad \text{(Equation A3.2)}$$

$$k_r = \frac{\phi_F}{\tau_F} \qquad \text{(Equation A3.3)}$$

where ϕ_F is the fluorescence quantum yield and τ_F is the fluorescence lifetime.

3.7.4. Computational Analysis

All geometry optimisations were carried out in Gaussian 16[4] employing the ωB97XD functional and 6-311G+(d,p) basis set at the DFT level of theory. The long-range Coulombic coupling for the molecules was computed using Excitation Energy Transfer (EET) method available in Gaussian 16. Electron and hole transfer coupling values were calculated by employing the CATNIP Tool version 1.9.9.[5] CATNIP uses post-processed Gaussian 16 output files for the respective analyses. The two types of dimers from the crystal packing of DMICE-D are denoted as DMICE-D1 and DMICE-D2. Hole-electron isosurfaces and NTO analysis for the systems were generated using Multiwfn 3.8. Visualization states were rendered using VMD 1.9.3 software. Reorganisation energy of the molecules was computed following the expression $\lambda_M = S_0@S_1 - S_0@S_0$ (*J. Chem. Theory Comput.*, 2023, 19, *8*, 2316–2326), where the reorganization energy is calculated as the energy difference in the S_0 potential energy surfaces at S_1 and S_0 equilibrium geometries. Detailed information regarding TheoDORE analysis and excitonic coupling calculations are provided in Sections 2.7.3.5 and 2.7.3.6 respectively.

3.7.5. Femtosecond Transient Absorption (fsTA) Measurement

A Spectra-Physics Mai Tai SP mode-locked laser, with an operating frequency of 86 MHz and emitting light at 800 nm, served as the seed for a Spectra-Physics Spitfire ace regenerative amplifier. The regenerative amplifier operated at a repetition rate of 1 kHz and produced an output energy of 5.5 mJ. A fraction of the amplified output was utilized to generate the pump pulse through TOPAS. Simultaneously, the remaining 800 nm pulse underwent an optical delay within an ExciPro pump-probe spectrometer. A sapphire crystal introduced into this path

generated a white light continuum, which was then split into two streams, serving as probe and reference pulses. Femtosecond transient absorption spectra of the sample were captured using a dual diode array detector with a detection window of 200 nm and an optical delay of 3.5 ns. Sample solutions housed in a rotating cuvette with a path length of 1.2 mm were employed for recording. To enable accurate deconvolution of the transient absorption data, an instrument response function (IRF) was determined. The IRF, established through a solvent (10% benzene in methanol) two-photon absorption, was approximately 110 fs at around 530 nm. An 80% neutral density filter regulated incident flux on the sample. The observed kinetic components were independent of laser intensity, eliminating the possibility of singlet–singlet annihilation. The fsTA experiments were performed at the magic angle polarization ~54.7° of the pump.

3.7.6. Sample Preparation for Thin Film for fsTA Analysis

For the fsTA thin film measurements, a round quartz substrate was cleaned by sequential sonication in deionized water, isopropanol, and acetone for 10 min each and dried under nitrogen. Followingly, 1 mM sample solutions in chloroform were uniformly dropcasted on the quartz substrate. The films were dried in a vacuum and stored in a nitrogen atmosphere prior to the experiments. The magic angle polarization ~54.7°, between pump and probe pulses for the fsTA experiments were used to ensure an isotropic signal of the sample.

3.7.7. Nanosecond Transient Absorption (nsTA) Measurement

Nanosecond laser flash photolysis experiments were performed on nitrogen-degassed solutions of the samples. The measurements were carried out using an Applied Photophysics LKS-60 laser kinetic spectrometer. Excitation was achieved with the third harmonic output (355 nm, ~10 ns pulse width) of a Quanta Ray INDI-40-10 series pulsed Nd:YAG laser.

3.7.8. Global Analysis

The fsTA spectra underwent global analyses using Glotaran software. This process involved assessing the instrument time response function and the group velocity dispersion of the white continuum, enabling the computation of decay time constants and dispersion-compensated

spectra. Parallel model was also tested but resulted in poor fits compared to the sequential model, which provided the best description of the observed kinetics. In global analysis of the fsTA data, all wavelengths were simultaneously scrutinized, utilizing a sequential model to generate the time constants associated with specific spectral changes.

3.7.9. Spectral Plotting and Data Handling

All transient absorption spectra were recorded over two probe windows (~200 nm each) and stitched together to span the visible region. The central probe wavelengths were set to 520 nm for solution samples and 540 nm for film samples, which results in visible spectral discontinuities at the stitching points. For improved visual clarity, fsTA spectra were plotted after smoothing the raw data using Savitzky-Golay over 25 points (OriginLab); this procedure did not alter the spectral dynamics or features, as all quantitative analyses using Glotaran were performed using the raw data.

Chapter 4

Eumelanin-Inspired Photoactive Molecules for Delayed Emission

Abstract

Exploring the impact of molecular aggregation on excited-state energy landscapes is key to tailoring long-lived delayed emission in organic materials. Here, we demonstrate aggregation-assisted energy gap modulation governing the balance between delayed fluorescence (DF) and room-temperature phosphorescence (RTP) in the eumelanin-inspired hybrid charge-transfer emitters – HD and its brominated analogue BrD. In HD, J-aggregation, facilitated by a collinear molecular arrangement, significantly reduces the singlet–triplet energy gap (ΔE_{ST}), enhances reverse intersystem crossing (RISC), and increases the efficiency of radiative decay from the regenerated singlet state, thereby favouring DF. In contrast, BrD forms H-aggregates through strong π–π interactions, which increase ΔE_{ST}, suppress RISC and stabilize triplet excitons, resulting in prominent RTP. Time-resolved spectroscopy and theoretical calculations reveal that the hybridization of local-excited and charge-transfer states mediates excited-state evolution, with J-aggregation promoting DF and H-aggregation favouring RTP. These results establish a direct link between aggregation and distinct photoluminescence pathways, offering a strategy to tune delayed emission in bio-inspired, organic materials.

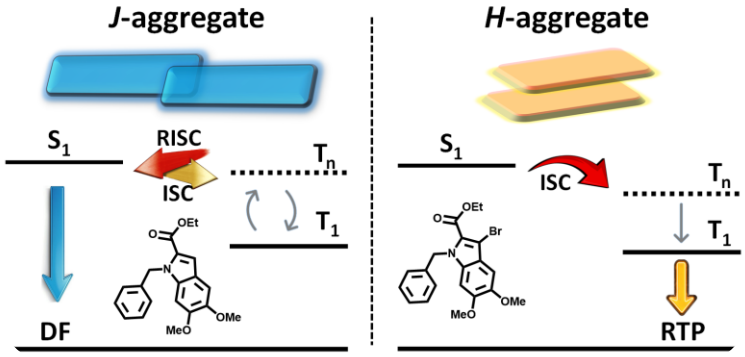

4.1. Introduction

Photoluminescent bio-organic materials have attracted significant attention due to their diverse optical behaviours.[165, 166] Notably, room-temperature phosphorescence (RTP) and delayed fluorescence (DF) have emerged as valuable mechanisms for developing advanced organic materials used in light-emitting diodes, sensors, and bioimaging.[167-170] RTP arises from intersystem crossing (ISC), where excitons undergo a nonradiative spin-flip to the triplet state followed by emission through a sequential spin-forbidden process.[171] In contrast, thermally activated DF arises from the reverse intersystem crossing (RISC) of triplet excitons to the singlet excited state, followed by radiative decay.[172, 173] For efficient RISC mediated DF, a small singlet–triplet energy gap (ΔE_{ST}) is essential, while persistent RTP requires mechanisms that stabilize triplet excitons and minimize energy loss through nonradiative pathways.[172] Approaches to enhance RTP include incorporating heavy atoms or heteroatoms to strengthen spin–orbit coupling (SOC) and using rigid molecular frameworks to limit vibrational dissipation.[174-176] In contrast, RISC mediated DF emitters typically feature donor–acceptor structures that spatially separate frontier orbitals, reducing ΔE_{ST}. Despite advances in these materials, achieving precise control over excited-state processes to regulate the delayed emission mechanisms remains a significant challenge.

Hybrid locally-excited and charge-transfer (HLCT) states offer a promising approach to address this issue.[177-180] While charge-transfer (CT) states generally suffer from weak fluorescence due to poor orbital overlap, their low exciton binding energy leads to near-degenerate singlet and triplet states, favouring RISC.[181, 182] In contrast, locally excited (LE) states have stronger radiative transitions but a larger ΔE_{ST}, limiting triplet harvesting.[180] By merging LE and CT characteristics into a single HLCT state, it is possible to achieve both efficient luminescence and enhanced exciton utilization.[181] Beyond molecular design, solid-state organization plays a key role in shaping excited-state properties.[183, 184] Unlike doped host–guest matrices where DF is commonly observed, RTP predominantly occurs in crystalline solids where aggregation suppresses nonradiative triplet deactivation.[185, 186] Unlike cross-aggregates[48], J- and H-aggregates strongly influence luminescence pathways,[187, 188] yet their role in balancing RTP and DF remains underexplored.[183, 189]

Recent studies have shown that distinct packing arrangements within molecular polymorphs can lead to concurrent RTP and DF emission, highlighting the importance of aggregate structure in governing excited-state dynamics.[190-195] Energy-gap modulation strategies have also been employed in CT co-crystals to achieve colour-tunable phosphorescence and control RTP/DF output by tuning donor strength and aggregation motifs.[196-198] We investigate how aggregation influences the excited-state properties of two eumelanin-based CT emitters, HD and its brominated analogue BrD (Figure 4.1a and 4.1b). Both molecules feature a weak donor–acceptor architecture and exhibit a HLCT state. While HD aggregates emit blue delayed fluorescence, BrD aggregates display yellow phosphorescence (Figure A4.1). We observe a correlation between the luminescence behaviour and aggregation pattern. Crystalline HD forms J-aggregates *via* oxygen-centred interactions, reducing ΔE_{ST}, promoting RISC and favouring DF. In contrast, crystalline BrD forms H-aggregates through π–π and Br···H interactions, increasing ΔE_{ST}, suppressing RISC and leading to dominant RTP. Spectroscopic and theoretical analyses establish a direct link between aggregation and delayed emission behaviours, offering a strategy to tune RTP and DF in bio-organic luminescent materials.

4.2. Results and Discussion

4.2.1. Synthesis, structural characterization and optical properties

Novel indole-based molecules, HD and BrD, were synthesized following synthetic procedures adapted from a previous report.[116] Benzylation of ethyl 5,6-dimethoxy-1*H*-indole-2-carboxylate (DMICE) with benzyl bromide yielded HD in 71% yield (Scheme A4.1, Figures A4.2 and A4.3). Similarly, bromination of DMICE using *N*-bromosuccinimide (NBS), followed by benzylation, produced BrD in 58% yield (Scheme A4.2, Figures A4.4 and A4.5). High-quality, colourless single crystals suitable for X-ray crystallography were obtained by slow evaporation of the indole-based derivatives in ethyl acetate/hexane mixtures at room temperature. The molecular structures of HD and BrD were unequivocally confirmed through single-crystal X-ray diffraction, which also revealed their solid-state packing arrangements (Figures 4.1c, 4.1d and A4.6). HD crystallized in the orthorhombic crystal system with the space group $Pca2_1$, while BrD adopted the monoclinic crystal system with the space

group $P2_1/c$ (Table A4.1). Dihedral angles of 78° and 79° were observed between the indole unit and the benzyl group in HD and BrD respectively, indicating similar conformational preferences in the solid state. To further validate these findings, geometry optimizations were performed at the cam-b3lyp/6-311+g(d,p) level of theory. The calculated dihedral angles of approximately 72° and 74° for HD and BrD respectively, were in agreement with the experimental values obtained from single-crystal X-ray diffraction (Figure A4.7), supporting the reliability of the computational approach.

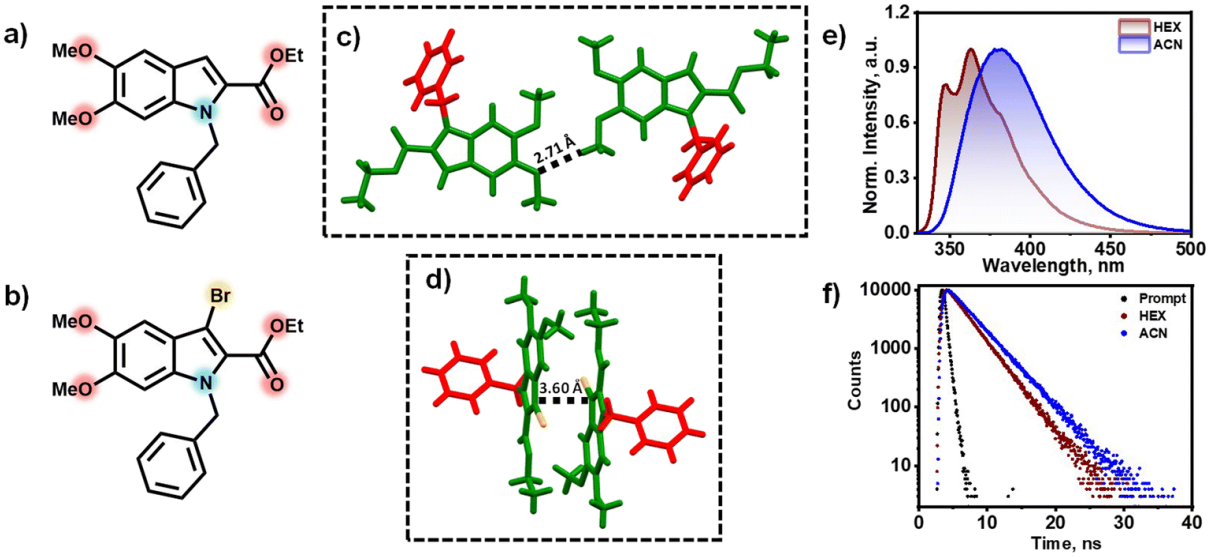

Figure 4.1: Chemical structures of a) HD and (b) BrD; crystal packing of c) HD and d) BrD showing the intermolecular distances; e) normalized fluorescence spectra of HD in HEX and ACN; f) prompt fluorescence lifetime profile of HD in HEX and ACN.

The electronic properties of HD and BrD were investigated using UV-vis absorption spectroscopy, fluorescence emission spectroscopy, and time-correlated single-photon counting (TCSPC) measurements. The UV-vis absorption spectrum of HD in hexane (HEX) exhibited a maximum at 303 nm, closely resembling the absorption characteristics of 5,6-dihydroxyindole carboxylic acid (DHICA), which is the monomer of the bio-pigment eumelanin.[23, 75, 98, 107] In contrast, the brominated analogue BrD showed a red-shifted absorption maximum at 309 nm in HEX compared to that of HD in HEX, attributed to a reduced HOMO–LUMO gap induced by bromine incorporation (Figure A4.8a).[199] Upon photoexcitation, HD in HEX displayed a fluorescence emission maximum at 363 nm, while BrD in HEX exhibited a slightly red-shifted

fluorescence maximum at 368 nm (Figure A4.8b), corresponding to a bathochromic shift of ~5 nm. Photoluminescence quantum yield measurements in HEX, determined by the relative method, revealed a significant decrease for BrD compared to HD, likely due to the heavy atom effect of bromine.[107] Specifically, HD exhibited a photoluminescence quantum yield (ϕ_f) of 52.0% in HEX, which dropped to 1.9% for BrD in HEX, highlighting the pronounced impact of bromine substitution on emission efficiency.[87]

To explore solvent effects, the steady-state UV-vis absorption and fluorescence spectra of HD and BrD were recorded in two solvents of different dielectric constants, *i.e.*, HEX (ε = 1.88) and acetonitrile (ACN, ε = 37.5). The UV-vis absorption spectra of both compounds showed minimal solvent dependence, indicating that the $S_0 \rightarrow S_1$ transition is dominated by an LE state with negligible solvent sensitivity (Figure A4.9). In contrast, the fluorescence spectra exhibited significant solvent-dependent changes. In nonpolar HEX, the emission spectra of HD and BrD displayed well-resolved vibronic features, whereas in polar ACN, the spectra broadened and red-shifted, suggesting the emergence of HLCT character in the relaxed S_1 state (Figure 4.1e and A4.10).[180] In both HD and BrD, the HLCT state likely arises from the interplay and coupling between LE and CT states. As solvent polarity increases, the CT energy level decreases due to stabilization from stronger solvent interactions, while the LE state remains largely unchanged.[181] In low-polarity solvents, luminescence is primarily governed by the LE component, as indicated by the vibronically resolved emission band. With increasing polarity, the lower-energy CT component progressively influences the emission process, leading to an inter-crossed HLCT character.

Solvent polarity also affected the fluorescence lifetimes of HD and BrD. In nonpolar HEX, HD showed a mono-exponential decay with a 2.8 ns lifetime, which increased to 3.4 ns in polar ACN, consistent with HLCT emission (Figure 4.1f). The mono-exponential behaviour suggests that LE and CT states merge into a single hybridized state.[181] This state likely combines the large dipole moment of the CT state with the strong orbital overlap of the LE state, resulting in high emission. BrD in HEX showed an average fluorescence decay of <1 ns. Meanwhile in ACN, BrD showed a mono-exponential fluorescence lifetime of 3.4 ns (Figure A4.11). The mono-exponential and increased fluorescence lifetimes in polar solvents for HD and BrD reflect the influence of solvation and the radiative nature of the excited-state hybrid

charge-transfer process.[180] The excited-state electronic configuration further confirms the HLCT nature of emission in HD and BrD, involving electron density redistribution between the indole ring and the benzyl unit (Figures 4.2e and A4.12; Tables A4.2 and A4.3), unlike their non-benzylated analogues, where both hole and electron densities remain confined only to the indole moiety (Figure A4.13).

The UV-vis absorption and emission spectra of HD and BrD in the crystalline state are presented in Figure A4.14a. Significant differences between the solution and crystalline spectra of HD and BrD highlight the impact of aggregation.[200] In the crystalline state, HD exhibited a broadened absorption band extending up to 390 nm, with a tail reaching 400 nm, indicative of strong intermolecular interactions. For crystalline BrD, the absorption spectrum showed even greater broadening and a pronounced red shift, with prominent absorption up to 400 nm. Fluorescence emission spectra in the crystalline state revealed maxima at 382 nm for HD and 392 nm for BrD (Figure A4.14b). The substantial red shifts in the electronic absorption spectra of the crystalline assemblies compared to their monomeric forms suggest excitonic interactions. Additionally, crystalline BrD exhibited a weak, red-shifted emission band at 475–650 nm, which we attribute to triplet-state emission, consistent with previous studies on modified indole molecules.[87] Photoluminescence quantum yield measurements in the crystalline state, determined using the absolute method, yielded values of 21.3% for HD and 0.18% for BrD.

To elucidate how structural motifs govern excited-state behaviour,[125] we analysed the crystal packing of the benzylated indole molecules HD and BrD, identifying their dominant dimeric arrangements (Figure A4.15). In HD, close intermolecular contacts are dominated by H···H interactions, as revealed by Hirshfeld surface analysis, which shows that these account for 51.4% of the total intermolecular contacts (Figure A4.16 and Table A4.4). A distinctive tail-to-tail dimeric configuration stabilized by CH···O contacts was observed in HD. In contrast, BrD features additional stabilizing contacts, including Br···H (10.9%) and C···C (3.3%) interactions (Figure A4.17 and Table A4.4). Notably, the C···C contacts in BrD facilitate π–π stacking with an intermolecular distance of 3.60 Å, forming a stacked dimeric assembly absent in HD (Figure 4.1d). To quantify the stabilizing forces in these aggregates, symmetry-adapted perturbation theory (SAPT(0)) calculations were performed on the dimers,[123] revealing dispersion interactions as the primary contributor for the tail-to-tail dimer in HD and π–π

stacked dimer in BrD (Table A4.5). Non-covalent interaction (NCI) index analysis and electrostatic potential (ESP) maps further corroborated these findings, indicating strong stabilization within both dimer assemblies (Figures A4.18 and A4.19).[201, 202]

Aggregation behaviour was further investigated in THF/H_2O mixtures. Decreasing the f_{THF} percent (f_{THF} is the fraction of THF in the total volume of solution) led to changes in the fluorescence emission of HD and BrD aggregates. For HD, the fluorescence intensity red-shifted from 373 nm in 100% THF to 413 nm in 10% THF (Figure A4.20). On the other hand, BrD exhibited an additional band appearing at 470–650 nm in 10% THF compared to the sharp emission band centred at 377 nm in 100% THF. The fluorescence intensity of BrD aggregates at 360–450 nm decreased by ~8.5 times in 10% THF solutions with respect to 100% THF solutions (Figure A4.21). These results demonstrate that aggregation significantly alters the photophysical properties of HD and BrD, modulating their decay pathways in the solution state. The spectral shifts and emission behaviour in THF/water mixtures closely parallel those observed in the crystalline state, indicating that solution-state aggregates can emulate solid-state electronic interactions.

4.2.2. Delayed Emission in Monomer Versus Aggregates

To elucidate the differences in excited-state behaviour among monomeric solutions, aggregate solutions, and crystalline states, gated-emission experiments were conducted. At room temperature, crystalline HD exhibited a strong, well-defined delayed emission peak at 387 nm with a lifetime of 484 μs upon 340 nm excitation (Figure 4.2a and 4.2b). This peak closely aligns with the prompt crystalline emission, suggesting DF originating from the singlet excited state ($S_1 \rightarrow S_0$). Temperature-dependent gated emission measurements further confirmed the role of thermal energy in activating the DF (Figure A4.22): at 77 K, the delayed emission intensity and lifetime significantly decreased, with the emergence of a vibronically resolved red-shifted band (480–650 nm), attributed to triplet-state emission ($T_1 \rightarrow S_0$). This behaviour indicates that thermal energy is essential for efficient RISC in HD, a hallmark of RISC mediated DF materials.[168] To exclude the possibility of triplet–triplet annihilation (TTA), we examined the excitation power dependence of the delayed emission lifetimes. The observed invariance in lifetime across different excitation intensities supports a monomolecular RISC pathway (Figure

A4.23). This is consistent with recent studies reporting efficient RISC in CT systems, even in the presence of relatively large S_1–T_1 energy gaps.[189, 203]

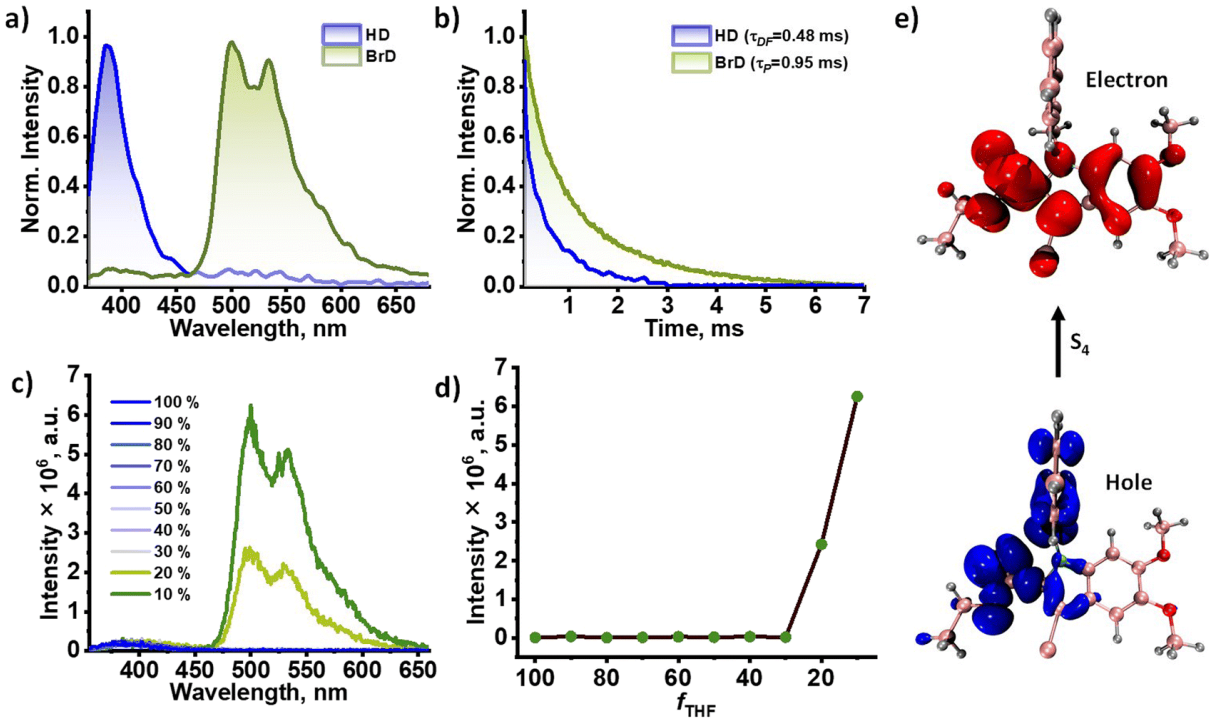

Figure 4.2: a) Normalized gated emission spectra of crystalline HD and BrD at room temperature (delay = 0.05 ms); b) decay profiles of gated emission of crystalline HD and BrD; c) gated emission spectra of BrD aggregates in different % of THF concentration (f_{THF}) in THF-water mixtures at room temperature (delay = 0.05 ms); d) plot showing emergence of RTP (λ_{em} = 500 nm) with increase in f_{THF}; e) singlet excited state of BrD showing partially delocalized hole and electron densities.

In solution, HD displayed weak DF with a lifetime of <10 μs, suggesting that aggregation provides a rigid environment and enhances RISC, facilitating upconversion to the CT state (Figure A4.24).[183] In contrast, crystalline BrD exhibited pronounced RTP, with a strong phosphorescence band spanning 480–650 nm and a lifetime of 950 μs (Figure 4.2a and 4.2b). A weaker DF band (370–450 nm) was also observed. The phosphorescence intensity was nearly 15 times greater than the DF, highlighting efficient triplet-state emission. The presence of bromine in BrD likely influences the dominance of phosphorescence by enhancing ISC, while crystallization favours radiative decay over nonradiative relaxation from the lowest

triplet state.[185, 204] In solution, BrD primarily emits *via* fluorescence at 360–440 nm at room temperature, but at 77 K, a distinct phosphorescence band (460–660 nm) emerged, with an intensity ~22 times greater than fluorescence intensity and a lifetime of 19.3 ms (Figure A4.25). The temperature dependence confirms the phosphorescent nature of the emission, with bromine facilitating the ISC. Crystallization further stabilizes triplet excitons by suppressing nonradiative decay and minimizing oxygen quenching, demonstrating the critical role of molecular packing in modulating excited-state dynamics (*vide infra*).[185]

To mimic interchromophore interactions and the rigid crystalline environment in solution, delayed emission measurements were performed for HD and BrD in THF/water mixtures. For HD, decreasing the THF fraction (f_{THF}) significantly altered the DF intensity, with a 3-fold increase at f_{THF} = 10% compared to f_{THF} = 100% (Figure A4.26). The DF lifetime of HD increased from >10 μs in f_{THF} = 100% to 0.15 ms in f_{THF} = 10% solutions. This suggests that aggregation induces rigidity within the chromophores, promoting RISC, even within solution-states.[203] For BrD, phosphorescence emerged in solutions where f_{THF} = 20% and further intensified as f_{THF} decreased (Figure 4.2c and 4.2d). At f_{THF} = 10%, the phosphorescence intensity was ~25 times greater than the fluorescence at 385 nm, with lifetimes extending from 0.55 ms (f_{THF} = 20%) to 0.75 ms (f_{THF} = 10%), indicative of aggregation-induced phosphorescence (Figure A4.27). Incorporating HD and BrD into poly(methyl methacrylate) (PMMA) matrix resulted in delayed emission lifetimes that were shorter than those observed in the crystalline state, though still significantly longer than in neat aggregate (f_{THF} = 100%) solutions. PMMA-coated thin films of HD exhibited DF at 385 nm with a lifetime <10 μs, while BrD films showed intense phosphorescence (470–650 nm) with a lifetime of 0.08 ms (Figure A4.28). Although the PMMA matrix acts as an oxygen barrier and suppresses quenching, the delayed emission lifetimes were reduced compared to the crystalline state, likely due to differences in molecular packing and rigidity.[203] This suggests that while PMMA can stabilize triplet excitons to some extent, the highly ordered crystalline environment provides superior stabilization for long-lived delayed emission.[205] Nevertheless, the PMMA films successfully replicated the key photophysical features of the crystalline state, demonstrating the potential of polymer matrices to mimic solid-state behaviour in thin-film applications. The ability to replicate crystalline electronic interactions and rigid environments

in solution-state aggregates and polymer matrices establishes a versatile platform for manipulating photophysical behaviour, bridging the gap between solution and solid-state properties.

4.2.3. Excited State Deactivation

To investigate the excited-state processes responsible for efficient delayed emission in the indole-based molecules HD and BrD, femtosecond transient absorption (fsTA) measurements were performed. The fsTA spectra of HD and BrD in THF are presented in Figure 4.3. For HD, photoexcitation at 330 nm using a 100-fs pump pulse generated a broad positive feature spanning 470–740 nm, resembling the singlet absorption observed in DHICA and its protected derivatives.[75, 86, 87] Within few tens of picoseconds, the absorption maximum red-shifted from 600 nm to 660 nm, and the resulting species persisted throughout the experimental time window of ~3.5 ns. Global fitting of the time-resolved fsTA spectra using an A → B → GS (GS = ground state) sequential model yielded the evolution-associated spectra (EAS) for HD. Deconvolution of the fsTA spectra of HD in THF revealed two spectral components. The first component (component A), attributed to the relaxation of the singlet excited state, decayed with a lifetime of 63.7 ps. The second component (component B), corresponding to the HLCT state, decayed within 3.66 ns, closely matching the fluorescence lifetime. Additionally, a marginal rise at ~460 nm was observed for HD at time delays >3.5 ns, which, based on previous studies of modified indoles, could reveal the triplet state evolution from the HLCT state.[87]

For BrD in THF, excitation at 330 nm produced a broad singlet absorption feature between 510–740 nm, peaking at 665 nm (Figure 4.3d). The decay of the singlet excited state within a few picoseconds was accompanied by the emergence of a peak at ~460 nm. Unlike HD, the initial broad feature at 600 nm was not observed for BrD, likely due to faster CT dynamics. Given that ISC occurs within a few picoseconds, solvent relaxation of the Frenkel exciton state may occur on a timescale comparable to or faster than the instrument's response function. Global fitting of the fsTA spectra of BrD using the A → B → GS model yielded two spectrally distinct components (Figure 4.3e). The first component (component A), representing the decay of the HLCT state, exhibited a lifetime of 9.5 ps, while the second component (component B), attributed to triplet states, persisted throughout the experimental time delay

(>3.5 ns).[87] The CT and ISC dynamics of HD and BrD mediate the delayed emission pathways observed for the molecules. The distinct spectral evolution and lifetimes of the HLCT and triplet states provide critical insights into the photophysical mechanisms underlying delayed emission in these modified indoles.[206] The benzyl groups in HD and BrD introduce low-energy CT states that hybridize with the main indole unit's singlet $^1(\pi–\pi^*)$ state. These HLCT states comprise a partially localized electron cloud across the indole backbone and benzyl ring, reducing the exchange energy and promoting triplet formation in both compounds. Furthermore, in BrD, bromine accelerates intersystem crossing (ISC) and yields efficient triplet-state population. In contrast, HD exhibits a long-lived CT state that facilitates RISC from the triplet excited state back to the emissive HLCT state, enabling DF.

Given the efficient DF and RTP observed in crystalline and polymer-coated films of HD and BrD, fsTA measurements were extended to concentrated thin films of HD and BrD embedded in PMMA matrices. The excited-state absorption peaks of these aggregated films exhibited subtle deviations from solution-phase peaks, likely due to perturbations in excited-state energetics induced by molecular aggregation.[207] For HD film, photoexcitation at 330 nm generated an excited-state absorption band with a maximum at 575 nm (Figure A4.29). Within a few picoseconds, the spectral intensity diminished, and a broader species developed at ∼440–700 nm. Spectral deconvolution revealed three components in the fsTA spectra. The first component (component A), associated with the singlet excited state, decayed within 4.9 ps to form component B. Component B is noteworthy due to its broadened characteristic and is attributed to the HLCT state. The HLCT state decayed within 113.8 ps to form a relaxed HLCT state with significant absorption in 440 nm range.[87, 107] The relaxed HLCT state persisted even at time delays greater than 3.5 ns. For BrD, the excited-state dynamics were significantly faster than those of HD (Figure 4.30). Photoexcitation initially produced an excited-state absorption band at 575 nm, which decayed within a few hundred femtoseconds to form a broad HLCT band. The population of triplet states was observed upon the decay of the broad HLCT state. Spectral deconvolution identified the singlet excited state (component A) with a lifetime of 1.9 ps, followed by the HLCT state (component B) with a decay time constant of 69.0 ps. Triplet excited states (component C) evolved with the decay of HLCT state and persisted for >3.5 ns. In both HD and BrD thin film aggregates, ultrafast population of intermediate HLCT and triplet

states as well as rigidification suppresses nonradiative internal conversion and vibronic relaxation, thereby enhancing delayed emission efficacy.

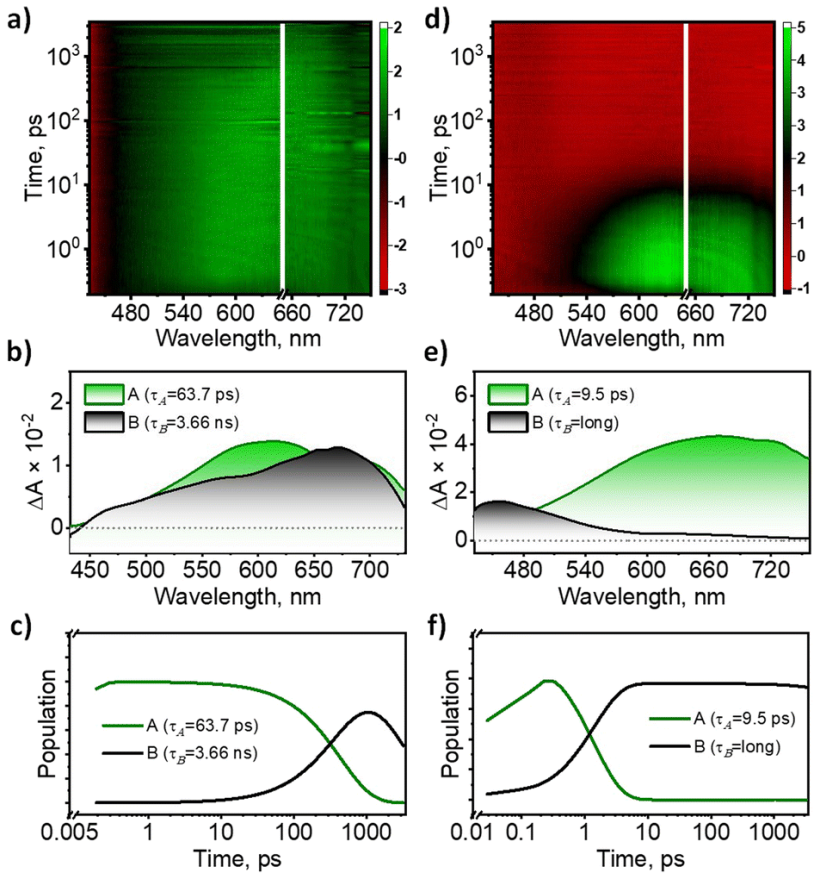

Figure 4.3: a) Femtosecond transient absorption (fsTA) contour plot of HD in THF (colour scale of the contour plot represents $\Delta A/10^2$ a.u.), b) deconvoluted EAS plot of HD in THF, c) deconvoluted decay time constants of the EAS for HD in THF; d) FsTA contour plot of BrD in THF, (e) deconvoluted EAS plot of BrD in THF, (f) deconvoluted decay time constants of the EAS for BrD in THF.

Time-resolved electron paramagnetic resonance (TR-EPR) measurements in crystalline HD and BrD further confirmed the triplet excited state populations in the crystalline samples. After photoexcitation at 355 nm by a nanosecond pulsed laser, a TR-EPR spectrum was observed with an electron spin polarization (ESP) pattern of E/E/E/A/A/A for both samples at 80 K, where A and E represent enhanced absorptive and emissive polarizations, respectively (Figure A4.31). The triplet states exhibit zero-field-splitting (ZFS) simulated by the parameters

of (D, E) = (0.107 cm^{-1}, −0.015 cm^{-1}) for HD and (0.107 cm^{-1}, −0.035 cm^{-1}) for BrD considering the relative sublevel populations by ISC of (P_x, P_y, P_z) = (0.5, 0.5, 0) for both samples. The EPR parameters are typical of the $^3(\pi–\pi^*)$ characters of the metal-free aromatic molecules, denoting that the in-plane sublevel populations occurs *via* the spin–orbit coupling through the vibronic effect between the $^1(\pi–\pi^*)$ and $^3(\pi–\pi^*)$ characters, while smaller magnitudes of the parameters of $|D|$ (<0.05 cm^{-1}) are reported for the ^{3}CT characters.[208-210] The observed triplet characters are consistent with the formation of low-lying T_1 states with $^3(\pi–\pi^*)$ character, stabilized by spin–spin exchange, as supported by DFT calculations (Figure A4.32).[211]

Our investigation provided fresh insights into the mechanisms governing delayed emission in these systems. In BrD aggregates, the energy levels were relatively well separated so that the initially excited singlet state predominantly evolved into HLCT states, which then efficiently generated lower-energy triplet excited states. These processes were strongly influenced by intermolecular interactions and the rigid constraints of the solid state, resulting in an alternative pathway for triplet exciton decay rather than efficient RISC.[206] On the other hand, HD aggregates displayed significant excited-state mixing due to the small singlet–triplet energy gap: a transient CT state rapidly relaxed into a lower-energy configuration with significant triplet mixing. The small energetic gap between the CT and higher triplet excited states enabled robust mixing, as suggested by correlated transient absorption features.[206] The nature of this CT-triplet mixture evolved over time, evidenced by the persistence of the relaxed HLCT absorption even at time delays greater than 3.5 ns. In HD, reverse internal conversion from the localized T_1 state to higher-lying HLCT triplet states could be facilitated. Further, a spin-flip transition to the ^{1}CT configuration could be enabled, which subsequently relaxes radiatively *via* mixing with the $^1(\pi–\pi^*)$ state. These findings are consistent with recent studies on small π-conjugated DF systems, which emphasize that a substantial CT contribution and close energetic proximity to a T_n state, can significantly enhance RISC.[212] A detailed analysis of the aggregate structures of HD and BrD, presented in the following section, elucidates why crystalline samples exhibit efficient delayed emission compared to their respective solution counterparts.

4.2.4. Influence of interchromophore interactions on delayed emission

Exciton coupling within the dimeric assemblies directly influence the difference in photophysical properties of HD and BrD crystals (Table A4.6). Exciton splitting arises from long-range coulombic coupling (J_{Coul}) and short-range CT coupling (J_{CT}) mediated by HOMO–LUMO overlaps (Figure A4.33).[51] For HD, electronic coupling calculations revealed a J_{Total} of −142 cm^{-1}, characteristic of J-aggregate behaviour dominated by coulombic interactions.[125] This J-type coupling aligns with the observed red-shifted, narrow absorption band in the crystalline state (Figure A4.14), as head-to-tail transition dipole alignment decreases energy of the allowed transition. On the other hand, BrD demonstrated J_{Total} = 213 cm^{-1}, reflecting H-aggregate behaviour with significant contributions from both coulombic and orbital overlap interactions. The absorption broadening in the blue-wavelength region for BrD crystals arises from face-to-face π-stacking, which increases the energy of the allowed excitonic state, which is a hallmark of H-aggregates (Figure A4.14).[125] Transition dipole moment analyses confirmed the aggregation patterns in HD and BrD (Figure A4.34).

Excited-state energy calculations on crystallographic dimers further underscored the role of aggregation in modulating excited-state pathways (Figure 4.4). In HD, the dimeric $S_0 \rightarrow S_1$ transition exhibited a significant oscillator strength (f = 0.15) which is characteristic of J-aggregation.[51, 125] Notably, while the HD monomer displayed an extremely small singlet–triplet energy gap (ΔE_{ST} = 0.003 eV), aggregation tuned this gap to ΔE_{ST} = −0.003 eV (Tables A4.7 and A4.8). This near-zero, marginally negative energy gap facilitates efficient RISC from T_n to S_1, following reverse internal conversion from T_1, thereby enabling and supporting the observed delayed fluorescence in HD aggregates.[189] In contrast, the $S_0 \rightarrow S_1$ transition in BrD aggregates exhibited near-zero oscillator strength, contrasting sharply with the monomer's value (f = 0.31), which is indicative of H-aggregation. As a result, the $S_0 \rightarrow S_2$ transition emerged as the first bright state. Moreover, for monomeric BrD, the ΔE_{ST} was 0.047 eV, which increased to 0.77 eV upon aggregation (Tables A4.9 and A4.10). Although crystallization-induced rigidity and the presence of bromine can suppress nonradiative decay and enhance ISC, these factors alone do not account for the observed RTP in BrD. Notably, previously reported brominated, non-benzylated indole-based analogues did not exhibit RTP in the crystalline state, despite comparable heavy-atom substitution and packing-induced rigidity.[87, 107] H-aggregation,

which favours strong π–π stacking, typically promotes ISC and the stabilization of triplet states, directing the system toward RTP rather than DF.

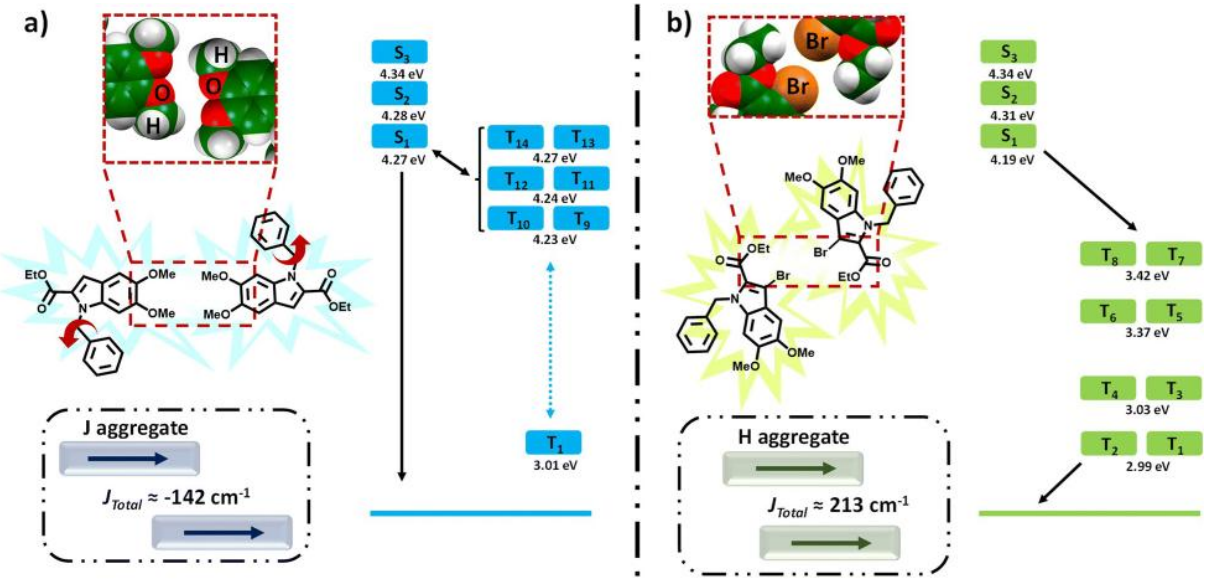

Figure 4.4: a) In crystalline state, HD molecules are arranged as an oxygen-centred J-type aggregate with reduced singlet–triplet energy gap, enabling DF; b) in crystalline state, BrD molecules are arranged as a π–π-stacked H-type aggregate with increased singlet–triplet energy gap, disabling DF and promoting RTP. The navy blue and olive-green arrows denote the transition dipole moments for the S_1 transition in J-aggregates of HD and S_2 transition in H-aggregates of BrD respectively.

In both HD and BrD aggregates, the number of high-lying triplet excited states increases (Figure 4.4), suggesting that crystalline packing facilitates additional ISC pathways compared to solution. To account for the stark contrast between the DF observed in HD crystals and the RTP in BrD crystals, the emission oscillator strength of the S_1 state also emerges as a key distinction factor. As supported by the excited state energy calculations (Tables A4.7–A4.10), the oscillator strength of S_1 state is substantially larger in the HD dimer than in the BrD dimer. This difference indicates more efficient radiative decay in HD ($k_{r,f} \approx 1.21 \times 10^8$ s^{-1}) and notably suppressed radiative decay in BrD ($k_{r,f} \approx 7.61 \times 10^4$ s^{-1}), according to Einstein's expression for spontaneous emission, $k_{r,f} = fE_g^2/1.499$, where E_g is the energy of S_1 state and f is the oscillator strength, highlighting the crucial role of aggregation in tuning emission properties. Although the oscillator strength (f) of the S_1 state increases upon aggregation in crystalline HD, the

photoluminescence quantum yield decreases in comparison to solution, owing to the emergence of closely spaced triplet states that introduce additional ISC pathways competing with radiative decay.

The excited-state energy landscape in crystalline HD and BrD offers key insights into their divergent emission behaviours. In HD aggregates, although higher triplet states such as T_{13} and T_{14} are nearly isoenergetic with S_1, delayed fluorescence occurs due to a thermally assisted, multistep RISC mechanism rather than direct RISC from these higher states. Transient absorption spectroscopy suggests that the T_n states exhibit HLCT character, while time-resolved EPR measurements identify T_1 as a localized $^3(\pi–\pi^*)$ state. These results, together with temperature-dependent gated emission, support that excitons initially relax to T_1, followed by vibrationally activated upconversion to higher-lying T_n states, which then undergo RISC to S_1.[213, 214] Importantly, the distinct electronic characters of T_1 (LE) and T_n (HLCT) enable non-adiabatic coupling, facilitating efficient RISC through a $T_1 \rightarrow T_n \rightarrow S_1$ pathway. The absence of strong π–π interactions around the benzyl substituents in HD may enable low-frequency torsional modes, which can couple to phonon modes in the aggregate to compensate the activation enthalpy-entropy to assist the upconversion.[215] In contrast, BrD aggregates exhibit neither near-resonant T_n states nor structural flexibility around the benzyl groups (Figure A4.35). The presence of strong π–π stacking interactions in BrD constrains molecular motion and restricts access to thermally driven pathways. Additionally, the narrower triplet manifold (T_n–T_1 ~ 0.43 eV) facilitates rapid internal conversion, precluding repopulation of T_n and suppressing RISC. Collectively, these findings illustrate how molecular packing modulated the excited-state dynamics: J-aggregates, as observed in HD, lowered ΔE_{ST} and enhanced RISC to favour DF, while H-aggregates in BrD increased ΔE_{ST} and suppressed RISC, channelling excitation energy into phosphorescence.

4.3. Conclusion

The present work demonstrates how molecular aggregation in bio-inspired HLCT systems can effectively modulate the energy gap between singlet and triplet states, enabling a tunable transition between the DF and RTP. By leveraging J-aggregation in a eumelanin-based molecule (HD) and H-aggregation in its brominated derivative (BrD), we show that the interplay between

oxygen-centred and bromine-induced interactions can significantly influence the excited-state dynamics, ultimately steering the emission pathway toward DF or RTP. The HLCT state integrates the orbital overlap of LE states with the dipolar character of CT states, enabling efficient radiative decay in crystalline HD. Gated emission measurements reveal that the phosphorescence lifetime for crystalline BrD is 0.95 ms, while the DF lifetime for crystalline HD is 0.48 ms, both at room temperature, underscoring the efficiency of the long-lived emission channels for both systems. Solution-phase aggregation of HD and BrD is achieved in THF/H_2O mixtures, where the DF lifetime for HD aggregates is 0.15 ms, while the RTP lifetime for BrD aggregates is 0.75 ms in 10% THF solutions. The hybrid CT states play a central role in mediating the excited-state evolution, with aggregation type (J-*versus* H-aggregate) deciphering the delayed emission mechanisms (DF *versus* RTP) in HD and BrD. Our findings highlight the importance of aggregation-assisted energy gap modulation in achieving long-lived, efficient emission in organic luminescent materials. Furthermore, the work presents new opportunities for controlling emission behaviour in solid-state materials, bridging the gap between solution and solid-state properties for practical applications.

4.4. Experimental Section

4.4.1. Syntheses and Characterization

4.4.1.1. Synthesis and Characterization of HD

NaH (45.7 mg, 1.15 mmol) was added in small portions to a solution of DMICE (0.50 mmol) in DMF (10 mL) under argon. After stirring for 30 min, benzyl bromide (178 mg, 0.90 mmol) was added, and the reaction was stirred for 1 h. The mixture was quenched with ice-cold water, extracted with EtOAc, dried over $MgSO_4$, filtered, and concentrated under reduced pressure. The crude product was purified by column chromatography (silica, 30% EtOAc/hexane) to afford HD as a white powder (71% yield).

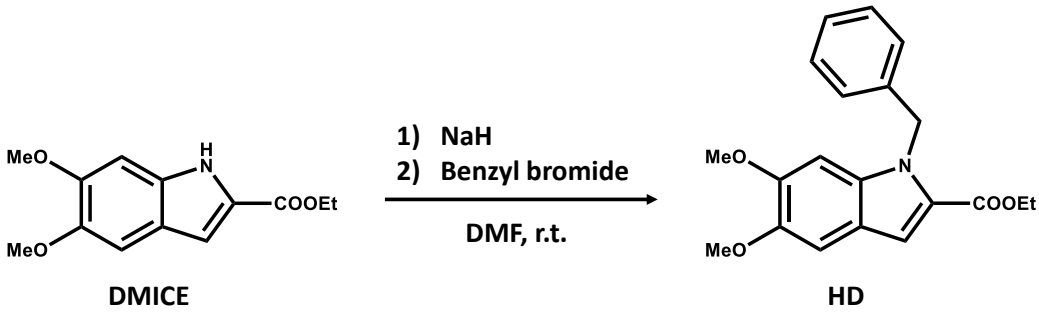

Scheme A4.1: The reaction scheme for the synthesis of HD.

^{1}H NMR (500 MHz, DMSO-d_6, ppm): δ = 7.42-7.33 (m, 4H), 7.29 (s,1H), 7.26 (s,1H), 7.16 (d, J= 7.9 Hz ,2H), 5.97 (s, 2H), 4.38 (q, 2H), 3.92 (s, 6H), 1.40 (t, *J* = 7.0 Hz, 3H).

^{13}C NMR (125 MHz, $CDCl_3$, ppm): δ =161.82, 150.04, 146.27, 138.32, 134.88, 128.60, 127.09, 126.19, 118.94, 110.93, 102.58, 92.77, 60.27, 56.17, 56.05, 48.04, 14.36.

Melting point: 97^{0}C.

4.4.1.2. Synthesis and Characterization of BrD

BrD was synthesized via bromination of DMICE followed by benzylation. Partially dissolved DMICE (0.50 mmol) in MeCN (2 mL) was placed in a 50 mL round-bottom flask, and a solution of N-bromosuccinimide (NBS, 0.525 mmol) in MeCN (7 mL) was added dropwise over 5 min. The mixture was stirred at room temperature for 30 min, diluted with water, and filtered at 0 °C to afford off-white Br-DMICE. To a solution of Br-DMICE (0.48 mmol) in DMF (5.79 mL), NaH (23 mg, 0.58 mmol) was added in small portions. After stirring for 30 min, benzyl bromide (104.3 mg, 0.53 mmol) was added, and the reaction was stirred for 1 h. The mixture was quenched with ice water, extracted with EtOAc, dried over $MgSO_4$, and concentrated under reduced pressure. The crude product was purified by column chromatography (silica, 45% EtOAc/hexane) to yield BrD as a white solid (58%).

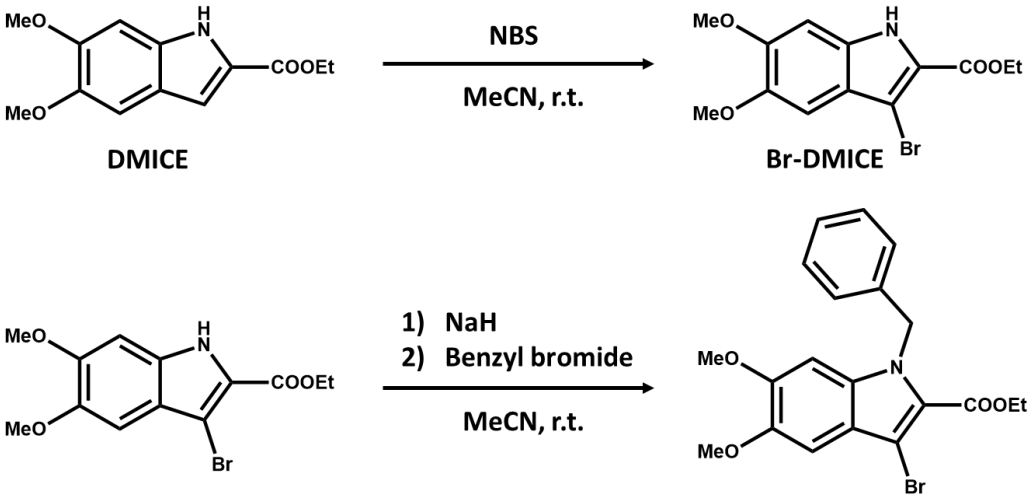

Scheme A4.2: The reaction scheme for the synthesis of BrD.

^{1}H NMR (500 MHz, DMSO-d_6, ppm): δ =7.4-7.2(m, 4H), 6.99 (dd, J=1.8 Hz ,2H), 6.94(s, 1H) 5.81 (s, 2H), 4.27 (q, *J* = 7.1 Hz, 2H), 3.84 (s, 3H), 3.81 (s, 3H), 1.26 (t, *J* = 7.1 Hz, 3H).

^{13}C NMR (125 MHz, $CDCl_3$, ppm): δ=161.07, 150.97, 147.02, 137.88, 133.16, 128.68, 127.28, 123.37, 120.07, 101.17, 99.61, 92.57, 60.87, 56.22, 56.18, 48.93, 14.21.

Melting point: 115^{0}C.

4.5. Additional Figures

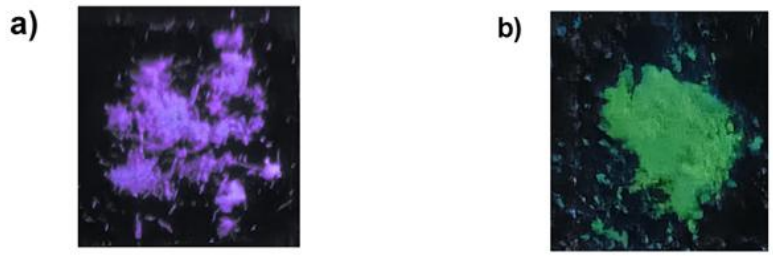

Figure A4.1: Crystalline a) HD; b) BrD upon UV irradiation.

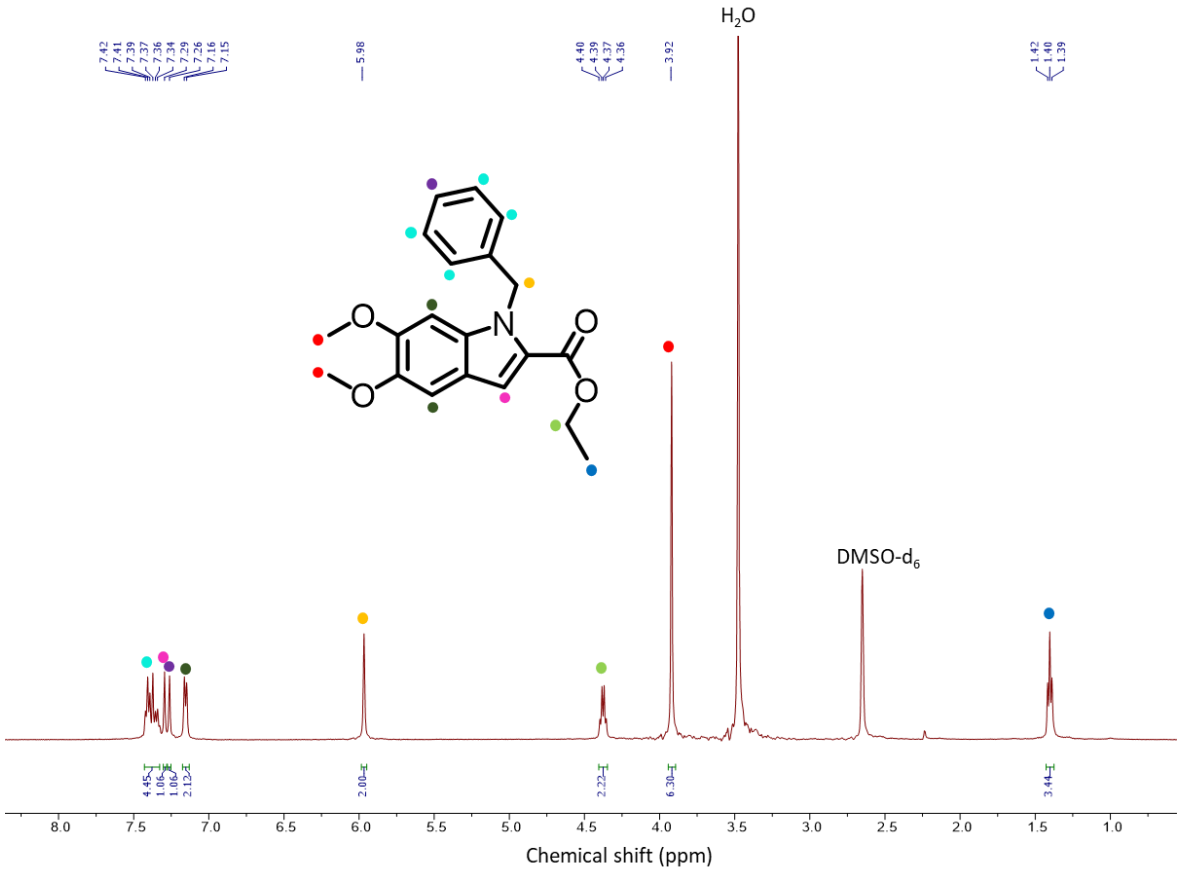

Figure A4.2: ^{1}H-NMR of HD in DMSO-d_6.

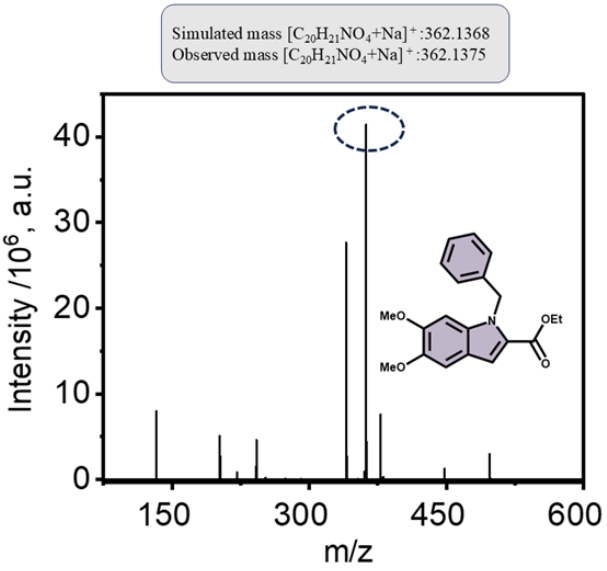

Figure A4.3: ESI-TOF Mass spectrum of HD.

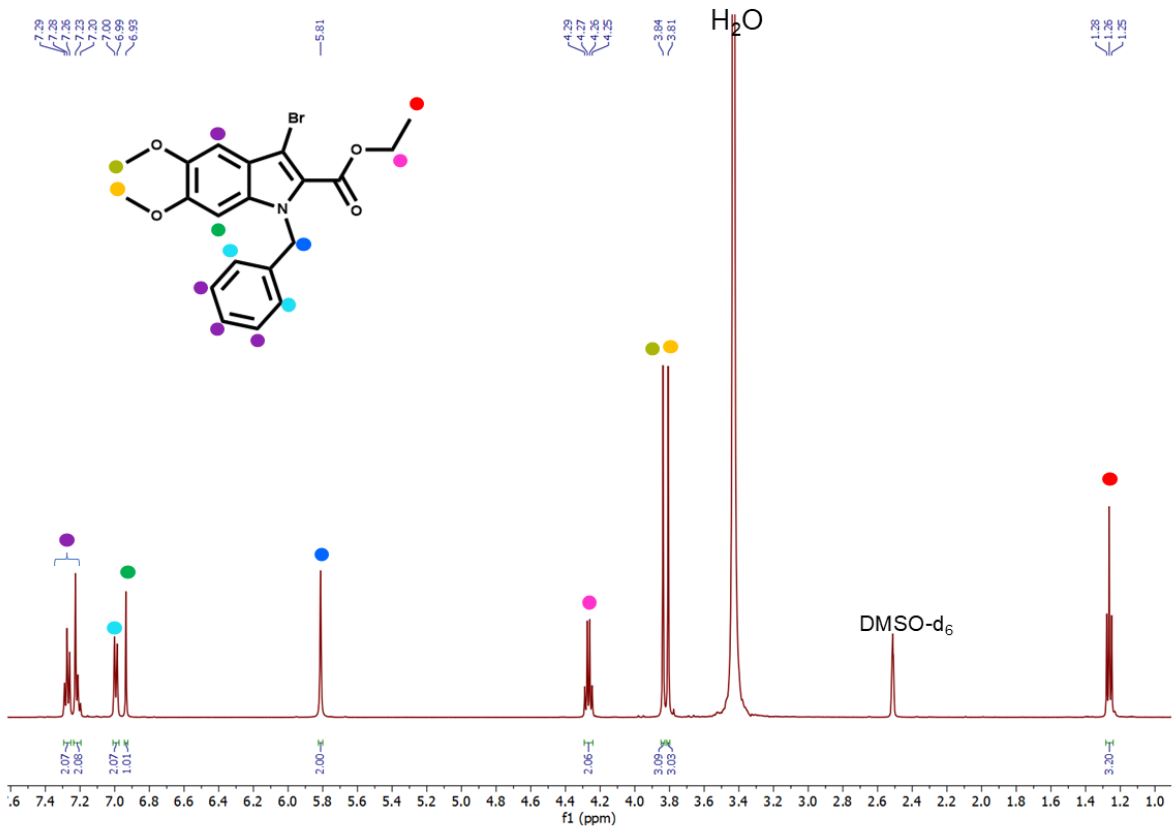

Figure A4.4: ^{1}H-NMR of BrD in DMSO-d_6.

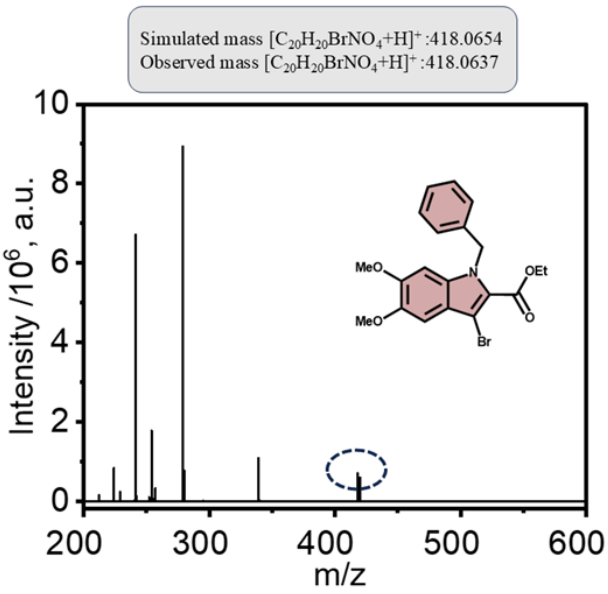

Figure A4.5: ESI-TOF Mass spectrum of BrD.

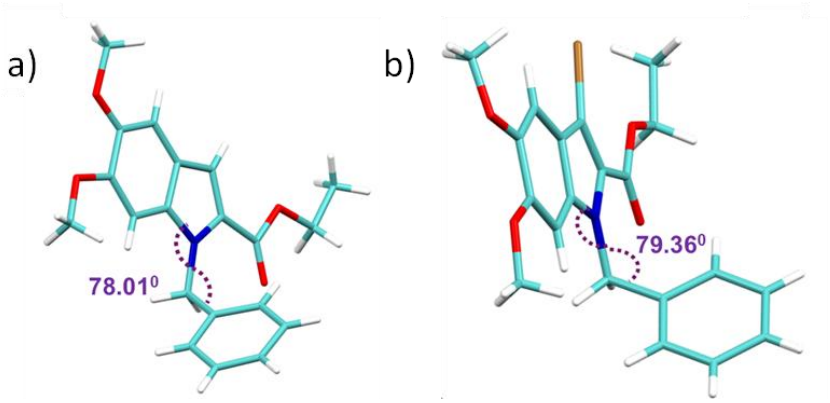

Figure A4.6: Crystal structure obtained for a) HD; b) BrD.

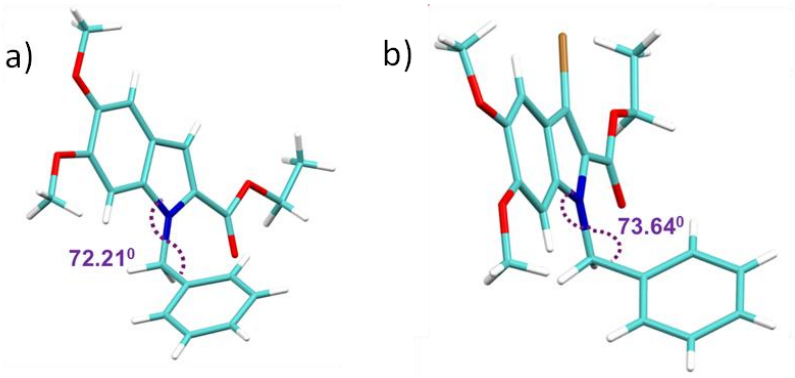

Figure A4.7: Optimised geometry computed at cam-b3lyp/6-311+g(d,p) level of theory for a) HD; b) BrD.

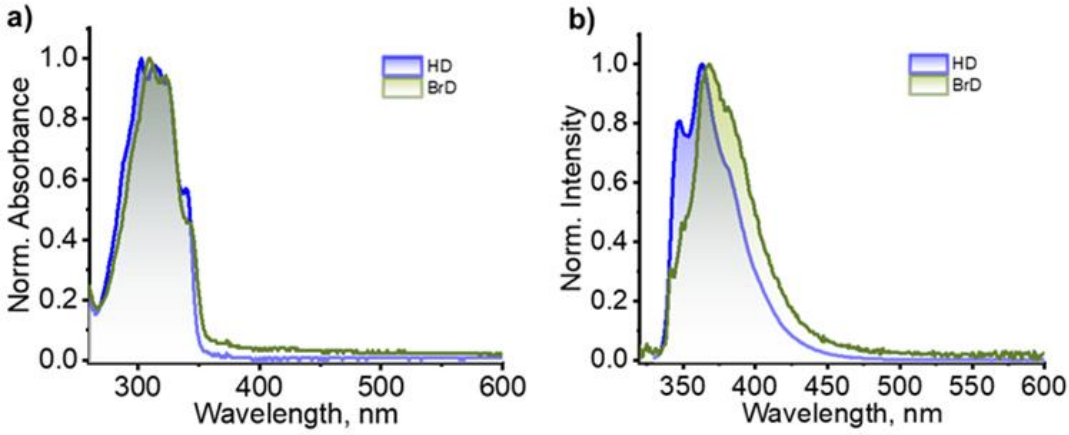

Figure A4.8: a) Normalized absorption spectra of HD and BrD in hexane; b) Normalized emission spectra of HD and BrD in hexane.

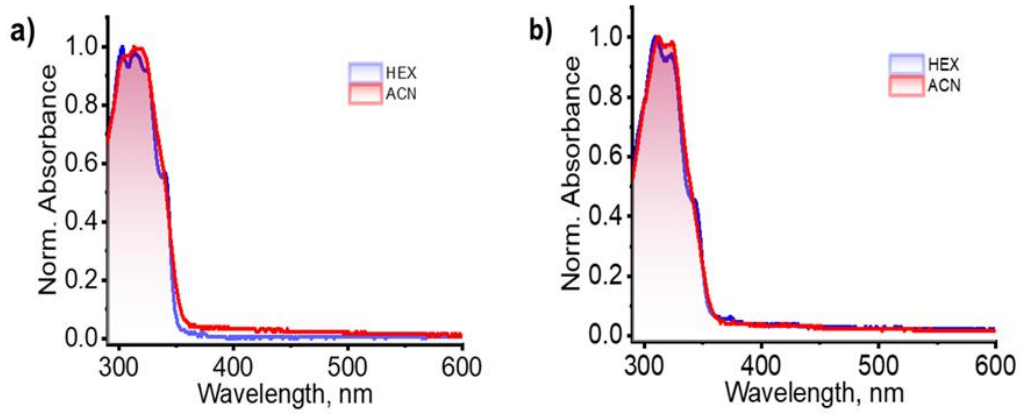

Figure A4.9: Solvent-dependent normalized absorption spectra of a) HD; b) BrD.

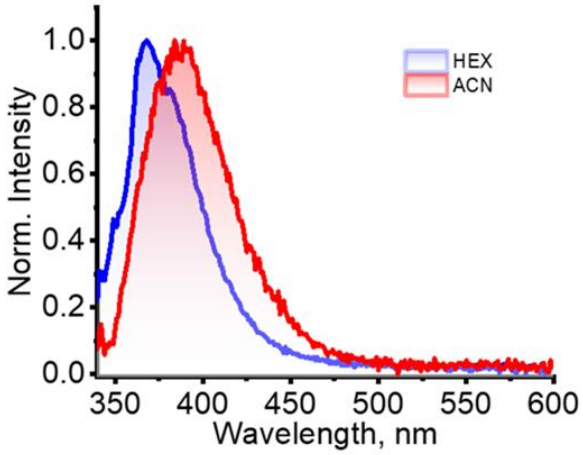

Figure A4.10: Solvent-dependent normalized emission spectra of BrD.

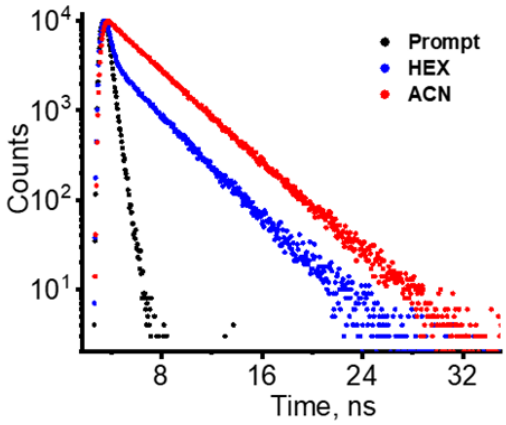

Figure A4.11: Prompt fluorescence lifetime profile of BrD in HEX and ACN.

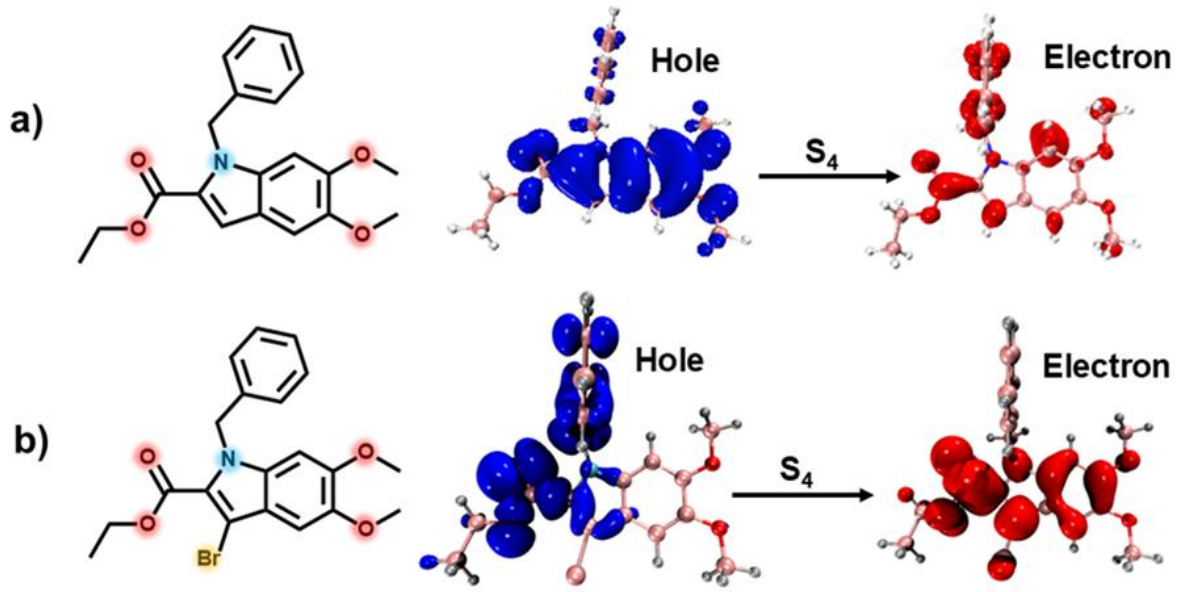

Figure A4.12: a) Singlet excited state of HD showing partial localized hole and electron densities; b) Singlet excited state of BrD showing partial localized hole and electron densities.

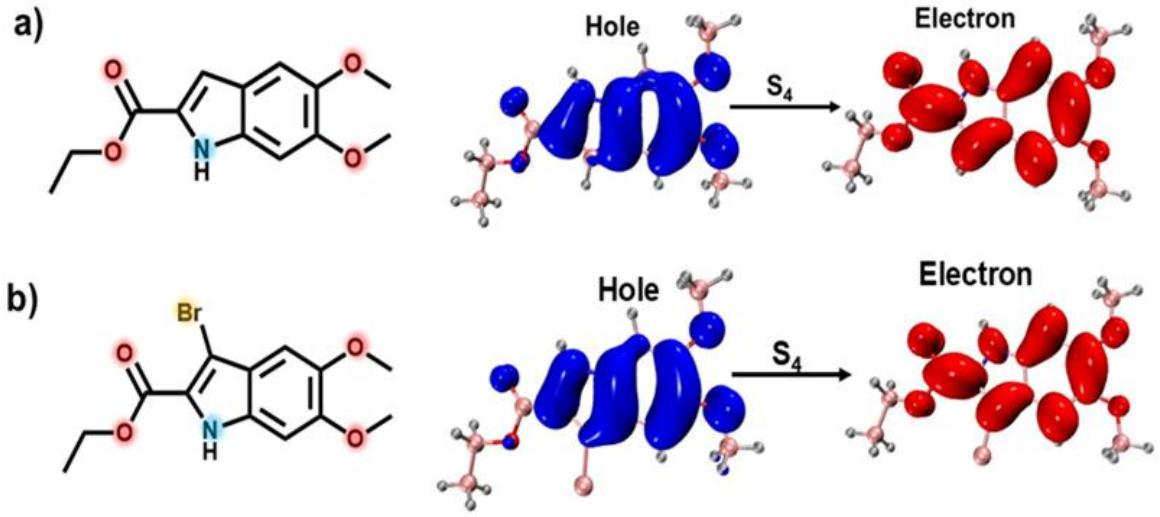

Figure A4.13: a) Singlet excited state of HD without benzyl group showing localized hole and electron densities; b) Singlet excited state of BrD without benzyl group showing localized hole and electron densities.

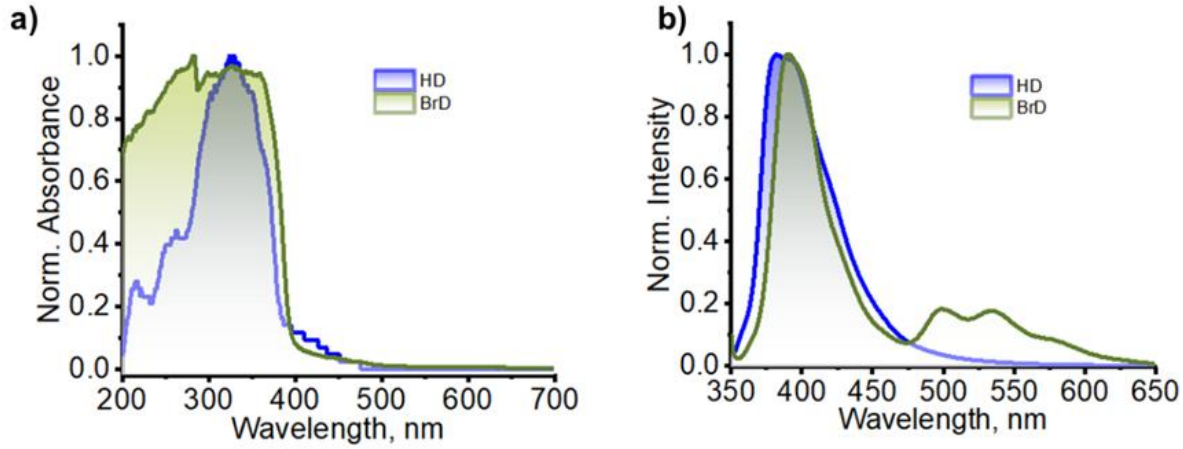

Figure A4.14: a) Normalized Kubelka-Munk transformed absorption in HD and BrD crystal; b) Normalized emission spectra in crystalline HD and BrD.

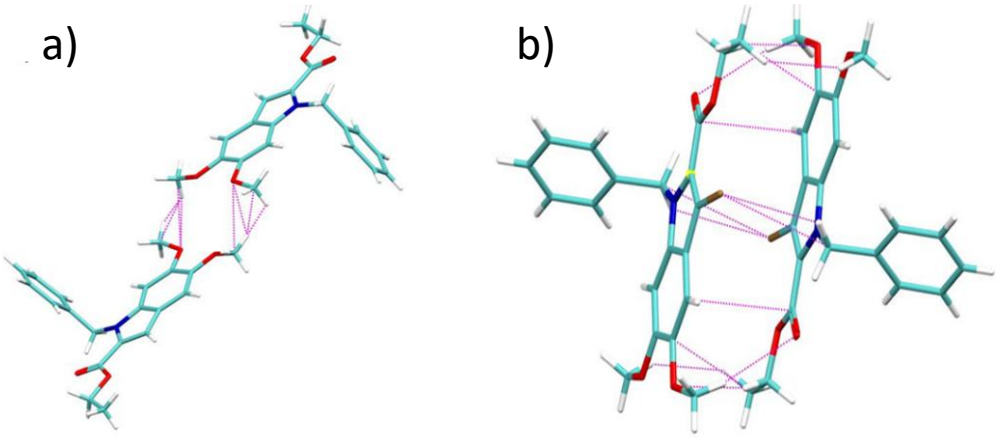

Figure A4.15: Identified dimer obtained from the crystal assembly of a) HD; b) BrD.

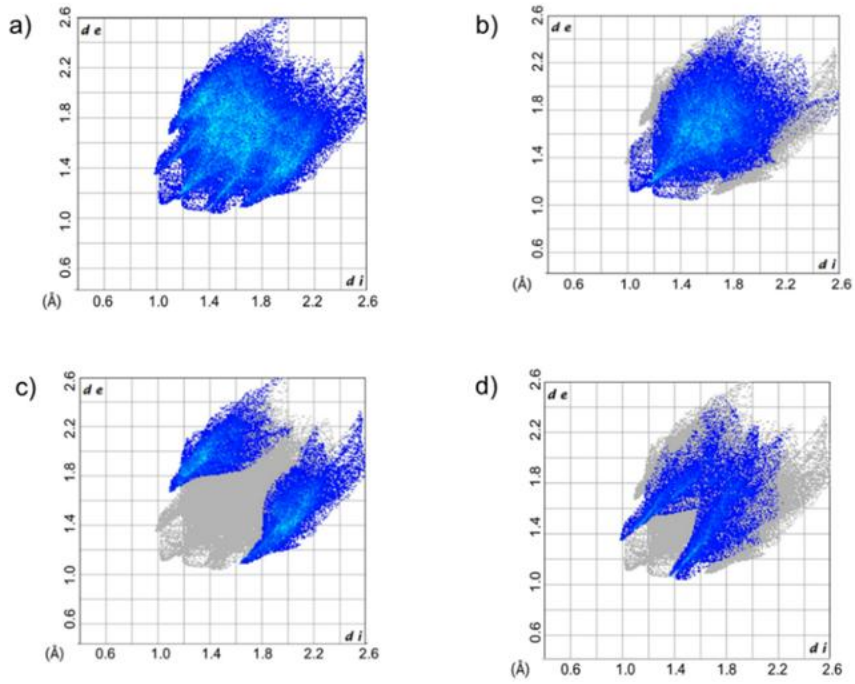

Figure A4.16: Hirshfeld 2D fingerprint plots a) Total; b) H•••H; c) H•••C and d) H•••O interactions of crystalline HD.

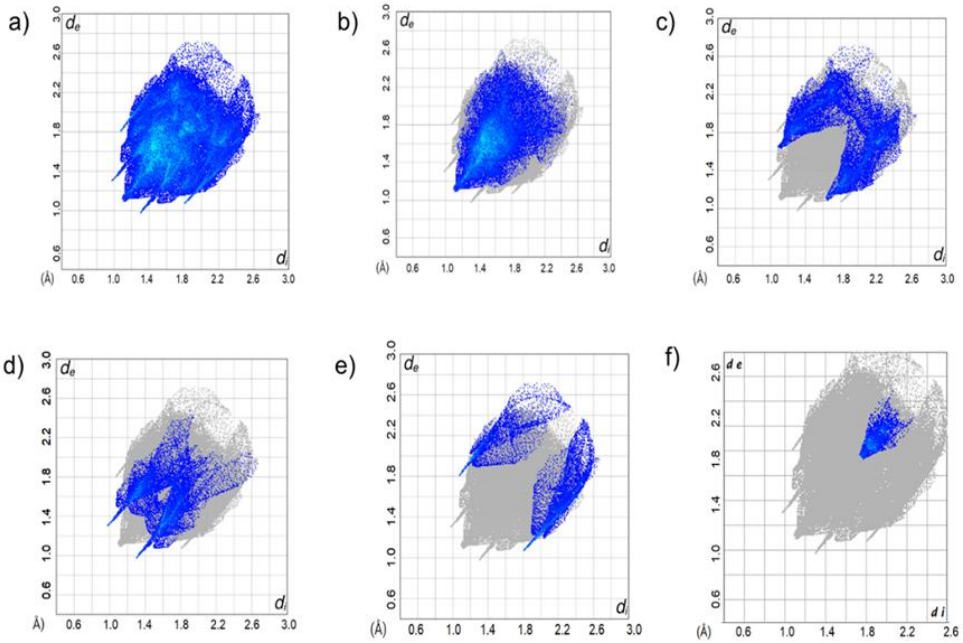

Figure A4.17: Hirshfeld 2D fingerprint plots a) Total, b) H•••H, c) H•••C, d) H•••O, e) H•••Br and f) C•••C interactions of crystalline BrD.

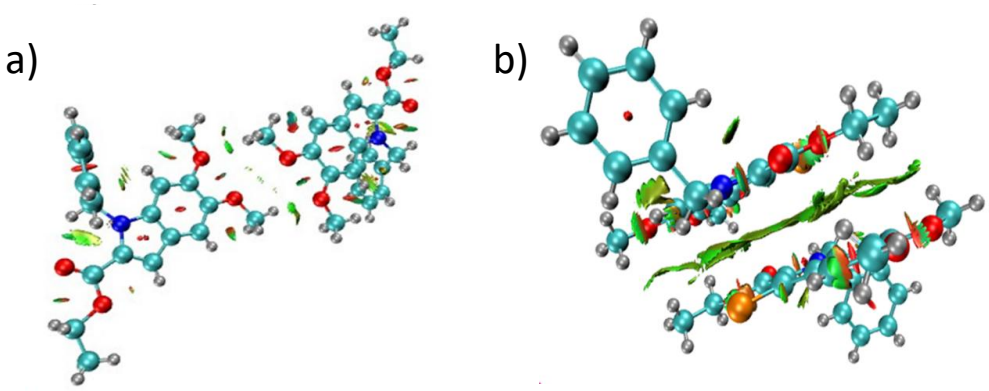

Figure A4.18: Non-covalent interactions in non-covalent dimers of a) HD; b) BrD.

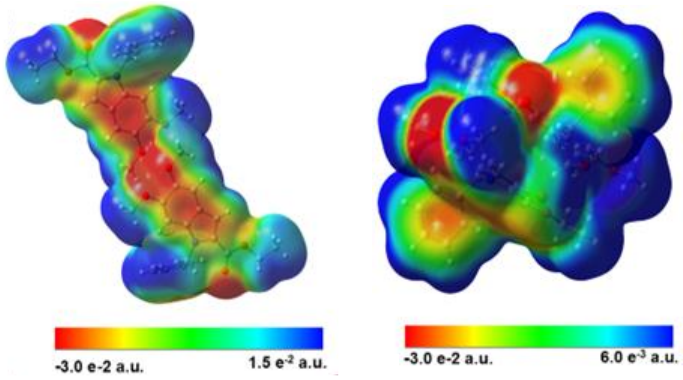

Figure A4.19: Electrostatic potential surface calculations of non-covalent dimers of a) HD; b) BrD.

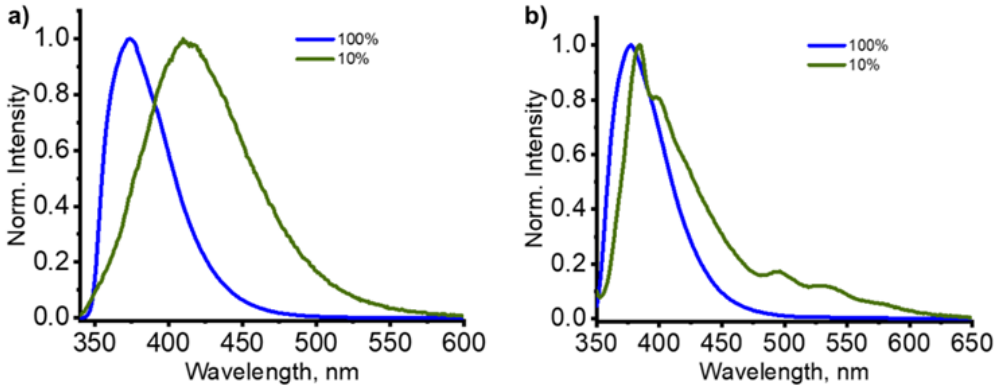

Figure A4.20: a) Normalized steady-state emission spectra of HD aggregates in THF/H_2O mixtures; b) Normalized steady-state emission spectra of BrD aggregates in THF/H_2O mixtures (% of THF is mentioned here).

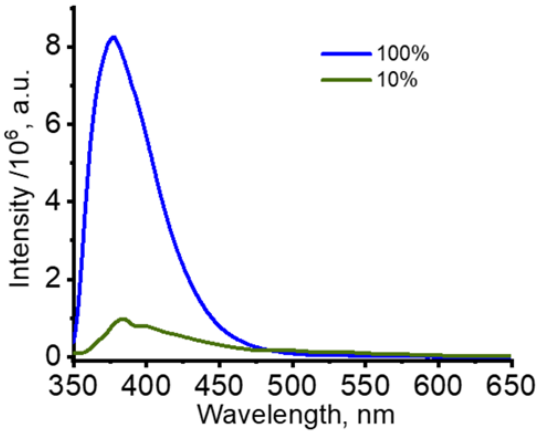

Figure A4.21: Steady-state emission spectra of BrD aggregates in THF/H_2O mixtures (% of THF is mentioned here).

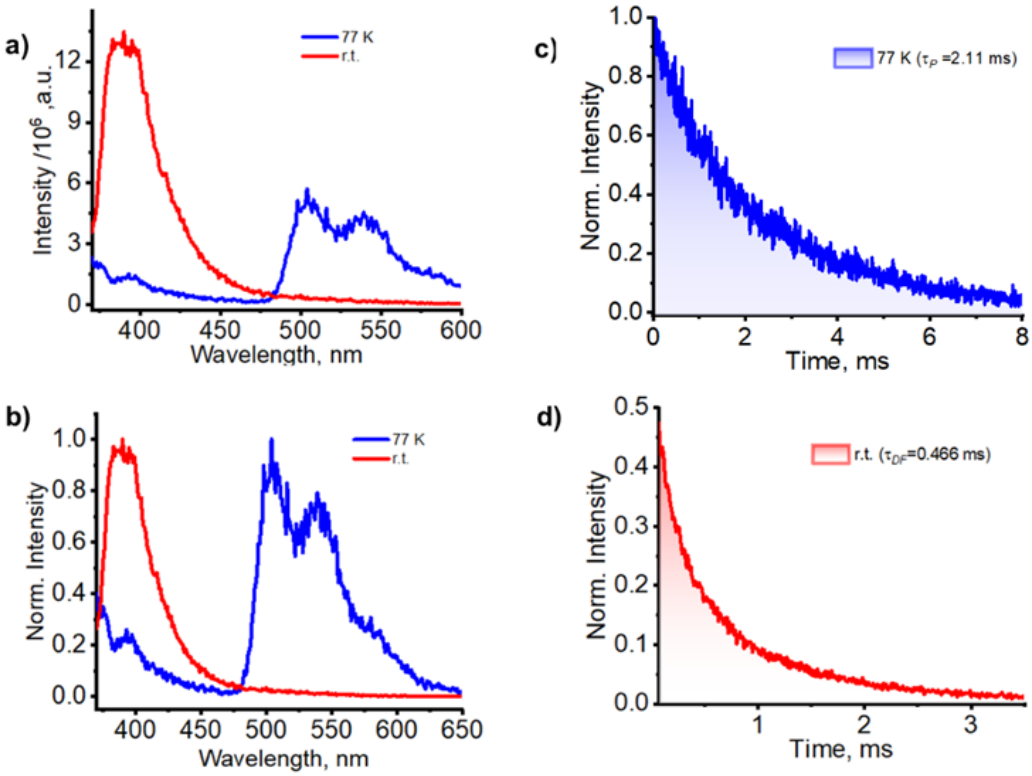

Figure A4.22: a) Gated emission spectra of crystalline HD at 77 K and room temperature; b) Normalized gated emission spectra of crystalline HD at 77 K and room temperature; c) Decay profile of crystalline HD at 77 K; d) Decay profile of crystalline HD at room temperature.

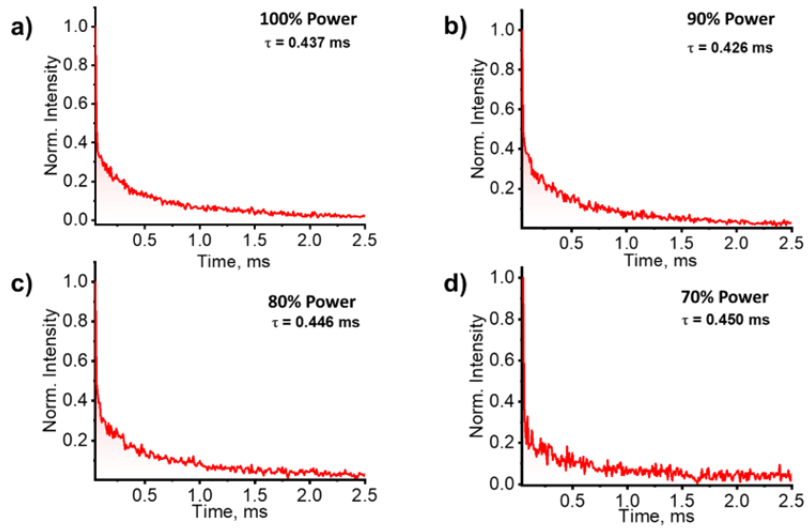

Figure A4.23: Excitation power dependent (normalized) delayed emission decay profiles of crystalline HD at a) 100% Power; b) 90% power; c) 80% power; d) 70% power (Excitation source is a 450 W pulsed Xe lamp).

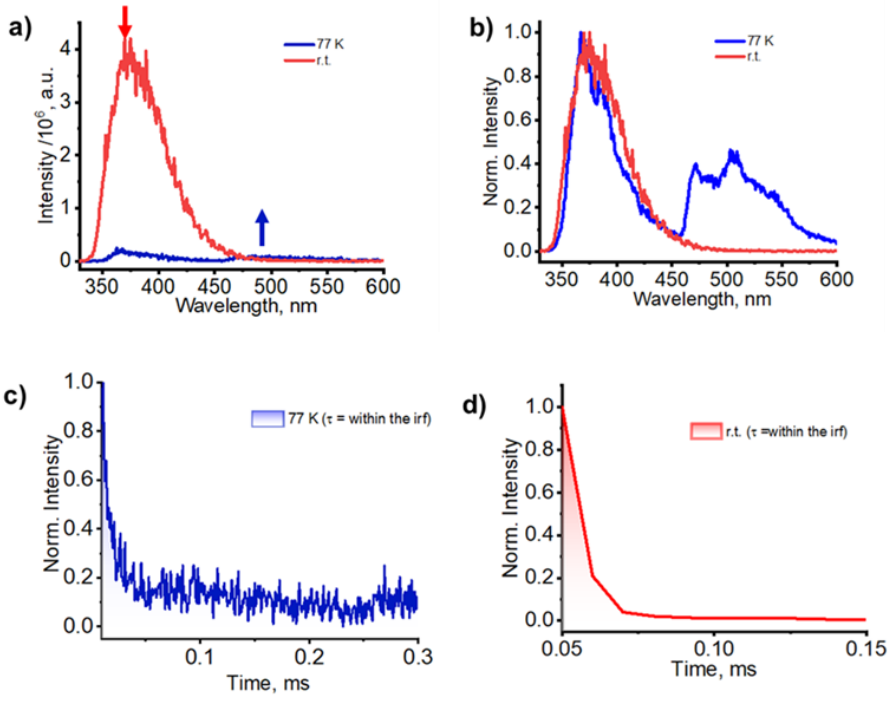

Figure A4.24: a) Gated emission spectra of HD in toluene at 77 K and room temperature; b) Normalized gated emission spectra of HD in toluene at 77 K and room temperature; c) Decay profile of HD in toluene at 77 K; d) Decay profile of HD in toluene at room temperature.

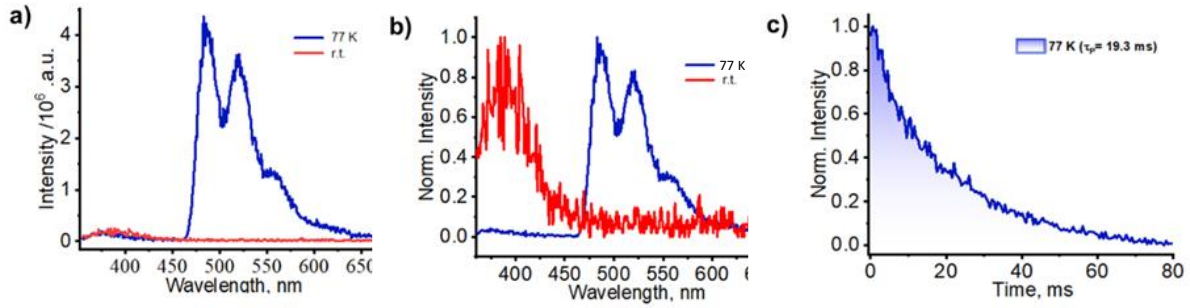

Figure A4.25: a) Gated emission spectra of BrD in toluene at 77 K and room temperature; b) Normalized gated emission spectra of BrD in toluene at 77 K and room temperature; c) Decay profile of BrD in toluene at 77 K.

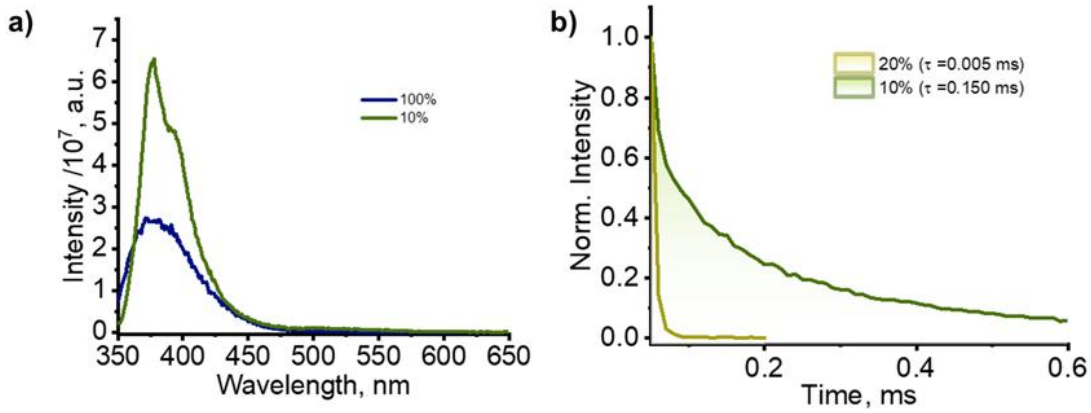

Figure A4.26: a) Gated emission spectra in HD aggregates in THF/H_2O mixtures; b) Decay profile of HD aggregates in THF/H_2O mixtures (% of THF is mentioned here).

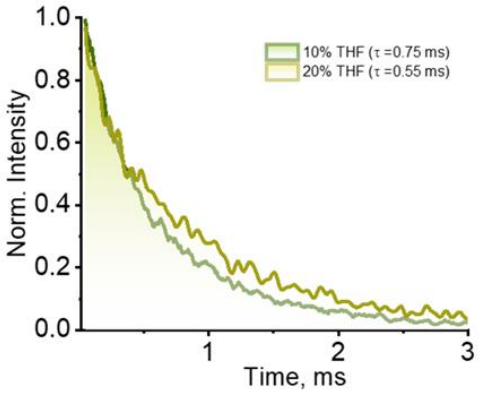

Figure A4.27: Decay profile of BrD aggregates in THF/H_2O mixtures.

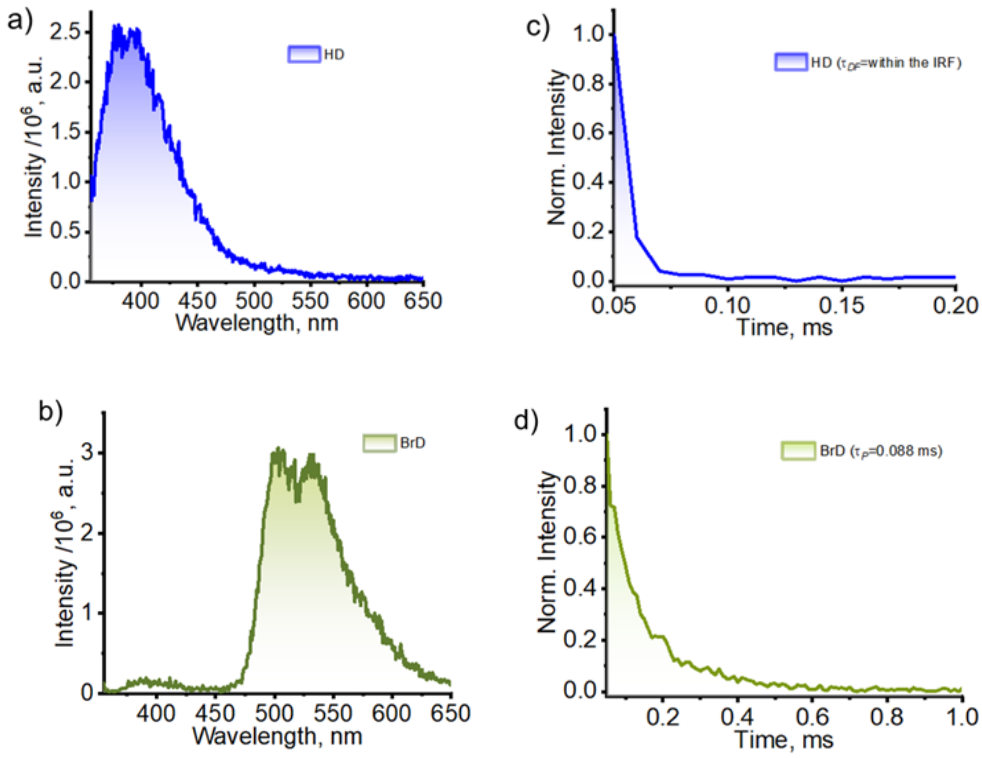

Figure A4.28: a) Gated emission spectra of HD in PMMA film; b) Gated emission spectra of BrD in film; c) Decay profile of gated emission in HD film; d) decay profile of gated emission in BrD film.

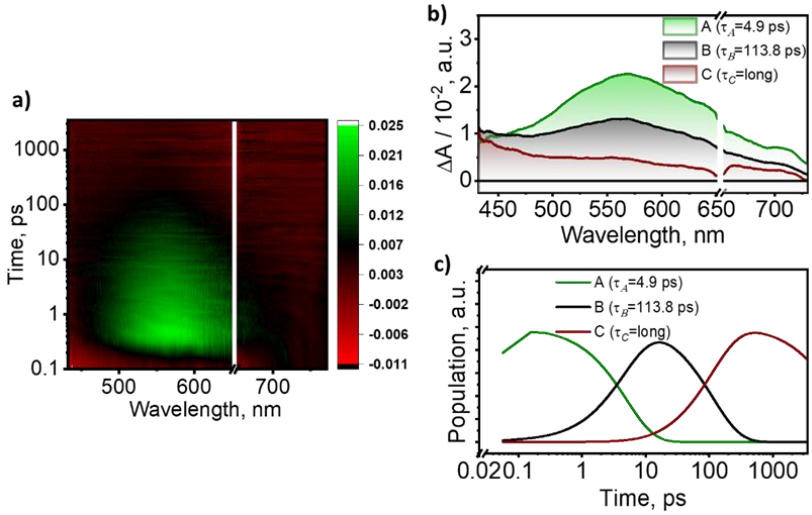

Figure A4.29: a) FsTA contour plot of HD in PMMA film, b) Deconvoluted EAS plot of HD in PMMA film, c) Deconvoluted decay time constants of the EAS for HD in PMMA film.

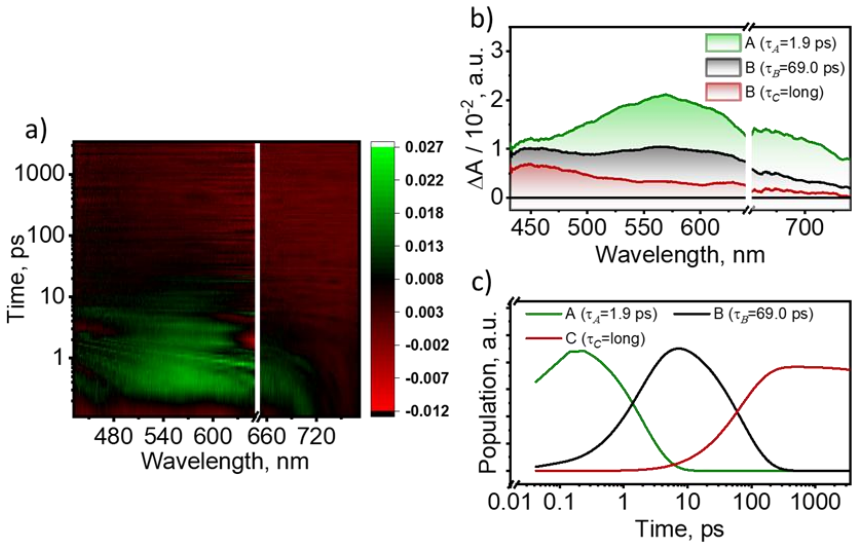

Figure A4.30: a) FsTA contour plot of BrD in PMMA film, b) Deconvoluted EAS plot of BrD in PMMA film, c) Deconvoluted decay time constants of the EAS for BrD in PMMA film.

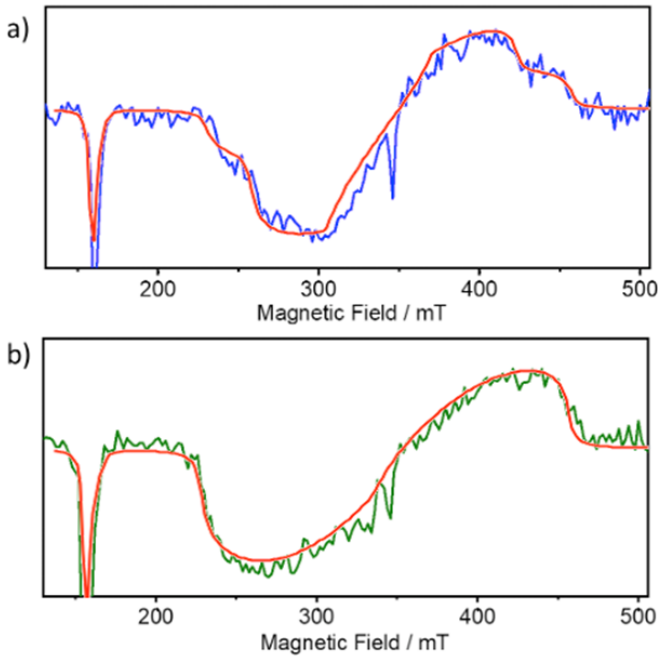

Figure A4.31: Experimental X-band transient EPR spectra of (a) HD and (b) BrD in the crystalline state, recorded at 0.6 µs and 80 K following unpolarized 355 nm photoexcitation. The simulation spectra are superimposed by the red lines.

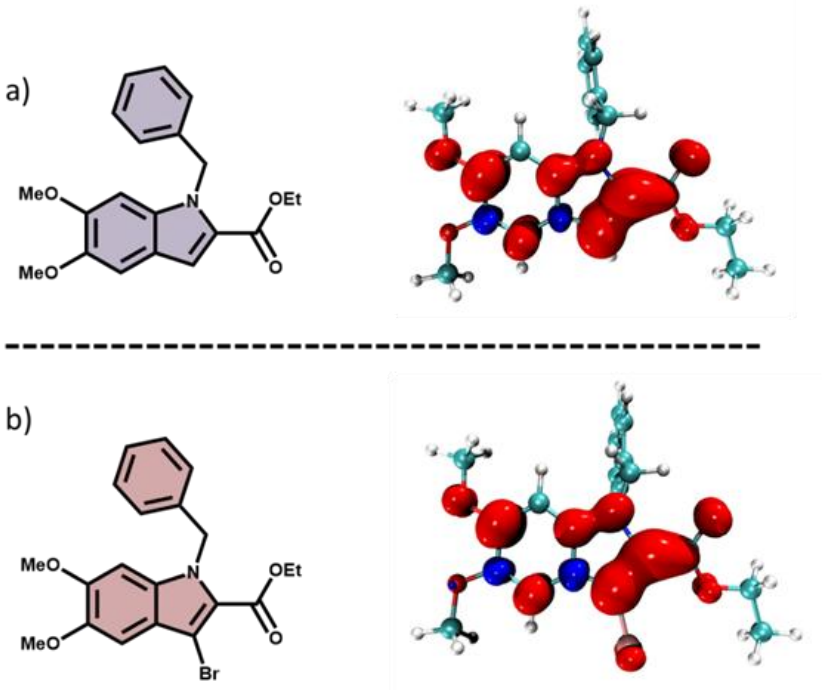

Figure A4.32: Spin density of the T_1 state for a) HD and b) BrD, computed at the cam-b3lyp/6-311+g(d,p).

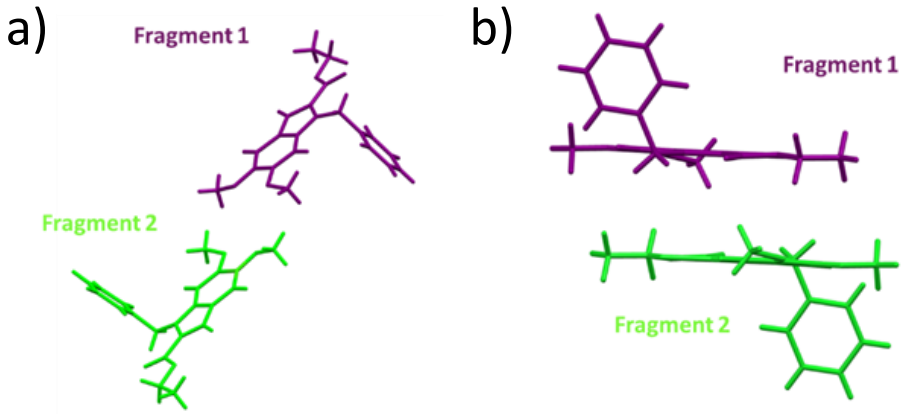

Figure A4.33: Fragmentation used for computing long-range Coulombic coupling via electronic excitation transfer (EET) method in a) HD and b) BrD.

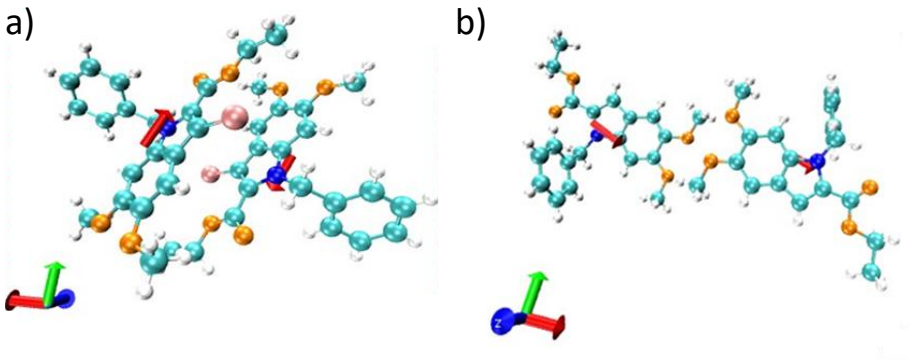

Figure A4.34: Transition dipole moment of a) HD in S_1 state; b) BrD in S_1 state.

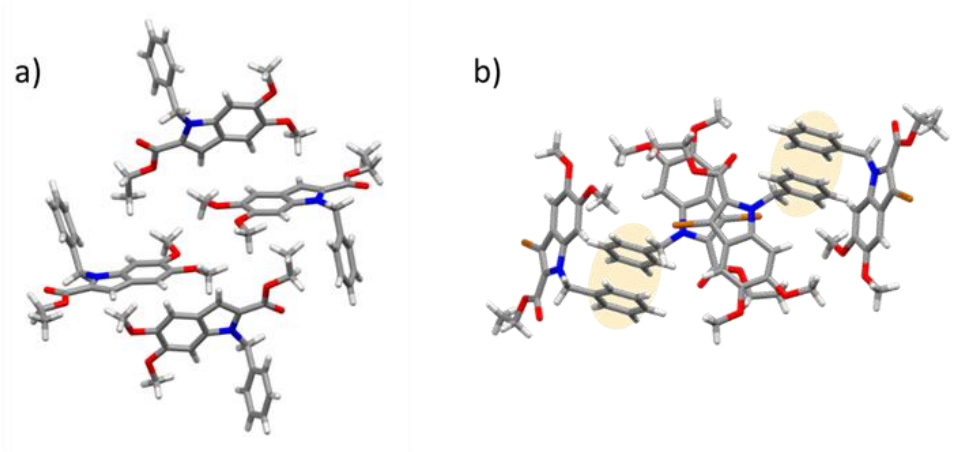

Figure A4.35: Crystal packing in a) HD showing the absence of benzyl group interactions and b) BrD showing the presence of benzyl group interactions, facilitating further rigidification of the benzyl groups in crystalline BrD compared to HD.

3.6. Additional Tables

Table A4.1: Crystallographic data and refinement parameters for HD and BrD.

Parameters	HD	BrD
Formula	$C_{20}H_{21}NO_4$	$C_{20}H_{20}BrNO_4$
Formula weight	339.38	418.28
Colour	Colourless	Colourless
Crystal system	Orthorhombic	Monoclinic
Space group, Z	$Pca2_1$	$P2_1/c$
A (Å)	17.7200(19)	10.8941(14)

B (Å)	5.9980(7)	19.2850(2)
C (Å)	33.0600(4)	9.3345(11)
A (deg)	90.00	90.00
B (deg)	90.00	106.77(4)
Γ (deg)	90.00	90.00
Volume, A^3	3514(7)	1877.6(4)
R-factor (%)	8.51	4.42
Temp (K)	296	296
$Density_{calc}$ (g/m^3)	1.283	1.480
No. of reflections collected	39620	26326
Independent reflections	6180	4676
$2\theta_{max}$ (deg)	49.99	56.83
R indices, wR2 (i>2s(i))	0.0851, 0.1844	0.0442, 0.0939
R indices, wR2 (all data)	0.2152, 0.2522	0.0914, 0.1090
Goodness of fit	1.003	1.025
CCDC number	2429518	2429519

Table A4.2: Mean position (POS), participation ratio (PR), charge transfer character (CT), and exciton character of excited states in HD computed at wb97xd/def2tzvp level of theory.

States	dE (eV)	f	POS	PR	CT
S_1	4.307	0.427	1.005	1.010	0.009
S_2	4.492	0.193	1.011	1.023	0.020
S_3	5.375	0.000	1.023	1.046	0.036
S_4	5.422	0.003	1.941	1.125	0.100
S_5	5.621	0.078	1.029	1.061	0.056
S_6	5.827	0.111	1.185	1.437	0.294
S_7	5.908	0.007	1.465	1.259	0.779
S_8	5.957	0.098	1.300	1.516	0.562
S_9	6.092	0.035	1.561	1.577	0.561
S_{10}	6.124	0.001	1.474	1.319	0.749

Table A4.3: Mean position (POS), participation ratio (PR), charge transfer character (CT), and exciton character of excited states in BrD computed at wb97xd/def2tzvp level of theory.

States	dE (eV)	f	POS	PR	CT
S_1	4.298	0.290	1.007	1.014	0.014
S_2	4.381	0.309	1.010	1.021	0.018
S_3	5.366	0.001	1.026	1.054	0.048
S_4	5.421	0.004	1.944	1.119	0.101
S_5	5.505	0.002	1.017	1.034	0.031
S_6	5.638	0.087	1.027	1.057	0.052
S_7	5.727	0.068	1.073	1.159	0.124
S_8	5.956	0.016	1.459	1.513	0.606
S_9	5.964	0.038	1.371	1.490	0.638
S_{10}	6.040	0.164	1.149	1.347	0.274

Table A4.4: Relative % intermolecular interactions obtained from Hirshfeld analyses.

HD-crystal				
%H•••H	%H•••C	%H•••O	%H•••Br	%C•••C
51.4	28.8	18.3	0.0	0.0
BrD-crystal				
%H•••H	% H•••C	%H•••O	%H•••Br	%C•••C
45.4	21.4	15.9	10.9	3.3

Table A4.5: Interaction energies in selected dimers determined by SAPT(0)/aug-cc-pVDZ calculations and SAPT(0) energy components for crystalline HD and BrD.

Dimer	Electrostatic (kJ/mol)	Exchange (kJ/mol)	Induction (kJ/mol)	Dispersion (kJ/mol)	Total energy (kJ/mol)
HD	-3.615	14.617	-3.060	-20.285	-12.315
BrD	-38.427	66.350	-7.444	-123.764	-103.301

Table A4.6: Computed long-range coulombic ($J_{Coulomb}$) and short-range charge transfer coupling (J_{CT}) for the dimers of HD and BrD using wb97xd/def2tzvp level of theory.

Dimers	$J_{Coulombic}$ (cm^{-1})	J_{CT} (cm^{-1})	J_{Total} (cm^{-1})
HD	-142.14	-0.12	-142.26
BrD	186.37	27.13	213.50

Table A4.7: Vertical excitation energies of HD computed at the cam-b3lyp/def2svp level of theory.

States	Energy (eV)	f	States	TDA Energy (eV)
S_1	4.3641	0.3340	T_1	3.0772
S_2	4.6099	0.2461	T_2	3.4732
S_3	5.6832	0.0416	T_3	4.1145
S_4	5.7152	0.0206	T_4	4.3606
S_5	5.7300	0.0073	T_5	4.5830
S_6	5.9045	0.1061	T_6	4.8146
S_7	5.9266	0.0865	T_7	4.8549
S_8	5.9953	0.0422	T_8	4.9849
S_9	6.2459	0.0255	T_9	5.1534
S_{10}	6.2886	0.0223	T_{10}	5.2945

Table A4.8: Vertical excitation energies of HD crystal unit cell computed at the cam b3lyp/def2svp level of theory.

States	Energy (eV)	f	States	TDA Energy (eV)
S_1	4.2707	0.1533	T_1	3.0074
S_2	4.2782	0.4567	T_2	3.0243
S_3	4.3434	0.5646	T_3	3.1718
S_4	4.3672	0.2198	T_4	3.1756
S_5	4.5359	0.0381	T_5	3.3377
S_6	4.5539	0.6803	T_6	3.3752
S_7	4.5963	0.0075	T_7	3.4038
S_8	4.6128	0.2758	T_8	3.4231
S_9	4.7691	0.0023	T_9	4.2295
S_{10}	4.8327	0.0018	T_{10}	4.2320
S_{11}	5.1915	0.0045	T_{11}	4.2406
S_{12}	5.1964	0.0044	T_{12}	4.2424
S_{13}	5.2753	0.0003	T_{13}	4.2738
S_{14}	5.2896	0.0000	T_{14}	4.2788
S_{15}	5.4163	0.0000	T_{15}	4.2877

Table A4.9: Vertical excitation energies of BrD computed at the cam-b3lyp/def2svp level of theory.

States	Energy (eV)	f	States	TDA Energy (eV)
S_1	4.3326	0.3155	T_1	3.0478
S_2	4.4702	0.3307	T_2	3.4321
S_3	5.4735	0.0003	T_3	4.1146
S_4	5.6913	0.0048	T_4	4.2849
S_5	5.7224	0.0030	T_5	4.5954
S_6	5.7587	0.0676	T_6	4.8160
S_7	5.9157	0.0653	T_7	4.8544
S_8	6.0585	0.0027	T_8	4.9761
S_9	6.0798	0.0411	T_9	5.1404
S_{10}	6.1139	0.0369	T_{10}	5.1872

Table A4.10: Vertical excitation energies of BrD crystal unit cell computed at the cam-b3lyp/def2svp level of theory.

States	Energy (eV)	f	States	TDA Energy (eV)
S_1	4.1956	0.0001	T_1	2.9900
S_2	4.3091	0.4828	T_2	2.9923
S_3	4.3373	0.0000	T_3	3.0302
S_4	4.3697	0.0000	T_4	3.0308
S_5	4.3752	0.3263	T_5	3.3701
S_6	4.4303	0.0545	T_6	3.3754
S_7	4.4604	0.0000	T_7	3.4235
S_8	4.4877	1.1491	T_8	3.4237
S_9	4.8244	0.0111	T_9	4.6095
S_{10}	4.8615	0.0000	T_{10}	4.6220
S_{11}	4.9101	0.0000	T_{11}	4.6411
S_{12}	4.9395	0.0450	T_{12}	4.6453
S_{13}	5.1756	0.0005	T_{13}	4.6584
S_{14}	5.1757	0.0001	T_{14}	4.6727
S_{15}	5.3588	0.0007	T_{15}	4.6812

4.7. Appendix

4.7.1. Materials and Methods

Detailed information regarding the materials and methods used is given in section 2.7.1.

4.7.2. X-ray Diffraction

Single-crystal data were collected using Mo Kα radiation on a Bruker APEXII CCD diffractometer. Structures were solved by direct methods and refined using standard procedures. Hydrogen atoms were placed in idealized positions. Full experimental and refinement details are described in section 3.7.2.

4.7.3. Computational Analysis

All geometry optimisations were carried out in Gaussian 16[75] employing the cam-b3lyp functional and 6-311G+(d,p) basis set at the DFT level of theory. The long-range Coulombic coupling for HD and BrD were computed using Excitation Energy Transfer (EET) method available in Gaussian 16. Electron and hole transfer coupling values were calculated by employing the CATNIP Tool version 1.9.9.[76] CATNIP uses post-processed Gaussian 16 output files for the respective analyses. The two types of dimers from the crystal packing of HD and BrD are denoted as HD-dimer and BrD-dimer. Detailed information regarding TheoDORE analysis and excitonic coupling calculations are provided in sections 2.7.3.5 and 2.7.3.6 respectively.

4.7.4. Sample preparation for thin film for fsTA analysis:

Round quartz substrates were cleaned following standard protocols. A 10 wt% PMMA solution in toluene was prepared and stirred at room temperature for 4–5 h to obtain a homogeneous solution. The compound was then added at 1 wt% relative to the PMMA weight and mixed thoroughly to ensure uniform dispersion. The resulting solution was drop-cast onto the quartz substrates, and the films were dried under vacuum and stored under nitrogen prior to measurements. A magic angle polarization (54.7°) between pump and probe pulses was used during fsTA experiments to ensure isotropic signal collection.

Chapter 5

Conclusion and Outlook

This thesis investigates how molecular structure, aggregation, and excitonic interactions shape the excited-state dynamics of eumelanin and eumelanin-inspired systems. By combining structural analysis with steady-state and ultrafast spectroscopy, the work establishes clear links between the architecture of eumelanin building blocks and the pathways by which they dissipate electronic energy. Structural elucidation of DHICA revealed how π–π stacking and hydrogen-bonded networks support charge-transfer–mediated exciton delocalization, offering insight into energy transport within eumelanin assemblies. Spectroscopic investigations on model eumelanin multimers showed that increasing molecular size and aggregation leads to stronger excitonic coupling, broader UV-visible absorption, and faster nonradiative decay, closely echoing the ultrafast relaxation that underpins natural photoprotection in natural eumelanin. Extending these principles to engineered charge-transfer indole-based emitters demonstrated that J- and H-type aggregation can be used to tune singlet–triplet energy gaps and modulate delayed fluorescence and phosphorescence, highlighting the broader relevance of eumelanin-inspired design strategies.

These results collectively emphasize that eumelanin's function emerges from the interplay of chemical heterogeneity and supramolecular arrangement, rather than from any single, well-defined structure. Excitonic coupling and aggregation are shown to be fundamental levers for controlling energy dissipation and emission in both natural and synthetic systems. Future progress will depend on expanding the molecular toolkit. Synthetic access to higher-order oligomers including, both alkyl-protected and unprotected, as well as more complex DHI/DHICA-based substructures will allow systematic exploration of disorder and coupling effects. Advanced techniques such as 3D electron diffraction, solid-state NMR, multidimensional electronic spectroscopy, and pulsed EPR will be crucial for resolving structure and dynamics across multiple length scales. Together, these efforts will move the field

closer to a unified, molecular-to-mesoscale understanding of eumelanin, enabling the rational design of next-generation bio-inspired photonic materials.

Bibliography

1) Simon, J. D.; Peles, D. N. The Red and the Black. *Accounts of Chemical Research* **2010**, *43*, 1452-1460.

2) Kaxiras, E.; Tsolakidis, A.; Zonios, G.; Meng, S. Structural Model of Eumelanin. *Physical Review Letters* **2006**, *97*, 218102.

3) Hong, S.; Wang, Y.; Park, S. Y.; Lee, H. Progressive fuzzy cation-π assembly of biological catecholamines. *Science Advances* **2018**, *4*, eaat7457.

4) Raper, H. S. The Tyrosinase-tyrosine Reaction: Production from Tyrosine of 5: 6-Dihydroxyindole and 5: 6-Dihydroxyindole-2-carboxylic Acid—the Precursors of Melanin. *Biochemical Journal* **1927**, *21*, 89-96.

5) Mason, H. S. The chemistry of melanin: III. Mechanism of the oxidation of dihydroxyphenylalanine by tyrosinase. *Journal of Biological Chemistry* **1948**, *172*, 83-99.

6) Cao, W.; Zhou, X.; McCallum, N. C.; Hu, Z.; Ni, Q. Z.; Kapoor, U.; Heil, C. M.; Cay, K. S.; Zand, T.; Mantanona, A. J.; et al. Unraveling the Structure and Function of Melanin through Synthesis. *Journal of the American Chemical Society* **2021**, *143*, 2622-2637.

7) D'Alba, L.; Shawkey, M. D. Melanosomes: Biogenesis, Properties, and Evolution of an Ancient Organelle. *Physiological Reviews* **2019**, *99*, 1-19.

8) Solano, F. Photoprotection versus photodamage: updating an old but still unsolved controversy about melanin. *Polymer International* **2016**, *65*, 1276-1287.

9) d'Ischia, M.; Napolitano, A.; Pezzella, A.; Meredith, P.; Buehler, M. Melanin Biopolymers: Tailoring Chemical Complexity for Materials Design. *Angewandte Chemie International Edition* **2020**, *59*, 11196-11205.

10) D'Ischia, M.; Napolitano, A.; Ball, V.; Chen, C. T.; Buehler, M. J. Polydopamine and eumelanin: From structure-property relationships to a unified tailoring strategy. *Accounts of Chemical Research* **2014**, *47*, 3541-3550.

11) Ito, S. Reexamination of the structure of eumelanin. *Biochimica et Biophysica Acta (BBA) - General Subjects* **1986**, *883*, 155-161.

12) Choudhury, A.; Ghosh, D.; Li, R.; Chemcomm; Communication, C. Charge transfer in DHICA eumelanin-like oligomers: role of hydrogen bonds. *Chemical Communications* **2020**, *56*, 10481-10484.

13) Nofsinger, J. B.; Forest, S. E.; Simon, J. D. Explanation for the Disparity among Absorption and Action Spectra of Eumelanin. *The Journal of Physical Chemistry B* **1999**, *103*, 11428-11432.

14) McGinness, J.; Corry, P.; Proctor, P. Amorphous Semiconductor Switching in Melanins. *Science* **1974**, *183*, 853-855.

15) McGinness, J. E. Mobility Gaps: A Mechanism for Band Gaps in Melanins. *Science* **1972**, *177*, 896-897.

16) Wolbarsht, M. L.; Walsh, A. W.; George, G. Melanin, a unique biological absorber. *Appl. Opt.* **1981**, *20*, 2184-2186.

17) Watson, J. D.; Crick, F. H. C. Molecular Structure of Nucleic Acids: A Structure for Deoxyribose Nucleic Acid. *Nature* **1953**, *171*, 737-738.

18) Ramachandran, G. N.; Kartha, G. Structure of Collagen. *Nature* **1955**, *176*, 593-595.

19) Kendrew, J. C. Myoglobin and the Structure of Proteins. *Science* **1963**, *139*, 1259-1266.

20) Russell, N. J.; Powell, G. M.; Jones, J. G.; Winterburn, P. J.; Basford, J. M. Haemoglobin: Structure and Function. In *Blood Biochemistry*, Springer Netherlands, 1982; pp 21-36.

21) Choudhury, A.; Ghosh, D. Elucidating the Structure of Melanin and Its Structure–Property Correlation. *Accounts of Chemical Research* **2025**, *58*, 1509-1518.

22) d'Ischia, M.; Wakamatsu, K.; Cicoira, F.; Di Mauro, E.; Garcia-Borron, J. C.; Commo, S.; Galván, I.; Ghanem, G.; Kenzo, K.; Meredith, P.; et al. Melanins and melanogenesis: from pigment cells to human health and technological applications. *Pigment Cell & Melanoma Research* **2015**, *28*, 520-544.

23) Vinod, K.; Mathew, R.; Jandl, C.; Thomas, B.; Hariharan, M. Electron diffraction and solid-state NMR reveal the structure and exciton coupling in a eumelanin precursor. *Chemical Science* **2024**, *15*, 16015-16024.

24) Della Vecchia, N. F.; Avolio, R.; Alfè, M.; Errico, M. E.; Napolitano, A.; d'Ischia, M. Building-Block Diversity in Polydopamine Underpins a Multifunctional Eumelanin-Type Platform Tunable Through a Quinone Control Point. *Advanced Functional Materials* **2013**, *23*, 1331-1340.

25) Panzella, L.; Gentile, G.; D'Errico, G.; Della Vecchia, N. F.; Errico, M. E.; Napolitano, A.; Carfagna, C.; d'Ischia, M. Atypical Structural and π-Electron Features of a Melanin Polymer That Lead to Superior Free-Radical-Scavenging Properties. *Angewandte Chemie International Edition* **2013**, *52*, 12684-12687.

26) Cecchini, M. M.; Reale, S.; Manini, P.; d'Ischia, M.; De Angelis, F. Modeling Fungal Melanin Buildup: Biomimetic Polymerization of 1,8-Dihydroxynaphthalene Mapped by Mass Spectrometry. *Chemistry – A European Journal* **2017**, *23*, 8092-8098.

27) Reale, S.; Crucianelli, M.; Pezzella, A.; d'Ischia, M.; De Angelis, F. Exploring the frontiers of synthetic eumelanin polymers by high-resolution matrix-assisted laser/desorption ionization mass spectrometry. *Journal of Mass Spectrometry* **2012**, *47*, 49-53.

28) Delparastan, P.; Malollari, K. G.; Lee, H.; Messersmith, P. B. Direct Evidence for the Polymeric Nature of Polydopamine. *Angewandte Chemie International Edition* **2019**, *58*, 1077-1082.

29) d'Ischia, M.; Napolitano, A.; Pezzella, A. 5,6-Dihydroxyindole Chemistry: Unexplored Opportunities Beyond Eumelanin. *European Journal of Organic Chemistry* **2011**, *2011*, 5501-5516.

30) Grieco, C.; Kohl, F. R.; Hanes, A. T.; Kohler, B. Probing the heterogeneous structure of eumelanin using ultrafast vibrational fingerprinting. *Nature Communications* **2020**, *11*, 4569.

31) Mostert, A. B.; Rienecker, S. B.; Noble, C.; Hanson, G. R.; Meredith, P. The photoreactive free radical in eumelanin. *Science Advances* **2018**, *4*, eaaq1293.

32) Wünsche, J.; Deng, Y.; Kumar, P.; Di Mauro, E.; Josberger, E.; Sayago, J.; Pezzella, A.; Soavi, F.; Cicoira, F.; Rolandi, M.; et al. Protonic and Electronic Transport in Hydrated Thin Films of the Pigment Eumelanin. *Chemistry of Materials* **2015**, *27*, 436-442.

33) Kang, M.; Kim, E.; Temoçin, Z.; Li, J.; Dadachova, E.; Wang, Z.; Panzella, L.; Napolitano, A.; Bentley, W. E.; Payne, G. F. Reverse Engineering To Characterize Redox Properties: Revealing Melanin's Redox Activity through Mediated Electrochemical Probing. *Chemistry of Materials* **2018**, *30*, 5814-5826.

34) Tarabella, G.; Pezzella, A.; Romeo, A.; D'Angelo, P.; Coppedè, N.; Calicchio, M.; d'Ischia, M.; Mosca, R.; Iannotta, S. Irreversible evolution of eumelanin redox states detected by an organic electrochemical transistor: en route to bioelectronics and biosensing. *Journal of Materials Chemistry B* **2013**, *1*, 3843-3849.

35) Watt, A. A. R.; Bothma, J. P.; Meredith, P. The supramolecular structure of melanin. *Soft Matter* **2009**, *5*, 3754-3760.

36) Büngeler, A.; Hämisch, B.; Strube, O. I. The Supramolecular Buildup of Eumelanin: Structures, Mechanisms, Controllability. *International Journal of Molecular Sciences* **2017**, *18*, 1901.

37) Li, Y.; Liu, J.; Wang, Y.; Chan, H. W.; Wang, L.; Chan, W. Mass Spectrometric and Spectrophotometric Analyses Reveal an Alternative Structure and a New Formation Mechanism for Melanin. *Analytical Chemistry* **2015**, *87*, 7958-7963.

38) Jelley, E. E. Spectral Absorption and Fluorescence of Dyes in the Molecular State. *Nature* **1936**, *138*, 1009-1010.

39) Scheibe, G. Über die Veränderlichkeit der Absorptionsspektren in Lösungen und die Nebenvalenzen als ihre Ursache. *Angewandte Chemie* **1937**, *50*, 212-219.

40) Bardeen, C. J. The Structure and Dynamics of Molecular Excitons. *Annual Review of Physical Chemistry* **2014**, *65*, 127-148.

41) Davydov, A. S. The theory of molecular excitons. *Soviet Physics Uspekhi* **1964**, *7*, 145.

42) Kasha, M.; Rawls, H. R.; El-Bayoumi, M. A. The exciton model in molecular spectroscopy. *Pure and Applied Chemistry* **1965**, *11*, 371-392.

43) Krueger, B. P.; Scholes, G. D.; Fleming, G. R. Calculation of Couplings and Energy-Transfer Pathways between the Pigments of LH2 by the ab Initio Transition Density Cube Method. *The Journal of Physical Chemistry B* **1998**, *102*, 5378-5386.

44) Scholes, G. D.; Ghiggino, K. P. Electronic Interactions and Interchromophore Excitation Transfer. *The Journal of Physical Chemistry* **1994**, *98*, 4580-4590.

45) Fassioli, F.; Dinshaw, R.; Arpin, P. C.; Scholes, G. D. Photosynthetic light harvesting: excitons and coherence. *Journal of The Royal Society Interface* **2014**, *11*.

46) Lijina, M. P.; Benny, A.; Sebastian, E.; Hariharan, M. Keeping the chromophores crossed: evidence for null exciton splitting. *Chemical Society Reviews* **2023**, *52*, 6664-6679.

47) Bricks, J. L.; Slominskii, Y. L.; Panas, I. D.; Demchenko, A. P. Fluorescent J-aggregates of cyanine dyes: basic research and applications review. *Methods and Applications in Fluorescence* **2018**, *6*, 012001.

48) Sebastian, E.; Philip, A. M.; Benny, A.; Hariharan, M. Null Exciton Splitting in Chromophoric Greek Cross (+) Aggregate. *Angewandte Chemie International Edition* **2018**, *57*, 15696-15701.

49) Zhou, J.; Zhang, W.; Jiang, X.-F.; Wang, C.; Zhou, X.; Xu, B.; Liu, L.; Xie, Z.; Ma, Y. Magic-Angle Stacking and Strong Intermolecular π–π Interaction in a Perylene Bisimide Crystal: An Approach for Efficient Near-Infrared (NIR) Emission and High Electron Mobility. *The Journal of Physical Chemistry Letters* **2018**, *9*, 596-600.

50) Yamagata, H.; Pochas, C. M.; Spano, F. C. Designing J- and H-Aggregates through Wave Function Overlap Engineering: Applications to Poly(3-hexylthiophene). *The Journal of Physical Chemistry B* **2012**, *116*, 14494-14503.

51) Hestand, N. J.; Spano, F. C. Expanded Theory of H- and J-Molecular Aggregates: The Effects of Vibronic Coupling and Intermolecular Charge Transfer. *Chemical Reviews* **2018**, *118*, 7069-7163.

52) Yamagata, H.; Norton, J.; Hontz, E.; Olivier, Y.; Beljonne, D.; Brédas, J. L.; Silbey, R. J.; Spano, F. C. The nature of singlet excitons in oligoacene molecular crystals. *The Journal of Chemical Physics* **2011**, *134*.

53) Vura-Weis, J.; Ratner, M. A.; Wasielewski, M. R. Geometry and Electronic Coupling in Perylenediimide Stacks: Mapping Structure−Charge Transport Relationships. *Journal of the American Chemical Society* **2010**, *132*, 1738-1739.

54) Benny, A.; Ramakrishnan, R.; Hariharan, M. Mutually exclusive hole and electron transfer coupling in cross stacked acenes. *Chemical Science* **2021**, *12*, 5064-5072.

55) Galvão, D. S.; Caldas, M. J. Polymerization of 5,6-indolequinone: A view into the band structure of melanins. *The Journal of Chemical Physics* **1988**, *88*, 4088-4091.

56) Vitkin, I. A.; Woolsey, J.; Wilson, B. C.; Anderson, R. R. OPTICAL AND THERMAL CHARACTERIZATION OF NATURAL (Sepia officinalis) MELANIN. *Photochemistry and Photobiology* **1994**, *59*, 455-462.

57) Sardar, D.; Mayo, M.; Glickman, R. Optical characterization of melanin. *Journal of Biomedical Optics* **2001**, *6*.

58) Nemkovich, N. A.; Rubinov, A. N.; Tomin, V. I. Inhomogeneous Broadening of Electronic Spectra of Dye Molecules in Solutions. In *Topics in Fluorescence Spectroscopy: Principles*, Lakowicz, J. R. Ed.; Springer US, 2002; pp 367-428.

59) Tran, M. L.; Powell, B. J.; Meredith, P. Chemical and Structural Disorder in Eumelanins: A Possible Explanation for Broadband Absorbance. *Biophysical Journal* **2006**, *90*, 743-752.

60) Stark, K. B.; Gallas, J. M.; Zajac, G. W.; Eisner, M.; Golab, J. T. Spectroscopic Study and Simulation from Recent Structural Models for Eumelanin: II. Oligomers. *The Journal of Physical Chemistry B* **2003**, *107*, 11558-11562.

61) Stark, K. B.; Gallas, J. M.; Zajac, G. W.; Eisner, M.; Golab, J. T. Spectroscopic Study and Simulation from Recent Structural Models for Eumelanin: I. Monomer, Dimers. *The Journal of Physical Chemistry B* **2003**, *107*, 3061-3067.

62) Powell, B. J. 5,6-Dihydroxyindole-2-carboxylic acid: a first principles density functional study. *Chemical Physics Letters* **2005**, *402*, 111-115.

63) Chen, C.-T.; Chuang, C.; Cao, J.; Ball, V.; Ruch, D.; Buehler, M. J. Excitonic effects from geometric order and disorder explain broadband optical absorption in eumelanin. *Nature Communications* **2014**, *5*, 3859.

64) Chen, C.-T.; Ball, V.; de Almeida Gracio, J. J.; Singh, M. K.; Toniazzo, V.; Ruch, D.; Buehler, M. J. Self-Assembly of Tetramers of 5,6-Dihydroxyindole Explains the Primary Physical Properties of Eumelanin: Experiment, Simulation, and Design. *ACS Nano* **2013**, *7*, 1524-1532.

65) Cheng, J.; Moss, S. C.; Eisner, M.; Zschack, P. X-Ray Characterization of Melanins—I. *Pigment Cell Research* **1994**, *7*, 255-262.

66) Cheng, J.; Moss, S. C.; Eisner, M. X-Ray Characterization of Melanins—II. *Pigment Cell Research* **1994**, *7*, 263-273.

67) Micillo, R.; Panzella, L.; Iacomino, M.; Prampolini, G.; Cacelli, I.; Ferretti, A.; Crescenzi, O.; Koike, K.; Napolitano, A.; D'Ischia, M. Eumelanin broadband absorption develops from aggregation-modulated chromophore interactions under structural and redox control. *Scientific Reports 2017 7:1* **2017**, *7*, 1-12.

68) Corani, A.; Huijser, A.; Gustavsson, T.; Markovitsi, D.; Malmqvist, P. Å.; Pezzella, A.; D'Ischia, M.; Sundström, V. Superior photoprotective motifs and mechanisms in eumelanins uncovered. *Journal of the American Chemical Society* **2014**, *136*, 11626-11635.

69) Corani, A.; Pezzella, A.; Pascher, T.; Gustavsson, T.; Markovitsi, D.; Huijser, A.; D'Ischia, M.; Sundström, V. Excited-state proton-transfer processes of DHICA resolved: From sub-picoseconds to nanoseconds. *Journal of Physical Chemistry Letters* **2013**, *4*, 1383-1388.

70) Nogueira, J. J.; Corani, A.; El Nahhas, A.; Pezzella, A.; d'Ischia, M.; González, L.; Sundström, V. Sequential Proton-Coupled Electron Transfer Mediates Excited-State Deactivation of a Eumelanin Building Block. *The Journal of Physical Chemistry Letters* **2017**, *8*, 1004-1008.

71) Gauden, M.; Pezzella, A.; Panzella, L.; Neves-Petersen, M. T.; Skovsen, E.; Petersen, S. B.; Mullen, K. M.; Napolitano, A.; d'Ischia, M.; Sundström, V. Role of Solvent, pH, and

Molecular Size in Excited-State Deactivation of Key Eumelanin Building Blocks: Implications for Melanin Pigment Photostability. *Journal of the American Chemical Society* **2008**, *130*, 17038-17043.

72) Meng, S.; Kaxiras, E. Mechanisms for Ultrafast Nonradiative Relaxation in Electronically Excited Eumelanin Constituents. *Biophysical Journal* **2008**, *95*, 4396-4402.

73) Olsen, S.; Riesz, J.; Mahadevan, I.; Coutts, A.; Bothma, J. P.; Powell, B. J.; McKenzie, R. H.; Smith, S. C.; Meredith, P. Convergent Proton-Transfer Photocycles Violate Mirror-Image Symmetry in a Key Melanin Monomer. *Journal of the American Chemical Society* **2007**, *129*, 6672-6673.

74) Kohl, F. R.; Grieco, C.; Kohler, B. Ultrafast spectral hole burning reveals the distinct chromophores in eumelanin and their common photoresponse. *Chemical Science* **2020**, *11*, 1248-1259.

75) Ilina, A.; Thorn, K. E.; Hume, P. A.; Wagner, I.; Tamming, R. R.; Sutton, J. J.; Gordon, K. C.; Andreassend, S. K.; Chen, K.; Hodgkiss, J. M. The photoprotection mechanism in the black–brown pigment eumelanin. *Proceedings of the National Academy of Sciences* **2022**, *119*, e2212343119.

76) Grieco, C.; Kohl, F. R.; Zhang, Y.; Natarajan, S.; Blancafort, L.; Kohler, B. Intermolecular Hydrogen Bonding Modulates O-H Photodissociation in Molecular Aggregates of a Catechol Derivative. *Photochemistry and Photobiology* **2019**, *95*, 163-175.

77) Petropoulos, V.; Mavridi-Printezi, A.; Menichetti, A.; Mordini, D.; Kabacinski, P.; Gianneschi, N. C.; Montalti, M.; Maiuri, M.; Cerullo, G. Sub-50 fs Formation of Charge Transfer States Rules the Fate of Photoexcitations in Eumelanin-Like Materials. *The Journal of Physical Chemistry Letters* **2024**, *15*, 3639-3645.

78) Grieco, C.; Kohl, F. R.; Kohler, B. Ultrafast Radical Photogeneration Pathways in Eumelanin. *Photochemistry and Photobiology* **2023**, *99*, 680-692.

79) Sarna, T.; Sealy, R. C. Free radicals from eumelanins: Quantum yields and wavelength dependence. *Archives of Biochemistry and Biophysics* **1984**, *232*, 574-578.

80) Sarna, T. Photodynamics of Melanin Radicals: Contribution to Photoprotection by Melanin. *Photochemistry and Photobiology* **2023**, *99*, 866-868.

81) Pezzella, A.; Crescenzi, O.; Panzella, L.; Napolitano, A.; Land, E. J.; Barone, V.; d'Ischia, M. Free Radical Coupling of o-Semiquinones Uncovered. *Journal of the American Chemical Society* **2013**, *135*, 12142-12149.

82) Gauden, M.; Pezzella, A.; Panzella, L.; Napolitano, A.; d'Ischia, M.; Sundström, V. Ultrafast Excited State Dynamics of 5,6-Dihydroxyindole, A Key Eumelanin Building Block: Nonradiative Decay Mechanism. *The Journal of Physical Chemistry B* **2009**, *113*, 12575-12580.

83) Crane, S. W.; Ghafur, O.; Cowie, T. Y.; Lindsay, A. G.; Thompson, J. O. F.; Greenwood, J. B.; Bebbington, M. W. P.; Townsend, D. Dynamics of electronically excited states in

the eumelanin building block 5,6-dihydroxyindole. *Physical Chemistry Chemical Physics* **2019**, *21*, 8152-8160.

84) Corani, A.; Huijser, A.; Iadonisi, A.; Pezzella, A.; Sundström, V.; D'Ischia, M. Bottom-Up approach to eumelanin photoprotection: Emission dynamics in parallel sets of water-soluble 5,6-dihydroxyindole-based model systems. *Journal of Physical Chemistry B* **2012**, *116*, 13151-13158.

85) Huijser, A.; Pezzella, A.; Hannestad, J. K.; Panzella, L.; Napolitano, A.; d'Ischia, M.; Sundström, V. UV-Dissipation Mechanisms in the Eumelanin Building Block DHICA. *ChemPhysChem* **2010**, *11*, 2424-2431.

86) Vinod, K.; Thomas, D.; Hariharan, M. Structural disorder as a key to photoprotection in eumelanin multimers. *Chemical Science* **2025**.

87) Vinod, K.; Hakeem K, L.; Thomas, D.; Das, P. P.; Hariharan, M. Probing intersystem crossing in multi-brominated eumelanin through transient absorption and surface hopping dynamics. *Organic Chemistry Frontiers* **2025**, *12*, 33-41.

88) Lea, A. J. Molecular Weight of Melanin. *Nature 1947 159:4051* **1947**, *159*, 843-843.

89) Clancy, C. M. R.; Simon, J. D. Ultrastructural Organization of Eumelanin from Sepia officinalis Measured by Atomic Force Microscopy. *Biochemistry* **2001**, *40*, 13353-13360.

90) Xie, W.; Dhinojwala, A.; Gianneschi, N. C.; Shawkey, M. D. Interactions of Melanin with Electromagnetic Radiation: From Fundamentals to Applications. *Chemical Reviews* **2024**, *124*, 7165-7213.

91) Wang, X.; Kinziabulatova, L.; Bortoli, M.; Manickoth, A.; Barilla, M. A.; Huang, H.; Blancafort, L.; Kohler, B.; Lumb, J.-P. Indole-5,6-quinones display hallmark properties of eumelanin. *Nature Chemistry* **2023**, *15*, 787-793.

92) Pathak, M. A.; Riley, F. J.; Fitzpatrick, T. B.; Curwen, W. L. Melanin Formation in Human Skin Induced by Long-Wave Ultra-Violet and Visible Light. *Nature 1962 193:4811* **1962**, *193*, 148-150.

93) Meredith, P.; Powell, B. J.; Riesz, J.; Nighswander-Rempel, S. P.; Pederson, M. R.; Moore, E. G. Towards structure–property–function relationships for eumelanin. *Soft Matter* **2006**, *2*, 37-44.

94) d'Ischia, M.; Napolitano, A.; Pezzella, A.; Meredith, P.; Sarna, T. Chemical and Structural Diversity in Eumelanins: Unexplored Bio-Optoelectronic Materials. *Angewandte Chemie International Edition* **2009**, *48*, 3914-3921.

95) Stark, K. B.; Gallas, J. M.; Zajac, G. W.; Golab, J. T.; Gidanian, S.; McIntire, T.; Farmer, P. J. Effect of Stacking and Redox State on Optical Absorption Spectra of Melanins−Comparison of Theoretical and Experimental Results. *The Journal of Physical Chemistry B* **2005**, *109*, 1970-1977.

96) Clancy, C. M. R.; Nofsinger, J. B.; Hanks, R. K.; Simon, J. D. A Hierarchical Self-Assembly of Eumelanin. *The Journal of Physical Chemistry B* **2000**, *104*, 7871-7873.

97) D'Ischia, M.; Napolitano, A.; Pezzella, A. 5,6-dihydroxyindole chemistry: Unexplored opportunities beyond eumelanin. *European Journal of Organic Chemistry* **2011**, 5501-5516.

98) Sasikumar, D.; Vinod, K.; Sunny, J.; Hariharan, M. Exciton interactions in helical crystals of a hydrogen-bonded eumelanin monomer. *Chemical Science* **2022**, *13*, 2331-2338.

99) Wang, J.; Blancafort, L. Stability and Optical Absorption of a Comprehensive Virtual Library of Minimal Eumelanin Oligomer Models. *Angewandte Chemie International Edition* **2021**, *60*, 18800-18809.

100) Pezzella, A.; Iadonisi, A.; Valerio, S.; Panzella, L.; Napolitano, A.; Adinolfi, M.; d'Ischia, M. Disentangling Eumelanin "Black Chromophore": Visible Absorption Changes As Signatures of Oxidation State- and Aggregation-Dependent Dynamic Interactions in a Model Water-Soluble 5,6-Dihydroxyindole Polymer. *Journal of the American Chemical Society* **2009**, *131*, 15270-15275.

101) Ghosh, P.; Ghosh, D. Non-radiative decay of an eumelanin monomer: to be or not to be planar. *Physical Chemistry Chemical Physics* **2019**, *21*, 6635-6642.

102) Pezzella, A.; Napolitano, A.; D'Ischia, M.; Prota, G. Oxidative polymerisation of 5,6-dihydroxyindole-2-carboxylic acid to melanin: A new insight. *Tetrahedron* **1996**, *52*, 7913-7920.

103) Thomas, B.; Dubey, R. K.; Clabbers, M. T. B.; Gupta, K. B. S. S.; van Genderen, E.; Jager, W. F.; Abrahams, J. P.; Sudholter, E. J. R.; de Groot, H. J. M. A Molecular Level Approach To Elucidate the Supramolecular Packing of Light-Harvesting Antenna Systems. *Chemistry – A European Journal* **2018**, *24*, 14989-14993.

104) Thomas, B.; Rombouts, J.; Gupta, K. B. S. S.; Orru, R. V. A.; Lammertsma, K.; de Groot, H. J. M. Determination of Controlled Self-Assembly of a Paracrystalline Material by Homology Modelling with Hybrid NMR and TEM. *Chemistry – A European Journal* **2017**, *23*, 9346-9351.

105) Mathew, R.; Mazumder, A.; Kumar, P.; Matula, J.; Mohamed, S.; Brazda, P.; Hariharan, M.; Thomas, B. Unveiling the topology of partially disordered micro-crystalline nitro-perylenediimide with X-aggregate stacking: an integrated approach. *Chemical Science* **2024**, *15*, 490-499.

106) Karothu, D. P.; Alhaddad, Z.; Göb, C. R.; Schürmann, C. J.; Bücker, R.; Naumov, P. The Elusive Structure of Levocetirizine Dihydrochloride Determined by Electron Diffraction. *Angewandte Chemie International Edition* **2023**, *62*, e202303761.

107) Vinod, K.; Jadhav, S. D.; Hariharan, M. Room Temperature Phosphorescence in Crystalline Iodinated Eumelanin Monomer. *Chemistry – A European Journal* **2024**, *30*, e202400499.

108) Gan, Z. Measuring multiple carbon–nitrogen distances in natural abundant solids using R-RESPDOR NMR. *Chemical Communications* **2006**, 4712-4714.

109) O'Dell, L. A.; Ratcliffe, C. I. Ultra-wideline 14N NMR spectroscopy as a probe of molecular dynamics. *Chemical Communications* **2010**, *46*, 6774-6776.

110) Wakamatsu, K.; Ito, S. Preparation of eumelanin-related metabolites 5,6-dihydroxyindole, 5,6-dihydroxyindole-2-carboxylic acid, and their O-methyl derivatives. *Analytical Biochemistry* **1988**, *170*, 335-340.

111) Fernández, Z.; Sánchez, L.; Santhosh Babu, S.; Fernández, G. Oligo(phenyleneethynylene)s: Shape-Tunable Building Blocks for Supramolecular Self-Assembly. *Angewandte Chemie International Edition* **2024**, *63*, e202402259-e202402259.

112) Meredith, P.; Sarna, T. The physical and chemical properties of eumelanin. *Pigment Cell Research* **2006**, *19*, 572-594.

113) Ligonzo, T.; Ambrico, M.; Augelli, V.; Perna, G.; Schiavulli, L.; Tamma, M. A.; Biagi, P. F.; Minafra, A.; Capozzi, V. Electrical and optical properties of natural and synthetic melanin biopolymer. *Journal of Non-Crystalline Solids* **2009**, *355*, 1221-1226.

114) Jarvis, J. A.; Concistre, M.; Haies, I. M.; Bounds, R. W.; Kuprov, I.; Carravetta, M.; Williamson, P. T. F. Quantitative analysis of 14N quadrupolar coupling using 1H detected 14N solid-state NMR. *Physical Chemistry Chemical Physics* **2019**, *21*, 5941-5949.

115) Wijesekara, A. V.; Venkatesh, A.; Lampkin, B. J.; VanVeller, B.; Lubach, J. W.; Nagapudi, K.; Hung, I.; Gor'kov, P. L.; Gan, Z.; Rossini, A. J. Fast Acquisition of Proton-Detected HETCOR Solid-State NMR Spectra of Quadrupolar Nuclei and Rapid Measurement of NH Bond Lengths by Frequency Selective HMQC and RESPDOR Pulse Sequences. *Chemistry – A European Journal* **2020**, *26*, 7881-7888.

116) Duong, H. A.; Chua, S.; Huleatt, P. B.; Chai, C. L. L. Synthesis of Biindolyls via Palladium-Catalyzed Reactions. *The Journal of Organic Chemistry* **2008**, *73*, 9177-9180.

117) Clark, S. J.; Segall, M. D.; Pickard, C. J.; Hasnip, P. J.; Probert, M. I. J.; Refson, K.; Payne, M. C. First principles methods using CASTEP. *Zeitschrift fur Kristallographie* **2005**, *220*, 567-570.

118) Donohue, J. Crystal Structure of Histidine Hydrochloride Monohydrate. *Nature* **1953**, *171*, 258-258.

119) Gullion, T.; Vega, A. J. Measuring heteronuclear dipolar couplings for I=1/2, S>1/2 spin pairs by REDOR and REAPDOR NMR. *Progress in Nuclear Magnetic Resonance Spectroscopy* **2005**, *47*, 123-136.

120) Spackman, M. A.; Jayatilaka, D. Hirshfeld surface analysis. *CrystEngComm* **2009**, *11*, 19-32.

121) Bader, R. F. W. A quantum theory of molecular structure and its applications. *Chemical Reviews* **1991**, *91*, 893-928.

122) John, A. T.; Narayanasamy, A.; Sudhakaran, K. P.; Hariharan, M. Resonance-Assisted Hydrogen Bonding and π-πStacking Modulates the Charge Transfer Coupling in Crystalline Naphthothiazoles. *Crystal Growth and Design* **2022**, *22*, 5686-5693.

123) Jeziorski, B.; Moszynski, R.; Szalewicz, K. Perturbation Theory Approach to Intermolecular Potential Energy Surfaces of van der Waals Complexes. *Chemical Reviews* **1994**, *94*, 1887-1930.

124) Menter, J. M.; Willis, I. Electron Transfer and Photoprotective Properties of Melanins in Solution. *Pigment Cell Research* **1997**, *10*, 214-217.

125) Hestand, N. J.; Spano, F. C. Molecular Aggregate Photophysics beyond the Kasha Model: Novel Design Principles for Organic Materials. *Accounts of Chemical Research* **2017**, *50*, 341-350.

126) *Gaussian 16 Rev. C.01*; Wallingford, CT, 2016. (accessed.

127) Plasser, F. TheoDORE: A toolbox for a detailed and automated analysis of electronic excited state computations. *The Journal of Chemical Physics* **2020**, *152*, 084108-084108.

128) Matta, M.; Pezzella, A.; Troisi, A. Relation between Local Structure, Electric Dipole, and Charge Carrier Dynamics in DHICA Melanin: A Model for Biocompatible Semiconductors. *The Journal of Physical Chemistry Letters* **2020**, *11*, 1045-1051.

129) Okuda, H.; Nakamura, A.; Wakamatsu, K.; Ito, S.; Sota, T. Mid-infrared absorption spectrum of 5,6-dihydroxyindole-2-carboxylic acid. *Chemical Physics Letters* **2007**, *433*, 355-359.

130) Dreyer, D. R.; Miller, D. J.; Freeman, B. D.; Paul, D. R.; Bielawski, C. W. Elucidating the structure of poly(dopamine). *Langmuir* **2012**, *28*, 6428-6435.

131) Ni, Q. Z.; Sierra, B. N.; La Clair, J. J.; Burkart, M. D. Chemoenzymatic elaboration of the Raper–Mason pathway unravels the structural diversity within eumelanin pigments. *Chemical Science* **2020**, *11*, 7836-7841.

132) Pezzella, A.; Napolitano, A.; d'Ischia, M.; Prota, G.; Seraglia, R.; Traldi, P. Identification of Partially Degraded Oligomers of 5,6-Dihydroxyindole-2-carboxylic Acid in Sepia Melanin by Matrix-assisted Laser Desorption/Ionization Mass Spectrometry. *Rapid Communications in Mass Spectrometry* **1997**, *11*, 368-372.

133) Capozzi, V.; Perna, G.; Carmone, P.; Gallone, A.; Lastella, M.; Mezzenga, E.; Quartucci, G.; Ambrico, M.; Augelli, V.; Biagi, P. F.; et al. Optical and photoelectronic properties of melanin. *Thin Solid Films* **2006**, *511-512*, 362-366.

134) Meng, S.; Kaxiras, E. Theoretical Models of Eumelanin Protomolecules and their Optical Properties. *Biophysical Journal* **2008**, *94*, 2095-2105.

135) Tuna, D.; Udvarhelyi, A.; Sobolewski, A. L.; Domcke, W.; Domratcheva, T. Onset of the Electronic Absorption Spectra of Isolated and π-Stacked Oligomers of 5,6-Dihydroxyindole: An Ab Initio Study of the Building Blocks of Eumelanin. *The Journal of Physical Chemistry B* **2016**, *120*, 3493-3502.

136) Gaeta, M.; Randazzo, R.; Villari, V.; Micali, N.; Pezzella, A.; Purrello, R.; d'Ischia, M.; D'Urso, A. En Route to a Chiral Melanin: The Dynamic "From-Imprinted-to-Template" Supramolecular Role of Porphyrin Hetero-Aggregates During the Oxidative Polymerization of L-DOPA. *Frontiers in Chemistry* **2020**, *8*.

137) Peles, D. N.; Lin, E.; Wakamatsu, K.; Ito, S.; Simon, J. D. Ultraviolet Absorption Coefficients of Melanosomes Containing Eumelanin As Related to the Relative Content of DHI and DHICA. *The Journal of Physical Chemistry Letters* **2010**, *1*, 2391-2395.

138) Xie, W.; Pakdel, E.; Liang, Y.; Kim, Y. J.; Liu, D.; Sun, L.; Wang, X. Natural Eumelanin and Its Derivatives as Multifunctional Materials for Bioinspired Applications: A Review. *Biomacromolecules* **2019**, *20*, 4312-4331.

139) Aebly, A. H.; Levy, Jeffrey N.; Steger, B. J.; Quirke, J. C.; Belitsky, J. M. Expedient synthesis of eumelanin-inspired 5,6-dihydroxyindole-2-carboxylate ethyl ester derivatives. *RSC Advances* **2018**, *8*, 28323-28328.

140) Choudhury, A.; Ramakrishnan, R.; Ghosh, D. Structure prediction from spectra amidst dynamical heterogeneity in melanin. *Chemical Communications* **2024**, *60*, 2613-2616.

141) Albrecht, C. Joseph R. Lakowicz: Principles of fluorescence spectroscopy, 3rd Edition. *Analytical and Bioanalytical Chemistry* **2008**, *390*, 1223-1224.

142) Poh, Y. R.; Pannir-Sivajothi, S.; Yuen-Zhou, J. Understanding the Energy Gap Law under Vibrational Strong Coupling. *The Journal of Physical Chemistry C* **2023**, *127*, 5491-5501.

143) Ghosh, P.; Alvertis, A. M.; Chowdhury, R.; Murto, P.; Gillett, A. J.; Dong, S.; Sneyd, A. J.; Cho, H.-H.; Evans, E. W.; Monserrat, B.; et al. Decoupling excitons from high-frequency vibrations in organic molecules. *Nature* **2024**, *629*, 355-362.

144) Mazumder, A.; Vinod, K.; Maret, P. D.; Das, P. P.; Hariharan, M. Symmetry-Breaking Charge Separation Mediated Triplet Population in a Perylenediimide Trimer at the Single-Molecule Level. *The Journal of Physical Chemistry Letters* **2024**, *15*, 5896-5904.

145) Mallia, A. R.; Salini, P. S.; Hariharan, M. Nonparallel Stacks of Donor and Acceptor Chromophores Evade Geminate Charge Recombination. *Journal of the American Chemical Society* **2015**, *137*, 15604-15607.

146) Yuan, W. Z.; Lu, P.; Chen, S.; Lam, J. W. Y.; Wang, Z.; Liu, Y.; Kwok, H. S.; Ma, Y.; Tang, B. Z. Changing the Behavior of Chromophores from Aggregation-Caused Quenching to Aggregation-Induced Emission: Development of Highly Efficient Light Emitters in the Solid State. *Advanced Materials* **2010**, *22*, 2159-2163.

147) Whitesides, G. M.; Grzybowski, B. Self-Assembly at All Scales. *Science* **2002**, *295*, 2418-2421.

148) Philips, D. S.; Kartha, K. K.; Politi, A. T.; Krüger, T.; Albuquerque, R. Q.; Fernández, G. Interplay between H-Bonding and Preorganization in the Evolution of Self-Assembled Systems. *Angewandte Chemie International Edition* **2019**, *58*, 4732-4736.

149) Zhou, X.; Gong, X.; Cao, W.; Forman, C. J.; Oktawiec, J.; D'Alba, L.; Sun, H.; Thompson, M. P.; Hu, Z.; Kapoor, U.; et al. Anisotropic Synthetic Allomelanin Materials via Solid-State Polymerization of Self-Assembled 1,8-Dihydroxynaphthalene Dimers. *Angewandte Chemie International Edition* **2021**, *60*, 17464-17471.

150) Zhou, X.; McCallum, N. C.; Hu, Z.; Cao, W.; Gnanasekaran, K.; Feng, Y.; Stoddart, J. F.; Wang, Z.; Gianneschi, N. C. Artificial Allomelanin Nanoparticles. *ACS Nano* **2019**, *13*, 10980-10990.

151) Nofsinger, J. B.; Forest, S. E.; Eibest, L. M.; Gold, K. A.; Simon, J. D. Probing the Building Blocks of Eumelanins Using Scanning Electron Microscopy. *Pigment Cell Research* **2000**, *13*, 179-184.

152) Maia, R.; Rubenstein, D. R.; Shawkey, M. D. Key ornamental innovations facilitate diversification in an avian radiation. *Proceedings of the National Academy of Sciences* **2013**, *110*, 10687-10692.

153) Ju, K.-Y.; Fischer, M. C.; Warren, W. S. Understanding the Role of Aggregation in the Broad Absorption Bands of Eumelanin. *ACS Nano* **2018**, *12*, 12050-12061.

154) Lv, M.; Wang, X.; Wang, D.; Li, X.; Liu, Y.; Pan, H.; Zhang, S.; Xu, J.; Chen, J. Unravelling the role of charge transfer state during ultrafast intersystem crossing in compact organic chromophores. *Physical Chemistry Chemical Physics* **2021**, *23*, 25455-25466.

155) Robertson, P. A.; Bishop, H. M.; Orr-Ewing, A. J. Tuning the Excited-State Dynamics of Acetophenone Using Metal Ions in Solution. *The Journal of Physical Chemistry Letters* **2021**, *12*, 5473-5478.

156) Ohmori, N.; Suzuki, T.; Ito, M. Why does intersystem crossing occur in isolated molecules of benzaldehyde, acetophenone, and benzophenone? *The Journal of Physical Chemistry* **1988**, *92*, 1086-1093.

157) Young, R. M.; Wasielewski, M. R. Mixed Electronic States in Molecular Dimers: Connecting Singlet Fission, Excimer Formation, and Symmetry-Breaking Charge Transfer. *Accounts of Chemical Research* **2020**, *53*, 1957-1968.

158) Kang, S.; Choi, W.; Ahn, J.; Kim, T.; Oh, J. H.; Kim, D. Impact of Packing Geometry on Excimer Characteristics and Mobility in Perylene Bisimide Polycrystalline Films. *ACS Applied Materials & Interfaces* **2024**, *16*, 18134-18143.

159) Wang, S.; Liu, H.; Zhao, S.; Wu, Q.; Yang, Z.; Yang, D.; Lv, Y.; Su, Q.; Zhang, S.-T.; Yang, B. A comparative investigation on excimer fluorescence toward its bright future. *Chemical Science* **2025**, *16*, 3275-3284.

160) Morgenroth, M.; Mirko, S.; Laure, G.; Kawon, O.; and Lenzer, T. Ultrafast excited-state dynamics of thin films consisting of helicene-like molecules based on dibenzo[c,h]acridine. *Molecular Physics* **2021**, *119*, e1959072.

161) Schlosser, M.; Lochbrunner, S. Exciton Migration by Ultrafast Förster Transfer in Highly Doped Matrixes. *The Journal of Physical Chemistry B* **2006**, *110*, 6001-6009.

162) Wood, P. D.; Redmond, R. W. Triplet State Interactions between Nucleic Acid Bases in Solution at Room Temperature: Intermolecular Energy and Electron Transfer. *Journal of the American Chemical Society* **1996**, *118*, 4256-4263.

163) Bauer, B.; Sharma, R.; Chergui, M.; Oppermann, M. Exciton decay mechanism in DNA single strands: back-electron transfer and ultrafast base motions. *Chemical Science* **2022**, *13*, 5230-5242.

164) Pecourt, J.-M. L.; Peon, J.; Kohler, B. Ultrafast Internal Conversion of Electronically Excited RNA and DNA Nucleosides in Water. *Journal of the American Chemical Society* **2000**, *122*, 9348-9349.

165) Kabe, R.; Adachi, C. Organic long persistent luminescence. *Nature* **2017**, *550*, 384-387.

166) Li, Y.; Gecevicius, M.; Qiu, J. Long persistent phosphors—from fundamentals to applications. *Chemical Society Reviews* **2016**, *45*, 2090-2136.

167) Si, C.; Wang, T.; Gupta, A. K.; Cordes, D. B.; Slawin, A. M. Z.; Siegel, J. S.; Zysman-Colman, E. Room-Temperature Multiple Phosphorescence from Functionalized Corannulenes: Temperature Sensing and Afterglow Organic Light-Emitting Diode. *Angewandte Chemie International Edition* **2023**, *62*, e202309718.

168) Kim, K.-H.; Kim, J.-J. Origin and Control of Orientation of Phosphorescent and TADF Dyes for High-Efficiency OLEDs. *Advanced Materials* **2018**, *30*, 1705600.

169) Kim, J. U.; Park, I. S.; Chan, C.-Y.; Tanaka, M.; Tsuchiya, Y.; Nakanotani, H.; Adachi, C. Nanosecond-time-scale delayed fluorescence molecule for deep-blue OLEDs with small efficiency rolloff. *Nature Communications* **2020**, *11*, 1765.

170) Li, X.; Baryshnikov, G.; Deng, C.; Bao, X.; Wu, B.; Zhou, Y.; Ågren, H.; Zhu, L. A three-dimensional ratiometric sensing strategy on unimolecular fluorescence–thermally activated delayed fluorescence dual emission. *Nature Communications* **2019**, *10*, 731.

171) Zhao, Y.; Yang, J.; Liang, C.; Wang, Z.; Zhang, Y.; Li, G.; Qu, J.; Wang, X.; Zhang, Y.; Sun, P.; et al. Fused-Ring Pyrrole-Based Near-Infrared Emissive Organic RTP Material for Persistent Afterglow Bioimaging. *Angewandte Chemie International Edition* **2024**, *63*, e202317431.

172) Dos Santos, J. M.; Hall, D.; Basumatary, B.; Bryden, M.; Chen, D.; Choudhary, P.; Comerford, T.; Crovini, E.; Danos, A.; De, J.; et al. The Golden Age of Thermally Activated Delayed Fluorescence Materials: Design and Exploitation. *Chemical Reviews* **2024**, *124*, 13736-14110.

173) Okumura, R.; Tanaka, H.; Shizu, K.; Fukushima, S.; Yasuda, Y.; Kaji, H. Development of an Organic Emitter Exhibiting Reverse Intersystem Crossing Faster than Intersystem Crossing. *Angewandte Chemie International Edition* **2024**, *63*, e202409670.

174) Zhao, W.; He, Z.; Tang, B. Z. Room-temperature phosphorescence from organic aggregates. *Nature Reviews Materials* **2020**, *5*, 869-885.

175) Kenry; Chen, C.; Liu, B. Enhancing the performance of pure organic room-temperature phosphorescent luminophores. *Nature Communications* **2019**, *10*, 2111.

176) Niyas, M. A.; Garain, S.; Shoyama, K.; Würthner, F. Room-Temperature Near-Infrared Phosphorescence from C64 Nanographene Tetraimide by π-Stacking Complexation with Platinum Porphyrin. *Angewandte Chemie International Edition* **2024**, *63*, e202406353.

177) Chen, D.; Wang, H.; Sun, D.; Wu, S.; Wang, K.; Zhang, X.-H.; Zysman-Colman, E. The Combination of a Donor–Acceptor TADF and a MR-TADF Emitting Core Results in Outstanding Electroluminescence Performance. *Advanced Materials* **2024**, *36*, 2412761.

178) Chen, L.; Zhang, S.; Li, H.; Chen, R.; Jin, L.; Yuan, K.; Li, H.; Lu, P.; Yang, B.; Huang, W. Breaking the Efficiency Limit of Fluorescent OLEDs by Hybridized Local and Charge-Transfer Host Materials. *The Journal of Physical Chemistry Letters* **2018**, *9*, 5240-5245.

179) Meng, G.; Dai, H.; Wang, Q.; Zhou, J.; Fan, T.; Zeng, X.; Wang, X.; Zhang, Y.; Yang, D.; Ma, D.; et al. High-efficiency and stable short-delayed fluorescence emitters with hybrid long- and short-range charge-transfer excitations. *Nature Communications* **2023**, *14*, 2394.

180) Liao, C.; Wang, S.; Chen, B.; Xie, Q.; Feng, J.; Bai, J.; Li, X.; Liu, H. Hybrid Local and Charge Transfer Emitters Utilizing Hyperconjugation Effect Towards Solution-Processed Ultra-Deep-Blue OLEDs with External Quantum Efficiency Approaching 12 %. *Angewandte Chemie International Edition* **2025**, *64*, e202414905.

181) Li, W.; Pan, Y.; Xiao, R.; Peng, Q.; Zhang, S.; Ma, D.; Li, F.; Shen, F.; Wang, Y.; Yang, B.; et al. Employing ~100% Excitons in OLEDs by Utilizing a Fluorescent Molecule with Hybridized Local and Charge-Transfer Excited State. *Advanced Functional Materials* **2014**, *24*, 1609-1614.

182) Aumiler, D.; Wang, S.; Chen, X.; Xia, A. Excited State Localization and Delocalization of Internal Charge Transfer in Branched Push−Pull Chromophores Studied by Single-Molecule Spectroscopy. *Journal of the American Chemical Society* **2009**, *131*, 5742-5743.

183) Tsujimoto, H.; Ha, D.-G.; Markopoulos, G.; Chae, H. S.; Baldo, M. A.; Swager, T. M. Thermally Activated Delayed Fluorescence and Aggregation Induced Emission with Through-Space Charge Transfer. *Journal of the American Chemical Society* **2017**, *139*, 4894-4900.

184) Gong, H.; Song, Y.; He, J.; Wang, P.; Xiang, Y.; Li, S.; Yao, J.; Liao, B.; Liao, Q.; Fu, H. Switching from Thermally Activated Delayed Fluorescence in Single Crystals for Low-Threshold Laser to Room-temperature Phosphorescence in Amorphous-Film for Highly Efficient OLEDs. *Angewandte Chemie International Edition* **2024**, *63*, e202400089.

185) Bolton, O.; Lee, K.; Kim, H.-J.; Lin, K. Y.; Kim, J. Activating efficient phosphorescence from purely organic materials by crystal design. *Nature Chemistry* **2011**, *3*, 205-210.

186) Stavrou, K.; Franca, L. G.; Monkman, A. P. Photophysics of TADF Guest–Host Systems: Introducing the Idea of Hosting Potential. *ACS Applied Electronic Materials* **2020**, *2*, 2868-2881.

187) Greciano, E. E.; Calbo, J.; Ortí, E.; Sánchez, L. N-Annulated Perylene Bisimides to Bias the Differentiation of Metastable Supramolecular Assemblies into J- and H-Aggregates. *Angewandte Chemie International Edition* **2020**, *59*, 17517-17524.

188) Manha Veedu, R.; Niemeyer, N.; Bäumer, N.; Kartha Kalathil, K.; Neugebauer, J.; Fernández, G. Sterically Allowed H-type Supramolecular Polymerizations. *Angewandte Chemie International Edition* **2023**, *62*, e202314211.

189) Li, S.; Fu, L.; Xiao, X.; Geng, H.; Liao, Q.; Liao, Y.; Fu, H. Regulation of Thermally Activated Delayed Fluorescence to Room-Temperature Phosphorescent Emission Channels by Controlling the Excited-States Dynamics via J- and H-Aggregation. *Angewandte Chemie International Edition* **2021**, *60*, 18059-18064.

190) Xue, J.; Liang, Q.; Wang, R.; Hou, J.; Li, W.; Peng, Q.; Shuai, Z.; Qiao, J. Highly Efficient Thermally Activated Delayed Fluorescence via J-Aggregates with Strong Intermolecular Charge Transfer. *Advanced Materials* **2019**, *31*, 1808242.

191) Lucenti, E.; Forni, A.; Botta, C.; Carlucci, L.; Giannini, C.; Marinotto, D.; Previtali, A.; Righetto, S.; Cariati, E. H-Aggregates Granting Crystallization-Induced Emissive Behavior and Ultralong Phosphorescence from a Pure Organic Molecule. *The Journal of Physical Chemistry Letters* **2017**, *8*, 1894-1898.

192) Gierschner, J.; Lüer, L.; Milián-Medina, B.; Oelkrug, D.; Egelhaaf, H.-J. Highly Emissive H-Aggregates or Aggregation-Induced Emission Quenching? The Photophysics of All-Trans para-Distyrylbenzene. *The Journal of Physical Chemistry Letters* **2013**, *4*, 2686-2697.

193) Xu, S.; Liu, T.; Mu, Y.; Wang, Y.-F.; Chi, Z.; Lo, C.-C.; Liu, S.; Zhang, Y.; Lien, A.; Xu, J. An Organic Molecule with Asymmetric Structure Exhibiting Aggregation-Induced Emission, Delayed Fluorescence, and Mechanoluminescence. *Angewandte Chemie International Edition* **2015**, *54*, 874-878.

194) Li, S.; Chen, J.; Wei, Y.; De, J.; Geng, H.; Liao, Q.; Chen, R.; Fu, H. An Organic Laser Based on Thermally Activated Delayed Fluorescence with Aggregation-Induced Emission and Local Excited State Characteristics. *Angewandte Chemie International Edition* **2022**, *61*, e202209211.

195) Jin, L.; Wang, Z.; Mo, W.; Deng, H.; Hong, W.; Chi, Z. Hierarchical Dual-Mode Efficient Tunable Afterglow via J-Aggregates in Single-Phosphor-Doped Polymer. *Angewandte Chemie International Edition* **2024**, *63*, e202410974.

196) Garain, S.; Ansari, S. N.; Kongasseri, A. A.; Chandra Garain, B.; Pati, S. K.; George, S. J. Room temperature charge-transfer phosphorescence from organic donor–acceptor Co-crystals. *Chemical Science* **2022**, *13*, 10011-10019.

197) Kongasseri, A. A.; Ansari, S. N.; Garain, S.; Wagalgave, S. M.; George, S. J. Revisiting organic charge-transfer cocrystals for wide-range tunable, ambient phosphorescence. *Chemical Science* **2023**, *14*, 12548-12553.

198) Xue, N.; Zhou, H.-Y.; Han, Y.; Li, M.; Lu, H.-Y.; Chen, C.-F. A general supramolecular strategy for fabricating full-color-tunable thermally activated delayed fluorescence materials. *Nature Communications* **2024**, *15*, 1425.

199) Kaur, I.; Jia, W.; Kopreski, R. P.; Selvarasah, S.; Dokmeci, M. R.; Pramanik, C.; McGruer, N. E.; Miller, G. P. Substituent Effects in Pentacenes: Gaining Control over HOMO−LUMO Gaps and Photooxidative Resistances. *Journal of the American Chemical Society* **2008**, *130*, 16274-16286.

200) Ma, F.; Zhang, S.; Jiang, J.; Liu, Y.; Sun, J.; Lam, J. W. Y.; Zhao, Z.; Tang, B. Z. Aggregate Science: from Molecules, beyond Molecules. *Advanced Materials* **2025**, *37*, 2414188.

201) Tasi, G.; Palinko, I.; Nyerges, L.; Fejes, P.; Foerster, H. Calculation of electrostatic potential maps and atomic charges for large molecules. *Journal of Chemical Information and Computer Sciences* **1993**, *33*, 296-299.

202) Contreras-García, J.; Johnson, E. R.; Keinan, S.; Chaudret, R.; Piquemal, J.-P.; Beratan, D. N.; Yang, W. NCIPLOT: A Program for Plotting Noncovalent Interaction Regions. *Journal of Chemical Theory and Computation* **2011**, *7*, 625-632.

203) Zhang, W.; Li, S.; Gong, Y.; Zhang, J.; Zhou, Y.; Kong, J.; Fu, H.; Zhou, M. Aggregation Enhanced Thermally Activated Delayed Fluorescence through Spin-Orbit Coupling Regulation. *Angewandte Chemie International Edition* **2024**, *63*, e202404978.

204) Matern, J.; Bäumer, N.; Fernández, G. Unraveling Halogen Effects in Supramolecular Polymerization. *Journal of the American Chemical Society* **2021**, *143*, 7164-7175.

205) Nidhankar, A. D.; Goudappagouda; Mohana Kumari, D. S.; Chaubey, S. K.; Nayak, R.; Gonnade, R. G.; Kumar, G. V. P.; Krishnan, R.; Babu, S. S. Self-Assembled Helical Arrays for the Stabilization of the Triplet State. *Angewandte Chemie International Edition* **2020**, *59*, 13079-13085.

206) Freeman, D. M. E.; Musser, A. J.; Frost, J. M.; Stern, H. L.; Forster, A. K.; Fallon, K. J.; Rapidis, A. G.; Cacialli, F.; McCulloch, I.; Clarke, T. M.; et al. Synthesis and Exciton Dynamics of Donor-Orthogonal Acceptor Conjugated Polymers: Reducing the Singlet–Triplet Energy Gap. *Journal of the American Chemical Society* **2017**, *139*, 11073-11080.

207) Peinkofer, K. R.; Williams, M. L.; Mantel, G. C.; Phelan, B. T.; Young, R. M.; Wasielewski, M. R. Polarity of Ordered Solvent Molecules in 9,9′-Bianthracene Single Crystals Selects between Singlet Fission or Symmetry-Breaking Charge Separation. *Journal of the American Chemical Society* **2024**, *146*, 34934-34942.

208) Imahori, H.; Kobori, Y.; Kaji, H. Manipulation of Charge-Transfer States by Molecular Design: Perspective from “Dynamic Exciton”. *Accounts of Materials Research* **2021**, *2*, 501-514.

209) Zhao, X.; Sukhanov, A. A.; Jiang, X.; Zhao, J.; Voronkova, V. K. Long-Lived Triplet Charge Separated State and Thermally Activated Delayed Fluorescence in a Compact Orthogonal Anthraquinone–Phenothiazine Electron Donor–Acceptor Dyad. *The Journal of Physical Chemistry Letters* **2022**, *13*, 2533-2539.

210) Ema, F.; Tanabe, M.; Saito, S.; Yoneda, T.; Sugisaki, K.; Tachikawa, T.; Akimoto, S.; Yamauchi, S.; Sato, K.; Osuka, A.; et al. Charge-Transfer Character Drives Möbius Antiaromaticity in the Excited Triplet State of Twisted [28]Hexaphyrin. *The Journal of Physical Chemistry Letters* **2018**, *9*, 2685-2690.

211) Higashi, K.; Okamoto, T.; Iwaya, N.; Sakuda, E.; Kay, C. W. M.; Ikoma, T.; Higashi, M.; Kobori, Y. Vibronic Trimer Design Enhancing Intramolecular Triplet-Exciton Hopping to Accelerate Triplet-Triplet Annihilation for Photon Upconversion. *Angewandte Chemie International Edition n/a*, e202503846.

212) Samanta, P. K.; Kim, D.; Coropceanu, V.; Brédas, J.-L. Up-Conversion Intersystem Crossing Rates in Organic Emitters for Thermally Activated Delayed Fluorescence: Impact of the Nature of Singlet vs Triplet Excited States. *Journal of the American Chemical Society* **2017**, *139*, 4042-4051.

213) Chen, D.; Zhang, L.; Matulaitis, T.; Cordes, D. B.; Slawin, A. M. Z.; Zhang, X.-H.; Samuel, I. D. W.; Zysman-Colman, E. Tuning the emission and exciton utilization mechanisms of pyrazine-based multi-carbazole emitters and their use in organic light-emitting diodes. *Journal of Materials Chemistry C* **2023**, *11*, 13095-13105.

214) Pander, P.; Motyka, R.; Zassowski, P.; Etherington, M. K.; Varsano, D.; da Silva, T. J.; Caldas, M. J.; Data, P.; Monkman, A. P. Thermally Activated Delayed Fluorescence Mediated through the Upper Triplet State Manifold in Non-Charge-Transfer Star-Shaped Triphenylamine–Carbazole Molecules. *The Journal of Physical Chemistry C* **2018**, *122*, 23934-23942.

215) Gelin, S.; Champagne-Ruel, A.; Mousseau, N. Enthalpy-entropy compensation of atomic diffusion originates from softening of low frequency phonons. *Nature Communications* **2020**, *11*, 3977.

List of Publications

Published

1) **K. Vinod**, N. Noushad, R. Mathew, D. Thomas, M. Gangopadhyay, B. Thomas and M. Hariharan*, Modulating Supramolecular Topology via Hydrogen Bonding in a Eumelanin Monomer, *Chem. Eur. J.* **2026**, e03052 (DOI: 10.1002/chem.202503052).

2) A. Mazumder, **K. Vinod**, Amalnadh T., P. D. Maret and M. Hariharan*, Ultrafast Symmetry-Breaking Charge Separation in Thin Films of J-Aggregated Perylenediimide Multimers in a Nonpolar Solid-State Environment, *Chem. Commun.* **2025**, *61*, 17641-17644 (DOI: 10.1039/d5cc04382d).

3) S. Sujilkumar, **K. Vinod**, Sharat Devadas, M. Hariharan*, Ultrafast Charge Transfer Dynamics of Near-infrared Emitting Nitro-Terrylenediimides, *J. Phys. Chem. C* **2025**, *129*, 18075–18082 (DOI: 10.1021/acs.jpcc.5c02980).

4) **K. Vinod**, N. Noushad, H. Tanaka, N. Mohan, Y. Kokado, D. Tomiya, Y. Kobori, M. Hariharan*, Aggregation-Assisted Energy Gap Modulation Controls Delayed Emission in Hybrid Charge-Transfer Emitters, *Chem. Sci.* **2025**, *16*, 15546-15554 (DOI: 10.1039/D5SC02071A).

5) **K. Vinod**, D. Thomas and M. Hariharan*, Structural Disorder as a Key to Photoprotection in Eumelanin Multimers, *Chem. Sci.* **2025**, *16*, 14304-14313 (DOI: 10.1039/D5SC00920K).

6) A. Mazumder, P. P. Das, **K. Vinod**, P. D. Maret, M. P. Lijina, B. Engels* and M. Hariharan*, Core-Twist Modulated Quantum Jumps in a π-Fused Single-Molecule, *J. Phys. Chem. Lett.* **2025**, *16*, 4643–4651 (DOI: 10.1021/acs.jpclett.5c01002).

7) J. Sivanarayanan, **K. Vinod**, A. Binoy, M. Hariharan*, Unlocking the Room Temperature Phosphorescence through Halogen Engineering in Carbazole Dimer, *Chem. Eur. J.* **2025**, *31*, e202500635 (DOI: 10.1002/chem.202500635).

8) A. Mazumder, **K. Vinod**, A. Thomas, M. Hariharan*, Accelerating Symmetry-Breaking Charge Separation in an Angular versus Linear Perylenediimide Dimer through the Modulation of Coulombic Coupling, *J. Phys. Chem. Lett.* **2025**, *16*, 4819–4827 (DOI: 10.1021/acs.jpclett.5c00372).

9) A. Muralidharan, **K. Vinod**, F. T. Pattanmarthodiyil, L. Hakeem K., M. Hariharan*, Long-lived Intramolecular Charge Transfer in Persubstituted Perylenediimide, *J. Phys. Chem. C* **2025**, *129*, 5148–5155 (DOI: 10.1021/acs.jpcc.5c00067).

10) **K. Vinod**[†], L. Hakeem K.[†], D. Thomas, P. P. Das and M. Hariharan*, Probing Intersystem Crossing in Multi-brominated Eumelanin through Transient Absorption and Surface Hopping Dynamics, *Org. Chem. Front.* **2025**, *12*, 33-41 (DOI: 10.1039/D4QO01832J).

11) **K. Vinod**[†], R. Mathew[†], C. Jandl, B. Thomas* and M. Hariharan*, Electron Diffraction and Solid-state NMR Reveal the Structure and Exciton Coupling in a Eumelanin Precursor, *Chem. Sci.* **2024**, *15*, 16015-16024 (DOI: 10.1039/D4SC05453A).

12) S. Sujilkumar, P. D. Maret, **K. Vinod**, A. T. John, M. Hariharan*, Single-Molecule Detection of a Terrylenediimide-Based Near-Infrared Emitter, *Chem. Sci.* **2024**, *15*, 17007-17016 (DOI: 10.1039/D4SC03861D).

13) J. Rühe, **K. Vinod**, H. Hoh, K. Shoyama, M. Hariharan*, and F. Würthner*, Guest-Mediated Modulation of Photophysical Pathways in a Coronene Bisimide Cyclophane, *J. Am. Chem. Soc.* **2024**, *146*, 28222–28232 (DOI: 10.1021/jacs.4c08479).

14) **K. Vinod**, S. Jadav and M. Hariharan*, Room Temperature Phosphorescence in Crystalline Iodinated Eumelanin Monomer, *Chem. Eur. J.* **2024**, *30*, e202400499 (DOI: 10.1002/chem.202400499).

15) A. Mazumder, **K. Vinod**, P. D. Maret, P. P. Das and M. Hariharan*, Symmetry-Breaking Charge Separation Mediated Triplet Population in a Perylenediimide Trimer at the Single-Molecule Level, *J. Phys. Chem. Lett.* **2024**, *15*, 5896–5904 (DOI: 10.1021/acs.jpclett.4c01201).

16) J. Sivanarayanan, E. Sebastian, **K. Vinod**, F. Würthner and M. Hariharan*, Ultrafast Intersystem Crossing in Selenium Annulated Perylenediimide, *J. Phys. Chem. C* **2022**, *126*, 13319–13326 (DOI: 10.1021/acs.jpcc.2c03847).

17) D. Sasikumar, **K. Vinod**, J. Sunny and M. Hariharan*, Exciton Interactions in the Helical Crystals of Hydrogen Bonded Eumelanin Monomer, *Chem. Sci.* **2022**, *13*, 2331-2338 (DOI: 10.1039/D1SC06755A).

Submitted

18) P. E. S. Krishna, H. Baiju, **K. Vinod**, V. Naik, M. Hariharan*, Protonation Driven Modulation of Excited State Dynamics in Tetraaza[7]helicene, (2026, Under Submission).

19) J. Sivanarayanan, **K. Vinod**, A. Benoy, T. Amalnadh, S. Suresh and M. Hariharan*, 3D Electron Diffraction Reveals the Structural Origin of Delayed Dual Emission in a Heavy Atom-Free Carbazole Hexamer (2026, Under Submission).

20) **K. Vinod**, C. Tonnele*, A. Rana, P. E. S. Krishna, J. C. Roldao, D. Casanova, H. Ottosson* and M. Hariharan*, Azulene as Anomaly in Triplet-State Engineering Via Bromination and/or Carbonylation: Internal Conversion Overrides Intersystem Crossing, (2026, Under Submission).

21) **K. Vinod**, B. Thomas, M. Hariharan*, Disorder, Dynamics and Design: Ultrafast Pathways of Energy Deactivation in Eumelanin, (2026, Under Submission).

22) **K. Vinod**[†], R. Mathew[†], T. Amalnadh, N. Noushad, Y. Nishyama*, B. Thomas*, M. Hariharan*, Cross-Linked Graphitic Network Stacks in the Dihydroxyindole-based Eumelanin, (2026, Under Submission).

23) S. Sujilkumar, **K. Vinod**, H. Tanaka, Y. Kokado, Y. Kobori*, M. Hariharan*, Enabling Thermally Activated Delayed Fluorescence in Organic Charge Transfer Cocrystal, (2026, Under Preparation).

24) J. Sivanarayanan, **K. Vinod**, S. Suresh, M. Hariharan*, Topological Control of Excited-State Dynamics in Carbazole Trimers via Rigidity, Coupling, and Conformation, (2026, Under Preparation).

Workshops and Conferences

1) Oral Slam Presentation at the **6th Frontiers Symposium in Chemistry (FS-CHM 2026)**, organised by School of Chemistry, IISER Thiruvananthapuram (January 30 - February 1, 2026).

2) Poster Presentation at the **13th Asian and Oceanian Photochemistry Conference (APC2025)**, organised by IISER Thiruvananthapuram, held at Kochi, Kerala (October 21-25, 2025).

3) Poster Presentation at the **5th Frontiers Symposium in Chemistry (FS-CHM 2025)**, organised by School of Chemistry, IISER Thiruvananthapuram (January 31 - February 2, 2025).

4) Participated in the **International Research Training Group (IRTG) 2991 Startup Meeting** at IISER Thiruvananthapuram, India (February 25-28, 2025).

5) Oral and poster presentation at the **12th International Symposium on Dynamic Exciton (ISDyEx 2024)**, Thiruvananthapuram, India (December 14-15, 2024).

6) Poster Presentation at the **International Winter School 2024 on "Frontiers in Material Science"**, JNCASR, India (December 2-6, 2024).

7) Poster Presentation at the **ChemSci 2024 LITF Symposium**, IISER Thiruvananthapuram, India (December 9-11, 2024).

8) Poster Presentation at the **ATOS Materials in Focus**, organized by IISER Mohali, India (December 15-17, 2023).

9) Poster Presentation at the **National Workshop on Fluorescence and Raman Spectroscopy (FCS XIV)**, IISER Mohali, India (December 9-15, 2023).

10) Poster presentation at the 10th Ultrafast Sciences 2023 DAE-BRNS 10th Theme Meeting (UFS-2023), held at National Physical Laboratory (CSIR NPL), India (November 25-27, 2023).

11) Teacher and facilitator at **Yusuf Hamied Chemistry Camp**, IISER Thiruvananthapuram, India (July 19-21, 2023).

12) Participated in the **3rd Edition of the Annual Symposium, Frontier Symposium in Chemistry 2023 (FS-CHM 2023)**, IISER Thiruvananthapuram, India (January 13-15, 2023).

13) Poster Presentation at the **13th National workshop on Fluorescence and Raman Spectroscopy (FCSXIII)**, Fluorescence Chemical Society, IISER Thiruvananthapuram and RGCB, India (January 6-11, 2023).

14) Participated in the **9th Theme meeting on Ultrafast Sciences (UFS 2022)**, IISER Thiruvananthapuram, India (November 3-5, 2022).

15) Participated in the **2nd Edition of the Annual Symposium, Frontier Symposium in Chemistry 2022 (FS-CHM 2022)**, IISER Thiruvananthapuram, India (April 8-10, 2022).

16) Participated in the **12th National workshop on Fluorescence and Raman Spectroscopy (FCS 2021)**, Fluorescence Chemical Society, IISER Thiruvananthapuram and RGCB, India (November 29 - December 4, 2021).

17) Participated in the **Virtual Chemistry Course "Functional π-Systems – Organic Materials Design by Molecular and Supramolecular Engineering"**, Department of Chemistry & Pharmacy at the Julius-Maximilians-Universität Würzburg, Germany (July 19-23, 2021).

Achievements in Workshops and Conferences

1) Invited flash talk at the upcoming ACS Spring 2026 Digital Meeting - Global Virtual Symposia – "Synergizing Crystallography and Spectroscopy: From Order to Dynamics" (22-26 March, 2026).

2) Best Oral Slam Presentation at the 6th Frontiers Symposium in Chemistry (FS-CHM 2026), organised by School of Chemistry, IISER Thiruvananthapuram (January 30 - February 1, 2026).

3) Best Poster Presentation Award at the 5th Frontiers Symposium in Chemistry (FS-CHM 2025), organised by School of Chemistry, IISER Thiruvananthapuram (31 January - 2 February, 2025).

4) Best Poster Presentation Award at the 12th International Symposium of Dynamic Exciton, jointly organised by Dynamic Exciton, Japan and IISER Thiruvananthapuram, held at Thiruvananthapuram, India (14-15 December 2024).

5) Best Poster Presentation Award at the 10th Ultrafast Sciences 2023 DAE-BRNS 10th Theme Meeting (UFS-2023), held at National Physical Laboratory (CSIR NPL), India (25-27 November, 2023).

6) Selected to deliver oral talk at 12th International Symposium of Dynamic Exciton, jointly organised by Dynamic Exciton, Japan and IISER Thiruvananthapuram, held at Thiruvananthapuram, India (14-15 December 2024).

Copyrights and Permissions

Copyright and permission details for Figures 1.1, 1.3, 1.5, 1.9, and 1.10 are provided below. The remaining figures used in the thesis could be reused from the respective articles without seeking further permission from the publisher, as long as proper acknowledgement is given.

1) Figure 1.1

AMERICAN CHEMICAL SOCIETY LICENSE
TERMS AND CONDITIONS

Dec 09, 2025

This Agreement between Kavya Vinod ("You") and American Chemical Society ("American Chemical Society") consists of your license details and the terms and conditions provided by American Chemical Society and Copyright Clearance Center.

License Number	6164770856729
License date	Dec 09, 2025
Licensed Content Publisher	American Chemical Society
Licensed Content Publication	Journal of the American Chemical Society
Licensed Content Title	Unraveling the Structure and Function of Melanin through Synthesis
Licensed Content Author	Wei Cao, Xuhao Zhou, Naneki C. McCallum, et al
Licensed Content Date	Feb 1, 2021
Licensed Content Volume	143
Licensed Content Issue	7
Volume number	143
Issue number	7
Type of Use	Thesis/Dissertation
Requestor type	Author (original work)

Format	Print and Electronic
Portion	Table/Figure/Micrograph
Number of Table/Figure/Micrographs	1
Title of new work	Unravelling the Structure–Property Relationship in Eumelanin: From Natural Photoprotection to Tailored Photophysics
Institution name	Indian Institute of Science Education and Research Thiruvananthapuram (IISER TVM)
Expected presentation date	Feb 2026
Portions	Figure 1
The Requesting Person / Organization to Appear on the License	Kavya Vinod
Requestor Location	Ms. Kavya Vinod School of Chemistry Indian Institute of Science Education and Research Thiruvananthapuram Thiruvananthapuram, None 695551 India
Order reference number	Figure 1.1
Payment Type	Invoice
Email Address	kavya.vnd20@iisertvm.ac.in
Billing Address	Kavya Vinod School of Chemistry Indian Institute of Science Education and Research Thiruvananthapuram Thiruvananthapuram, India 695551
Total	0.00 USD

2) Figure 1.3

AMERICAN CHEMICAL SOCIETY LICENSE
TERMS AND CONDITIONS

Dec 09, 2025

This Agreement between Kavya Vinod ("You") and American Chemical Society ("American Chemical Society") consists of your license details and the terms and conditions provided by American Chemical Society and Copyright Clearance Center.

License Number	6164780196786
License date	Dec 09, 2025
Licensed Content Publisher	American Chemical Society
Licensed Content Publication	The Journal of Physical Chemistry B
Licensed Content Title	Explanation for the Disparity among Absorption and Action Spectra of Eumelanin
Licensed Content Author	J. Brian Nofsinger, Susan E. Forest, John D. Simon
Licensed Content Date	Dec 1, 1999
Licensed Content Volume	103
Licensed Content Issue	51
Volume number	103
Issue number	51
Type of Use	Thesis/Dissertation
Requestor type	Author (original work)

Format	Print and Electronic
Portion	Table/Figure/Micrograph
Number of Table/Figure/Micrographs	1
Title of new work	Unravelling the Structure–Property Relationship in Eumelanin: From Natural Photoprotection to Tailored Photophysics
Institution name	Indian Institute of Science Education and Research Thiruvananthapuram (IISER TVM)
Expected presentation date	Feb 2026
Portions	Figure 1
The Requesting Person / Organization to Appear on the License	Kavya Vinod
Requestor Location	Ms. Kavya Vinod School of Chemistry Indian Institute of Science Education and Research Thiruvananthapuram Thiruvananthapuram, None 695551 India
Order reference number	Figure 1.3
Payment Type	Invoice
Email Address	kavya.vnd20@iisertvm.ac.in
Billing Address	Kavya Vinod School of Chemistry Indian Institute of Science Education and Research Thiruvananthapuram Thiruvananthapuram, India 695551
Total	0.00 USD

3) Figure 1.5

AMERICAN CHEMICAL SOCIETY LICENSE
TERMS AND CONDITIONS

Dec 09, 2025

This Agreement between Kavya Vinod ("You") and American Chemical Society ("American Chemical Society") consists of your license details and the terms and conditions provided by American Chemical Society and Copyright Clearance Center.

License Number	6164780381291
License date	Dec 09, 2025
Licensed Content Publisher	American Chemical Society
Licensed Content Publication	Accounts of Chemical Research
Licensed Content Title	Polydopamine and Eumelanin: From Structure–Property Relationships to a Unified Tailoring Strategy
Licensed Content Author	Marco d'Ischia, Alessandra Napolitano, Vincent Ball, et al
Licensed Content Date	Dec 1, 2014
Licensed Content Volume	47
Licensed Content Issue	12
Volume number	47
Issue number	12
Type of Use	Thesis/Dissertation
Requestor type	Author (original work)

Format	Print and Electronic
Portion	Table/Figure/Micrograph
Number of Table/Figure/Micrographs	1
Title of new work	Unravelling the Structure–Property Relationship in Eumelanin: From Natural Photoprotection to Tailored Photophysics
Institution name	Indian Institute of Science Education and Research Thiruvananthapuram (IISER TVM)
Expected presentation date	Feb 2026
Portions	Scheme 3
The Requesting Person / Organization to Appear on the License	Kavya Vinod
Requestor Location	Ms. Kavya Vinod School of Chemistry Indian Institute of Science Education and Research Thiruvananthapuram Thiruvananthapuram, None 695551 India
Order reference number	Figure 1.5
Payment Type	Invoice
Email Address	kavya.vnd20@iisertvm.ac.in
Billing Address	Kavya Vinod School of Chemistry Indian Institute of Science Education and Research Thiruvananthapuram Thiruvananthapuram, India 695551
Total	0.00 USD

4) Figure 1.9

ELSEVIER LICENSE
TERMS AND CONDITIONS

Dec 09, 2025

This Agreement between Kavya Vinod ("You") and Elsevier ("Elsevier") consists of your license details and the terms and conditions provided by Elsevier and Copyright Clearance Center.

License Number	6164780727671
License date	Dec 09, 2025
Licensed Content Publisher	Elsevier
Licensed Content Publication	Biophysical Journal
Licensed Content Title	Chemical and Structural Disorder in Eumelanins: A Possible Explanation for Broadband Absorbance
Licensed Content Author	M. Linh Tran,Ben J. Powell,Paul Meredith
Licensed Content Date	Feb 1, 2006
Licensed Content Volume	90
Licensed Content Issue	3
Licensed Content Pages	10
Start Page	743
End Page	752
Type of Use	reuse in a thesis/dissertation

Portion	figures/tables/illustrations
Number of figures/tables/illustrations	1
Format	both print and electronic
Are you the author of this Elsevier article?	No
Will you be translating?	No
Title of new work	Unravelling the Structure–Property Relationship in Eumelanin: From Natural Photoprotection to Tailored Photophysics
Institution name	Indian Institute of Science Education and Research Thiruvananthapuram (IISER TVM)
Expected presentation date	Feb 2026
Portions	Figure 6
The Requesting Person / Organization to Appear on the License	Kavya Vinod
Requestor Location	Ms. Kavya Vinod School of Chemistry Indian Institute of Science Education and Research Thiruvananthapuram Thiruvananthapuram, None 695551 India
Order reference number	Figure 1.9
Publisher Tax ID	GB 494 6272 12
Total	0.00 USD
Terms and Conditions	

INTRODUCTION

5) Figure 1.10

SPRINGER NATURE LICENSE
TERMS AND CONDITIONS

Dec 09, 2025

This Agreement between Kavya Vinod ("You") and Springer Nature ("Springer Nature") consists of your license details and the terms and conditions provided by Springer Nature and Copyright Clearance Center.

License Number	6164780968123
License date	Dec 09, 2025
Licensed Content Publisher	Springer Nature
Licensed Content Publication	Nature Communications
Licensed Content Title	Excitonic effects from geometric order and disorder explain broadband optical absorption in eumelanin
Licensed Content Author	Chun-Teh Chen et al
Licensed Content Date	May 22, 2014
Type of Use	Thesis/Dissertation
Requestor type	academic/university or research institute
Format	print and electronic
Portion	figures/tables/illustrations
Number of figures/tables/illustrations	1
Would you like a high resolution image with your order?	no

Will you be translating?	no
Circulation/distribution	30 - 99
Author of this Springer Nature content	no
Title of new work	Unravelling the Structure–Property Relationship in Eumelanin: From Natural Photoprotection to Tailored Photophysics
Institution name	Indian Institute of Science Education and Research Thiruvananthapuram (IISER TVM)
Expected presentation date	Feb 2026
Portions	Figure 1
The Requesting Person / Organization to Appear on the License	Kavya Vinod
Requestor Location	Ms. Kavya Vinod School of Chemistry Indian Institute of Science Education and Research Thiruvananthapuram Thiruvananthapuram, None 695551 India
Order reference number	Figure 1.10
Payment Type	Invoice
Email Address	kavya.vnd20@iisertvm.ac.in
Billing Address	Kavya Vinod School of Chemistry Indian Institute of Science Education and Research Thiruvananthapuram Thiruvananthapuram, India 695551
Total	0.00 USD